



International Centre
for Mechanical Sciences

Bernd R. Noack
Marek Morzyński
Gilead Tadmor
Editors

Reduced-Order Modelling for Flow Control

CISM Courses and Lectures, vol. 528



SpringerWien New York

 SpringerWienNewYork

CISM COURSES AND LECTURES

Series Editors:

The Rectors

Giulio Maier - Milan

Franz G. Rammerstorfer - Wien

Jean Salençon - Palaiseau

The Secretary General

Bernhard Schrefler - Padua

Executive Editor

Paolo Serafini - Udine

The series presents lecture notes, monographs, edited works and proceedings in the field of Mechanics, Engineering, Computer Science and Applied Mathematics.

Purpose of the series is to make known in the international scientific and technical community results obtained in some of the activities organized by CISM, the International Centre for Mechanical Sciences.

INTERNATIONAL CENTRE FOR MECHANICAL SCIENCES

COURSES AND LECTURES - No. 528



REDUCED-ORDER MODELLING FOR FLOW CONTROL

EDITED BY

BERND R. NOACK
INSTITUT PPRIME, POITIERS, FRANCE

MAREK MORZYŃSKI
POZNAN UNIVERSITY OF TECHNOLOGY, POZNAN, POLAND

GILEAD TADMOR
NORTHEASTERN UNIVERSITY, BOSTON, MA, USA

SpringerWienNewYork

FOREWORD

Practical interests in flow control have no longer to be demonstrated. Flow control has motivated rapid developments in the past two decades in experiments, flow stability theory and computational fluid dynamics (CFD). Recent advances in experimental studies include applications of more and more sophisticated actuators and sensors. However, up to now, most of the results are predominantly related to open loop, at most, adaptive approaches. Early closed-loop applications of control methods were in noise control based on anti-noise concepts. These studies established the pioneering link between fluid mechanics and control theory. However, in most aerodynamic applications, turbulent flows are encountered. Due to the intrinsic nonlinearities, turbulence gives rise to a large variety of temporal and spatial scales of more or less organized nature. Turbulence has remained one of the last not satisfactorily resolved physical phenomenon of practical importance in engineering sciences. It is obvious that the complexity of these flows is so pronounced that simpler – if this term can be used for turbulent flows – descriptions need to be derived.

The encountered complexity is observed at three levels. First, the characterization of the flow itself is complex and depends on the type of available information (e.g. sensors). Any state information is by nature incomplete or of excessive extent for turbulent flows. Second, the effect of any actuator is by nature 3D and unsteady, thus difficult to characterize. Third, the complete modelling of the flow (CFD), its sensitivity to perturbations, etc. exceeds available computer power by many orders of magnitudes, particularly for online capability in experiment. In the same vein, the predominantly (locally) linear approaches of control theory need to be adapted to the reality of the complex, turbulent flow characteristics. This leads to different levels of fluid mechanics one has to take into account. These levels can start from a detailed fluid mechanics characterization, including the more or less organized nature of the turbulent flows, the so called white-box model and end with entirely black and eventually 'empty-box' models.

The communities of flow control, applied mathematics and turbulence in fluids have then to work altogether in a close manner. Each domain enriches the other for the dedicated goal of controlling different types of flows. No currently available approach can be re-

tained, due to the variability of the physics to be controlled (e.g. flow separation, drag, lift, mixing, noise generation and fluid structure interactions). The present volume is written by leading experts of flow control and represents the state of the art of the different approaches whose complementarity will open new areas by mutual fertilization.

Jean-Paul Bonnet

Research Director, CNRS

Institut Pprime, CNRS – Université de Poitiers – ENSMA

This volume contains 101 illustrations

This work is subject to copyright.

All rights are reserved,

whether the whole or part of the material is concerned
specifically those of translation, reprinting, re-use of illustrations,
broadcasting, reproduction by photocopying machine
or similar means, and storage in data banks.

© 2011 by CISM, Udine

Printed in Italy

SPIN 80061174

All contributions have been typeset by the authors.

ISBN 978-3-7091-0757-7 SpringerWienNewYork

PREFACE

Active turbulence control is a rapidly evolving new field of fluid dynamics with large industrial importance. Several developments serve as catalysts. Actuators and sensors have become increasingly more powerful, cheaper and more reliable to be considered for practical applications. In fact, aeronautic, car and other transport-related industries work at active turbulence control solutions for selected demonstrators. Examples are the high-lift configuration of an airfoil or drag reduction of cars. The past stigma of active control as proof of a inferior aerodynamic design is replaced by the realization that active control is a critical enabler for future performance enhancements. Not much phantasy is required to envision a not-too-far future in which active control will be commonly seen on cars, trains, airplanes, helicopters, wind energy plants, air-conditioning systems, and virtually all flow related products. Active turbulence control is having an impact of epic proportions.

Active control requires at minimum parameter adjustments for flow conditions and occasionally in-time response using flow sensors. Hence, active control generally requires — or at least benefits — from a closed-loop scheme for optimal performance. Closed-loop control has clearly been demonstrated to be superior to (blind) open-loop control in many cases. Performance of closed-loop control does not only depend on the chosen actuators and sensors. It critically depends also on the control logic with its underlying model.

Model development and control design for closed-loop flow control is the focus of this book. Wiener (1948) discriminates between black-, grey-, and white-box models. The black-box models identify the dynamics between the input (actuation) and the output (sensing) from data — ignoring any other aspect of the flow. The white boxes represent the full-state representation, here: Navier-Stokes discretizations. And the grey boxes resolve a small yet relevant portion of the full state dynamics, here: the evolution of coherent structures. All models have their relative merits and shortcomings. Black-box models represent the behavior of experiments with accessible accuracy. On the downside, physical understanding of coherent structures and associated nonlinearities is discarded. Navier-Stokes discretizations are accurate representations of the flow but come with a large com-

putational load. This computational expense is a large challenge for control design and too large for any foreseeable operation in experiments. Reduced-order models for the coherent-structures are a good compromise between required resolution and necessary simplicity for online-capability in experiment. Their price is a large experience in model development. For later reference, we add to Wiener's classification model-free approaches (or 'empty boxes') which make only qualitative assumptions about the dynamics.

The authors describe the current state on closed-loop flow control from various, necessarily biased experimental and computational angles. In particular, we have attempted to provide a book with elementary self-consistent descriptions of the main methods. Thus, our book may serve also as guide through the large jungle of myriad of publications in the field. Topics include the complete span of flow control based on white-box models (first two chapters), grey-box models (second two chapters) and black- to empty-box models (final two chapters):

These lecture notes originate from a course held at the Centre International des Sciences Mécaniques (CISM) in Udine, Italy in September 2008. The Editors thank Prof. W. Schneider for the kind invitation to this course. We thank the CISM staff and the Rector Prof. G. Maier for dependable, professional support in all technical aspects of the course. The beautiful city of Udine, the cooperating late-summer weather, and the magnificent Palazzo del Torso provided the perfect forum for many memorable interactions during class-room time, breakfast, lunch and dinner. We thank the authors for their excellent lectures and equally illuminating chapters. Each chapter condenses a long-term research and teaching effort of the corresponding authors. We thank the participants for coming with large curiosity and penetrating questions, making our course a lively worthwhile event.

*Poitiers, Poznań and Boston in February 2010
Bernd Noack, Marek Morzyński and Gilead Tadmor
on behalf of the whole co-author team*

CONTENTS

Flow Control and Constrained Optimization Problems <i>by L. Cordier</i>	1
Global Stability Analysis for Linear Dynamics <i>by M. Morzyński, B.R. Noack & G. Tadmor</i>	77
Galerkin Method for Nonlinear Dynamics <i>by B.R. Noack, M. Schlegel, M. Morzyński & G. Tadmor</i>	111
Galerkin Models Enhancements for Flow Control <i>by G. Tadmor, O. Lehmann, B.R. Noack & M. Morzyński</i>	151
Feedback Flow Control in Experiment and Simulation Using Global Neural Network Based Models <i>by S. Siegel</i>	253
Optimal Closed-Loop Approaches in Flow Control <i>by R. King</i>	287

Flow control and constrained optimization problems

Laurent Cordier

Institut Pprime, CNRS – Université de Poitiers – ENSMA, UPR 3346,
Département Fluides, Thermique, Combustion, CEAT, 43 rue de l'Aérodrome,
F-86036 Poitiers Cedex, France

Abstract Constrained optimization is presented as a key enabler for answering numerous important questions in the heart of flow control. These problems range from the extraction of Proper Orthogonal Decomposition modes and tools from linear control theory to optimal control which can be applied to any type of non-linear systems. The determination of optimal growth disturbances is presented as a particular case of constrained optimization. The chapter shall provide a complete description for deriving analytically and solving numerically any specific formulation of constrained optimization.

1 Introduction

The objective of this chapter is to present within the unified framework of constrained optimization problems, different numerical tools which change completely our ideas on flow control in the last decade. We will see in particular that reduced-order modeling based on Proper Orthogonal Decomposition modes (see the contribution by B. Noack et al. in this book), as well as classical techniques of linear control (Linear Quadratic Regulator and Linear Quadratic Gaussian methods) and optimal control, have in common the resolution of a constrained optimization problem. Beyond that, we will also show that the concept of optimal disturbances, introduced in stability theory to explain the transition to turbulence of linearly stable flows, can be also formulated as a constrained optimization problem and, if needed, be solved simultaneously to a control problem. Lastly, we will highlight that inverse methods (model identification or parameter estimation) can be interpreted as a particular constrained optimization problem. The objective is to give the possibility to the interested reader of rapidly developing by

him/her-self the analytical and numerical solutions to the constrained optimization problem of his/her interest. The choice was thus made to detail as much as possible the different stages.

The current chapter is organized as follows: In section 2.1, we introduce the issues of flow control and present, for facilitating future discussions, the different actors on the control scene. Then we introduce the linearized framework, often used in flow control, and finish by formulating a series of questions related directly to different aspects of flow control. In section 2.2, we give some essential elements of linear control theory and continue in section 2.3 by an introduction of model reduction seen under the specific angle of projection methods. In section 3, we focus on the fundamental aspects of optimal control theory. At this stage, the presentation will remain very similar to what can be found in Gunzburger (1997a) and more recently in Gunzburger (2003). Section 4 considers the case of LQR control for a generic system and shows that the solution of a high-dimensional Riccati differential equation is necessary to determine the feedback control law that minimizes the value of the cost function. Section 5 highlights that the determination of optimal disturbances corresponds to a constrained optimization problem for which the control is the initial condition of the dynamical system. Lastly, sections 6 and 7 consider the case where the constraint corresponds to a time-dependent partial differential equation, linear and nonlinear respectively. Section 7 finishes with some numerical results of optimal control for the Burgers equation.

2 Elements of control theory and model reduction

2.1 Flow control

First, in section 2.1.1, we give the scope of flow control and introduce the terminology necessary to present constrained optimization problems as a main topic in modern fluid mechanics. Then, in section 2.1.2, we introduce the linearized framework used in linear control theory. Finally, in section 2.1.3, we list different types of problems which can appear within the framework of flow control while insisting on their similarity.

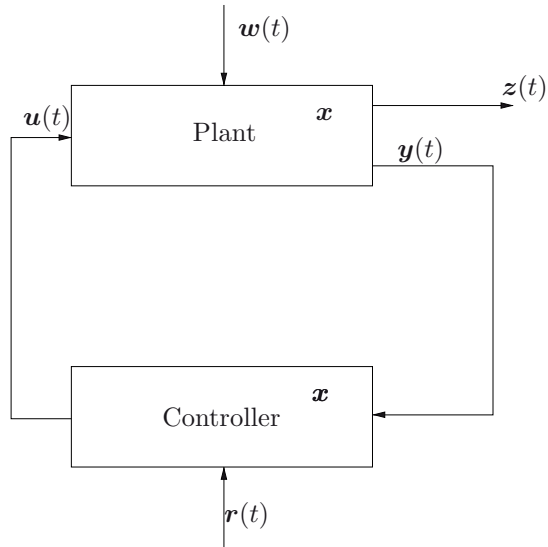
2.1.1 Scope and objectives of flow control

2.1.1.1 General points The goal of a flow control system is to achieve some desired objective by manipulating properly the flow configuration (physical properties, volume forcing or boundary conditions). Based on the type of actuation, either *passive* (no energy expenditure) or *active*, and

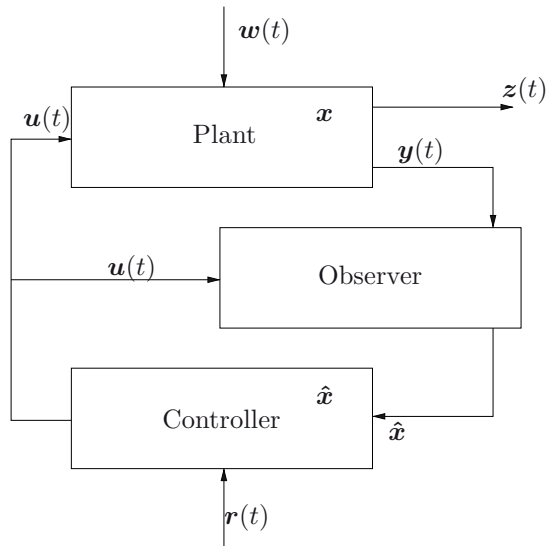
on the means by which the control evolves in response to changes in the flow, *open-loop* or *closed-loop*, different strategies can be considered (see Gad-el-Hak, 2000, for a discussion on this classification). By nature, passive control strategies are similar to shape optimization. Determining the shape that a surface of revolution must have to offer the least resistance to the motion goes back to Newton (end of 17th century) and involved the invention of the calculus of variations. We will see in section 3.1.1 that this question can be formalized as a constrained optimization problem by simply modifying the space on which the solutions are required. In open-loop, the parameters of the actuators are set once for all at the design stage and remain constant throughout the optimization procedure whatever the changes undergone by the flow. With this type of strategy, the sensitivity of the system to external disturbances or to error modeling (change in the parameters of the system) is then important. In addition, stabilizing an unstable solution - what may sometimes be interesting from a point of view of the performances - becomes difficult. For these reasons, we will consider throughout this chapter the case of closed-loop control or feedback control where there exist sensors for measuring at least partially the effects of the control on the system.

2.1.1.2 Terminology In the control literature¹, the mathematical model of the system to be controlled is called *plant*. In general, this model only approximates the behavior of the physical system. We will go back to this point and to the consequences in terms of optimization in section 2.3. The corresponding *state variables* of the plant is noted \mathbf{x} . The objective of a control system is to make the *reference output* \mathbf{z} behave in a desired way by manipulating the *plant input* \mathbf{u} (see Fig. 1). The *reference input* \mathbf{r} specifies the desired behavior of the reference output. In feedback flow control the *measured plant output* \mathbf{y} is fed back into the controller for determining the control. Compared to \mathbf{u} , the *disturbance input* \mathbf{w} consists of those inputs to the plant that are generated by the environment. It includes one contribution coming from the state disturbances \mathbf{w}_1 and another contribution coming from the measurement noise \mathbf{w}_2 . In the idealized case called *full-state configuration* (see Fig. 1(a)), the entire state \mathbf{x} is assumed to be available for the controller. In the general case called *observer-based*

¹Here, and in the rest of the chapter, we decide to use the standard notations in textbooks of control theory to familiarize the reader coming from fluid mechanics to these notations. Then, otherwise stated, \mathbf{u} denotes the control and not a velocity field. Moreover, quantities expressed in boldface correspond to vector quantities.



(a) Full state configuration.



(b) Observer-based configuration.

Figure 1. Typical block diagrams for feedback control.

configuration (see Fig. 1(b)), the plant states that are not measured directly is estimated by an observer. Thereafter, all the quantities with a hat correspond to estimated variables: for instance, $\hat{\mathbf{x}}$ are estimated states.

2.1.1.3 Plant modelling The next stage is the determination of the system of equations for the plant (Fig. 2). Starting from a physical system and some measured data, the modelling phase consists of deriving a set of Partial Differential Equations (PDEs) or Ordinary Differential Equations (ODEs). In the first case, after discretization in space of the PDEs with any numerical method (finite element, finite volume, ...), a set of ODEs is obtained. Sometimes the ODEs are discretized in time as well, yielding discrete-time dynamical systems. Here, to simplify the presentation, we will concentrate on continuous-time systems. Finally, since any dynamical system can be reduced to a first-order system of differential equations by changing the set of variables, we obtain a non-linear *state space model* given by

$$\mathcal{S} : \begin{cases} \dot{\mathbf{x}}(t) = \mathbf{f}(t, \mathbf{x}(t), \mathbf{u}(t), \mathbf{w}(t)), \\ \mathbf{z}(t) = \mathbf{h}(t, \mathbf{x}(t), \mathbf{u}(t), \mathbf{w}(t)), \\ \mathbf{y}(t) = \mathbf{g}(t, \mathbf{x}(t), \mathbf{u}(t), \mathbf{w}(t)), \end{cases}$$

where $\mathbf{x}(t) \in \mathbb{R}^{n_x}$, $\mathbf{u} \in \mathbb{R}^{n_u}$, $\mathbf{w} \in \mathbb{R}^{n_w}$, $\mathbf{y}(t) \in \mathbb{R}^{n_y}$ and $\mathbf{z} \in \mathbb{R}^{n_z}$. The non-linear functions \mathbf{f} , \mathbf{g} and \mathbf{h} are defined accordingly.

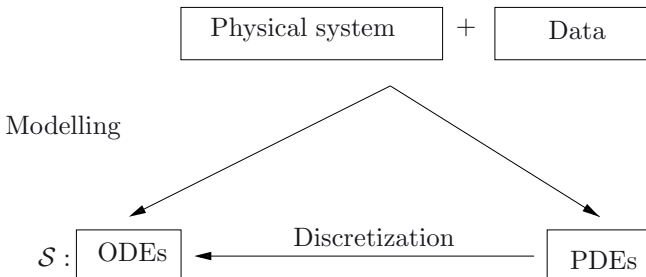


Figure 2. Broad framework of the determination of the plant equations (after Antoulas, 2005).

2.1.2 Linearized framework

Often, in practice, the non-linear system \mathbf{f} is linearized around an operating condition of interest. To simplify the future notations, we will assume that the system does not depend explicitly on time and suppress for the moment

the dependance on the external disturbance \mathbf{w} writing for the plant equations $\dot{\mathbf{x}}(t) = \mathbf{f}(\mathbf{x}(t), \mathbf{u}(t))$. Depending on the applications, this operating condition can be a particular solution of the unsteady dynamical system \mathbf{f} , that is to say $\mathbf{f}(\mathbf{x}_e(t), \mathbf{u}_e(t)) = \mathbf{0}$ or an equilibrium point of \mathbf{f} characterized by $\dot{\mathbf{x}}_e = \mathbf{f}(\mathbf{x}_e, \mathbf{u}_e) = \mathbf{0}$. In the domain of flow instabilities, this equilibrium point corresponds to a steady solution of the Navier-Stokes equations.

We then introduce the first-order perturbations $\tilde{\mathbf{x}}(t)$ and $\tilde{\mathbf{u}}(t)$ such that

$$\mathbf{x}(t) = \mathbf{x}_e(t) + \tilde{\mathbf{x}}(t) \quad \text{and} \quad \mathbf{u}(t) = \mathbf{u}_e(t) + \tilde{\mathbf{u}}(t).$$

Expanding \mathbf{f} in a Taylor series about $(\mathbf{x}_e, \mathbf{u}_e)$, we obtain

$$\begin{aligned} \dot{\mathbf{x}}_e(t) + \dot{\tilde{\mathbf{x}}}(t) &= \mathbf{f}(\mathbf{x}_e(t), \mathbf{u}_e(t)) + J_x(\mathbf{x}_e(t), \mathbf{u}_e(t))\tilde{\mathbf{x}}(t) + J_u(\mathbf{x}_e(t), \mathbf{u}_e(t))\tilde{\mathbf{u}}(t) \\ &\quad + \text{higher order terms} \end{aligned}$$

where J_x (respectively J_u) is the Jacobian matrix of \mathbf{f} with respect to \mathbf{x} (respectively \mathbf{u}):

$$(J_x)_{ij} = \frac{\partial f_i}{\partial x_j} \quad \text{with} \quad 1 \leq i \leq n_x ; \quad 1 \leq j \leq n_x$$

and

$$(J_u)_{ij} = \frac{\partial f_i}{\partial u_j} \quad \text{with} \quad 1 \leq i \leq n_x ; \quad 1 \leq j \leq n_u.$$

Neglecting the higher order terms and letting

$$A(t) = J_x(\mathbf{x}_e(t), \mathbf{u}_e(t)) \quad \text{and} \quad B(t) = J_u(\mathbf{x}_e(t), \mathbf{u}_e(t))$$

we obtain the linearized state space model

$$\dot{\tilde{\mathbf{x}}}(t) = A(t)\tilde{\mathbf{x}}(t) + B(t)\tilde{\mathbf{u}}(t)$$

where $A(t) \in \mathbb{R}^{n_x \times n_x}$ is the state matrix and $B(t) \in \mathbb{R}^{n_x \times n_u}$ is the input matrix.

Similarly, the nonlinear functions $\mathbf{z} = \mathbf{h}(\mathbf{x}, \mathbf{u})$ and $\mathbf{y} = \mathbf{g}(\mathbf{x}, \mathbf{u})$ may be linearized around the equilibrium point, resulting in a linear, parameter time-varying (LPTV) system given by

$$\mathcal{S}_{LPTV} : \begin{cases} \dot{\mathbf{x}}(t) = A(t)\mathbf{x}(t) + B(t)\mathbf{u}(t), \\ \mathbf{z}(t) = C_1(t)\mathbf{x}(t) + D_1(t)\mathbf{u}(t), \\ \mathbf{y}(t) = C_2(t)\mathbf{x}(t) + D_2(t)\mathbf{u}(t), \end{cases}$$

where for convenience the notation of the fluctuations was removed.

The state model \mathcal{S}_{LPTV} can be further simplified when the system is time-invariant. Adding the linearized contribution from the external disturbances, the system becomes

$$\begin{aligned}\dot{\mathbf{x}}(t) &= A\mathbf{x}(t) + B_1\mathbf{w}(t) + B_2(t)\mathbf{u}(t), \\ \mathbf{z}(t) &= C_1\mathbf{x}(t) + D_{11}\mathbf{w}(t) + D_{12}\mathbf{u}(t), \\ \mathbf{y}(t) &= C_2\mathbf{x}(t) + D_{21}\mathbf{w}(t) + D_{22}\mathbf{u}(t).\end{aligned}$$

This is the more general class of model that we can consider for linear-time invariant (LTI) systems. Throughout this chapter, we will restrict our attention to the simplified² linear system

$$\mathcal{S}_{LTI} : \begin{cases} \dot{\mathbf{x}}(t) = A\mathbf{x}(t) + B\mathbf{u}(t), \\ \mathbf{z}(t) = C_1\mathbf{x}(t) + D_1\mathbf{u}(t), \\ \mathbf{y}(t) = C_2\mathbf{x}(t) + D_2\mathbf{u}(t), \end{cases} \quad (1)$$

where $C_1 \in \mathbb{R}^{n_z \times n_x}$ and $C_2 \in \mathbb{R}^{n_y \times n_x}$ are the output matrices and where $D_1 \in \mathbb{R}^{n_z \times n_u}$ and $D_2 \in \mathbb{R}^{n_y \times n_u}$ are the input to output coupling matrices. A dynamical system with single input ($n_u = 1$) and single output ($n_y = 1$) is called a SISO (single input and single output) system, otherwise it is called MIMO (multiple input and multiple output) system. When this is not necessary, we will not mention the variable \mathbf{z} thereafter.

The advantage of linear systems is that the state, solution of (1), can be found explicitly from the input and the initial conditions (see Zhou et al., 1996):

$$\mathbf{x}(t) = e^{At}\mathbf{x}(0) + \int_0^t e^{A(t-\tau)}B\mathbf{u}(\tau) d\tau$$

where the matrix exponential is defined by the power series:

$$e^{At} = I + At + \frac{1}{2!}A^2t^2 + \frac{1}{3!}A^3t^3 + \dots$$

The reference and measured plant outputs are then generated as a function of the initial conditions and the input:

$$\mathbf{z}(t) = C_1 e^{At}\mathbf{x}(0) + \int_0^t C_1 e^{A(t-\tau)}B\mathbf{u}(\tau) d\tau + D_1\mathbf{u}(t)$$

and

$$\mathbf{y}(t) = C_2 e^{At}\mathbf{x}(0) + \int_0^t C_2 e^{A(t-\tau)}B\mathbf{u}(\tau) d\tau + D_2\mathbf{u}(t).$$

We will see in section 2.2.2 the consequences in terms of observability and controllability of the system \mathcal{S} .

² $B_1 = D_{11} = D_{21} = 0$, $B \triangleq B_2$, $D_1 \triangleq D_{12}$ and $D_2 \triangleq D_{22}$.

2.1.3 Different types of problems

Within the general framework of flow control, various types of problems can be considered:

Problem 1: How to determine the control law \mathbf{u} to apply to the dynamical system \mathcal{S} to minimize a given norm³ of \mathbf{z} ?

In lack of particular assumption on the model, this problem is designated as optimal control. The model \mathbf{f} can then be a Direct Numerical Simulation (Bewley et al., 2001), a Large Eddy Simulation (El Shrif, 2008) or a reduced-order model (see section 2.3) obtained by Proper Orthogonal Decomposition (Bergmann et al., 2005; Bergmann and Cordier, 2008).

Problem 2: Now let us assume that the control system design corresponds to state feedback *i.e.* $\mathbf{u} = K\mathbf{x}$ for the full state configuration or $\mathbf{u} = K\hat{\mathbf{x}}$ for the observer-based configuration. Then how to determine the control law \mathbf{u} , or equivalently the gain matrix K , to apply to \mathcal{S} to minimize a given norm of \mathbf{z} ?

If the system \mathcal{S} is Linear Time Invariant (LTI) then the problem is called Linear Quadratic Regulator or LQR, see section 4 or in Burl (1999).

Problem 3: Let $\hat{\mathbf{y}}$ be the estimated value of the output based on the estimated state $\hat{\mathbf{x}}$. For an LTI system \mathcal{S} , the state space system for the observer is

$$\begin{aligned}\dot{\hat{\mathbf{x}}}(t) &= A\hat{\mathbf{x}}(t) + B_2\mathbf{u}(t) + L(\mathbf{y}(t) - \hat{\mathbf{y}}(t)), \\ \hat{\mathbf{y}}(t) &= C_2\hat{\mathbf{x}}(t)\end{aligned}\tag{2}$$

where L is the observer gain matrix.

Then how to determine the gain matrix L so that $\hat{\mathbf{x}}$ is roughly equal to \mathbf{x} ? This question corresponds to the observer design. It can be shown (see section 2.2.2) that this problem is dual to the control problem described at the previous item.

Problem 4: How to determine one or more parameters of the system \mathcal{S} knowing the input \mathbf{x} and the corresponding output \mathbf{y} ?

Depending on the authors, this question corresponds to the estimation of physical parameters or data inversion (Tarantola, 2005), to systems' identification (Juang and Phan, 2001) or to model calibration (see Cordier et al., 2010, for an application to reduced-order models derived by POD).

³An exact definition will be given in section 3.1.2.

Problem 5: The model \mathcal{S} being known, how to determine the input \mathbf{u} to apply to \mathcal{S} to obtain given output \mathbf{y} ?

This question, which is very similar to that of the first item, corresponds to a problem of data inversion.

Problem 6: How to determine the initial condition \mathbf{x}_0 which maximizes the energetic amplification of the dynamical system \mathcal{S} ?

With this question, we can introduce the concept of optimal disturbances and optimal growth (Schmid and Henningson, 2001). We will see an application in section 5 for the linearized channel flow.

All these problems are sufficiently general to appear in many scientific disciplines sometimes very distant from each other (engineering, medical or social sciences, ...). In addition, these problems clearly all involve at a different level the resolution of a constrained optimization problem (minimization for the great majority, maximization for the problem of optimal disturbances). The solution of constrained optimization problems will thus be the object of a detailed description in section 3.

2.2 Input-output framework

In section 2.1.2 we learned how, starting from a nonlinear model of dynamics \mathcal{S} resulting from any physical modeling, to determine a linear-time invariant system. Is this step sufficient for control? On one hand, the answer is affirmative because there exist many methods of control dedicated to the linearized systems. On the other hand, we will now see that in general it is necessary to be much more careful since the mapping of measurements \mathbf{y} (output) to the control \mathbf{u} (input) is crucial to have a chance of success for the control.

2.2.1 Similarity transformations

The objective of this section is to demonstrate that the equations of the state-space system are not unique. Starting from the state-space system (1), reproduced here for convenience:

$$\begin{aligned}\dot{\mathbf{x}}(t) &= A\mathbf{x}(t) + B_2\mathbf{u}(t), \\ \mathbf{y}(t) &= C_2\mathbf{x}(t) + D_2\mathbf{u}(t)\end{aligned}$$

we consider a new state vector

$$\tilde{\mathbf{x}}(t) = \mathbb{T}^{-1}\mathbf{x}(t)$$

where \mathbb{T} is a constant, invertible transformation matrix. Since \mathbb{T} is invertible, we have $\mathbf{x}(t) = \mathbb{T}\tilde{\mathbf{x}}(t)$ and $\dot{\mathbf{x}}(t) = \mathbb{T}\dot{\tilde{\mathbf{x}}}(t)$ (\mathbb{T} independent of time). We

then obtain immediately a new state-space system defined in terms of the state $\tilde{\mathbf{x}}$:

$$\begin{aligned}\dot{\tilde{\mathbf{x}}}(t) &= (\mathbb{T}^{-1} A \mathbb{T}) \tilde{\mathbf{x}}(t) + (\mathbb{T}^{-1} B_2) \mathbf{u}(t), \\ \mathbf{y}(t) &= (C_2 \mathbb{T}) \tilde{\mathbf{x}}(t) + D_2 \mathbf{u}(t)\end{aligned}$$

In summary, the new state-space model is generated by using the following similarity transformations:

$$A \longrightarrow \mathbb{T}^{-1} A \mathbb{T} \quad ; \quad B_2 \longrightarrow \mathbb{T}^{-1} B_2 \quad ; \quad C_2 \longrightarrow C_2 \mathbb{T} \quad ; \quad D_2 \longrightarrow D_2.$$

Since there exists an infinite number of state representations for a given system, a natural question is then how we can determine the transformation \mathbb{T} best adapted to control?

2.2.2 Controllability and observability

This section addresses the following fundamental questions:

1. Can we always control a flow?
2. Can the state of a system be estimated from the measurements?

In practice, the answers to these questions provide a guide to the selection of actuators and sensors, and are also useful for developing controllers and observers.

Controllability describes the ability of the control \mathbf{u} to influence the state \mathbf{x} . Conversely, observability describes the ability to reconstruct the state \mathbf{x} based on available measurements \mathbf{y} . To simplify the description, consider \mathcal{SLTI} given by (1) with $D_2 = 0$. In this case, the output \mathbf{y} is given (see section 2.1.2) by:

$$\mathbf{y}(t) = \underbrace{\int_0^t C_2 e^{A(t-\tau)} B_2 \mathbf{u}(\tau) d\tau}_{T_1} + \underbrace{C_2 e^{At} \mathbf{x}(0)}_{T_2}.$$

The term T_1 defines a mapping from the space of the control \mathbf{u} to the space of the state \mathbf{x} . Since this map is linear, the image is a subspace of the state-space \mathbb{R}^{n_x} called the controllability subspace. This subspace depends only on the matrices A and B_2 , and is denoted S_C . Similarly, the term T_2 defines a mapping from the space of the state \mathbf{x} to the space of measurement \mathbf{y} . Since this map is also linear, the image is a subspace of the state-space \mathbb{R}^{n_y} called the observability subspace. This subspace depends only on the matrices C_2 and A , and is denoted by S_O . The kernel of this linear map forms a subspace, called the unobservable subspace. Since for these states,

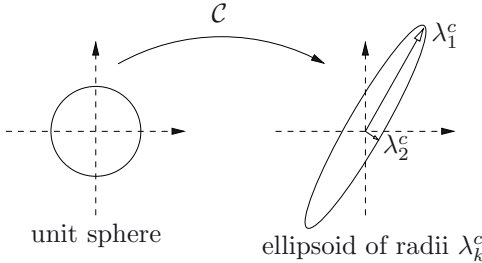


Figure 3. Geometric interpretation of the controllability operator: mapping of unit sphere onto ellipsoid. The direction corresponding to λ_1^c is more controllable than the direction corresponding to λ_2^c .

$\mathbf{y} = \mathbf{0}$, it means that the elements of the kernel⁴ may be added to any another initial state without changing the output.

2.2.2.1 Controllability Suppose the system defined in (1) is stable. Then, for $\mathbf{x}(-\infty) = \mathbf{0}$, the state at time zero $\mathbf{x}(0) = \mathbf{x}_0$ is given by

$$\mathbf{x}_0 = \int_{-\infty}^0 e^{-A\tau} B_2 \mathbf{u}(\tau) d\tau.$$

This defines the controllability operator \mathcal{C} by $\mathbf{x}_0 = \mathcal{C}\mathbf{u}$. In geometric terms analogous to the moment of inertia tensor, \mathcal{C} defines a controllability ellipsoid in the state space, with the longest principal axes along the most controllable directions (see Fig. 3).

The controllability gramian is an $n_x \times n_x$ matrix whose eigenvectors span the controllability subspace. It is defined⁵ for the system (1) as

$$W_c(t) = \mathcal{C}\mathcal{C}^H = \int_0^t e^{A\tau} B_2 B_2^H e^{A^H\tau} d\tau \quad (3)$$

where the exponent H denotes the transconjugate operator (transpose conjugate).

⁴The kernel or null space of a linear transformation is the set of vectors that map to zero. If we associate a matrix \mathcal{A} to the linear transformation, the null space of \mathcal{A} is the set of all vectors x for which $\mathcal{A}x = 0$.

⁵The controllability gramian and later the observability gramian (section 2.2.2.2) can be defined in a more general way by considering a weighted inner product (see appendix A or Ilak 2009).

If the system (1) is stable, we can consider the infinite horizon Gramian ($t \rightarrow +\infty$) and forget the dependance on time. Since W_c is clearly self-adjoint, it admits a set of real, non-negative eigenvalues λ_k^c and orthonormal eigenvectors \mathbf{x}_k^c . The eigenvalues are a measure of the amount of control energy required to obtain the corresponding eigenvectors. For two states, \mathbf{x}_1^c and \mathbf{x}_2^c with $\|\mathbf{x}_1^c\|_2 = \|\mathbf{x}_2^c\|_2$ where $\|\cdot\|_2$ denote the classical L_2 norm ($\|\mathbf{x}\|_2^2 = \mathbf{x}^H \mathbf{x}$) then if

$$\lambda_1^c = (\mathbf{x}_1^c)^H W_c \mathbf{x}_1^c = \|\mathbf{x}_1^c\|_{W_c}^2 > \|\mathbf{x}_2^c\|_{W_c}^2 = (\mathbf{x}_2^c)^H W_c \mathbf{x}_2^c = \lambda_2^c$$

it means that \mathbf{x}_1^c is more controllable than \mathbf{x}_2^c .

When the size of the system \mathcal{S} is not too high, the controllability gramian can be determined⁶ directly as the solution of a Lyapunov⁷ equation given by:

$$AW_c + W_c A^H + B_2 B_2^H = 0.$$

By definition, the dynamical system (1), or equivalently the pair (A, B_2) is said to be state controllable if and only if, for any initial state $\mathbf{x}(0) = \mathbf{x}_0$ and any final state \mathbf{x}_f , there exists an input $\mathbf{u}(t)$ such that $\mathbf{x}(t_f) = \mathbf{x}_f$ for $t_f - t_0 < +\infty$. Unfortunately, this criterion is not very usable. In practice, the controllability of a system will be verified using one or the other of the following equivalent criteria⁸ (Lewis and Syrmos, 1995; Zhou et al., 1996; Skogestad and Postlethwaite, 2005):

1. Kalman criterion

$$\text{rank} \left(\begin{bmatrix} B_2 & AB_2 & A^2 B_2 & \cdots A^{n_x-1} B_2 \end{bmatrix} \right) = n_x.$$

2. $W_c > 0$.
3. W_c is full-rank.
4. $\text{Im}(\mathcal{C}) = \mathbb{R}^{n_x}$.

Finally, let

$$E_u \triangleq \int_{-\infty}^0 \|\mathbf{u}\|_2^2 dt = \int_{-\infty}^0 \mathbf{u}^H(t) \mathbf{u}(t) dt,$$

⁶The proof is based on the time differentiation of (3). It can be found in section A7 of Burl (1999).

⁷A common way to solve continuous-time Lyapunov equation is with the function `lyap` of Matlab or with the Slicot library that can be found in <http://www.slicot.net>.

⁸We remind that the rank of a matrix \mathcal{A} corresponds to the maximal number of linearly independent rows or columns of \mathcal{A} . Moreover, a symmetric matrix \mathcal{A} is said positive definite (simply denoted $\mathcal{A} > 0$) if $\mathbf{x}^H \mathcal{A} \mathbf{x} > 0$ for all non-zero vectors \mathbf{x} . Finally, $\text{Im}(f)$ denotes the image of the operator f . If f is a mapping from E to F , then $\text{Im}(f) = \{\mathbf{y} \in F \text{ such that } f(\mathbf{x}) = \mathbf{y}, \text{ for some } \mathbf{x} \in E\}$.

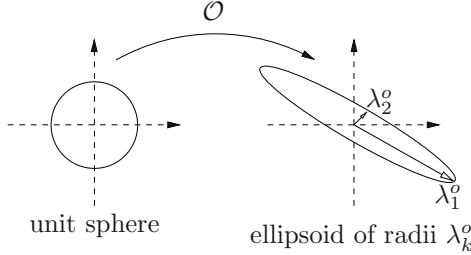


Figure 4. Geometric interpretation of the observability operator: mapping of unit sphere onto ellipsoid. The direction corresponding to λ_1^o is more observable than the direction corresponding to λ_2^o .

with $\mathbf{u}(t)$ defined for $t \in]-\infty; 0]$, be the past input energy, it can be shown (Mehrmann and Stykel, 2005) that:

$$E_{u_{min}} = \min_{\mathbf{u}} E_u = \mathbf{x}_0^H W_c^{-1} \mathbf{x}_0.$$

2.2.2.2 Observability We now consider the similar notions as in the previous section but for the output. We will thus follow a similar structure of presentation.

Suppose the system (1) is in some initial state $\mathbf{x}(0) = \mathbf{x}_0$ and $\mathbf{u}(t) = \mathbf{0}$ for $t \in [0; +\infty[$. Integrating the dynamics (1), it yields:

$$y(t) = C_2 e^{At} \mathbf{x}(0) \quad (4)$$

which defines the observability operator \mathcal{O} by $y(t) = \mathcal{O}\mathbf{x}_0$. Similarly to what we have made in section 2.2.2.1 for the controllability, we can analyze this operator in geometric terms (see Fig. 4). Here, \mathcal{O} defines an observability ellipsoid in the state space, with the longest principal axes along the most observable directions.

The observability gramian is an $n_x \times n_x$ matrix whose eigenvectors span the observability subspace. It is defined for the system (1) as

$$W_o(t) = \mathcal{O}^H \mathcal{O} = \int_0^t e^{A^H \tau} C_2^H C_2 e^{A\tau} d\tau. \quad (5)$$

For a stable system, observability can be characterized only by the infinite horizon Gramian ($t \rightarrow +\infty$) and we can forget the explicit dependance on time in W_o . The eigenvalues λ_k^o of W_o are a measure of the amount of

state energy required to obtain the corresponding eigenvectors \mathbf{x}_k^o . Obviously, we have the result that for two states, \mathbf{x}_1^o and \mathbf{x}_2^o with $\|\mathbf{x}_1^o\|_2 = \|\mathbf{x}_2^o\|_2$ then if

$$\lambda_1^o = (\mathbf{x}_1^o)^H W_o \mathbf{x}_1^o = \|\mathbf{x}_1^o\|_{W_o}^2 > \|\mathbf{x}_2^o\|_{W_o}^2 = (\mathbf{x}_2^o)^H W_o \mathbf{x}_2^o = \lambda_2^o$$

it means that \mathbf{x}_1^o is more observable than \mathbf{x}_2^o .

When the dimension of \mathcal{S} is not too high, a common way of determining the observability gramian W_o is to solve the following Lyapunov equation:

$$A^H W_o + W_o A + C_2^H C_2 = 0.$$

By definition, the dynamical system (1), or equivalently the pair (A, C_2) is said to be state observable if and only if, for any time $t_f > 0$, the initial state $\mathbf{x}(0) = \mathbf{x}_0$ can be determined from knowledge of the input $\mathbf{u}(t)$ and output $\mathbf{y}(t)$ in the interval $[0; t_f]$. In practice, the observability of a system is verified through one of the following equivalent criteria (Lewis and Syrmos, 1995; Zhou et al., 1996; Skogestad and Postlethwaite, 2005):

1. Kalman criterion

$$\text{rank} \left(\begin{bmatrix} C_2 \\ C_2 A \\ \vdots \\ C_2 A^{n_x-1} \end{bmatrix} \right) = n_x.$$

2. $W_o > 0$.
3. W_o is full-rank.
4. $\ker(\mathcal{O}) = \mathbf{0}$.

To conclude this section, let

$$E_y = \int_0^{+\infty} \|\mathbf{y}\|_2^2 dt = \int_0^{+\infty} \mathbf{y}^H(t) \mathbf{y}(t) dt,$$

with $\mathbf{y}(t)$ defined for $t \in [0; +\infty[$, be the future output energy, it can be shown easily by substituting (4) in E_y that

$$E_y = \mathbf{x}_0^H W_o \mathbf{x}_0.$$

2.2.2.3 Duality Duality is an important concept in linear control theory because, used advisedly, it can save a considerable time in the derivation of properties for the systems under investigation. To go further, we will initially admit that for any primal system defined by (1), that is to say

$$\mathcal{S} : \begin{cases} \dot{\mathbf{x}}(t) = A\mathbf{x}(t) + B_2\mathbf{u}(t), \\ \mathbf{y}(t) = C_2\mathbf{x}(t) \end{cases}$$

we can associate another state-space system, known as dual system, and given by

$$\mathcal{S}_{\text{dual}} : \begin{cases} \dot{\xi}(t) = A^H \xi(t) + C_2^H \zeta(t), \\ \eta(t) = B_2^H \xi(t). \end{cases}$$

Here, ξ is the dual state vector, and ζ and η contain the dual inputs and outputs. Comparing \mathcal{S} and $\mathcal{S}_{\text{dual}}$ it can be seen that we can deduce the dual system from the knowledge of the primal system with the transformations:

$$A \longrightarrow A^H \quad \text{and} \quad B_2 \longrightarrow C_2^H. \quad (6)$$

Duality of controllability and observability From the transformations (6) and the definitions (3) and (5), it is evident that the controllability gramian of the primal system is equal to the observability gramian of the dual system, and vice versa. As a consequence, the following results hold:

1. $\mathcal{S}(A, B_2)$ is controllable if and only if $\mathcal{S}_{\text{dual}}(A^H, B_2^H)$ is observable,
2. $\mathcal{S}_{\text{dual}}(A^H, C_2^H)$ is controllable if and only if $\mathcal{S}(A, C_2)$ is observable.

Duality of the control problem and the observer design If we now consider the cost function

$$\mathcal{J}_y = \int_0^T \|y\|_2^2 dt$$

and the corresponding cost function

$$\mathcal{J}_\eta = \int_0^T \|\eta\|_2^2 dt$$

based on the dual system, it can easily be proved⁹ that $\mathcal{J}_y = \mathcal{J}_\eta$. This property is fundamental in control theory since it can be employed to determine the observer gain matrix L for the observer design (see problem 2.1.3 in section 2.1.3) based on the solution of the dual control problem. Indeed, let $x_e(t) = x(t) - \hat{x}(t)$ be the state error, the main purpose of state observer design is to minimize $\mathcal{J} = \int_0^T \|x_e\|_2^2 dt$ where \hat{x} is given by

⁹Essentially, the proof is based on two results:

1. the transformations (6), and
2. the following equalities

$$\mathcal{J}_y = \text{trace} \left(C_2 W_c C_2^H \right) = \text{trace} \left(B_2^H W_o B_2 \right) \quad (\text{see Burl, 1999, p. 113}).$$

(2). An elegant method of determination of the observer gain matrix then consists in minimizing the same functional \mathcal{J} but by introducing the dual problem of the initial system (Huerre, 2006). We then arrive at a Linear Quadratic Regulator problem whose solution is already known (see section 4). Consequently, we will not detail thereafter the observer design (see classical textbooks Zhou et al., 1996; Burl, 1999; Skogestad and Postlethwaite, 2005, for instance) and we will concentrate on the control problem.

2.2.2.4 Balanced truncation The notions of controllability and observability, as defined respectively in sections 2.2.2.1 and 2.2.2.2, give us a means of deciding whether a state affects the system's input-output map: if a state is unobservable, it does not affect the output, and if a state is uncontrollable, it is unaffected by the input. In terms of model reduction dedicated to control (see section 2.3), in opposition to model reduction for physical understanding, it is then capital to preserve controllable and observable modes, but in which proportion? A simple answer was given by Moore (1981) for stable, linear, input-output systems. This method called balanced truncation consists in transforming the state space system into a balanced form whose controllability and observability Gramians become diagonal and equal (balanced realization), together with a truncation of those states that are both difficult to reach and to observe.

Starting from the similarity transformations given in section 2.2.1, it can be easily shown that the controllability and observability gramians become:

$$W_c \longrightarrow \mathbb{T}^{-1} W_c (\mathbb{T}^{-1})^H \quad \text{and} \quad W_o \longrightarrow \mathbb{T}^H W_o \mathbb{T}.$$

In the system of coordinates defined by \mathbb{T} , we thus have for a balanced realization:

$$\mathbb{T}^{-1} W_c (\mathbb{T}^{-1})^H = \mathbb{T}^H W_o \mathbb{T} = \Sigma = \begin{bmatrix} \sigma_1 & & \\ & \ddots & \\ & & \sigma_{n_x} \end{bmatrix}$$

where the Hankel singular values σ_i are real, positive and ordered by convention from largest to smallest. An equivalent way of finding the balancing transformation \mathbb{T} is to compute the eigendecomposition of $W_c W_o$ ($W_c W_o = \mathbb{T} \Sigma^2 \mathbb{T}^{-1}$). It can be shown (Burl, 1999) that a balanced realization exists whenever the system is stable and minimal¹⁰. A geometric interpretation of the balanced truncation is given in Fig. 5.

¹⁰A state space system is minimal if and only if the system is controllable and observable (Zhou et al., 1996). Moreover, a minimal realization of the system is associated with a matrix A of smallest possible dimension.

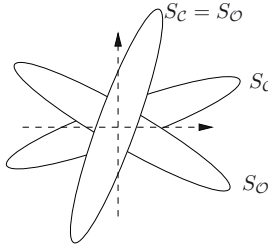


Figure 5. Geometric interpretation of the balanced truncation. S_C and S_O are respectively the controllability and observability subspaces.

An attractive feature of balanced truncation is that there exists a priori error bounds that are close to the lower bound achievable by any reduced-order model (Zhou et al., 1996, for instance). Let G denote the transfer function¹¹ of the LTI system (1) and G_r the corresponding transfer function of a reduced-order model of order r . It can be proved that, in any reduced-order model, the lower bound for the H_∞ error¹² is

$$\|G - G_r\|_\infty \geq \sigma_{r+1}$$

and that the upper bound for the error obtained by balanced truncation is given by

$$\|G - G_r\|_\infty \leq 2 \sum_{j=r+1}^{n_x} \sigma_j.$$

If the Hankel singular values are decreasing sufficiently fast, it means that the error norm of the reduced-order model of order r is very close to the lowest possible value.

¹¹For a SISO system, the transfer function G from \mathbf{u} to \mathbf{y} is defined as

$$G(s) = Y(s)/U(s)$$

where $U(s)$ and $Y(s)$ are the Laplace transform of $\mathbf{u}(t)$ and $\mathbf{y}(t)$. Moreover, it can be demonstrated that for an LTI system, we have

$$G(s) = C_2 (sI - A)^{-1} B_2 + D_2$$

where I is the identity matrix.

¹²The H_∞ norm of the system is defined in terms of the transfer function G as:

$$\|G\|_\infty = \sup_{\omega} \sigma_1 (G(j\omega))$$

where $\sigma_1(\mathcal{A})$ corresponds to the maximum singular value of the matrix \mathcal{A} and ω represents frequency.

The procedure of balanced truncation is very attractive in terms of control but the determination of the controllability and observability gramians via the solution of Lyapunov equations is not computationally tractable for very large systems. In addition, the original method suggested by Moore (1981) is limited to the linear systems. These limitations were raised recently by Lall et al. (2002) and then by Rowley (2005) who introduced approximation methods of gramians based only on snapshots of the primal and dual systems (see section 2.2.2.3). The initial method suggested by Lall et al. (2002) was to first estimate the two gramians, and then in a second time to perform the balanced truncation. The main contribution presented in Rowley (2005) is a specific algorithm that can be used to determine the balanced truncation directly from snapshots of the system *i.e.* without needing to compute the gramians themselves. This method is called Balanced POD for deep connections that it shares with POD. The reader will find all the details of the numerical setting in Rowley (2005).

2.3 Model reduction

In section 2.2.2.4, model reduction was already evoked when the least controllable and observable modes of the system were truncated based on the decrease of the Hankel singular values. In this section, we will first justify the interest of reduced-order modeling for flow control (section 2.3.1), and then present in a general way the current methods of model reduction while giving an emphasis on projection-based methods (section 2.3.2).

2.3.1 Need for reduced-order modeling

For a wing considered at cruising flight conditions *i.e.* for a Reynolds number of about 10^7 , Spalart et al. (1997) considered that to obtain numerically a converged solution, it is necessary to integrate the Navier-Stokes equations during about $5 \cdot 10^6$ time steps on about 10^{11} grid points. Then, in spite of the recent and considerable progresses of computers, it remains difficult to solve numerically problems where

- either, a great number of resolution of the state equations is necessary (continuation methods, parametric studies, optimization problems or optimal control, . . .),
- either a solution in real time is searched (active control in closed-loop control for instance).

Not surprisingly, the reduction of the costs of solving nonlinear state equations became a major issue in many scientific disciplines ranging from linear algebra to computer graphics. Sometimes, as it is the case in fluid mechanics/turbulence, model reduction has a long tradition but the objective

is more centered on the improvement of the understanding of the physical mechanisms. Let us quote for example¹³:

- Prandtl boundary layer equations (Schlichting and Gersten, 2003),
 - Reynolds-Averaged Navier-Stokes models (Chassaing, 2000),
 - Large Eddy Simulation (Sagaut, 2005),
 - Low-order dynamical system based on Proper Orthogonal Decomposition (Aubry et al., 1988),
 - Reduced-order models based on global modes (Åkervik et al., 2007),
- to name a few. Since less than ten years, the methods of model reduction are mainly considered in fluid mechanics for flow control. Lately, these methods progressed considerably under the efforts of the applied mathematicians who were interested in flow control. It is this specific point of view that is retained in the following presentation of the model reduction methods.

2.3.2 Overview of model-reduction methods

Broadly speaking, model order reduction techniques fall into two major categories:

1. projection-based methods,
2. non-projection based methods.

The first group corresponds to the methods that are currently the most used in fluid mechanics. Therefore, this approach will be detailed in section 2.3.2.1. The second group consists mainly of such methods as Hankel optimal model reduction and state-residualization. More information can be found for these methods in Antoulas (2005).

2.3.2.1 Projection-based methods The projection-based methods can be used for dynamical models going from general nonlinear systems given¹⁴ by

$$\mathcal{S} : \begin{cases} \dot{\mathbf{x}}(t) = \mathbf{f}(t, \mathbf{x}(t), \mathbf{u}(t)), \\ \mathbf{y}(t) = \mathbf{g}(t, \mathbf{x}(t), \mathbf{u}(t)), \end{cases}$$

to LTI models

$$\mathcal{S}_{LTI} : \begin{cases} E\dot{\mathbf{x}}(t) = A\mathbf{x}(t) + B_2\mathbf{u}(t), \\ \mathbf{y}(t) = C_2\mathbf{x}(t) + D_2\mathbf{u}(t), \end{cases}$$

¹³The traditional numerical methods used to solve partial derivative equations (finite difference, finite volume, finite element, spectral method,...) can also be classified in the framework of reduced-order models since these methods consist in reducing an infinite-dimensional problem to a finite-dimensional one (discretized problems).

¹⁴To simplify the formulations, we did not consider in this section the contribution of the disturbances \mathbf{w} to the models.

written here in the so-called descriptor form. The matrix E is not necessarily invertible but, when it is the case, the traditional LTI formulation is found. For these two systems, the state variables \mathbf{x} and output variables \mathbf{y} are respectively of size n_x and n_y .

The objective of reduced-order modeling is to determine for \mathcal{S} and \mathcal{S}_{LTI} the corresponding simplified models

$$\hat{\mathcal{S}} : \begin{cases} \dot{\hat{\mathbf{x}}}(t) = \hat{\mathbf{f}}(t, \hat{\mathbf{x}}(t), \mathbf{u}(t)), \\ \hat{\mathbf{y}}(t) = \hat{\mathbf{g}}(t, \hat{\mathbf{x}}(t), \mathbf{u}(t)), \end{cases}$$

and

$$\hat{\mathcal{S}}_{LTI} : \begin{cases} \hat{E}\dot{\hat{\mathbf{x}}}(t) = \hat{A}\hat{\mathbf{x}}(t) + \hat{B}_2\mathbf{u}(t), \\ \hat{\mathbf{y}}(t) = \hat{C}_2\hat{\mathbf{x}}(t) + \hat{D}_2\mathbf{u}(t) \end{cases}$$

where the control \mathbf{u} is unchanged. These simplified models are now called reduced-order models since $\hat{\mathbf{x}} \in \mathbb{R}^r$ with $r \ll n_x$ and $\mathbf{y} \simeq \hat{\mathbf{y}} \in \mathbb{R}^{n_y}$. A simplified description of model reduction is given in Fig. 6.

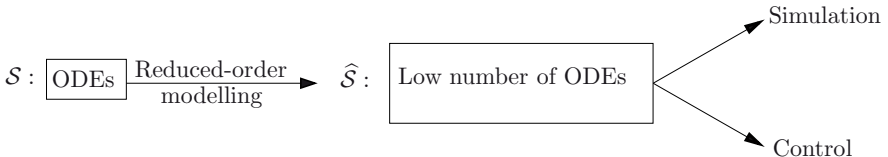


Figure 6. Broad framework of reduced-order modelling (after Antoulas, 2005).

If we want that these reduced-order models can be really usable for the applications concerned, it is necessary that the methods used to derive these simplified models satisfy various constraints:

1. Small approximation error for all admissible input signals \mathbf{u} i.e.

$$\|\mathbf{y} - \hat{\mathbf{y}}\| < \epsilon \times \|\mathbf{u}\| \quad \text{with } \epsilon \text{ a tolerance.}$$

It means that we need to have estimates of computable error bounds.

2. Stability and passivity (no generation of energy) preserved.
3. Procedure of model reduction numerically stable and efficient.
4. If possible, automatic generation of models.

In what follows we will describe an algorithm that can be used to derive a reduced-order model of any dynamical system. This algorithm, called Petrov-Galerkin projection, is based on a general bi-orthogonal projection

basis. Let V and W be two¹⁵ bi-orthogonal matrices of size $\mathbb{C}^{n_x \times r}$, and $Q \in \mathbb{C}^{n_x \times n_x}$ be the weight matrix such that

$$W^H Q V = I_r$$

where I_r is the identity matrix of size r . In the first step of the algorithm, \mathbf{x} is projected on the space spanned by the columns of V i.e. $\mathbf{x} = V\hat{\mathbf{x}}$. In the second step, this projection is inserted in the dynamical system where we have introduced the residual \mathcal{R} of the state equations. At this stage, we obtain for \mathcal{S}

$$\begin{cases} \mathcal{R} = V\dot{\hat{\mathbf{x}}}(t) - \mathbf{f}(t, V\hat{\mathbf{x}}(t), \mathbf{u}(t)), \\ \hat{\mathbf{y}}(t) = \mathbf{g}(t, V\hat{\mathbf{x}}(t), \mathbf{u}(t)), \end{cases}$$

and for \mathcal{S}_{LTI}

$$\begin{cases} \mathcal{R} = EV\dot{\hat{\mathbf{x}}}(t) - AV\hat{\mathbf{x}}(t) - B_2\mathbf{u}(t), \\ \hat{\mathbf{y}}(t) = C_2V\hat{\mathbf{x}}(t) + D_2\mathbf{u}(t). \end{cases}$$

The last step corresponds to a weak projection of the residual on the space spanned by the columns of W i.e. $W^H Q \mathcal{R} = \mathbf{0}_r$. Finally, we obtain the reduced-order model $\hat{\mathcal{S}}$ where

$$\hat{\mathcal{S}} : \begin{cases} \hat{\mathbf{f}}(t, \hat{\mathbf{x}}(t), \mathbf{u}(t)) = W^H Q \hat{\mathbf{f}}(t, V\hat{\mathbf{x}}(t), \mathbf{u}(t)), \\ \hat{\mathbf{g}}(t, \hat{\mathbf{x}}(t), \mathbf{u}(t)) = \mathbf{g}(t, V\hat{\mathbf{x}}(t), \mathbf{u}(t)), \end{cases}$$

and the reduced-order model $\hat{\mathcal{S}}_{LTI}$ where

$$\begin{aligned} \hat{A} &= W^H Q A V, & \hat{B}_2 &= W^H Q B_2, \\ \hat{C}_2 &= C_2 V, & \hat{D}_2 &= D_2, \\ \hat{E} &= W^H Q E V. \end{aligned}$$

For the choice of the matrices V and W , various possibilities exist for the linear systems:

1. In the case of Krylov methods (Gugercin and Antoulas, 2006), it corresponds to the projection on the Krylov subspace of the controllability gramian coupled with an identification of the moments of the transfer function.
2. For balanced realizations, this choice corresponds to the projection on dominant modes of the controllability and observability gramians as already discussed in section 2.2.2.4.

¹⁵When $V \neq W$, it corresponds to an oblique projection, and when $V \equiv W$ it is called Galerkin projection or orthogonal projection.

-
3. For instabilities, the projection is made on the global and adjoint global modes (Schmid and Henningson, 2001; Barbagallo et al., 2009).
 4. Finally, in the case of the Proper Orthogonal Decomposition (Lumley, 1967; Sirovich, 1987), it corresponds to the projection on the subspace determined optimally with snapshots of the system (see the contribution by B. Noack et al. in this book).

For the non-linear systems, the situation is different because, until now, there exists only the Proper Orthogonal Decomposition what explains its intensive use in the past years.

3 Optimal control theory

3.1 Constrained optimization problems

3.1.1 Abstract description

All the constrained optimization problems appearing in fluid mechanics and heat transfers (shape optimization, active flow control, optimal growth, control of thermal systems, ...) can be described mathematically by the following quantities¹⁶ (Gunzburger, 1997a, 2003):

state variables ϕ which describe the flow. Depending on the problem, these variables might be mechanical or thermodynamic, for instance velocity vectors, pressure, temperature, ...

control parameters c . In practice, these variables occur as boundary conditions of the state equations¹⁷, when the control is applied at the boundaries of the domain, or directly as a source term in the state equations if the control is distributed inside the domain (volume forcing). In data assimilation (meteorology, oceanography) and for optimal growth (see section 5) these control parameters intervene as initial conditions. According to the application, these parameters might be velocities prescribed at the boundaries (suction/blowing), heat flux or temperature at a wall, or for a shape optimization problem (Mohammadi and Pironneau, 2001), it might be variables allowing to describe

¹⁶To simplify the presentation, all the variables are here considered as scalars. However, the method extends naturally to the case of vectorial variables. For instance, an optimal control problem is solved for the Linear Quadratic Regulator approach in section 4, and for the three-dimensional Navier-Stokes equations in Bewley et al. (2001) or El Shrif (2008).

¹⁷Here, we use the traditional terminology in optimal control and call state equations, the equations which govern the dynamics of the system. Other terminologies are primal or direct equations.

geometrically the shape of the boundary. In this last case, the control parameters are rather called design variables.

a **cost or objective functional** \mathcal{J} which describes a measure of the objectives we wish to achieve. It might be drag minimization, maximization of lift or heat flux, stabilization of a temperature, flow targets, ... This functional \mathcal{J} depends on the state variables ϕ and on the control parameters c , i.e. $\mathcal{J}(\phi, c)$.

physical constraints F which represent the evolution of the state variables ϕ in terms¹⁸ of the control parameters c with respect to the physical laws. Mathematically, these constraints are noted:

$$F(\phi, c) = 0.$$

In fluid mechanics, these constraints correspond generally to the Navier-Stokes equations and their associate initial and boundary conditions. If a problem of optimal disturbance is concerned then the initial condition is imposed as a constraint (see section 5). If the control is exerted at the boundaries of the flow domain, the boundary condition can also be included as constraint (see section 6 for an example). Moreover, we will see in section 3.1.2 that an additional constraint must in general be added so that the problem is well posed mathematically.

Finally, the constrained optimization problem can be stated in the following way:

determine the state variables ϕ and the control parameters c , such that the objective functional \mathcal{J} is optimal (minimum or maximum according to the case) under the constraints F .

3.1.2 Ill-posed optimization problem and choice of the cost functional

The choice of the cost functional \mathcal{J} is central in an optimization problem. From a mathematical point of view, the physical quantity to be optimized is represented by

$$\mathcal{J} = \mathcal{M}$$

where \mathcal{M} is an appropriate measure of any physical quantity of interest: drag, lift, disturbance energy, ... The choice of this cost functional is essential in practice so that the optimization problem is well posed. This choice

¹⁸Rigorously, it would be necessary to note the variables $\phi(c)$ because ϕ depend on the control variables c via the constraints. However, to reduce the notations, we will note the state variables simply as ϕ .

is sometimes difficult to achieve. For instance, it is not obvious to know in advance if it is better to choose as cost functional a measure of the drag to minimize this quantity. In some cases (Bewley et al., 2001; El Shrif, 2008), it seems that it is preferable to minimize the averaged kinetic energy of the flow in order to minimize the drag. In addition, beyond the mathematical difficulty that is raised, we can imagine that the implementation of the control will be eased if the cost functional is based on a relevant quantity for the physics of the problem.

In general, there is no explicit relation between the objective to be reached and the control variable. This can involve that the optimization problem is ill-posed and that its solution is then divergent. To solve this difficulty, the cost of the control should be limited¹⁹. Let \mathcal{M}_c be a measure of the cost of the control, this limitation can be done:

1. By adding an additional constraint to the physical constraints (F)

This constraint corresponds to a maximum value which should not be exceeded by the control cost. Let $(\mathcal{M}_c)_{max}$ be an arbitrary positive constant, the problem is then equivalent to impose that $\mathcal{M}_c \leq (\mathcal{M}_c)_{max}$. In optimization, the inequality constraints make intervene optimality conditions known as Karush-Kuhn-Tucker (Bonnans et al., 2003) which are often delicate to take into account. For this reason, it is generally preferred to retain equality type constraints which can be imposed more easily using Lagrange multipliers (see section 3.2). It will thus be sufficient to set an additional constraint of the type $\mathcal{M}_c = \mathcal{M}_c^u$ where $\mathcal{M}_c^u > 0$ is a cost imposed by the user, to do not have to change the nature of the optimization problem to be solved.

2. By modifying the cost functional \mathcal{J}

A possible modification of the cost functional is to consider

$$\mathcal{J} = \mathcal{M} + \ell \mathcal{M}_c$$

where ℓ is a positive real constant whose value is fixed by the user according to the importance given to the cost of the control. If the value of the parameter ℓ is low then it means that the cost of the control is not a priority in the practical implementation (low costs of control). On the contrary, if the value of ℓ is high, then the cost of the control is a priority (expensive control). A more thorough discussion is given in section 4 for the LQR control.

¹⁹Apart from a mathematical justification, a limitation of the control cost is necessary since from an economic point of view the ratio saving/cost is a determining factor.

Since the approach 1 with the inequality constraint is more difficult to implement, the limitation of the cost control is introduced in most of the studies through a modification of the cost functional \mathcal{J} . In addition, another interest of the approach is that the penalization parameter ℓ clearly introduces a compromise between the objective to be reached (saving) and the importance of the control (cost).

3.1.3 Three different approaches

The current methods of solving a constrained optimization problem are distinguished in two classes (Gunzburger, 1997a, 2003). The first consists in transforming the original problem of optimization with constraints in an unconstrained optimization problem via the method of Lagrange multipliers (section 3.2) giving optimality conditions of first order. The control is then obtained by resolution of a system of coupled partial derivative equations known as *optimality system*. The second class of methods uses directly an algorithm of optimization (see section 3.3), which then requires the determination of the gradient of the objective functional, or at least of an approximation of this one. Two approaches can be used to evaluate this gradient: approach by the sensitivities described in section 3.3.1 and approach by the adjoint variables developed in section 3.3.2.

3.2 Adjoint or Lagrange multiplier methods

The principle consists to enforce implicitly the constraints of the problem via Lagrange multipliers²⁰. A new functional \mathcal{L} , known as Lagrange functional, is then introduced to define an unconstrained optimization problem. The validity of such approach can be rigorously demonstrated using theories developed in optimal control by applied mathematicians (see Gunzburger, 1997b, for elements of answers).

3.2.1 Introduction of the Lagrange multiplier

In this section, we follow the procedure outlined in Guegan et al. (2006) and introduce a single vector space $\Theta = \phi \times c \times \xi$ where ξ is the adjoint variable or Lagrange multiplier associated to the constraint $F = 0$. Let $\Phi^i = (\phi^i, c^i, \xi^i)$ with $i = I, II$ be two arbitrary elements of Θ , we define a

²⁰The Lagrange multipliers are often called adjoint variables. Strictly speaking, this appellation is abusive. A justification will be given *a posteriori* when the adjoint equations of the optimality system will be derived.

generalized inner product as

$$\{\Phi^I, \Phi^{II}\} = \langle \phi^I, \phi^{II} \rangle_s + \langle c^I, c^{II} \rangle_c + \langle \xi^I, \xi^{II} \rangle_a, \quad (7)$$

where $\langle \cdot, \cdot \rangle_s$, $\langle \cdot, \cdot \rangle_c$ and $\langle \cdot, \cdot \rangle_a$ are three inner products. These scalar products can be defined in space, in time, in space-time or defined specifically according to the problem which is considered (see later in sections 4, 5 and 6). In the case of optimal disturbances, we will consider in section 5 an energy inner product in order to determine the energy of the initial disturbances.

The constraint F is then enforced by introducing a Lagrangian functional \mathcal{L} defined as:

$$\mathcal{L}(\phi, c, \xi) \triangleq \mathcal{J}(\phi, c) - \langle F(\phi, c), \xi \rangle_a. \quad (8)$$

The new unconstrained optimization problem can then be stated as:

determine the state variables ϕ , the control parameters c and the adjoint variables ξ , such as the Lagrangian functional \mathcal{L} reaches an extremum.

3.2.2 Derivation of the optimality system

The Lagrangian functional \mathcal{L} admits an extremum when \mathcal{L} is rendered stationary. A first-order necessary condition for an extremum of \mathcal{L} is that its first-order variation $\delta\mathcal{L}$ is equal to 0 i.e.

$$\delta\mathcal{L} = \frac{\partial\mathcal{L}}{\partial\phi}\delta\phi + \frac{\partial\mathcal{L}}{\partial c}\delta c + \frac{\partial\mathcal{L}}{\partial\xi}\delta\xi = 0.$$

For simplifying further the expression of $\delta\mathcal{L}$, each argument of \mathcal{L} is considered²¹ as independent of the others. The necessary condition is then equivalent to

$$\frac{\partial\mathcal{L}}{\partial\phi}\delta\phi = \frac{\partial\mathcal{L}}{\partial c}\delta c = \frac{\partial\mathcal{L}}{\partial\xi}\delta\xi = 0, \quad (9)$$

where the variations $\delta\phi$, δc and $\delta\xi$ are arbitrary.

Equivalently, the stationary points of the Lagrangian \mathcal{L} can be characterized by the gradients of \mathcal{L} with respect to all the variables. By convention, the gradients of \mathcal{L} with respect to ϕ , c and ξ are denoted in the following respectively by $\nabla_\phi\mathcal{L}$, $\nabla_c\mathcal{L}$ and $\nabla_\xi\mathcal{L}$. The stationary points of \mathcal{L} then correspond to:

$$\nabla_\phi\mathcal{L} = \nabla_c\mathcal{L} = \nabla_\xi\mathcal{L} = 0. \quad (10)$$

²¹Note that this is obviously wrong for the original problem involving \mathcal{J} since the variables ϕ and c were constrained to satisfy $F(\phi, c) = 0$.

These gradients are determined as projections of $\nabla \mathcal{L}(\Phi)$, gradient of the Lagrangian at point Φ , onto the different subspaces corresponding to each of the variables ϕ , c and ξ . Assuming that \mathcal{L} is Fréchet-differentiable, $\nabla \mathcal{L}(\Phi)$ is such that for any variation $\delta\Phi$ we have:

$$\{\nabla \mathcal{L}(\Phi), \delta\Phi\} = d\mathcal{L}|_{\Phi}(\delta\Phi), \quad (11)$$

where $\{\cdot, \cdot\}$ is the scalar product introduced in (7). Furthermore, the Gâteau differential $d\mathcal{L}|_{\Phi}$ of the Lagrangian \mathcal{L} evaluated at point Φ is given by

$$d\mathcal{L}|_{\Phi}(\delta\Phi) = \lim_{\epsilon \rightarrow 0} \frac{\mathcal{L}(\Phi + \epsilon\delta\Phi) - \mathcal{L}(\Phi)}{\epsilon}. \quad (12)$$

The expressions (9) and (10) correspond to a necessary and sufficient condition for determining a local extremum of \mathcal{L} , but it constitutes only a necessary condition for obtaining a minimum or a maximum. This type of method thus ensures only to obtain a local extremum but not a global one. We then have to keep in mind while using it that the algorithm of optimization may be remain trapped in a local minimum without any physical interest. Obviously, it would be better to use methods of global optimization (genetic algorithms for instance) but those are still too expensive to be used currently in fluid mechanics.

We will now derive the optimality system by setting successively the first variations of \mathcal{L} with respect to the adjoint variable ξ , direct variable ϕ and control variable c equal to zero.

▷ **Determination of $\nabla_{\xi}\mathcal{L}$ or directional derivative in the direction $\delta\xi$:**

A variation $\delta\Phi$ given by $(0, 0, \delta\xi)$ is considered. Using the definition (8) of the Lagrangian functional \mathcal{L} , and the definitions (11) and (12) respectively of the Fréchet and Gâteau derivatives, it yields to:

$$\begin{aligned} \langle \nabla_{\xi}\mathcal{L}, \delta\xi \rangle_a &= \\ \lim_{\epsilon \rightarrow 0} \frac{\mathcal{J}(\phi, c) - \langle F(\phi, c), \xi + \epsilon\delta\xi \rangle_a - \mathcal{J}(\phi, c) + \langle F(\phi, c), \xi \rangle_a}{\epsilon} &= 0, \end{aligned}$$

i.e. after simplification,

$$\langle F(\phi, c), \delta\xi \rangle_a = 0.$$

Since $\delta\xi$ is arbitrary, it can be deduced that

$$F(\phi, c) = 0, \quad (13)$$

what corresponds to the constraints of the original problem of optimization.

Thus, setting the first variation of \mathcal{L} with respect to the Lagrange multiplier equal to zero gives back the equations of constraints (**state equations**).

▷ **Determination of $\nabla_\phi \mathcal{L}$ or directional derivative in the direction $\delta\phi$:**

In this case, we consider a perturbation $\delta\Phi$ given by $(\delta\phi, 0, 0)$. Following the same procedure as for the state equations, we obtain:

$$\langle \nabla_\phi \mathcal{L}, \delta\phi \rangle_s = \lim_{\epsilon \rightarrow 0} \frac{\mathcal{J}(\phi + \epsilon\delta\phi, c) - \langle F(\phi + \epsilon\delta\phi, c), \xi \rangle_a - \mathcal{J}(\phi, c) + \langle F(\phi, c), \xi \rangle_a}{\epsilon} = 0.$$

Introducing the Taylor series of \mathcal{J} and F at the order $\mathcal{O}(\epsilon)$, the previous relation becomes:

$$\lim_{\epsilon \rightarrow 0} \left(\frac{\partial \mathcal{J}}{\partial \phi} \delta\phi - \langle \frac{\partial F}{\partial \phi} \delta\phi, \xi \rangle_a + \mathcal{O}(1) \right) = 0$$

i.e.

$$\frac{\partial \mathcal{J}}{\partial \phi} \delta\phi - \langle \frac{\partial F}{\partial \phi} \delta\phi, \xi \rangle_a = 0.$$

The first term can be expressed with the inner product $\langle ., . \rangle_a$ yielding to:

$$\langle \frac{\partial \mathcal{J}}{\partial \phi} \delta\phi, 1 \rangle_a - \langle \frac{\partial F}{\partial \phi} \delta\phi, \xi \rangle_a = 0.$$

Introducing the adjoint operator (see appendix A) $(.)^+$ with respect to the inner product $\langle ., . \rangle_a$, we can write the previous relation as:

$$\langle \delta\phi, \left(\frac{\partial \mathcal{J}}{\partial \phi} \right)^+ \rangle_a - \langle \delta\phi, \left(\frac{\partial F}{\partial \phi} \right)^+ \xi \rangle_a = 0.$$

This equality must be verified whatever the variation $\delta\phi$ of ϕ is. We then obtain the **adjoint equations**:

$$\left(\frac{\partial F}{\partial \phi} \right)^+ \xi = \left(\frac{\partial \mathcal{J}}{\partial \phi} \right)^+. \quad (14)$$

These equations correspond to the adjoint of the state equations linearized around the state. They are thus linear in the adjoint variables ξ ,

thus facilitating their resolution. In addition, the Lagrange multipliers satisfy the equations associated to the constraints with a source term resulting from the cost functional; this justifies the name of adjoint variables given to the Lagrange multipliers.

When the state equations are non-linear (a typical case being the Navier-Stokes equations), the adjoint equations (14) depend on the solution of the state equations (13). The solution of the direct equations is then required before the adjoint equations can be solved. Moreover, it can be shown that for time-dependent problems, the adjoint equations are defined backward in time (see section 4.3.2 for the LQR control). Therefore, in solving the adjoint equations, the calculations start from the terminal condition rather than an initial condition. This characteristic poses a unique challenge for efficient solution of unsteady adjoint equations since the solution of the adjoint equations at each time step requires the solution of the direct equations at the same time step. This leads to a serious demand on computer memory. Some solutions to this problem are proposed in section 3.2.3.

▷ **Determination of $\nabla_c \mathcal{L}$ or directional derivative in the direction δc :**

Here, we consider $\delta\Phi = (0, 0, \delta c)$. We obtain immediately that:

$$\begin{aligned} \langle \nabla_c \mathcal{L}, \delta c \rangle_c &= \\ \lim_{\epsilon \rightarrow 0} \frac{\mathcal{J}(\phi, c + \epsilon \delta c) - \langle F(\phi, c + \epsilon \delta c), \xi \rangle_a - \mathcal{J}(\phi, c) + \langle F(\phi, c), \xi \rangle_a}{\epsilon} &= 0. \end{aligned}$$

Then we proceed as we did for the adjoint equations. We first introduce the Taylor series of \mathcal{J} and F at the order $\mathcal{O}(\epsilon)$. It comes

$$\frac{\partial \mathcal{J}}{\partial c} \delta c - \langle \frac{\partial F}{\partial c} \delta c, \xi \rangle_a = 0,$$

i.e. after writing the first term with an inner product

$$\langle \frac{\partial \mathcal{J}}{\partial c} \delta c, 1 \rangle_a - \langle \frac{\partial F}{\partial c} \delta c, \xi \rangle_a = 0.$$

Finally, we introduce the adjoint operators to yield

$$\langle \nabla_c \mathcal{L}, \delta c \rangle_c = \langle \delta c, \left(\frac{\partial \mathcal{J}}{\partial c} \right)^+ \rangle_a - \langle \delta c, \left(\frac{\partial F}{\partial c} \right)^+ \xi \rangle_a = 0. \quad (15)$$

Since the variation δc of c is arbitrary, we obtain the **optimality conditions**:

$$\left(\frac{\partial F}{\partial c} \right)^+ \xi = \left(\frac{\partial \mathcal{J}}{\partial c} \right)^+. \quad (16)$$

These optimality conditions are first order. They are satisfied exactly only when an extremum of the cost functional is achieved. One advantage of the Lagrangian-based formulation is to provide not only the optimality condition but also an expression for the gradient of the cost functional \mathcal{J} with respect to the control c . Indeed, in the constrained subspace where $F(\phi, c) = 0$, the gradient of the Lagrangian simply reduces to

$$\nabla_c \mathcal{L} = \nabla_c \mathcal{J}. \quad (17)$$

Starting from (15), we can determine an expression for $\nabla_c \mathcal{L}$ when the relation between the inner products $\langle \cdot, \cdot \rangle_c$ and $\langle \cdot, \cdot \rangle_a$ is known. A striking example can be found in section 5.1.2.3 for the optimal growth perturbation. Finally, the optimality condition (16) must be interpreted as the gap to zero of the gradient of the cost functional $\nabla_c \mathcal{J}$.

The necessary conditions (13), (14) and (16) form a coupled system of partial differential equations called *optimality system*. When the number of unknowns of the optimality system is not too important, a direct method of resolution known as "one shot method" can be used to obtain without iteration the optimal solution (see Galletti et al., 2007, for example, for an application to the calibration of POD reduced order models). Unfortunately, in fluid mechanics, the optimization problems comprise too many degrees of freedom (10^7 for the turbulent channel flow studied by Direct Numerical Simulation in Bewley et al. 2001) to prevent the use of a direct method. It turns out that it is necessary to have recourse to iterative methods for which the optimal control is approximated step by step until convergence. This approach is described in the next section.

3.2.3 Numerical resolution

The optimality system can be solved iteratively in the following manner. The resolution is initialized with a given control $c^{(0)}$ (here and below, the superscripts (n) denote the iteration number). Then, for $n = 0, 1, 2, \dots$ and as long as a given criterion of convergence is not satisfied, the following steps are carried out:

Step 1: Solve the state equations (13) forward in time to determine the state variables $\phi^{(n)}$

$$F(\phi^{(n)}, c^{(n)}) = 0.$$

Step 2: Use the state variables computed in step 3.2.3 to solve the adjoint equations (14) backward in time for the adjoint variables $\xi^{(n)}$

$$\left(\frac{\partial F}{\partial \phi} \right)^{+(n)} \xi^{(n)} = \left(\frac{\partial \mathcal{J}}{\partial \phi} \right)^{+(n)}.$$

Step 3: Use the state variables $\phi^{(n)}$ computed in step 3.2.3 and the adjoint variables $\xi^{(n)}$ computed in step 3.2.3 to estimate the optimality conditions (16)

$$\left(\frac{\partial \mathcal{J}}{\partial c} \right)^{+(n)} = \left(\frac{\partial F}{\partial c} \right)^{+(n)} \xi^{(n)}.$$

Step 4: Set $n = n + 1$ and return at step 3.2.3 until a given criterion of convergence is satisfied.

At stage 3.2.3 of the iterative process, a new control can be determined with a gradient type method:

$$c^{(n+1)} = c^{(n)} - \omega^{(n)} (\nabla_c \mathcal{J})^{(n)}. \quad (18)$$

The relaxation parameter $\omega^{(n)}$ is given using a line search method (Nocedal and Wright, 1999). It can be shown that this simple iterative method corresponds to a steepest descent algorithm for the unconstrained functional $\mathcal{J}(\phi(c), c)$. Figure 7 represents schematically the above algorithm.

This iterative procedure enables the reduction of the memory required for the resolution of the optimality system. However, for time-dependent problems, the adjoint equations are marched backward in time. For solving the adjoint equations at any time step, it is then necessary to know the solution of the state equations at the same time step. According to the relative importance of CPU and memory in the optimization procedure, several numerical strategies are possible. Let us consider²² for the discussion that the memory is the limiting criterion in our application. The first method, referred to as instantaneous control in the control literature (see Fig. 8), consists in dividing the time horizon T_o on which optimization is performed

²²In most of the applications, the memory is indeed the limiting criterion. One exception is the case of real-time flow control where the main objective is to reduce the CPU time necessary for solving the optimality system.

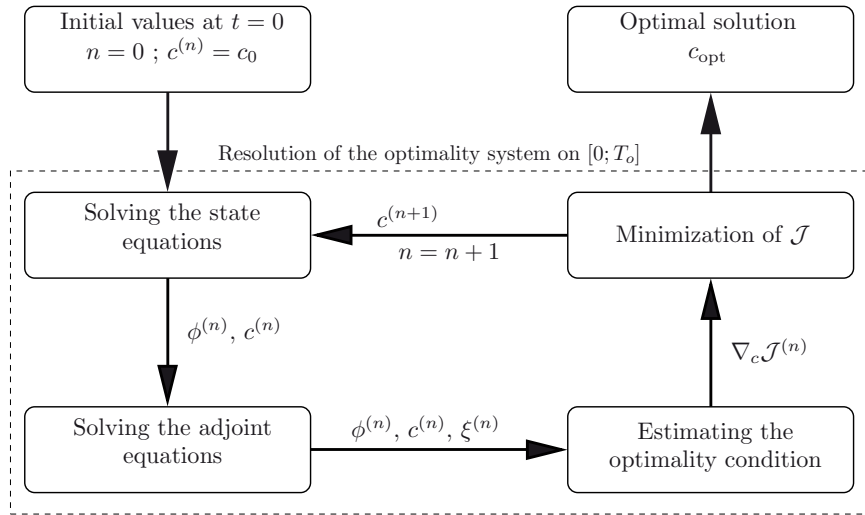


Figure 7. Iterative resolution of the optimality system (schematic representation).

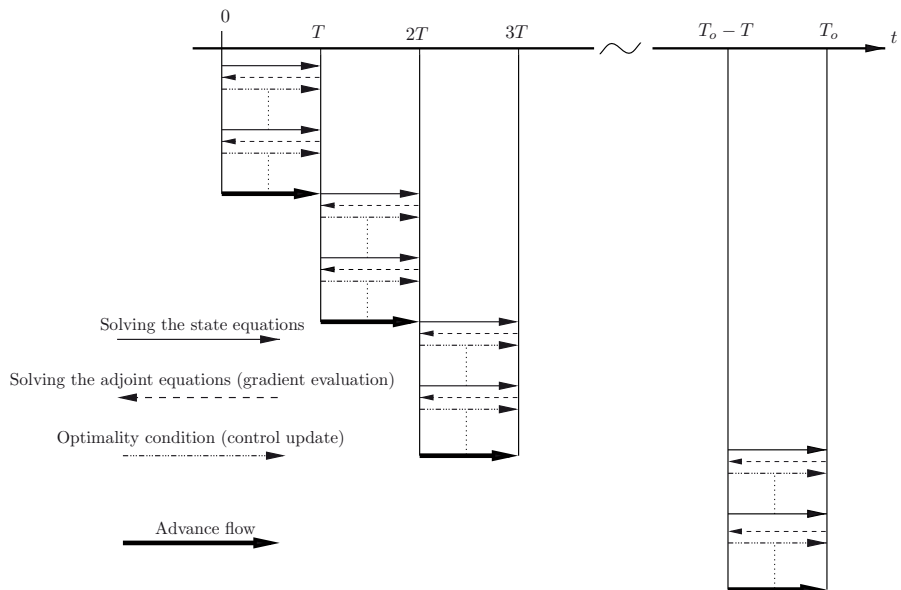


Figure 8. Instantaneous control approach.

in N smaller time window $[T_k; T_{k+1}]$ ($k = 0, \dots, N$) of size T . The optimality system is successively solved on each window, where the state reached by the optimized flow at the end of a given interval is taken as guess values for optimization on the following interval (see Fig. 9). Of course, instantaneous control will not lead in general to the same control that would be obtained by optimizing the cost functional over T_o . However, this strategy was used successfully in the past for the turbulent channel flow (Bewley et al., 2001; Chang, 2000; El Shrif, 2008) and for the cylinder wake flow in laminar regime (Protas, 2002; Bergmann et al., 2005). Another method for reduc-

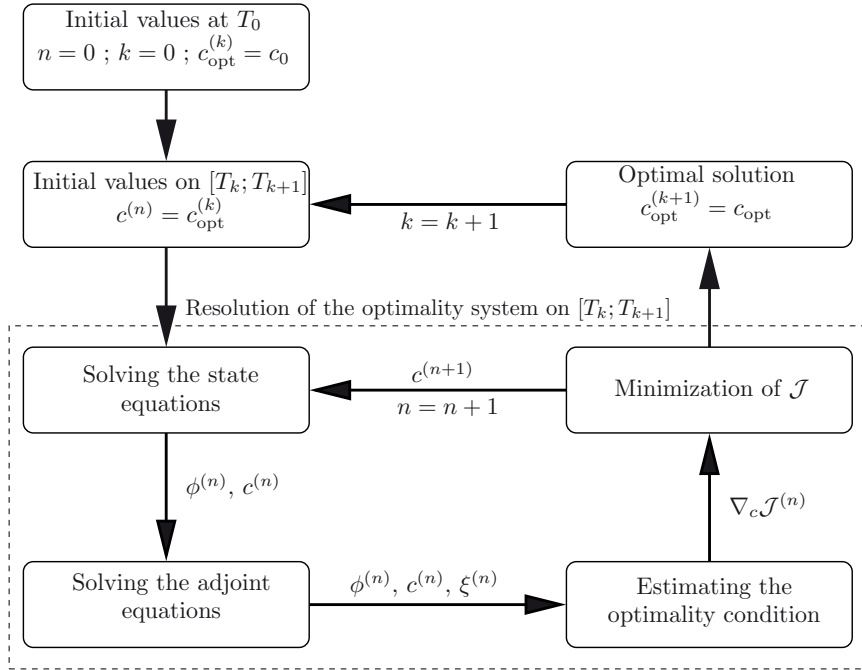


Figure 9. Iterative resolution of the optimality system for the instantaneous control approach (schematic representation).

ing the memory requirement is the use of reduced-order models (see section 2.3) as state equations. Depending on the configurations, these approximation models can be mathematically or physically derived. For instance, in Bergmann et al. (2005), a POD reduced-order model was derived as state equations for the cylinder wake flow and, in El Shrif (2008), a Large Eddy Simulation was used as approximate model for the turbulent channel flow.

Compared to previous studies where a Direct Numerical Simulation was employed as state equations, drastic reductions of the computational costs (memory and CPU) were found. The conceptual drawback of this method is that there is no mathematical assurance that the solution of the optimization algorithm working with the approximation models will correspond to the solution of the optimization problem for the original dynamical system. To circumvent this limitation, one possibility is to embed POD reduced-order modeling in the framework of trust-region optimization as was done with the Trust Region Proper Orthogonal Decomposition algorithm introduced in Fahl (2000). Indeed, with this algorithm, mathematical proofs exist that the solutions converge at least to a local optimum of the original high-fidelity problem (see Bergmann and Cordier, 2008, for numerical evidence in the case of the cylinder wake flow). A third method for simplifying the resolution of the optimality system is to change the time-reversed nature of the adjoint equations. For that, Wang et al. (2008) proposed recently to use a Monte Carlo linear solver for solving forward in time the unsteady adjoint equations. This method was only demonstrated for the Burgers' equation. Many issues remain to be solved before this method can be employed for the Navier-Stokes equations. A last method is using a dynamic checkpointing scheme. The basic idea of checkpointing methods is to solve the state equations first, and store its solution at selected time steps called checkpoints. When the adjoint equations are integrated backward in time, the solutions at corresponding time steps are calculated by re-solving the state equations starting from the nearest checkpoint (Griewank and Walther, 2008). Recently, Wang et al. (2009) suggested a dynamic checkpoint scheme that minimizes the maximum number of recalculations for each time step, and guarantees an efficient calculation of the adjoint equations when memory storage is limited. Moreover, in contrast to previous checkpointing methods, their scheme has provable performance bounds and works for arbitrarily large number of time steps.

3.3 Optimization methods

The second class of methods for solving constrained optimization problems corresponds to the use of optimization algorithms. Many of these algorithms require the gradient of the cost functional with respect to the control parameters or at least an approximation of this gradient. Since the iterative algorithm presented in section 3.2.3 is equivalent to a steepest descent algorithm which does not converge very quickly, it is preferable to use more sophisticated methods of optimization. A typical algorithm of optimization is written as follows:

Start with an initial guess $c^{(0)}$ for the control. Then, for $n = 0, 1, 2, \dots$ and until a given convergence criterion is achieved, the following phases are carried out:

Step 1: Solve the state equations $F(\phi^{(n)}, c^{(n)}) = 0$ to determine the state variables $\phi^{(n)}$.

Step 2: Compute the gradient of the functional \mathcal{J} with respect to the control variables c : $d\mathcal{J}/dc|_{c^{(n)}}$ or $(\nabla_c \mathcal{J})^{(n)}$.

Step 3: Use the results of stages 3.3 and 3.3 to compute an increment $\delta c^{(n)}$.

Step 4: Determine new control parameters

$$c^{(n+1)} = c^{(n)} + \delta c^{(n)}$$

Step 5: Set $n = n + 1$ and return at stage 3.3.

For each iteration of the optimization algorithm, it is necessary to solve at least one state equation. To reduce the computational costs, it is thus interesting to replace the state equations by reduced-order models (see section 2.3). In addition, many points of this algorithm must be specified:

1. How to determine the gradient of the cost functional at stage 3.3?
2. How to determine the increment of the control at stage 3.3?
3. How to choose the criterion of convergence for the optimization algorithm?

The possible methods that can be used to determine the gradient of the cost functional is discussed in more details in section 3.3.1. For determining the increment of the control, different gradient-based optimization methods (Nocedal and Wright, 1999) can be used such as non-linear conjugate gradient methods (Fletcher-Reeves, Polak-Ribire, Hestenes-Stiefel, ...), trust-region methods, quasi-Newton methods (BFGS, DFP, SR1, ...). Finally, for the convergence criterion, a stopping test $\| d\mathcal{J}/dc|_{c^{(n)}} \| < \epsilon$ for $\epsilon \rightarrow 0$ is in general sufficient.

3.3.1 Functional gradients through sensitivities

To obtain the gradient of the cost functional with respect to the control variables at stage 3.3 of the previous algorithm, the chain rule can be applied to $\mathcal{J}(\phi(c), c)$. The following expression is then obtained²³:

$$\frac{d\mathcal{J}(\phi, c)}{dc} = \frac{\partial \mathcal{J}(\phi, c)}{\partial \phi} \frac{d\phi}{dc} + \frac{\partial \mathcal{J}(\phi, c)}{\partial c}. \quad (19)$$

²³There will be an equation similar to (19) for each control parameter.

Since the cost functional \mathcal{J} depends explicitly of ϕ and c (see section 3.1.2), the partial derivatives $\frac{\partial \mathcal{J}}{\partial \phi}$ and $\frac{\partial \mathcal{J}}{\partial c}$ will be "easy" to determine. On the other hand, the implicit dependency of the state variables ϕ on the control variables c renders more delicate the evaluation of the sensitivities $\frac{d\phi}{dc}$. In practice, two approaches can however be used:

By finite differences. Indeed, the sensitivities can be approximated by finite difference in the following way:

$$\left. \frac{d\phi}{dc} \right|_{c^{(n)}} \simeq \frac{\phi(c^{(n)} + \Delta c^{(n)}) - \phi(c^{(n)})}{\Delta c^{(n)}}$$

where the step size $\Delta c^{(n)}$ is chosen as small as possible to minimize truncation error but not too small for avoiding that errors due to subtractive cancellation become dominant.

The cost of calculating sensitivities with finite differences is proportional to the number of design variables. This method is expensive numerically since the state equations must be solved for each perturbation of $c^{(n)}$.

By solving linear systems. Another method for calculating the sensitivities consists in differentiating the state equation $F(\phi, c) = 0$. We then obtain:

$$dF = \frac{\partial F}{\partial \phi} d\phi + \frac{\partial F}{\partial c} dc = 0,$$

i.e.

$$\left(\frac{\partial F}{\partial \phi} \Big|_{c^{(n)}} \right) \left. \frac{d\phi}{dc} \right|_{c^{(n)}} = - \left. \frac{\partial F}{\partial c} \right|_{c^{(n)}}. \quad (20)$$

Finally, the sensitivities are obtained by resolution of this linear system. The major drawback of this approach is that it is necessary to solve as many²⁴ linear systems that there are control parameters. This method is however much more efficient than the approach by finite differences: indeed, the sensitivities are determined exactly by resolution of linear systems.

²⁴One can however reduce the computational cost related to this method by noticing that only the right-hand side of (20) depends on a particular control parameter. Then, at a given iteration number n , the left-hand side operator can be discretized once for all and then used to solve all the linear systems.

3.3.2 Functional gradients through adjoint equations

The gradient of the cost functional \mathcal{J} with respect to the control variables c can also be obtained while combining the adjoint equation (14) and the expression (19) giving $\frac{d\mathcal{J}}{dc}$.

Indeed, the adjoint of (14) corresponds to

$$\xi^+ \frac{\partial F}{\partial \phi} = \frac{\partial \mathcal{J}}{\partial \phi}. \quad (21)$$

By introducing this equation into the expression (19) of the gradient of the cost functional with respect to the control variables, one obtains:

$$\frac{d\mathcal{J}(\phi, c)}{dc} = \xi^+ \frac{\partial F(\phi, c)}{\partial \phi} \frac{d\phi}{dc} + \frac{\partial \mathcal{J}(\phi, c)}{\partial c}.$$

Finally, using (20), it yields to:

$$\frac{d\mathcal{J}}{dc}(\phi^{(n)}, c^{(n)}) = - (\xi^+)^{(n)} \left. \frac{\partial F}{\partial c} \right|_{c^{(n)}} + \left. \frac{\partial \mathcal{J}}{\partial c} \right|_{c^{(n)}}. \quad (22)$$

The advantage of this method compared to that of the sensitivities is that it is necessary to solve only one linear system (the adjoint system 21) and that independently of the number of control parameters.

3.4 Differentiation and discretization

Two distinct approaches exist for formulating the adjoint system: continuous and discrete, or using the terminology of Gunzburger (2003) differentiate-then-discretize and discretize-then-differentiate. In the differentiate-then-discretize approach (see Fig. 10), the adjoint problem is derived analytically, based on the original system of partial differential equations, and then discretized using similar numerical methods to those used for discretizing the state equations. In the discretize-then-differentiate approach (see Fig. 11), the continuous direct problem is first discretized and these equations are then differentiated to obtain the discretized adjoint equations. For finite values of the grid sizes, the approximations of the discrete adjoints obtained by the continuous and discrete approaches are different, because the differentiation and discretization steps do not commute. Thus, we have to decide which approach is better for a specific problem.

The main advantage of the discretize-then-differentiate approach is that it yields to the exact gradient (except for round-off errors) of the discretized

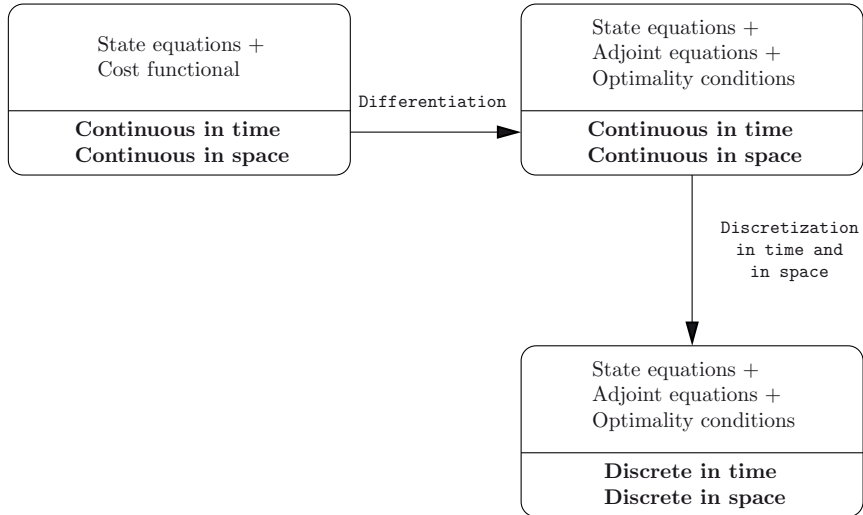


Figure 10. Differentiate-then-discretize approach for adjoint-based optimization methods.

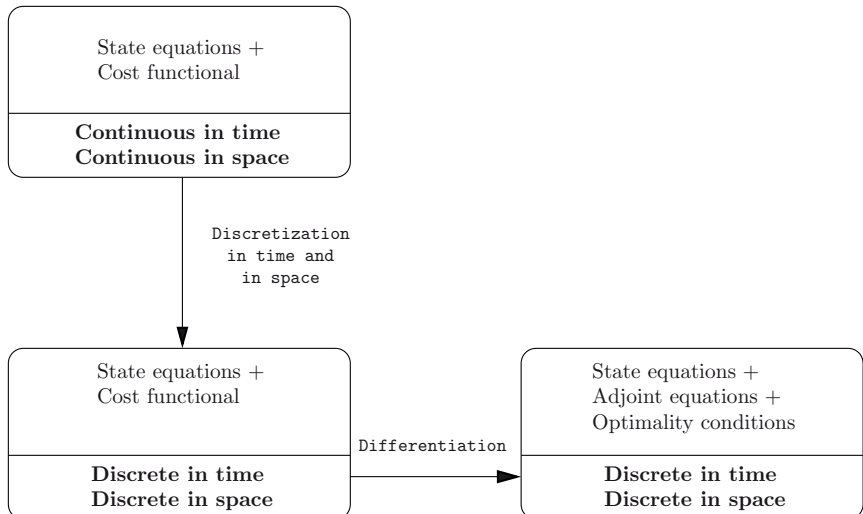


Figure 11. Discretize-then-differentiate approach for adjoint-based optimization methods.

functional. On the other hand, discrete adjoints obtained through the differentiate-then-discretize approach can yield to inconsistent gradients of cost functionals. Indeed, the approximate discrete adjoints are not the exact derivatives of the continuous functional, nor of a discretized functional. If the consistency of functional gradients is the only criterion that is considered then the advantage goes clearly to the discrete approach. However, differentiating by hand the discretized equations may become rapidly a formidable task, all the more if the state equations are strongly non-linear and if the discretization schemes are complex. Fortunately, to simplify the writing of adjoint codes, automatic differentiation software (see the web site <http://www.autodiff.org>) can be used to generate discrete adjoints. However, as one can imagine, adjoint codes created by automatic differentiation tools such as ADIFOR, TAMC, FastOpt, Tapenade, ... usually require more storage and CPU time than those written with the continuous approach. One advantage of using the differentiate-then-discretize approach is the possibility that is offered to design numerical grids that are specifically well suited to the adjoint systems. Indeed, if automatic differentiation tool is used to evaluate the approximate adjoint variables, the same grids are used for the state and adjoint equations what is clearly not optimal for numerical convergence. In the end, the continuous approach seems more natural for deriving the adjoint equations. For this reason, this is the approach that will be used in all the applications described in this chapter.

4 Linear quadratic optimal control

The Linear Quadratic Regulator (LQR) is an optimal control problem where the state equation is linear, the cost functional is quadratic, and the objective of the controller is to regulate, *i.e.* return to zero, some measure of the reference output \mathbf{z} without using excessive amounts of control. The cost is evaluated subject to the initial condition $\mathbf{x}(0) = \mathbf{x}_0$ and with the assumption of no disturbance input \mathbf{w} . Therefore, we can use for plant model the LTI system given by (1). We must now specify the measure which is used for minimizing the reference output.

4.1 Choice of the cost functional

Let the time horizon for the optimal control be T , a natural choice of the cost functional is

$$\mathcal{J} = \int_0^T \|\mathbf{z}\|_2^2 \, dt.$$

To evaluate $\|\mathbf{z}\|_2^2$, we start from the definition of the L^2 norm and consider that the variable \mathbf{z} is given by

$$\mathbf{z}(t) = C_1 \mathbf{x}(t) + D_{12} \mathbf{u}(t).$$

We then obtain immediately that:

$$\begin{aligned} \|\mathbf{z}\|_2^2 &= \mathbf{z}^H \mathbf{z} = (C_1 \mathbf{x} + D_{12} \mathbf{u})^H (C_1 \mathbf{x} + D_{12} \mathbf{u}) \\ &= (\mathbf{x}^H C_1^H + \mathbf{u}^H D_{12}^H)(C_1 \mathbf{x} + D_{12} \mathbf{u}) \\ &= \mathbf{x}^H C_1^H C_1 \mathbf{x} + \mathbf{u}^H D_{12}^H D_{12} \mathbf{u} + \underbrace{\mathbf{u}^H D_{12}^H C_1 \mathbf{x} + \mathbf{x}^H C_1^H D_{12} \mathbf{u}}_{=2\mathbf{x}^H C_1^H D_{12} \mathbf{u}}. \end{aligned} \quad (23)$$

The next step is to simplify this expression. A traditional assumption in control theory (Burl, 1999; Zhou et al., 1996) is to postulate that $C_1^H D_{12} = 0$. For that, a natural choice is to consider that

$$C_1 = \begin{pmatrix} Q_x^{1/2} \\ 0 \end{pmatrix} \quad \text{and} \quad D_{12} = \begin{pmatrix} 0 \\ Q_u^{1/2} \end{pmatrix}$$

where $Q_x^{1/2}$ and $Q_u^{1/2}$ are respectively the square root of two positive-definite matrices Q_x and Q_u , to be justified below. Introducing C_1 and D_{12} in the expression of the norm of the reference output \mathbf{z} , we obtain for the cost functional:

$$\mathcal{J} = \int_0^T \|\mathbf{z}\|_2^2 dt = \int_0^T (\mathbf{x}^H Q_x \mathbf{x} + \mathbf{u}^H Q_u \mathbf{u}) dt.$$

Furthermore, since Q_x and Q_u are positive-definite matrices, the following weighted inner products

$$\|\mathbf{x}\|_{Q_x}^2 \triangleq \mathbf{x}^H Q_x \mathbf{x} \quad \text{and} \quad \|\mathbf{u}\|_{Q_u}^2 \triangleq \mathbf{u}^H Q_u \mathbf{u}$$

can be defined, and thus we can rewrite \mathcal{J} as

$$\mathcal{J} = \int_0^T (\|\mathbf{x}\|_{Q_x}^2 + \|\mathbf{u}\|_{Q_u}^2) dt.$$

A typical choice for the weight matrix Q_u is $Q_u = \ell^2 \text{Id}$ where ℓ is a real positive number ($\ell \neq 0$) and Id is the identity matrix. Finally, the cost functional may be expressed²⁵ as

$$\mathcal{J} = \int_0^T (\|\mathbf{x}\|_{Q_x}^2 + \ell^2 \mathbf{u}^H \mathbf{u}) dt. \quad (24)$$

²⁵In this form, the link with the optimal perturbation problem discussed in section 5 becomes obvious. Indeed, when the penalization term ℓ is equal to zero, the expression under the integral is equivalent to the amplification rate of energy G considered in section 5.

The term involving $\|\boldsymbol{x}\|_{Q_x}^2$ is a measure of the energy of the state variable \boldsymbol{x} integrated over the time horizon of optimization. The term involving $\boldsymbol{u}^H \boldsymbol{u}$ corresponds to the energy of the control signal. The role of the scalar ℓ^2 is to establish a trade off between two conflicting goals: *i*) decreasing the energy of the state variable which may require a large control signal, and *ii*) a small magnitude of the control which may lead to large amplitude of the state variable. The penalization term ℓ^2 must thus be viewed as a measure of the control cost. When the value of ℓ^2 is large, it means that the practical implementation of the control is "expensive". At the opposite, when the value of ℓ^2 is small, the control is considered as "cheap". Consequently, the minimal value of the cost functional \mathcal{J} is expected when ℓ tends to zero. A first choice for the matrix Q_x and the scalar ℓ^2 is given by the Bryson's rule (Bryson Jr. and Ho, 1975).

4.2 Original problem and Lagrange multipliers

The objective of this section is to formulate the LQR problem in the general framework of optimal control theory (see section 3). For that, in addition to the state variables \boldsymbol{x} and control variables \boldsymbol{u} , it is necessary to introduce successively the state equation and the cost functional.

As it was already mentioned at the beginning of section 4, the state equation is written here in the form of an LTI system, *i.e.*

$$\boldsymbol{F}(\boldsymbol{x}, \boldsymbol{u}) = \dot{\boldsymbol{x}} - A\boldsymbol{x} - B_2\boldsymbol{u} = \mathbf{0}.$$

The development of the expression of the cost functional was the subject of section 4.1. On the basis of (24), the objective functional can also be written as

$$\mathcal{J} = \frac{1}{2} [\langle C_1\boldsymbol{x}, C_1\boldsymbol{x} \rangle + \ell^2 \langle \boldsymbol{u}, \boldsymbol{u} \rangle]$$

where the inner product $\langle \cdot, \cdot \rangle$ is defined as

$$\langle \boldsymbol{a}, \boldsymbol{b} \rangle = \int_0^T \boldsymbol{a}^H(t) \boldsymbol{b}(t) dt + \text{complex conjugate.} \quad (25)$$

In the case of the LQR problem, the three inner products $\langle \cdot, \cdot \rangle_s$, $\langle \cdot, \cdot \rangle_c$ and $\langle \cdot, \cdot \rangle_a$ introduced in section 3.2.1 are identical and correspond to (25) since all the direct, adjoint and control variables are only functions of time. This way, the derivation of the optimality condition in section 4.3.3 will be simplified.

The original constrained optimization problem is:

Determine the solution $\mathbf{x}(t)$ and the control parameter $\mathbf{u}(t)$ such that the cost functional \mathcal{J} reaches a minimum subject to $\mathbf{F}(\mathbf{x}, \mathbf{u}) = \mathbf{0}$.

Following the philosophy of the optimal control theory, we then introduce the Lagrange multiplier or adjoint variable $\mathbf{x}^+(t)$ to enforce the constraint $\mathbf{F} = \mathbf{0}$, and define the Lagrangian functional as

$$\mathcal{L}(\mathbf{x}, \mathbf{u}, \mathbf{x}^+) \triangleq \mathcal{J}(\mathbf{x}, \mathbf{u}) - \langle \mathbf{F}(\mathbf{x}, \mathbf{u}), \mathbf{x}^+ \rangle.$$

We then consider the unconstrained optimization problem given by:

Determine the solution $\mathbf{x}(t)$, the control parameter $\mathbf{u}(t)$ and the Lagrange multipliers $\mathbf{x}^+(t)$ such that the Lagrangian functional \mathcal{L} reaches a minimum.

Since each argument of \mathcal{L} is supposed to be independent of the others, the first-order necessary conditions for the minimum of \mathcal{L} yield to an optimality system derived in the general case in section 3.2.2.

4.3 Derivation of the optimality system

For deriving the optimality system, we now have to set successively the first variation of \mathcal{L} with respect to \mathbf{x}^+ , \mathbf{x} and \mathbf{u} equal to zero.

4.3.1 Direct problem

Setting the first variation of \mathcal{L} with respect to the Lagrange multiplier \mathbf{x}^+ equal to zero is equivalent to the condition:

$$\begin{aligned} \langle \nabla_{\mathbf{x}^+} \mathcal{L}, \delta \mathbf{x}^+ \rangle &= \lim_{\epsilon \rightarrow 0} \frac{\mathcal{L}(\mathbf{x}, \mathbf{u}, \mathbf{x}^+ + \epsilon \delta \mathbf{x}^+) - \mathcal{L}(\mathbf{x}, \mathbf{u}, \mathbf{x}^+)}{\epsilon} = 0 \\ &= \lim_{\epsilon \rightarrow 0} \frac{\mathcal{J}(\mathbf{x}, \mathbf{u}) - \mathcal{J}(\mathbf{x}, \mathbf{u})}{\epsilon} \\ &\quad - \lim_{\epsilon \rightarrow 0} \frac{\langle \dot{\mathbf{x}} - A \mathbf{x} - B_2 \mathbf{u}, \mathbf{x}^+ + \epsilon \delta \mathbf{x}^+ \rangle - \langle \dot{\mathbf{x}} - A \mathbf{x} - B_2 \mathbf{u}, \mathbf{x}^+ \rangle}{\epsilon} \\ &= - \langle \dot{\mathbf{x}} - A \mathbf{x} - B_2 \mathbf{u}, \delta \mathbf{x}^+ \rangle = 0. \end{aligned}$$

Since the variation $\delta \mathbf{x}^+$ is arbitrary, we recover the state equation:

$$\dot{\mathbf{x}} = A \mathbf{x} + B_2 \mathbf{u}.$$

4.3.2 Adjoint problem

Setting the first variation of \mathcal{L} with respect to the state \mathbf{x} equal to zero is equivalent to the condition

$$\langle \nabla_{\mathbf{x}} \mathcal{L}, \delta \mathbf{x} \rangle = \lim_{\epsilon \rightarrow 0} \frac{\mathcal{L}(\mathbf{x} + \epsilon \delta \mathbf{x}, \mathbf{u}, \mathbf{x}^+) - \mathcal{L}(\mathbf{x}, \mathbf{u}, \mathbf{x}^+)}{\epsilon} = 0,$$

where the variation $\delta \mathbf{x}$ is arbitrary. Substituting \mathcal{L} with its definition, we have

$$\begin{aligned} \langle \nabla_{\mathbf{x}} \mathcal{L}, \delta \mathbf{x} \rangle &= \lim_{\epsilon \rightarrow 0} \frac{\mathcal{J}(\mathbf{x} + \epsilon \delta \mathbf{x}, \mathbf{u}) - \mathcal{J}(\mathbf{x}, \mathbf{u})}{\epsilon} \\ &\quad - \lim_{\epsilon \rightarrow 0} \frac{\left\langle (\mathbf{x} + \dot{\epsilon} \delta \mathbf{x}) - A(\mathbf{x} + \epsilon \delta \mathbf{x}) - B_2 \mathbf{u}, \mathbf{x}^+ \right\rangle - \left\langle \dot{\mathbf{x}} - A\mathbf{x} - B_2 \mathbf{u}, \mathbf{x}^+ \right\rangle}{\epsilon} \\ &= \underbrace{\frac{\partial \mathcal{J}}{\partial \mathbf{x}} \delta \mathbf{x}}_{T_I} - \underbrace{\left\langle (\dot{\delta \mathbf{x}}), \mathbf{x}^+ \right\rangle}_{T_{II}} + \underbrace{\left\langle A \delta \mathbf{x}, \mathbf{x}^+ \right\rangle}_{T_{III}} = 0. \end{aligned} \quad (26)$$

The objective is now to write the terms T_I to T_{III} , appearing in the right-hand side, as a particular inner product utilizing $\delta \mathbf{x}$. For T_I , we have by definition

$$T_I = \lim_{\epsilon \rightarrow 0} \frac{\mathcal{J}(\mathbf{x} + \epsilon \delta \mathbf{x}, \mathbf{u}) - \mathcal{J}(\mathbf{x}, \mathbf{u})}{\epsilon} = \frac{1}{2} [\langle C_1 \delta \mathbf{x}, C_1 \mathbf{x} \rangle + \langle C_1 \mathbf{x}, C_1 \delta \mathbf{x} \rangle].$$

Using the symmetry of the inner product (25) and introducing the adjoint C_1^+ of C_1 with respect to (25), T_I becomes

$$T_I = \langle C_1 \delta \mathbf{x}, C_1 \mathbf{x} \rangle = \langle \delta \mathbf{x}, C_1^+ C_1 \mathbf{x} \rangle.$$

For T_{II} , we first use the definition of the inner product and then integrate by part in time. We obtain²⁶:

$$\begin{aligned} T_{II} &= \left\langle (\dot{\delta \mathbf{x}}), \mathbf{x}^+ \right\rangle = \int_0^T (\dot{\delta \mathbf{x}})^H \mathbf{x}^+ dt + \text{c.c.} \\ &= [\delta \mathbf{x}^H \mathbf{x}^+]_0^T - \int_0^T \delta \mathbf{x}^H \dot{\mathbf{x}}^+ dt + \text{c.c.} \end{aligned}$$

Since the initial condition $\mathbf{x}(0)$ is perfectly known, we have $\delta \mathbf{x}(0) = \mathbf{0}$. To simplify further T_{II} , we then consider that $\mathbf{x}^+(T) = \mathbf{0}$. Finally, T_{II} is

²⁶The symbol c.c. denotes the complex conjugate.

reduced²⁷ to

$$T_{II} = \langle \delta \mathbf{x}, -\dot{\mathbf{x}}^+ \rangle.$$

Lastly, to transform T_{III} we introduce the adjoint matrix A^+ of A with respect to the inner product (25). We thus obtain:

$$T_{III} = \langle A \delta \mathbf{x}, \mathbf{x}^+ \rangle = \langle \delta \mathbf{x}, A^+ \mathbf{x}^+ \rangle.$$

By gathering the terms T_I to T_{III} , we can then write (26) as

$$\begin{aligned} \langle \nabla_{\mathbf{x}} \mathcal{L}, \delta \mathbf{x} \rangle &= \langle \delta \mathbf{x}, C_1^+ C_1 \mathbf{x} \rangle + \langle \delta \mathbf{x}, \dot{\mathbf{x}}^+ \rangle + \langle \delta \mathbf{x}, A^+ \mathbf{x}^+ \rangle \\ &= \langle \delta \mathbf{x}, C_1^+ C_1 \mathbf{x} + \dot{\mathbf{x}}^+ + A^+ \mathbf{x}^+ \rangle = 0. \end{aligned}$$

Since the variation $\delta \mathbf{x}$ in the state \mathbf{x} is arbitrary, we obtain the adjoint equation

$$-\dot{\mathbf{x}}^+ = A^+ \mathbf{x}^+ + C_1^+ C_1 \mathbf{x}.$$

With this definition, the adjoint state must be marched backward in time over the optimization horizon, starting the time integration with the terminal condition

$$\mathbf{x}^+(T) = \mathbf{0}.$$

4.3.3 Optimality conditions

Setting the first variation of \mathcal{L} with respect to the control \mathbf{u} equal to zero is equivalent to the condition

$$\langle \nabla_{\mathbf{u}} \mathcal{L}, \delta \mathbf{u} \rangle = \lim_{\epsilon \rightarrow 0} \frac{\mathcal{L}(\mathbf{x}, \mathbf{u} + \epsilon \delta \mathbf{u}, \mathbf{x}^+) - \mathcal{L}(\mathbf{x}, \mathbf{u}, \mathbf{x}^+)}{\epsilon} = 0,$$

where the variation $\delta \mathbf{u}$ of the control \mathbf{u} is arbitrary. If we now substitute the Lagrangian \mathcal{L} with its definition, we directly obtain:

$$\begin{aligned} \langle \nabla_{\mathbf{u}} \mathcal{L}, \delta \mathbf{u} \rangle &= \lim_{\epsilon \rightarrow 0} \frac{\mathcal{J}(\mathbf{x}, \mathbf{u} + \epsilon \delta \mathbf{u}) - \mathcal{J}(\mathbf{x}, \mathbf{u})}{\epsilon} \\ &\quad - \lim_{\epsilon \rightarrow 0} \frac{\langle \dot{\mathbf{x}} - A \mathbf{x} - B_2(\mathbf{u} + \epsilon \delta \mathbf{u}), \mathbf{x}^+ \rangle - \langle \dot{\mathbf{x}} - A \mathbf{x} - B_2 \mathbf{u}, \mathbf{x}^+ \rangle}{\epsilon} \\ &= \underbrace{\frac{\partial \mathcal{J}}{\partial \mathbf{u}} \delta \mathbf{u}}_{T_I} + \underbrace{\langle B_2 \delta \mathbf{u}, \mathbf{x}^+ \rangle}_{T_{II}} = 0. \end{aligned} \tag{27}$$

²⁷The minus sign, which appeared in front of $\dot{\mathbf{x}}^+$ following the temporal integration by part, makes that the adjoint equation is now defined backward in time.

Proceeding similarly as we did for the adjoint equation in section 4.3.2, we immediately find:

$$T_I = \lim_{\epsilon \rightarrow 0} \frac{\mathcal{J}(\mathbf{x}, \mathbf{u} + \epsilon \delta \mathbf{u}) - \mathcal{J}(\mathbf{x}, \mathbf{u})}{\epsilon} = \frac{\ell^2}{2} [\langle \mathbf{u}, \delta \mathbf{u} \rangle + \langle \delta \mathbf{u}, \mathbf{u} \rangle] = \ell^2 \langle \delta \mathbf{u}, \mathbf{u} \rangle$$

and

$$T_{II} = \langle B_2 \delta \mathbf{u}, \mathbf{x}^+ \rangle = \langle \delta \mathbf{u}, B_2^+ \mathbf{x}^+ \rangle$$

where B_2^+ is the adjoint matrix of B_2 with respect to the inner product (25).

If we gather the two terms, (27) simplifies to

$$\langle \nabla_{\mathbf{u}} \mathcal{L}, \delta \mathbf{u} \rangle = \ell^2 \langle \delta \mathbf{u}, \mathbf{u} \rangle + \langle \delta \mathbf{u}, B_2^+ \mathbf{x}^+ \rangle = 0 \quad \forall \delta \mathbf{u}.$$

Finally, since the variation $\delta \mathbf{u}$ of \mathbf{u} is arbitrary, we obtain the optimality condition

$$B_2^+ \mathbf{x}^+ = -\ell^2 \mathbf{u},$$

and the gradient of \mathcal{J} with respect to \mathbf{u}

$$\nabla_{\mathbf{u}} \mathcal{L} = B_2^+ \mathbf{x}^+ + \ell^2 \mathbf{u}.$$

Collecting the results of setting the first variations of the Lagrangian functional to zero yields the optimality system given in Fig. 12. The aim of the next section is to solve this optimality system by utilizing a nonlinear matrix differential equation, known as the Riccati equation.

4.4 Riccati equation

In order to solve the optimality system of the LQR problem (see Fig. 12), we must eliminate two variables among the three unknowns \mathbf{x} , \mathbf{u} and \mathbf{x}^+ . Solving for the optimal control \mathbf{u} in the optimality condition yields

$$\mathbf{u}(t) = -\frac{1}{\ell^2} B_2^+ \mathbf{x}^+(t) \tag{28}$$

where the inverse of ℓ is guaranteed to exist since ℓ is a positive real number (see section 4.1). Eliminating \mathbf{u} from the direct and adjoint equations, and combining the resulting equations into a single state equation yields

$$\begin{pmatrix} \dot{\mathbf{x}} \\ \dot{\mathbf{x}}^+ \end{pmatrix} = \begin{pmatrix} A & -\frac{1}{\ell^2} B_2 B_2^+ \\ -C_1^+ C_1 & -A^+ \end{pmatrix} \begin{pmatrix} \mathbf{x} \\ \mathbf{x}^+ \end{pmatrix} \tag{29}$$

with

$$\mathbf{x}(0) = \mathbf{x}_0 \quad \text{and} \quad \mathbf{x}^+(T) = \mathbf{0}. \tag{30}$$

STATE EQUATION:

$$\begin{aligned}\dot{\boldsymbol{x}} &= A\boldsymbol{x} + B_2\boldsymbol{u} \\ \boldsymbol{x}(0) &= \boldsymbol{x}_0 \quad (\text{I.C.})\end{aligned}$$

ADJOINT EQUATION:

$$\begin{aligned}-\dot{\boldsymbol{x}}^+ &= A^+\boldsymbol{x}^+ + C_1^+C_1\boldsymbol{x} \\ \boldsymbol{x}^+(T) &= \mathbf{0} \quad (\text{T.C.})\end{aligned}$$

OPTIMALITY CONDITION:

$$B_2^+\boldsymbol{x}^+ = -\ell^2\boldsymbol{u}$$

COST FUNCTIONAL:

$$\mathcal{J} = \frac{1}{2} \int_0^T (\boldsymbol{x}^H C_1^H C_1 \boldsymbol{x} + \ell^2 \boldsymbol{u}^H \boldsymbol{u}) dt$$

Figure 12. Optimality system for the linear quadratic regulator problem.
I.C.: initial condition, T.C.: terminal condition.

The Hamiltonian system (29) represents a set of necessary and sufficient conditions for the control to minimize the cost functional \mathcal{J} . This results from the fact that \mathcal{J} is quadratic and from the positivity requirements on the weighting matrix $Q_x = C_1^H C_1$.

By integrating in time the Hamiltonian system (29) subject to the initial and final conditions (30), it can be shown (Burl, 1999, p. 186) that the adjoint variable can be found from the state variable using the linear relationship

$$\boldsymbol{x}^+(t) = \Pi(t)\boldsymbol{x}(t) \tag{31}$$

where $\Pi(t)$ is a square matrix of size n_x . The optimal state-feedback control is found from (28):

$$\boldsymbol{u}(t) = -\frac{1}{\ell^2} B_2^+ \Pi(t) \boldsymbol{x}(t) = K(t) \boldsymbol{x}(t)$$

where $K(t)$ is called the feedback gain matrix. To evaluate the gain matrix K , it is thus necessary to determine the matrix Π . A differential equation for $\Pi(t)$ can then be obtained by first taking the time derivative of (31) and then substituting $\dot{\mathbf{x}}$ and \mathbf{x}^+ from (29). After rearrangement, we obtain the Riccati²⁸ equation:

$$-\dot{\Pi} = A^+ \Pi + \Pi A - \frac{1}{\ell^2} \Pi B_2 B_2^+ \Pi + C_1^+ C_1. \quad (32)$$

This equation depends only on the Hamiltonian matrix introduced in (29). The matrix $\Pi(t)$ is found by solving (32) backward in time from the terminal condition given by:

$$\Pi(T) = 0.$$

In applications where the control is designed to operate for $T \rightarrow +\infty$, it is reasonable to ignore the transient time of the optimal gains and use steady-state gains instead. The steady-state solution of the Riccati equation is then generated from (31) by setting the derivative to zero. We then obtain the continuous time algebraic Riccati equation (CARE) given by²⁹:

$$A^+ \Pi + \Pi A - \frac{1}{\ell^2} \Pi B_2 B_2^+ \Pi + C_1^+ C_1 = 0. \quad (33)$$

The solution of (33) can be used to generate the cost associated with the optimal control. Given $\mathbf{x}(0)$, the optimal cost \mathcal{J}_{\min} is given (Burl, 1999) by:

$$\mathcal{J}_{\min} = \mathbf{x}^H(0) \Pi(0) \mathbf{x}(0).$$

To conclude this section, we give in Fig. 13 a summary of the solutions for the LQR problem considered in the general case where the weighting matrix Q_u is not necessarily equal to $\ell^2 Id$.

²⁸The name Riccati is given to the equation by analogy to the Riccati differential equation: the unknown appears linearly and in a quadratic term (but no higher-order terms).

²⁹When the system order is not too high (about 300), (33) can be solved directly with the `care` function under Matlab (Control System Toolbox) or alternatively with the Slicot library. However, numerical algorithms for the solution of large-scale algebraic Riccati equations are still nowadays a topic of research (Benner et al., 2008, for instance). It is then evident that if we want to have a chance to apply sophisticated control algorithms in real systems, strategies of model reduction, such as those discussed in section 2.3, are fundamental.

STATE-SPACE SYSTEM:

$$\begin{aligned}\dot{\boldsymbol{x}}(t) &= A\boldsymbol{x}(t) + B_2\boldsymbol{u}(t), \quad \text{with } \boldsymbol{x}(0) = \boldsymbol{x}_0. \\ \boldsymbol{z}(t) &= C_1\boldsymbol{x}(t) + D_{12}\boldsymbol{u}(t), \quad \text{with } C_1 = \begin{pmatrix} Q_x^{1/2} \\ 0 \end{pmatrix} \text{ and } D_{12} = \begin{pmatrix} 0 \\ Q_u^{1/2} \end{pmatrix}.\end{aligned}$$

COST FUNCTIONAL:

$$\mathcal{J} = \int_0^T (\|\boldsymbol{x}\|_{Q_x}^2 + \|\boldsymbol{u}\|_{Q_u}^2) dt$$

STATE FEEDBACK:

$$\boldsymbol{u}(t) = K\boldsymbol{x}(t)$$

OPTIMAL FEEDBACK GAIN:

$$K(t) = -Q_u^{-1}B_2^+\Pi(t)$$

RICCATI EQUATION:

$$-\dot{\Pi}(t) = A^+ \Pi(t) + \Pi(t) A - \Pi(t) B_2 Q_u^{-1} B_2^+ \Pi(t) + Q_x, \quad \text{with } \Pi(T) = 0.$$

Figure 13. Solutions of the Linear Quadratic Regulator (LQR) problem.

5 Optimal growth perturbation

In stability theory (Schmid and Henningson, 2001), people are interested by the determination of the initial condition which maximizes the energy amplification of the disturbances on a given time horizon $0 \leq t \leq T$. Since stability analysis is concerned with the disturbances around a base flow, we will consider the linearized Navier-Stokes equations. Using compact notations, those equations can be written (Bewley and Liu, 1998, for instance)

as³⁰:

$$\mathbf{F}(\mathbf{q}) = \dot{\mathbf{q}} - A\mathbf{q} = \mathbf{0} \quad \text{with} \quad \mathbf{q}(\mathbf{x}, t=0) = \mathbf{q}_0(\mathbf{x}) \quad (34)$$

where the matrix A corresponds to the linearized Navier-Stokes operator and \mathbf{x} belongs to the spatial domain Ω_x . By definition, the search of optimal disturbances is thus equivalent to an optimization problem. A measure of performance of the optimization can be given by the ratio of disturbance energy at time T to the initial energy *i.e.*

$$\mathcal{J}(\mathbf{q}, \mathbf{q}_0) = \frac{\|\mathbf{q}(\mathbf{x}, T)\|_E^2}{\|\mathbf{q}_0(\mathbf{x})\|_E^2}. \quad (35)$$

The energy inner product $(\cdot, \cdot)_E$ is defined as

$$(\mathbf{q}^I, \mathbf{q}^{II})_E = \int_{\Omega_x} (\mathbf{q}^I)^H M \mathbf{q}^{II} \, d\mathbf{x} + c.c. \quad (36)$$

where M is a matrix that is case dependent, see Guegan et al. (2006) or Antkowiak and Brancher (2007) for two typical examples.

The optimization process corresponding to the maximization of \mathcal{J} should respect the constraints given by the linearized Navier-Stokes equations and the specified boundary and initial conditions. This problem is then amenable to the classical framework of constrained optimization problem as discussed in the next section.

5.1 Variational formulation

The objective of this section is to formulate the problem of optimal energy growth in the framework of optimal control theory (see section 3). As we will see thereafter, this problem has many points in common with the LQR control considered in section 4. Indeed, the constraints (34) are also linear and the cost functional (35) is also quadratic. The only differences are that there are now two constraint equations instead of one and that the control corresponds to the initial condition of the linearized system instead of a boundary condition.

³⁰In this section, we use the traditional notations in stability theory, \mathbf{q} for the perturbation, \mathbf{x} for the spatial variable and t for time.

5.1.1 Original problem, inner products and Lagrangian formulation

To enforce the initial condition, we relate the solution \mathbf{q} at initial time and \mathbf{q}_0 , the optimal growth perturbation we are looking for, through the relation

$$\mathbf{H}(\mathbf{q}, \mathbf{q}_0) = \mathbf{q}(\mathbf{x}, 0) - \mathbf{q}_0(\mathbf{x}) = \mathbf{0}. \quad (37)$$

The original constrained optimization problem is then formulated as:

Determine the solution $\mathbf{q}(\mathbf{x}, t)$ and the control parameter $\mathbf{q}_0(t)$ (optimal disturbance) such that the cost functional \mathcal{J} reaches a maximum subject to $\mathbf{F}(\mathbf{q}) = \mathbf{0}$ and $\mathbf{H}(\mathbf{q}, \mathbf{q}_0) = \mathbf{0}$.

As outlined in section 3.2, the optimal control procedure requires the introduction of Lagrange multipliers or adjoint variables $\tilde{\mathbf{q}}(\mathbf{x}, t)$ and $\tilde{\mathbf{q}}_0(\mathbf{x})$ to enforce respectively the constraints $\mathbf{F} = \mathbf{0}$ and $\mathbf{H} = \mathbf{0}$. Furthermore, to lead properly the developments of the optimality system, we need to introduce two additional inner products:

$$\langle \tilde{\mathbf{q}}^I, \tilde{\mathbf{q}}^{II} \rangle = \int_0^T \int_{\Omega_x} (\tilde{\mathbf{q}}^I)^H \tilde{\mathbf{q}}^{II} \, d\mathbf{x} \, dt + c.c. \quad (38)$$

and

$$(\tilde{\mathbf{q}}^I, \tilde{\mathbf{q}}^{II}) = \int_{\Omega_x} (\tilde{\mathbf{q}}^I)^H \tilde{\mathbf{q}}^{II} \, d\mathbf{x} + c.c. \quad (39)$$

Following the procedure presented in section 3.2.1, a single vector space $\Theta = \mathbf{q} \times \mathbf{q}_0 \times \tilde{\mathbf{q}} \times \tilde{\mathbf{q}}_0$ including all the direct and adjoint variables is introduced. Let $\mathbf{Q}^i = (\mathbf{q}^i, \mathbf{q}_0^i, \tilde{\mathbf{q}}^i, \tilde{\mathbf{q}}_0^i)$ with $i = I, II$ be two arbitrary elements of Θ , an inner product including all the three inner products (36), (38) and (39) is defined as

$$\{\mathbf{Q}^I, \mathbf{Q}^{II}\} = \langle \mathbf{q}^I, \mathbf{q}^{II} \rangle + (\mathbf{q}_0^I, \mathbf{q}_0^{II})_E + \langle \tilde{\mathbf{q}}^I, \tilde{\mathbf{q}}^{II} \rangle + (\tilde{\mathbf{q}}_0^I, \tilde{\mathbf{q}}_0^{II}). \quad (40)$$

The constrained optimization problem is circumvented by introducing the Lagrangian functional

$$\mathcal{L}(\mathbf{q}, \mathbf{q}_0, \tilde{\mathbf{q}}, \tilde{\mathbf{q}}_0) = \mathcal{J}(\mathbf{q}, \mathbf{q}_0) - \langle \mathbf{F}(\mathbf{q}), \tilde{\mathbf{q}} \rangle - (\mathbf{H}(\mathbf{q}, \mathbf{q}_0), \tilde{\mathbf{q}}_0),$$

where the constraints have already been included by means of appropriate Lagrange multipliers.

5.1.2 Gradients of the Lagrangian

As outlined in section 3.2.2, determining the stationary points of the Lagrangian \mathcal{L} requires the computation of the gradients of \mathcal{L} with respect to all the variables. By convention, the gradients of \mathcal{L} with respect to \mathbf{q} , \mathbf{q}_0 , $\tilde{\mathbf{q}}$ and $\tilde{\mathbf{q}}_0$ are denoted in the following respectively by $\nabla_{\mathbf{q}}\mathcal{L}$, $\nabla_{\mathbf{q}_0}\mathcal{L}$, $\nabla_{\tilde{\mathbf{q}}}\mathcal{L}$ and $\nabla_{\tilde{\mathbf{q}}_0}\mathcal{L}$. These gradients are determined as projections of $\nabla\mathcal{L}(\mathbf{Q})$, gradient of the Lagrangian at point \mathbf{Q} , onto the different subspaces corresponding to each of the variables \mathbf{q} , \mathbf{q}_0 , $\tilde{\mathbf{q}}$ and $\tilde{\mathbf{q}}_0$. Assuming that \mathcal{L} is Fréchet-differentiable, $\nabla\mathcal{L}(\mathbf{Q})$ is such that for any variation $\delta\mathbf{Q}$ we have:

$$\{\nabla\mathcal{L}(\mathbf{Q}), \delta\mathbf{Q}\} = \lim_{\epsilon \rightarrow 0} \frac{\mathcal{L}(\mathbf{Q} + \epsilon\delta\mathbf{Q}) - \mathcal{L}(\mathbf{Q})}{\epsilon}. \quad (41)$$

5.1.2.1 Determination of $\nabla_{\tilde{\mathbf{q}}}\mathcal{L}$ and $\nabla_{\tilde{\mathbf{q}}_0}\mathcal{L}$: direct equations Considering respectively $\delta\mathbf{Q} = (0, 0, \delta\tilde{\mathbf{q}}, 0)$ and $\delta\mathbf{Q} = (0, 0, 0, \delta\tilde{\mathbf{q}}_0)$ in (41), we obtain immediately (see section 4.3.1 for similar developments):

$$\begin{aligned} \langle \nabla_{\tilde{\mathbf{q}}}\mathcal{L}, \delta\tilde{\mathbf{q}} \rangle &= -\langle \mathbf{F}(\mathbf{q}), \delta\tilde{\mathbf{q}} \rangle, \\ \langle \nabla_{\tilde{\mathbf{q}}_0}\mathcal{L}, \delta\tilde{\mathbf{q}}_0 \rangle &= -\langle \mathbf{H}(\mathbf{q}, \mathbf{q}_0), \delta\tilde{\mathbf{q}}_0 \rangle. \end{aligned}$$

At the stationary points of \mathcal{L} , these gradients are by definition equal to zero. Since the variations $\delta\tilde{\mathbf{q}}$ and $\delta\tilde{\mathbf{q}}_0$ are arbitrary, the constraints $\mathbf{F}(\mathbf{q}) = \mathbf{0}$ and $\mathbf{H}(\mathbf{q}, \mathbf{q}_0) = \mathbf{0}$ are recovered.

5.1.2.2 Determination of $\nabla_{\mathbf{q}}\mathcal{L}$: adjoint equations For evaluating $\nabla_{\mathbf{q}}\mathcal{L}$, $\delta\mathbf{Q} = (\delta\mathbf{q}, 0, 0, 0)$ is introduced in (41). After some developments which are exactly similar to those presented in section (4.3.2) for the LQR control, we obtain

$$\begin{aligned} \langle \nabla_{\mathbf{q}}\mathcal{L}, \delta\mathbf{q} \rangle &= \frac{2}{\|\mathbf{q}_0\|_E^2} (\delta\mathbf{q}|_T, \mathbf{q}|_T)_E + \left\langle \delta\mathbf{q}, \frac{d\tilde{\mathbf{q}}}{dt} + A^+ \tilde{\mathbf{q}} \right\rangle - (\delta\mathbf{q}|_T, \tilde{\mathbf{q}}|_T) \\ &\quad - (\delta\mathbf{q}|_0, \tilde{\mathbf{q}}_0) + (\delta\mathbf{q}|_0, \tilde{\mathbf{q}}|_0), \end{aligned} \quad (42)$$

where $\delta\mathbf{q}|_t$ stands for $\delta\mathbf{q}(\mathbf{x}, t)$ with $t = 0$ or T . The expression (42) has to hold true for any $\delta\mathbf{q}$ which entails:

1. Adjoint equations

$$\frac{d\tilde{\mathbf{q}}}{dt} = -A^+ \tilde{\mathbf{q}}, \quad (43)$$

2. Terminal adjoint condition

$$\tilde{\mathbf{q}}|_T = \frac{2}{\|\mathbf{q}_0\|_E^2} \mathbf{q}|_T, \quad (44)$$

3. Compatibility condition

$$\tilde{\mathbf{q}}_0 = \tilde{\mathbf{q}}|_0. \quad (45)$$

5.1.2.3 Determination of $\nabla_{\mathbf{q}_0} \mathcal{L}$: optimality conditions Finally, to determine $\nabla_{\mathbf{q}_0} \mathcal{L}$, we consider $\delta \mathbf{Q} = (0, \delta \mathbf{q}_0, 0, 0)$ in (41). While proceeding similarly that in section 4.3.3, we obtain:

$$(\nabla_{\mathbf{q}_0} \mathcal{L}, \delta \mathbf{q}_0)_E = -2 \frac{\|\mathbf{q}|_T\|_E^2}{(\|\mathbf{q}_0\|_E^2)^2} (\mathbf{q}_0, \delta \mathbf{q}_0)_E + (\delta \mathbf{q}_0, \tilde{\mathbf{q}}_0). \quad (46)$$

According to definitions (36) and (39) of the inner products, the following expression holds:

$$(\delta \mathbf{q}_0, \tilde{\mathbf{q}}_0) = (M^{-1} \tilde{\mathbf{q}}_0, \delta \mathbf{q}_0)_E$$

where M^{-1} is the inverse of the matrix M . Consequently, (46) is equivalent to

$$(\nabla_{\mathbf{q}_0} \mathcal{L}, \delta \mathbf{q}_0)_E = -2 \frac{\|\mathbf{q}|_T\|_E^2}{(\|\mathbf{q}_0\|_E^2)^2} (\mathbf{q}_0, \delta \mathbf{q}_0)_E + (M^{-1} \tilde{\mathbf{q}}_0, \delta \mathbf{q}_0)_E. \quad (47)$$

Since $\delta \mathbf{q}_0$ is arbitrary, the gradient of the Lagrangian with respect to the initial perturbation is

$$\nabla_{\mathbf{q}_0} \mathcal{L} = -2 \frac{\|\mathbf{q}|_T\|_E^2}{(\|\mathbf{q}_0\|_E^2)^2} \mathbf{q}_0 + M^{-1} \tilde{\mathbf{q}}_0,$$

and the optimality condition corresponds to

$$\mathbf{q}_0 = \frac{(\|\mathbf{q}_0\|_E^2)^2}{2 \|\mathbf{q}|_T\|_E^2} M^{-1} \tilde{\mathbf{q}}_0 \quad (48)$$

where $\tilde{\mathbf{q}}_0 = \tilde{\mathbf{q}}(\mathbf{x}, t = 0)$ due to the compatibility condition (45). If we suppose that M is equal to the identity matrix then the optimality system given in Schmid (2007) on page 145 is recovered. Furthermore, in the constrained subspace where $\mathbf{F}(\mathbf{q}) = \mathbf{0}$ and $\mathbf{H}(\mathbf{q}, \mathbf{q}_0) = \mathbf{0}$, the gradient of the Lagrangian simply reduces to

$$\nabla_{\mathbf{q}_0} \mathcal{L}(\mathbf{Q}) = \nabla_{\mathbf{q}_0} \mathcal{J}(\mathbf{Q}). \quad (49)$$

The optimality system corresponding to the search of optimal growth perturbation at a fixed time T is given in Fig. 14. This optimality system can be solved iteratively using the procedure described in section 3.2.3 where $\nabla_{\mathbf{q}_0} \mathcal{J}$ given by (49) is used for determining the descent direction (see section 7). By varying the time T over which the optimization is performed, the maximum growth curve $G(t)$ (see Fig. 15 for an example) is

STATE EQUATION:

$$\begin{aligned}\dot{\mathbf{q}} &= A \mathbf{q} \\ \mathbf{q}(\mathbf{x}, t = 0) &= \mathbf{q}_0(\mathbf{x})\end{aligned}\quad (\text{I.C.}) \text{ and control parameter}$$

ADJOINT EQUATION:

$$\begin{aligned}\frac{d\tilde{\mathbf{q}}}{dt} &= -A^+ \tilde{\mathbf{q}} \\ \tilde{\mathbf{q}}|_T &= \frac{2}{\|\mathbf{q}_0\|_E^2} \mathbf{q}|_T\end{aligned}\quad (\text{T.C.})$$

OPTIMALITY CONDITION:

$$\mathbf{q}_0 = \frac{(\|\mathbf{q}_0\|_E^2)^2}{2\|\mathbf{q}|_T\|_E^2} M^{-1} \tilde{\mathbf{q}}_0$$

COMPATIBILITY CONDITION:

$$\tilde{\mathbf{q}}_0 = \tilde{\mathbf{q}}|_0$$

COST FUNCTIONAL:

$$\mathcal{J}(\mathbf{q}, \mathbf{q}_0) = \frac{\|\mathbf{q}(\mathbf{x}, T)\|_E^2}{\|\mathbf{q}_0(\mathbf{x})\|_E^2}$$

Figure 14. Optimality system for the optimal growth perturbation problem. I.C.: initial condition, T.C.: terminal condition.

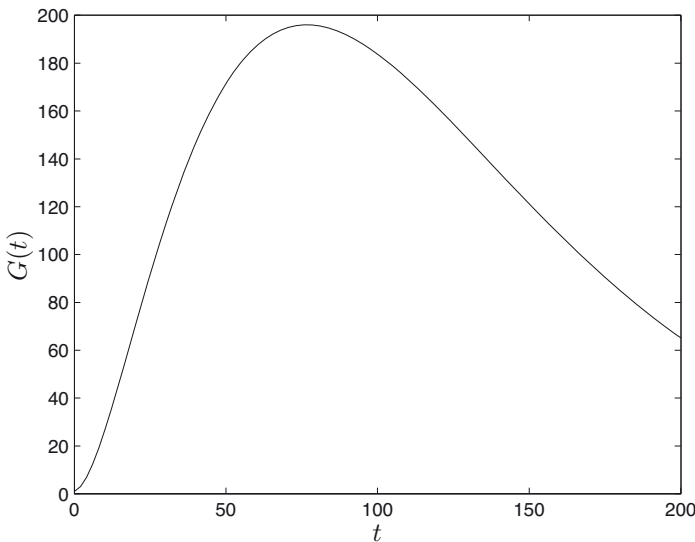


Figure 15. Maximum growth curve $G(t)$ for Poiseuille flow at $Re = 1000$. The streamwise and spanwise wavenumbers are $\alpha = 0$ and $\beta = 2$ (see Cordier, 2009, for the details). The number of Chebyshev points for the discretization is 200.

obtained. A second step consists in seeking the time t_{\max} for which the curve $G(t)$ reached its maximum. The corresponding initial condition \mathbf{q}_0 is called global optimal perturbation, or, in short, optimal perturbation. An example of optimal perturbation for the Poiseuille flow is given in Fig. 16 and the corresponding solution $\mathbf{q}(\mathbf{x}, t_{\max})$ displayed in Fig. 17.

Another way of determining the optimal disturbances is based on the use of matrix exponential directly related to the linear system (34). This is the method which is the most used in the literature because, as it will be described in the following section, it is not necessary to use iterative methods to determine the curve of temporal amplification energy.

5.2 Formulation based on matrix exponential

In this section, the same notations as in Schmid and Henningson (2001) are used what means that the disturbance \mathbf{q} is now discretized in space. We

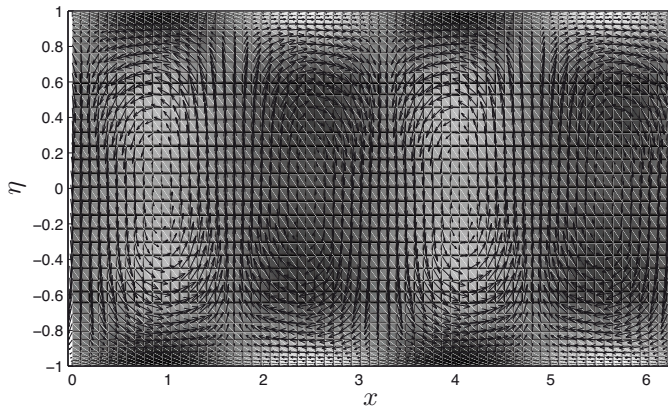


Figure 16. Optimal initial condition for Poiseuille flow at $Re = 1000$. The streamwise and spanwise wavenumbers are $\alpha = 0$ and $\beta = 2$ (see Cordier, 2009, for the details). The number of Chebyshev points for the discretization is 200. x and η are respectively the streamwise and wall-normal non-dimensional coordinates.

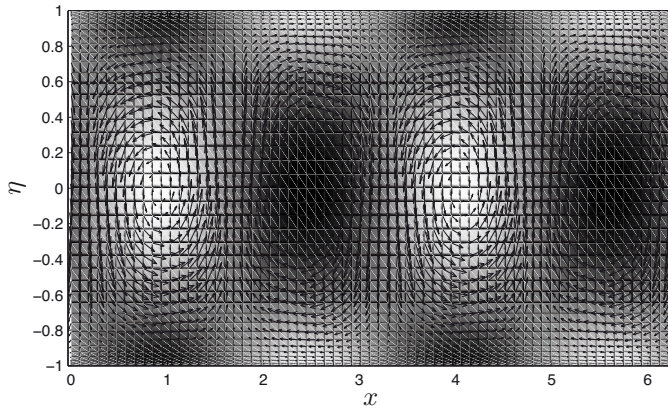


Figure 17. Optimal perturbation for Poiseuille flow at $t = t_{\max}$ and $Re = 1000$. The streamwise and spanwise wavenumbers are $\alpha = 0$ and $\beta = 2$ (see Cordier, 2009, for the details). The number of Chebyshev points for the discretization is 200. x and η are respectively the streamwise and wall-normal non-dimensional coordinates.

will thus have $\mathbf{q} \triangleq \mathbf{q}(t)$ and no more $\mathbf{q} = \mathbf{q}(\mathbf{x}, t)$ as in section 5.1. The objective is to determine the maximum possible amplification G of initial energy density *i.e.*

$$G(t) = \max_{\mathbf{q}_0 \neq \mathbf{0}} \frac{\|\mathbf{q}(t)\|_E^2}{\|\mathbf{q}_0\|_E^2} \quad \text{with} \quad \mathbf{q}_0 = \mathbf{q}(0) \quad (50)$$

where the energy inner product is now defined as $\|\mathbf{q}(t)\|_E^2 = \mathbf{q}(t)^H Q_q \mathbf{q}(t)$ with Q_q an appropriate weighting matrix. For practical reasons, it is more desirable to work with the standard- L_2 norm than with weighting matrices. Using the Cholesky decomposition, we then decompose the weight matrix Q_q as $Q_q = F^H F$. This way, the energy inner product can be written also as

$$\|\mathbf{q}(t)\|_E^2 = \mathbf{q}(t)^H Q_q \mathbf{q}(t) = \mathbf{q}(t)^H F^H F \mathbf{q}(t) = \|F \mathbf{q}(t)\|_2^2. \quad (51)$$

Furthermore, for a linear state-space model defined by

$$\dot{\mathbf{q}} = A \mathbf{q} \quad \text{with} \quad \mathbf{q}(0) = \mathbf{q}_0, \quad (52)$$

the solution at all positive times is given by (see section 2.1.2)

$$\mathbf{q}(t) = e^{At} \mathbf{q}_0. \quad (53)$$

Consequently, the maximum energy amplification G may be written also:

$$G(t) = \max_{\mathbf{q}_0 \neq \mathbf{0}} \frac{\|\mathbf{q}(t)\|_E^2}{\|\mathbf{q}_0\|_E^2} = \max_{\mathbf{q}_0 \neq \mathbf{0}} \frac{\|F \mathbf{q}(t)\|_2^2}{\|F \mathbf{q}_0\|_2^2} = \max_{\mathbf{q}_0 \neq \mathbf{0}} \frac{\|F e^{At} \mathbf{q}_0\|_2^2}{\|F \mathbf{q}_0\|_2^2}.$$

Introducing the change of variable $\mathbf{s}_0 = F \mathbf{q}_0$, the previous expression becomes:

$$\begin{aligned} G(t) &= \max_{\mathbf{s}_0 \neq \mathbf{0}} \frac{\|F e^{At} F^{-1} \mathbf{s}_0\|_2^2}{\|\mathbf{s}_0\|_2^2} = \max_{\|\mathbf{s}_0\|_2=1} \|F e^{At} F^{-1} \mathbf{s}_0\|_2^2 \triangleq \|F e^{At} F^{-1}\|_2^2 \\ &= \sigma_1^2 \end{aligned}$$

where σ_1 is the maximum singular value of $F e^{At} F^{-1}$. Computationally, it is expensive in general to evaluate e^{At} since, depending on the numerical discretization, A may be a dense matrix. A better solution is to change the formulation of the original problem by writing it in the basis of the eigenvectors of A . Using the eigenvalue decomposition of A , *i.e.* $A = P D P^{-1}$, it is obvious that the linear state-space system (52) simplifies in

$$\dot{\mathbf{K}} = D \mathbf{K} \quad \text{with} \quad \mathbf{K}(0) = \mathbf{K}_0. \quad (54)$$

Here, $\mathbf{K}(t)$ corresponds to the coefficients of the development of \mathbf{q} into the eigenvectors of A : $\mathbf{q}(t) = P\mathbf{K}(t)$. The solution of (54) writes immediately

$$\mathbf{K}(t) = e^{Dt} \mathbf{K}_0, \quad (55)$$

where D is the diagonal matrix of eigenvalues of A .

With this new formulation, the energy inner product is:

$$\begin{aligned} \|\mathbf{q}(t)\|_E^2 &= \mathbf{q}(t)^H Q_q \mathbf{q}(t) = \mathbf{K}(t)^H P^H Q_q P \mathbf{K}(t) = \mathbf{K}(t)^H F^H F \mathbf{K}(t) \\ &= \|F \mathbf{K}(t)\|_2^2 \end{aligned}$$

where this time the matrix F corresponds to the Cholesky decomposition of $P^H Q_q P$.

Following exactly the same approach as previously in this section, we obtain

$$G(t) = \|F e^{Dt} F^{-1}\|_2^2 = \sigma_1^2. \quad (56)$$

This expression corresponds to a convenient and efficient way of computing the maximum transient growth. Indeed, (56) involves the L_2 -norm (very convenient) and evaluates the matrix exponential of a diagonal matrix (very efficient).

6 Linearized Burgers equation

In section 4, we considered the LQR control where the state equation was written as a Linear Time Invariant state-space model, the cost objective was quadratic and the control was distributed. Section 5 was dedicated to the study of optimal growth disturbances where, compared to the case of LQR, the control corresponded to the initial condition of the linear state equation and where the objective was to maximize the energy amplitude of the perturbations. In this section, we now consider the case of the boundary control where the state equation is a Partial Differential Equation. This configuration is characteristic from the applications that can be met in fluid mechanics (Bewley et al., 2001; El Shrif, 2008), heat transfers and thermal systems (Müller, 2006). To simplify the presentation, we consider a one-dimensional configuration and take for state equation the linearized Burgers equation. The optimality system for the nonlinear Burgers equation with boundary and distributed control is given in section 7.

We will follow as closely as possible the presentation made in section 5 for the optimal growth perturbations.

6.1 Problem formulation and Lagrangian-based approach

Define $\Xi = \{(x, t) | (x, t) \in [0, L] \times [t_0, t_f]\}$ as the physical domain of the process. To simplify the future developments, we consider that $\Xi = \Omega_x \times \Omega_t$ where $\Omega_x = [0, L]$ and $\Omega_t = [t_0, t_f]$ and introduce three inner products

$$\langle u, v \rangle_{\Xi} = \int_{\Xi} u(x, t)v(x, t) \, dx \, dt, \quad (57)$$

$$\langle u, v \rangle_{\Omega_x} = \int_{\Omega_x} u(x, t)v(x, t) \, dx, \quad (58)$$

$$\langle u, v \rangle_{\Omega_t} = \int_{\Omega_t} u(x, t)v(x, t) \, dt, \quad (59)$$

where $u(x, t)$ and $v(x, t)$ are two sufficiently regular real-valued functions defined on Ξ .

The linearized Burgers equation is given by

$$F_U(u) = u_t + U(x)u_x - u_{xx} = 0 \quad \text{with} \quad u(x, t_0) = u_0(x), \quad (60)$$

where $u_t = \frac{\partial u}{\partial t}$, $u_x = \frac{\partial u}{\partial x}$ and $u_{xx} = \frac{\partial^2 u}{\partial x^2}$. In (60), $U(x)$ is a real-valued function defined on Ω_x . Furthermore, we consider that at the upper boundary of Ω_x , we have $u(L, t) = 0$.

In this section, our objective is to determine the function $u_w(t) = u(x = 0, t)$ (*i.e.* the temporal disturbance at the lower boundary of the domain) such that the classical L_2 norm of u is minimized at the final time of integration ($t = t_f$). In other words, we seek to minimize the cost functional defined by

$$\mathcal{J}(u, u_w) = \left(\int_{\Omega_x} u^2 \, dx \right)_{t=t_f} = \langle u, u \rangle_{\Omega_x} |_{t=t_f}.$$

In addition, the optimization problem must be mathematically well-posed (see the discussion in section 3.1.2). It is then necessary to add a regularization term to the cost functional \mathcal{J} . Finally, the cost functional

$$\begin{aligned} \mathcal{J}(u, u_w) &= \left(\int_0^L u^2 \, dx \right)_{t=t_f} + \ell \int_{t_0}^{t_f} u_w^2 \, dt, \\ &= [[u, u]] + \ell \langle u_w, u_w \rangle_{\Omega_t}, \end{aligned} \quad (61)$$

is used where the penalty parameter $\ell > 0$ allows us to set the "price" of the control effort. To simplify further the expression of \mathcal{J} , an additional inner product was introduced in (61). This scalar product is defined as

$$[[u, v]] = \left(\int_{\Omega_x} u(x, t)v(x, t) \, dx \right)_{t=t_f} = \langle u, v \rangle_{\Omega_x}|_{t=t_f}. \quad (62)$$

Contrary to the case of the optimal disturbances (see section 5.1), the control intervenes as a boundary condition and no more as an initial condition. However, the same formalism remains applicable and the boundary condition can be enforced through the relation:

$$H(u, u_w) = u(0, t) - u_w(t) = 0.$$

The original constrained optimization problem is then stated:

Determine the solution $u(x, t)$ and the control parameter $u_w(t)$ (upper boundary condition) such that the cost functional \mathcal{J} reaches a minimum subject to $F_U(u) = 0$ and $H(u, u_w) = 0$.

The procedure described in section 3.2 is then followed for enforcing the constraints³¹. For that, we introduce a single vector space $\Theta = u \times u_w \times u^+ \times \lambda^+$ where $u^+(x, t)$ and $\lambda^+(t)$ are the Lagrange multipliers corresponding respectively to $F_U = 0$ and $H = 0$. Let $\mathbf{Q}^i = (u^i, u_w^i, (u^+)^i, (\lambda^+)^i)$ with $i = I, II$ be two arbitrary elements of Θ , an inner product including the inner products (57) and (59) is defined as

$$\begin{aligned} \{\mathbf{Q}^I, \mathbf{Q}^{II}\} = & \langle u^I, u^{II} \rangle_{\Xi} + \langle u_w^I, u_w^{II} \rangle_{\Omega_t} \\ & + \langle (u^+)^I, (u^+)^{II} \rangle_{\Xi} + \langle (\lambda^+)^I, (\lambda^+)^{II} \rangle_{\Omega_t}. \end{aligned} \quad (63)$$

The constraints are then enforced by introducing the Lagrangian functional

$$\mathcal{L}(u, u_w, u^+, \lambda^+) = \mathcal{J}(u, u_w) - \langle F_U(u), u^+ \rangle_{\Xi} - \langle H(u, u_w), \lambda^+ \rangle_{\Omega_t}. \quad (64)$$

The new unconstrained optimization problem can then be stated as:

³¹The constraints of the problem which are not imposed by Lagrange multipliers (initial condition and boundary condition at the upper boundary of the spatial domain) will be enforced a posteriori on the solutions.

Determine the solution $u(x, t)$, the control parameter $u_w(t)$ and the Lagrange multipliers $u^+(x, t)$ and $\lambda^+(t)$ such that the Lagrangian functional \mathcal{L} reaches a minimum.

6.2 Optimality system

As it was discussed in details in section 3.2.2, a necessary condition for obtaining a minimum or maximum of the Lagrangian is to set the gradients of \mathcal{L} with respect to u , u_w , u^+ and λ^+ equal to zero *i.e.*

$$\nabla_u \mathcal{L} = \nabla_{u_w} \mathcal{L} = \nabla_{u^+} \mathcal{L} = \nabla_{\lambda^+} \mathcal{L} = 0.$$

The derivation of the optimality system thus passes by the computation of the gradients of \mathcal{L} with respect to all the variables.

6.2.1 Direct equations

Differentiating (64) with respect to the adjoint variables u^+ and λ^+ yields immediately to

$$\begin{aligned} \langle \nabla_{u^+} \mathcal{L}, \delta u^+ \rangle_{\Xi} &= \lim_{\epsilon \rightarrow 0} \frac{\mathcal{L}(u, u_w, u^+ + \epsilon \delta u^+, \lambda^+) - \mathcal{L}(u, u_w, u^+, \lambda^+)}{\epsilon} \\ &= -\langle F_U(u), \delta u^+ \rangle_{\Xi} = 0, \end{aligned} \quad (65)$$

and

$$\begin{aligned} \langle \nabla_{\lambda^+} \mathcal{L}, \delta \lambda^+ \rangle_{\Omega_t} &= \lim_{\epsilon \rightarrow 0} \frac{\mathcal{L}(u, u_w, u^+, \lambda^+ + \epsilon \delta \lambda^+) - \mathcal{L}(u, u_w, u^+, \lambda^+)}{\epsilon} \\ &= -\langle H(u, u_w), \delta \lambda^+ \rangle_{\Omega_t} = 0. \end{aligned} \quad (66)$$

Since the variations δu^+ and $\delta \lambda^+$ are arbitrary, F_U and H necessarily have to vanish, and we thus recover the constraints.

6.2.2 Adjoint equations

For differentiating (64) with respect to the direct variable u , we consider a variation $\delta Q = (\delta u, 0, 0, 0)$. It yields

$$\langle \nabla_u \mathcal{L}, \delta u \rangle_{\Xi} = \lim_{\epsilon \rightarrow 0} \frac{\mathcal{L}(u + \epsilon \delta u, u_w, u^+, \lambda^+) - \mathcal{L}(u, u_w, u^+, \lambda^+)}{\epsilon} = 0. \quad (67)$$

Substituting \mathcal{L} with its definition, we have immediately due to the linearity of F_U and H :

$$\begin{aligned} \langle \nabla_u \mathcal{L}, \delta u \rangle_{\Xi} &= \lim_{\epsilon \rightarrow 0} \frac{\mathcal{J}(u + \epsilon \delta u, u_w) - \mathcal{J}(u, u_w)}{\epsilon} \\ &\quad - \lim_{\epsilon \rightarrow 0} \frac{\langle F_U(u + \epsilon \delta u), u^+ \rangle_{\Xi} - \langle F_U(u), u^+ \rangle_{\Xi}}{\epsilon} \\ &\quad - \lim_{\epsilon \rightarrow 0} \frac{\langle H(u + \epsilon \delta u, u_w), \lambda^+ \rangle_{\Omega_t} - \langle H(u, u_w), \lambda^+ \rangle_{\Omega_t}}{\epsilon} \\ &= 2[[u, \delta u]] - \langle F_U(\delta u), u^+ \rangle_{\Xi} - \langle \delta u(0, t), \lambda^+ \rangle_{\Omega_t}. \end{aligned} \quad (68)$$

The objective is now to write the term $\langle F_U(\delta u), u^+ \rangle_{\Xi}$ as a particular inner product utilizing δu . By definitions of the scalar product (57) and of F_U , we have:

$$\langle F_U(\delta u), u^+ \rangle_{\Xi} = \underbrace{\langle (\delta u)_t, u^+ \rangle_{\Xi}}_{T_I} + \underbrace{\langle U(x)(\delta u)_x, u^+ \rangle_{\Xi}}_{T_{II}} - \underbrace{\langle (\delta u)_{xx}, u^+ \rangle_{\Xi}}_{T_{III}}.$$

The simplification of the terms T_I to T_{III} is then equivalent to an exercise of integration by parts. We obtain immediately:

$$T_I = \int_{\Xi} u^+ (\delta u)_t \, dx \, dt = \left[\int_{\Omega_x} u^+ \delta u \, dx \right]_{t=t_0}^{t=t_f} - \langle \delta u, u_t^+ \rangle_{\Xi},$$

$$T_{II} = \int_{\Xi} u^+ U(x) (\delta u)_x \, dx \, dt = \left[\int_{\Omega_t} U u^+ \delta u \, dt \right]_{x=0}^{x=L} - \langle \delta u, (U u^+)_x \rangle_{\Xi},$$

and

$$T_{III} = \int_{\Xi} u^+ (\delta u)_{xx} \, dx \, dt = \left[\int_{\Omega_t} u^+ (\delta u)_x \, dt \right]_{x=0}^{x=L} - \int_{\Xi} u_x^+ (\delta u)_x \, dx \, dt$$

where

$$\int_{\Xi} u_x^+ (\delta u)_x \, dx \, dt = \left[\int_{\Omega_t} \delta u u_x^+ \, dt \right]_{x=0}^{x=L} - \langle \delta u, u_{xx}^+ \rangle_{\Xi}.$$

By replacing the terms T_I to T_{III} by their expressions, we can write (68) as

$$\begin{aligned} 2 \left(\int_{\Omega_x} u \delta u \, dx \right)_{t=t_f} - \int_{\Omega_t} \lambda^+ \delta u(0, t) \, dt + \langle u_t^+ + (U u^+)_x + u_{xx}^+, \delta u \rangle_{\Xi} \\ - \left[\int_{\Omega_t} ((U u^+ + u_x^+) \delta u - u^+ (\delta u)_x) \, dt \right]_{x=0}^{x=L} - \left[\int_{\Omega_x} u^+ \delta u \, dx \right]_{t=t_0}^{t=t_f} = 0. \end{aligned} \quad (69)$$

This last expression has to hold true for any variation δu . That means that (69) must be in particular true for variations presumed unspecified on Ξ , except at its boundaries $\partial\Xi$ where we consider

$$\delta u(x, t) = 0 \quad \forall (x, t) \in \partial\Xi.$$

Introducing this particular perturbation in (69) yields to

$$\langle u_t^+ + (Uu^+)_x + u_{xx}^+, \delta u \rangle_\Xi = 0,$$

what leads to the adjoint equation of the linearized Burgers equation

$$F_U^+(u^+) = u_t^+ + (Uu^+)_x + u_{xx}^+ = 0 \quad \forall (x, t) \in \Xi. \quad (70)$$

Contrary to the direct equation (60), the adjoint equation is now parabolic in decreasing time. As a consequence, it is then necessary to provide (70) with a terminal condition. In addition, since the cost functional \mathcal{J} that we considered is defined locally in time (minimization of the norm of u at final time t_f), the adjoint equation is independent of the optimization problem. This was not the case for the LQR problem (see section 4.3.2) where a source term coming directly from \mathcal{J} appears in the adjoint equation.

According to the adjoint equation, (69) is now equivalent to

$$\begin{aligned} & 2 \left(\int_{\Omega_x} u \delta u \, dx \right)_{t=t_f} - \int_{\Omega_t} \lambda^+ \delta u(0, t) \, dt \\ & - \left[\int_{\Omega_t} ((Uu^+ + u_x^+) \delta u - u^+ (\delta u)_x) \, dt \right]_{x=0}^{x=L} - \left[\int_{\Omega_x} u^+ \delta u \, dx \right]_{t=t_0}^{t=t_f} = 0. \end{aligned} \quad (71)$$

In terms of perturbations, the initial and upper boundary conditions of the original problem result in

$$\delta u(x, t_0) = 0 \quad \text{and} \quad \delta u(L, t) = 0.$$

Using these conditions, (71) may then be rewritten as

$$\begin{aligned} & \left(\int_{\Omega_x} (2u - u^+) \delta u \, dx \right)_{t=t_f} + \left(\int_{\Omega_t} u^+ (\delta u)_x \, dt \right)_{x=L} \\ & + \left[\int_{\Omega_t} ((Uu^+ + u_x^+ - \lambda^+) \delta u - u^+ (\delta u)_x) \, dt \right]_{x=0} = 0. \end{aligned} \quad (72)$$

Since the perturbation δu may be chosen arbitrarily, we can consider:

- Functions u which are unspecified at $t = t_f$ but with constant values along $x = 0$ and $x = L$. In terms of perturbations, this choice corresponds to

$$\delta u(0, t) = 0 \quad \text{and} \quad \delta u(L, t) = 0.$$

Inserting these particular perturbations in (72) lead to the terminal condition of the adjoint equation:

$$u^+(x, t_f) = 2u(x, t_f). \quad (73)$$

- Functions u which are constant everywhere on Ξ except at $x = L$, i.e.

$$\delta u(0, t) = 0 \quad \text{and} \quad (\delta u)_x(0, t) = 0.$$

This choice yields to a first boundary condition for the adjoint equation:

$$u^+(L, t) = 0. \quad (74)$$

- Finally, we consider functions u which are constant everywhere on Ξ except at $x = 0$, i.e.

$$(\delta u)_x(L, t) = 0.$$

This type of perturbation leads to a second boundary condition for the adjoint equation:

$$u^+(0, t) = 0 \quad (75)$$

and to the compatibility condition

$$u_x^+(0, t) - \lambda^+(t) = 0. \quad (76)$$

6.2.3 Optimality conditions

For the differentiation of (64) with respect to the control variable u_w , a variation $\delta Q = (0, \delta u_w, 0, 0)$ is considered. By definition of the Fréchet and Gâteau differentials, we obtain:

$$\langle \nabla_{u_w} \mathcal{L}, \delta u_w \rangle_{\Omega_t} = \lim_{\epsilon \rightarrow 0} \frac{\mathcal{L}(u, u_w + \epsilon \delta u_w, u^+, \lambda^+) - \mathcal{L}(u, u_w, u^+, \lambda^+)}{\epsilon} = 0. \quad (77)$$

If we then replace the Lagrangian functional \mathcal{L} by its definition, we obtain immediately by linearizing the expression of \mathcal{J} and by linearity of H that:

$$\begin{aligned} \langle \nabla_{u_w} \mathcal{L}, \delta u_w \rangle_{\Omega_t} &= \lim_{\epsilon \rightarrow 0} \frac{\mathcal{J}(u, u_w + \epsilon \delta u_w) - \mathcal{J}(u, u_w)}{\epsilon} \\ &\quad - \lim_{\epsilon \rightarrow 0} \frac{\langle H(u, u_w + \epsilon \delta u_w) - H(u, u_w), \lambda^+ \rangle_{\Omega_t}}{\epsilon} \\ &= 2\ell \langle u_w, \delta u_w \rangle_{\Omega_t} + \langle \lambda^+, \delta u_w \rangle_{\Omega_t} = 0. \end{aligned} \quad (78)$$

Since the variation δu_w is arbitrary, we determine the gradient of \mathcal{J} with respect to u

$$\nabla_{u_w} \mathcal{L} = 2\ell u_w + \lambda^+,$$

and the optimality condition

$$-2\ell u_w(t) = \lambda^+(t).$$

Using the compatibility condition (76), the optimality condition simplifies in

$$-2\ell u_w(t) = u_x^+(0, t). \quad (79)$$

The optimality system corresponding to the linearized Burgers equation is given in Fig. 18.

7 Non-linear Burgers equation

In this section, we consider the case of the nonlinear Burgers equation where the control is both distributed and applied at the boundaries of the spatial domain. Since this is a natural extension to the linearized Burgers equation studied in section 6, we will not detail the derivation of the optimality system (see El Shrif, 2008, for that) but we will present some numerical results of optimal control (section 7.2).

7.1 Formulation and optimality system

The Burgers equation that we consider is given by

$$F(u, \Phi) = \frac{\partial u}{\partial t} + \frac{1}{2} \frac{\partial u^2}{\partial x} - \nu \frac{\partial^2 u}{\partial x^2} - \Phi = 0 \quad \text{with} \quad u(x, t_0) = u_0(x),$$

where ν is the kinematic viscosity and $\Phi(x, t)$ corresponds to the distributed control. In our application, this equation is solved on a physical domain defined by $\Xi = \{(x, t) \setminus (x, t) \in \Omega_x \times \Omega_t\}$ with $\Omega_x = [0, L]$ and $\Omega_t = [t_0, t_f]$. Furthermore, we suppose that boundary controls are applied at the left and right boundaries of the domain. The boundary conditions are then

$$u(0, t) = \phi_L(t)$$

$$u(L, t) = \phi_R(t)$$

where ϕ_L and ϕ_R correspond to control parameters.

STATE EQUATION:

$$\begin{aligned}
 F_U(u) &= u_t + U(x)u_x - u_{xx} = 0 \\
 u(x, t_0) &= u_0(x) \quad (\text{I.C.}) \\
 u(0, t) &= u_w(t) \quad (\text{B.C.}) \text{ and control parameter} \\
 u(L, t) &= 0 \quad (\text{B.C.})
 \end{aligned}$$

ADJOINT EQUATION:

$$\begin{aligned}
 F_U^+(u^+) &= u_t^+ + (Uu^+)_x + u_{xx}^+ = 0 \quad \forall(x, t) \in \Xi \\
 u^+(0, t) &= 0 \quad (\text{B.C.}) \\
 u^+(L, t) &= 0 \quad (\text{B.C.}) \\
 u^+(x, t_f) &= 2u(x, t_f) \quad (\text{T.C.})
 \end{aligned}$$

OPTIMALITY CONDITION:

$$-2\ell u_w(t) = u_x^+(0, t)$$

COST FUNCTIONAL:

$$\mathcal{J}(u, u_w) = \left(\int_0^L u^2 \, dx \right)_{t=t_f} + \ell \int_{t_0}^{t_f} u_w^2 \, dt$$

Figure 18. Optimality system for the linearized Burgers equation. B.C.: boundary condition, I.C.: initial condition, T.C.: terminal condition.

In this section, we seek to minimize the cost functional defined by

$$\begin{aligned}\mathcal{J}(u, \Phi, \phi_L, \phi_R) = & \frac{\omega_1}{2} \int_{\Omega_t} \int_{\Omega_x} (u - \hat{u})^2 \, dx \, dt + \frac{\omega_2}{2} \int_{\Omega_x} [u(x, t_f) - \bar{u}(x)]^2 \, dx \\ & + \frac{\ell_1}{2} \int_{\Omega_t} \phi_L^2(t) \, dt + \frac{\ell_2}{2} \int_{\Omega_t} \phi_R^2(t) \, dt \\ & + \frac{\ell}{2} \int_{\Omega_t} \int_{\Omega_x} \Phi^2(x, t) \, dx \, dt.\end{aligned}$$

The first two terms try to match the solution u respectively on Ξ and over the spatial domain Ω_x at t_f to given functions \hat{u} and \bar{u} . These two targets are generally determined based on physical arguments: laminar flow, solutions of minimum drag, unstable steady solutions,... This type of functional corresponds to a target optimization problem. The last three terms are penalty terms that limit the size of the control functions Φ , ϕ_L and ϕ_R . The positive constants ω_1 , ω_2 , ℓ , ℓ_1 and ℓ_2 are chosen to adjust the relative importance of the five terms in \mathcal{J} .

The problem of optimization that we are interested to solve is

Determine the solution u and the control parameters Φ , ϕ_L and ϕ_R such that the cost functional \mathcal{J} reaches a minimum.

This constrained optimization problem is absolutely similar to the one treated in section 6.2 for the linearized Burgers equation. After developments (see El Shrif, 2008, for the details), the optimality system summarized in Fig. 19 is obtained.

7.2 Results of optimal control

7.2.1 Numerical parameters and space-time discretization

For the numerical applications, we consider a simplified version of the original optimization problem described in section 7.1. First, we suppose that the control is not applied at the spatial boundaries *i.e.* $\phi_L = \phi_R = 0$ in Fig. 19. Second, we assume that the targets \hat{u} and \bar{u} are equal to the initial condition u_0 (see below for the expression). Third, we take as weighting coefficients for the two targets $\omega_1 = \omega_2 = 1$. Finally, the cost functional

STATE EQUATION:

$$\begin{aligned} F(u) &= \frac{\partial u}{\partial t} + \frac{1}{2} \frac{\partial u^2}{\partial x} - \nu \frac{\partial^2 u}{\partial x^2} - \Phi = 0 \\ u(0, t) &= \phi_L \quad (\text{B.C.}) \\ u(L, t) &= \phi_R \quad (\text{B.C.}) \\ u(x, 0) &= u_0(x) \quad (\text{I.C.}) \end{aligned} \tag{80a}$$

ADJOINT EQUATION:

$$F^+(u^+) = -\frac{\partial u^+}{\partial t} - u \frac{\partial u^+}{\partial x} - \nu \frac{\partial^2 u^+}{\partial x^2} = \omega_1 (u - \hat{u}) \tag{80b}$$

$$u^+(0, t) = 0 \quad (\text{B.C.})$$

$$u^+(L, t) = 0 \quad (\text{B.C.})$$

$$u^+(x, t_f) = \omega_2 (u(x, t_f) - \bar{u}(x)) \quad (\text{T.C.}) \tag{80c}$$

OPTIMALITY CONDITION:

$$\nabla_{\Phi} \mathcal{J} = \ell \Phi + u^+ \tag{80d}$$

$$\nabla_{\phi_L} \mathcal{J} = \ell_1 \phi_L + \nu \frac{\partial u^+}{\partial x}(0, t)$$

$$\nabla_{\phi_R} \mathcal{J} = \ell_2 \phi_R - \nu \frac{\partial u^+}{\partial x}(L, t)$$

COST FUNCTIONAL:

$$\begin{aligned} \mathcal{J} &= \frac{\omega_1}{2} \int_{\Omega_t} \int_0^L (u - \hat{u})^2 \, dx \, dt + \frac{\omega_2}{2} \int_{\Omega_x} [u(x, t_f) - \bar{u}(x)]^2 \, dx \\ &\quad + \frac{\ell}{2} \int_{\Omega_t} \int_{\Omega_x} \Phi^2(x, t) \, dx \, dt + \frac{\ell_1}{2} \int_{\Omega_t} \phi_L^2(t) \, dt + \frac{\ell_2}{2} \int_{\Omega_t} \phi_R^2(t) \, dt \end{aligned}$$

Figure 19. Optimality system for the non-linear Burgers equation. B.C.: boundary condition, IC: initial condition, T.C.: terminal condition.

corresponds to

$$\begin{aligned}\mathcal{J}(u, \Phi) = & \frac{1}{2} \int_{\Omega_t} \int_{\Omega_x} (u - u_0)^2 \, dx \, dt + \frac{1}{2} \int_{\Omega_x} [u(x, t_f) - u_0(x)]^2 \, dx \\ & + \frac{\ell}{2} \int_{\Omega_t} \int_{\Omega_x} \Phi^2(x, t) \, dx \, dt\end{aligned}$$

with $\Omega_x = [0, 1]$ and $\Omega_t = [0, 1]$. Here the initial condition is selected as

$$u_0(x) = \sin \left(\pi \frac{\tan(c_s(2x-1))}{\tan(c_s)} \right)$$

where c_s is a stretching coefficient introduced to represent correctly the boundary layers. In our simulations, we choose $c_s = 1.3$ and $\nu = 0.01$.

To solve numerically the Burgers equation (80a) and the adjoint equation (80b), a numerical scheme known as *Forward Time, Centered Space* (FTCS) is used. This method corresponds to a forward scheme in time and to a centered finite difference scheme of order 2 in space. The main interest of this scheme is its easiness of implementation. The direct and adjoint equations are discretized in time and space on a constant mesh (Δt , Δx). Noting $u_{j,n} = u(j\Delta x, n\Delta t)$, the discretized versions of (80a) and (80b) are respectively

$$\begin{aligned}u_{j,n+1} = & u_{j,n} (1 - 2s) + s(u_{j+1,n} + u_{j-1,n}) \\ & - \frac{\Delta t}{2\Delta x} u_{j,n} (u_{j+1,n} - u_{j-1,n}) + \Phi_{j,n},\end{aligned}\quad (81)$$

and

$$\begin{aligned}u_{j,n+1}^+ = & u_{j,n}^+ (1 + 2s) - s(u_{j+1,n}^+ + u_{j-1,n}^+) \\ & - \frac{\Delta t}{2\Delta x} u_{j,n}^+ (u_{j+1,n}^+ - u_{j-1,n}^+) - \omega_1 (u_{j,n} - \hat{u}_{j,n}) \Delta t,\end{aligned}\quad (82)$$

where $s = \nu \frac{\Delta t}{\Delta x^2}$.

7.2.2 Optimization procedure

The optimality system given in Fig. 19 is now solved iteratively. The procedure is similar to the one described in section 3.2.3 in the general framework. Let k ($k = 0, \dots, +\infty$) be the iteration number of the optimization procedure, the gradient $\mathbf{g}^{(k)}$ determined from the adjoint formulation can be used

to estimate a descent³² direction $\mathbf{p}^{(k)}$. A strategy for optimization of the control parameters³³ $\mathbf{c}^{(k)}$ is then to approach the minimum by a sequence of steps constructed as

$$\mathbf{c}^{(k+1)} = \mathbf{c}^{(k)} + \alpha^{(k)} \mathbf{p}^{(k)} \quad (83)$$

where $\alpha^{(k)}$ is a positive scalar called step length.

The computation of $\alpha^{(k)}$ is the linesearch, and may itself be iterative. It can be proved (Gould and Leyffer, 2002) that if the linesearch allows steps that are either too long or too short relative to the amount of decrease that they provide, then wrong convergences may appear. For determining the values of $\alpha^{(k)}$, one possibility is to search for the minimizer of $\mathcal{J}(u, \mathbf{c}^{(k)} + \alpha^{(k)} \mathbf{p}^{(k)})$. Due to the expensive cost of the method, this type of exact linesearch is rarely employed nowadays. Here, we prefer to use the backtracking Armijo method for which there exists some guarantee of sufficient decrease of the cost functional (see Nocedal and Wright, 1999, for the algorithm).

The simplest choice of the descent direction corresponds to the steepest-descent method for which $\mathbf{p}^{(k)} = -\mathbf{g}^{(k)}$. The drawback of such a steepest descent technique is that the descent direction is only based on local information whereas after some iterations, we have a more global description of the cost functional. For this reason, a particular variant of the conjugate gradient algorithm, referred as the Hestenes-Stiefel method (Nocedal and Wright, 1999), was selected. It is given by

$$\mathbf{p}^{(k+1)} = -\mathbf{g}^{(k+1)} + \beta^{(k+1)} \mathbf{p}^{(k)} \quad \text{with} \quad \mathbf{p}^{(0)} = -\mathbf{g}^{(0)} \quad (84)$$

where the coefficient $\beta^{(k+1)}$ is defined as

$$\beta^{(k+1)} = \frac{(\mathbf{g}^{(k+1)})^T (\mathbf{g}^{(k+1)} - \mathbf{g}^{(k)})}{(\mathbf{g}^{(k+1)} - \mathbf{g}^{(k)})^T \mathbf{p}^{(k)}}.$$

The optimization algorithm is the following:

Step 1: Starting from a guess value $\mathbf{c}^{(k)}$ for the distributed control (no control is in general an acceptable guess value for $k = 0$), the discretized version (81) of the direct Burgers equation (80a) is solved forward in time from $t = 0$ to $t = t_f$.

³²By definition, $\mathbf{p}^{(k)}$ is a descent direction if $(\mathbf{p}^{(k)})^T \mathbf{g}^{(k)} < 0$ where $(\cdot)^T$ denotes the transposition.

³³For the Burgers equation, the control parameter \mathbf{c} is Φ .

Step 2: The terminal condition $u^+(x, t_f)$ for the adjoint variable is computed using (80c).

Step 3: The discretized version (82) of the adjoint Burgers equation (80b) is solved backward in time from $t = t_f$ to $t = 0$.

Step 4: The gradient of the cost functional \mathcal{J} with respect to the control variable \mathbf{c} is computed using (80d). This gradient $\mathbf{g}^{(k)} = (\nabla_{\mathbf{c}} \mathcal{J})^{(k)}$ is estimated based on the adjoint variable u^+ determined in step 7.2.2.

Step 5: The gradient-based optimization method (83) is used for updating the control.

Step 5.1: The direction of descent $\mathbf{p}^{(k)}$ is determined by (84) based on the gradient $\mathbf{g}^{(k)}$ computed in step 7.2.2 and previous descent directions (conjugate gradient).

Step 5.2: An inexact linesearch (backtracking Armijo method) is used to determine the step length $\alpha^{(k)}$.

Step 5.3: The previous estimate of the optimal control is updated by $\mathbf{c}^{(k+1)} = \mathbf{c}^{(k)} + \alpha^{(k)} \mathbf{p}^{(k)}$.

Step 6: Return to step 7.2.2 and iterate until a given criterion of convergence is satisfied.

7.2.3 Results

Figure 20 represents at the final time of integration t_f , the solution u obtained by optimal control of the Burgers equation for the three first iterations of the optimization procedure. In accordance with what is expected, u converges rapidly to the target solution u_0 . Indeed, we observe in Fig. 21 that about twenty iterations of the iterative procedure are sufficient for the cost functional \mathcal{J} to converge. Finally, Fig. 22 represents the spatial evolution of the distributed control obtained at convergence at four different time instants.

8 Conclusion

In this chapter, we have outlined the interest of constrained optimization for solving different types of problems encountered in fluid mechanics, and particularly in flow control. Indeed, constrained optimization methods are in the heart of reduced-order modeling techniques such as POD, and of data assimilation methods used everyday in weather forecast or, within a different framework, for determining optimal growth perturbations. In addition, constrained optimization appears naturally in control theory, whether in linear control techniques such as LQR and LQG, or in nonlinear approaches such as Model Predictive Control (see the contribution by R. King in this

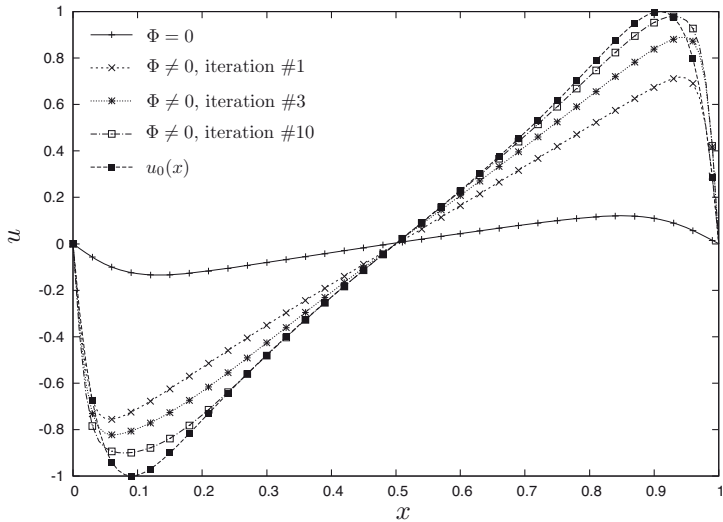


Figure 20. Distributed control of the Burgers equation with $\ell = 0.01$. Comparison of the solutions at final time t_f with and without control.

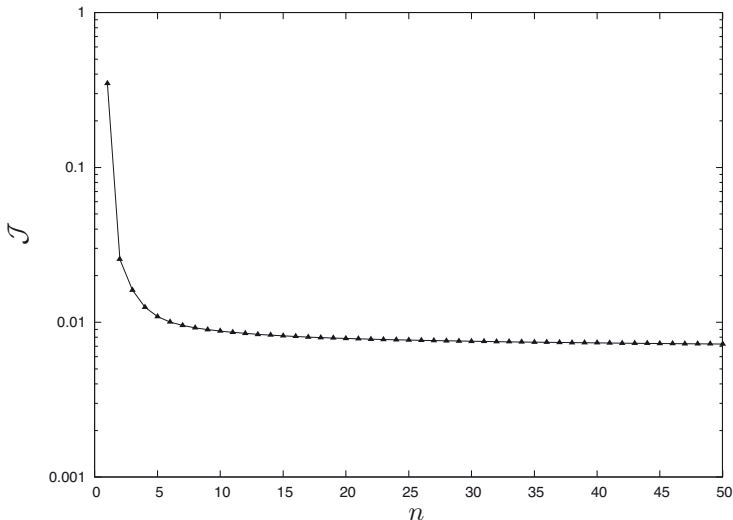


Figure 21. Distributed control of the Burgers equation with $\ell = 0.01$. Decrease of the cost functional \mathcal{J} with the iteration number.

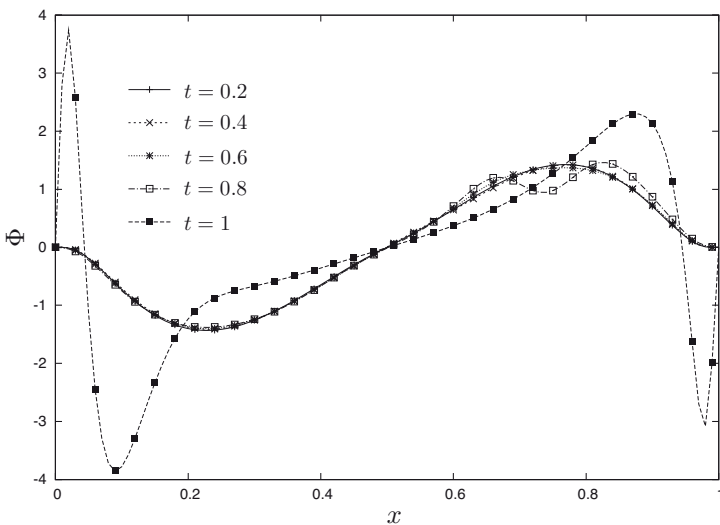


Figure 22. Distributed control of the Burgers equation with $\ell = 0.01$. Distributed control $\Phi(x, t)$ at convergence.

book), frequently used experimentally in process engineering. Lastly, optimal control and shape optimization, often considered in many fields of applied mathematics (computer fluid dynamics, computer graphics, multi-disciplinary optimization to name a few), are nothing else than constrained optimization methods adapted to the resolution of a given problem. In section 3, fundamentals aspects of optimal control theory have been explained in details. This should allow an interested reader to derive a corresponding optimality system for his/her own problem of interest. In sections 4 to 6, different constrained optimization problems were formulated for linear 1D configuration. Finally, in section 7, the formalism is extended to a non-linear 1D PDE equation. The reader is referred to El Shrif (2008) for the derivation of optimality systems for the Navier-Stokes equations where a Direct Numerical Simulation and a Large Eddy Simulation of the flow are both considered. Particularly noteworthy is the similarity of the formulation between the determination of optimal growth perturbations and other methods employed in control.

A Adjoint operator and inner product

Suppose Ω is an Hilbert space, with inner product $\langle \cdot, \cdot \rangle$. Consider a continuous linear operator $\mathcal{N} : \Omega \rightarrow \Omega$. Using the Riesz representation theorem, one can show that there exists a unique continuous operator $\mathcal{N}^+ : \Omega \rightarrow \Omega$ with the following property:

$$\langle \mathcal{N}\mathbf{x}, \mathbf{y} \rangle = \langle \mathbf{x}, \mathcal{N}^+\mathbf{y} \rangle \quad \forall \mathbf{x}, \mathbf{y} \in \Omega.$$

Here, the symbol $+$ denotes the adjoint, and the operator \mathcal{N}^+ is the adjoint of \mathcal{N} . Since \mathcal{N} is assumed linear, this definition can be extended directly to the matrix \mathcal{A} associated to \mathcal{N} .

It should be noted that in general for a given matrix \mathcal{A} , we have $\mathcal{A}^+ \neq \mathcal{A}^H$, the two being equal only when the inner product used to derive the adjoint does not have an associated weight (classical Euclidean inner product). Indeed, if we consider the weighted inner product of two vectors \mathbf{x} and \mathbf{y} given by

$$\langle \mathbf{x}, \mathbf{y} \rangle_W = \mathbf{x}^H W \mathbf{y}$$

where W is positive definite, the continuous adjoint operator of \mathcal{A} with respect to this inner product is defined as:

$$\begin{aligned} \langle \mathcal{A}\mathbf{x}, \mathbf{y} \rangle_W &= \langle \mathbf{x}, \mathcal{A}^+\mathbf{y} \rangle_W \quad \forall \mathbf{x}, \mathbf{y} \in \Omega \\ \iff (\mathcal{A}\mathbf{x})^H W \mathbf{y} &= \mathbf{x}^H W \mathcal{A}^+ \mathbf{y} \\ \iff \mathbf{x}^H \mathcal{A}^H W \mathbf{y} &= \mathbf{x}^H W \mathcal{A}^+ \mathbf{y} \\ \iff \mathcal{A}^H W &= W \mathcal{A}^+ \\ \iff \mathcal{A}^+ &= W^{-1} \mathcal{A}^H W. \end{aligned}$$

Since W is positive definite, W^{-1} is well defined and we thus have $\mathcal{A}^+ = W^{-1} \mathcal{A}^H W$ i.e. $\mathcal{A}^+ = \mathcal{A}^H$ only when W is equal to the identity matrix.

Bibliography

- E. Åkervik, J. Hoepffner, U. Ehrenstein, and D. S. Henningson. Optimal growth, model reduction and control in a separated boundary-layer flow using global eigenmodes. *J. Fluid Mech.*, 579:305–314, 2007.
- A. Antkowiak and P. Bracher. On vortex rings around vortices: an optimal mechanism. *J. Fluid Mech.*, 578:295–304, 2007.
- A. C. Antoulas. *Approximation of Large-Scale Dynamical Systems*. Advances in Design and Control. SIAM, 2005.

- N. Aubry, P. Holmes, J. L. Lumley, and E. Stone. The dynamics of coherent structures in the wall region of a turbulent boundary layer. *J. Fluid Mech.*, 192:115–173, 1988.
- A. Barbagallo, D. Sipp, and P. Schmid. Closed-loop control of an open cavity flow using reduced order models. *J. Fluid Mech.*, 641:1–50, 2009.
- P. Benner, J.-R. Li, and T. Penzl. Numerical solution of large-scale Lyapunov equations, Riccati equations, and linear-quadratic optimal control problems. *Numer. Linear Algebra Appl.*, 15:755–777, 2008.
- M. Bergmann and L. Cordier. Optimal control of the cylinder wake in the laminar regime by Trust-Region methods and POD Reduced Order Models. *J. Comp. Phys.*, 227:7813–7840, 2008.
- M. Bergmann, L. Cordier, and J.-P. Branger. Optimal rotary control of the cylinder wake using POD Reduced Order Model. *Phys. Fluids*, 17(9):097101:1–21, 2005.
- T. R. Bewley and S. Liu. Optimal and robust control and estimation of linear paths to transition. *J. Fluid Mech.*, 365:305–349, 1998.
- T. R. Bewley, P. Moin, and R. Temam. DNS-based predictive control of turbulence: an optimal benchmark for feedback algorithms. *J. Fluid Mech.*, 447:179–225, 2001.
- J.-F. Bonnans, J.-C. Gilbert, C. Lemarchal, and C. A. Sagastizbal. *Numerical Optimization*. Springer, 2003.
- A. E. Bryson Jr. and Y. Ho. *Applied Optimal Control: Optimization, Estimation and Control*. Taylor & Francis, 1975.
- J. B. Burl. *Linear Optimal Control: H_2 and H_∞ Methods*. Addison-Wesley Publishing, 1999.
- Y. Chang. *Approximate models for optimal control of turbulent channel flow*. PhD thesis, universit de Rice, 2000.
- P. Chassaing. *Turbulence en mécanique des fluides*. Polytech. Cépadués, 2000.
- L. Cordier. Elements of control theory. In *Workshop "Flow Control Methods and Applications"*, Poitiers, December 7-11, 2009.
- L. Cordier, B. Abou El Majd, and J. Favier. Calibration of POD Reduced-Order models using Tikhonov regularization. *Int. J. Numer. Meth. Fluids*, 63(2), 2010.
- A. El Shrif. *Contrôle optimal d'un écoulement de canal turbulent*. PhD thesis, Institut National Polytechnique de Lorraine, 2008.
- M. Fahl. *Trust-Region methods for flow control based on Reduced Order Modeling*. PhD thesis, Trier university, 2000.
- M. Gad-el-Hak. *Flow Control: Passive, Active and Reactive Flow Management*. Cambridge University Press, London, United Kingdom, 2000.

- B. Galletti, A. Bottaro, C.-H. Bruneau, and A. Iollo. Accurate model reduction of transient and forced wakes. *Eur. J. Mech. B/Fluids*, 26(3):354–366, 2007.
- N. I. M. Gould and S. Leyffer. An introduction to algorithms for nonlinear optimization. Technical Report RAL-TR-2002-031, Rutherford Appleton Laboratory, 2002. URL <http://www.numerical.rl.ac.uk/reports/reports.shtml>.
- A. Griewank and A. Walther. *Evaluating Derivatives: Principles and Techniques of Algorithmic Differentiation, Second Edition*. SIAM, 2008.
- A. Guegan, P. J. Schmid, and P. Huerre. Optimal energy growth and optimal control in swept Hiemenz flow. *J. Fluid Mech.*, 566:11–45, 2006.
- S. Gugercin and A. C. Antoulas. Model reduction of large-scale systems by least squares. *Linear Algebra and its Applications*, 415(2-3):290–321, 2006.
- M. D. Gunzburger. Introduction into mathematical aspects of flow control and optimization. In *Lecture series 1997-05 on inverse design and optimization methods*. Von Kármán Institute for Fluid Dynamics, 1997a.
- M. D. Gunzburger. Lagrange multiplier techniques. In *Lecture series 1997-05 on inverse design and optimization methods*. Von Kármán Institute for Fluid Dynamics, 1997b.
- M. D. Gunzburger. *Perspectives in flow control and optimization*. SIAM, 2003.
- P. Huerre. Optimal control. In *First Summer School on Optimization and Control of Flows and Transfers*, Aussois, 12-17 March, 2006. Lecture notes.
- M. Ilak. *Model reduction and feedback control of transitional channel flow*. PhD thesis, Princeton University, 2009.
- J.-N. Juang and M. Q. Phan. *Identification and control of mechanical systems*. Cambridge University Press, 2001.
- S. Lall, J. E. Marsden, and S. Glavaski. A Subspace Approach to Balanced Truncation for Model Reduction of Nonlinear Control Systems. *International Journal of Robust and Nonlinear Control*, 12(6):519–535, 2002.
- F. L. Lewis and V. L. Syrmos. *Optimal Control*. John Wiley and Sons, New York, second edition, 1995.
- J. L. Lumley. *Atmospheric Turbulence and Wave Propagation. The structure of inhomogeneous turbulence*, pages 166–178. Nauka, Moscow, 1967.
- V. Mehrmann and T. Stykel. Balanced truncation model reduction for large-scale systems in descriptor form. In V. Mehrmann P. Benner and D. Sorensen, editors, *Dimension Reduction of Large-Scale Systems*, volume 45 of *Lecture Notes in Computational Science and Engineering*, pages 83–115. Springer-Verlag, Berlin/Heidelberg, 2005.

-
- B. Mohammadi and O. Pironneau. *Applied Shape Optimization for Fluids*. Oxford University Press, 2001.
 - B. Moore. Principal component analysis in linear systems: Controllability, observability, and model reduction. *IEEE Transactions on Automatic Control*, 26:17–32, 1981.
 - E. A. Müller. *Optimal control of thermal systems*. PhD thesis, ETH Zurich, 2006.
 - J. Nocedal and S. J. Wright. *Numerical Optimization*. Springer series in operations research, 1999.
 - B. Protas. On the "Vorticity" Formulation of the Adjoint Equations and its Solution Using Vortex Method. *Journal of Turbulence*, 3:48–55, 2002.
 - C. W. Rowley. Model reduction for fluids using balanced proper orthogonal decomposition. *International Journal of Bifurcation and Chaos*, 15(3):997–1013, 2005.
 - P. Sagaut. *Large-eddy simulation for incompressible flows - An introduction*. Springer-Verlag, 2005.
 - H. Schlichting and K. Gersten. *Boundary Layer Theory*. Springer, 8th edition, 2003.
 - P. J. Schmid. Nonmodal stability theory. *Ann. Rev. Fluid Mech.*, 39:129–162, 2007.
 - P. J. Schmid and D. S. Henningson. *Stability and Transition in Shear Flows*. Applied Mathematical Sciences. Springer Verlag, 2001.
 - L. Sirovich. Turbulence and the dynamics of coherent structures. *Quarterly of Applied Mathematics*, XLV(3):561–590, 1987.
 - S. Skogestad and I. Postlethwaite. *Multivariable feedback control - Analysis and design, 2nd Edition*. Wiley, 2005.
 - P. R. Spalart, W. H. Jou, M. Strelets, and S. R. Allmaras. Comments on the Feasibility of LES for Wings, and on a Hybrid RANS/LES Approach. In *1st AFOSR Int. Conf. on DNS/LES*, Ruston, L.A., Aug. 4–8, 1997. In: Advances in DNS/LES, C. Liu and Z. Liu (eds.), Greyden Press, Columbus, OH.
 - A. Tarantola. *Inverse Problem Theory and Methods for Model Parameter Estimation*. SIAM, 2005.
 - Q. Wang, D. Gleich, A. Saberi, N. Etemadi, and P. Moin. A Monte Carlo method for solving unsteady adjoint equations. *J. Comp. Phys.*, 227(12):6184–6205, 2008.
 - Q. Wang, P. Moin, and G. Iaccarino. Minimal Repetition Dynamic Checkpointing Algorithm for Unsteady Adjoint Calculation. *SIAM J. Sci. Comput.*, 31:2549, 2009.
 - K. Zhou, J. C. Doyle, and K. Glover. *Robust and optimal control*. Prentice Hall, 1996.

Global Stability Analysis for Linear Dynamics

Marek Morzyński,^{*}

Bernd R. Noack[†] and Gilead Tadmor[‡]

^{*} Institute of Combustion Engines and Transportation Technical University of Poznań, Poznań, Poland

[†] Institut Pprime, CNRS – Université de Poitiers – ENSMA, Département Fluides, Thermique, Combustion, CEAT, Poitiers, France

[‡] Department of Electrical and Computer Engineering, Northeastern University, Boston, MA, USA

Abstract Global stability analysis of fluid flows is presented as a method of extracting physical eigenmodes with associated linear dynamic models. These reduced-order models (ROM) are optimal for the transients near the onset of instability. We describe the computational aspects of the eigenmode extraction in detail. This outline includes (i) the discretization technique of the eigenproblem in the framework of computational fluid dynamics (CFD) and (ii) the solution algorithms for the discretized eigenproblem. As regards physical aspects, the linear ROM are improved by enriching the basis with POD modes and by incorporating weakly nonlinear base flow variations. Results of stability computations are presented for the circular cylinder wake, the flow around a NACA-0012 airfoil and the optimization of passive control. Preliminary 3D eigensolutions show the potential of the global stability method.

1 Introduction

The first pioneering papers on global flow stability (Zebib, 1987; Jackson, 1987) presented a novel method of investigating non-parallel flows. These and other early articles concentrated mainly on critical Reynolds numbers and on the leading eigenvalues comprising growth rates and frequencies. Interest in the corresponding spectrum of physical eigenmodes was small. The opportunities of global stability in designing passive control means was realized from the very beginning but not widely exploited. Active, feedback flow control applications with physical ROM were beyond the scope at that time.

The birth of global stability was possible due to computer power brought by a new generation of vector computers like, for example, the Cray YMP.

Global non-parallel flow stability does not need a frequently employed assumption of a dominating flow direction. It generates a large, fully two- or three-dimensional eigenvalue problem. The new hardware and solution techniques allowed to solve it for the first time for two dimensions. In this way, methods that assume weakly non-parallel flow, being effectively one-dimensional, were enriched by the new approach (Wolter et al., 1989).

The recent period brought a boost of interest in reduced order models (ROM) for various purposes. For example, modern aeroelastics presently uses ROMs of the flow, mode interpolation and many of the techniques described in this chapter. These ROMs serve as cheaper surrogate plants for costly unsteady RANS computations (Lieu et al., 2006; Amsallem and Farhat, 2008). Here, we concentrate on ROM for model based flow control and the role of physical modes in flow modeling.

Flow control is a key technology in improving the performance of transport systems, like cars, trains and airplanes. Actuators may be operate in passive, active open-loop or active closed-loop mode. The latter variant may be considered as the most general type of control. The potential of closed-loop flow control is increasingly realized and exploited (Becker et al., 2002). A systematic control-theoretical treatment of flow control has actively been pursued since one decade. The review article (Theofilis, 2003) serves as a good starting point for a more detailed reading. The use of model-based feed-back control, requires low dimensionality of the model for online capability and robustness (see chapter of R. King in this volume). POD modes, being the result of pure signal processing, were used in early days of flow modeling are now enriched by numerous novel and interesting improvements (Bergmann et al., 2005; Deane et al., 1991; Jørgensen et al., 2003; Khilnik et al., 2000; Ma and Karniadakis, 2002; Siegel et al., 2006). The more successful ROM approaches typically incorporated more physical information about the modeled system. The need for new methods in flow modeling enhanced interest also in global stability method and led to development of new tools (Schmid and Sesterhenn, 2008; Rowley et al., 2009). In (Åkervik et al., 2007; Bagheri et al., 2009), control design employs stability modes.

This chapter is organized as follows. After a description of the global stability problem in § 2, computational aspects are outlined, namely the FEM discretization in § 3 and iterative eigensolvers in § 4. Results for the cylinder wake are presented for the natural wake stability (§ 5) and control design (§ 6). In § 7, we outline the role of nonlinearity for dynamic model development.

2 Global flow stability analysis

We consider the flow stability problem for the incompressible fluid motion in a Cartesian coordinate system (x_1, x_2, x_3) . The velocity vector (u_1, u_2, u_3) comprises components in these three coordinate directions. The pressure is denoted by p . We assume that all quantities are non-dimensionalized with scale D , velocity U and density ρ . The flow properties are thus characterized by the Reynolds number $Re = UD/\nu$, ν being the kinematic viscosity of the fluid.

The fluid motion is described by the incompressibility condition

$$u_{i,i} = 0$$

and the unsteady Navier-Stokes equation:

$$\dot{u}_i + u_{i,j}u_j + p_{,i} - \frac{1}{Re}u_{i,jj} = 0. \quad (1)$$

Here and henceforth, we apply the summation convention for double indices. The subscripts ', j ' and ', jj ' denote the first and second derivatives in j -th direction and \dot{u}_i is the time derivative of u_i , respectively.

We decompose the unsteady solution of the Navier-Stokes equation (1) as the sum of its steady solution (indicated by the bar) and the disturbance (indicated by the prime):

$$\begin{aligned} u_i &= \bar{u}_i + \acute{u}_i, \\ p &= \bar{p} + \acute{p}. \end{aligned}$$

This decomposition leads us to the disturbance equation in the form:

$$\acute{u}_i + \acute{u}_j\bar{u}_{i,j} + \bar{u}_j\acute{u}_{i,j} + \acute{u}_j\acute{u}_{i,j} + \acute{p}_{,i} - \frac{1}{Re}\acute{u}_{i,jj} = 0 \quad (2)$$

and the continuity equation for the disturbance:

$$\acute{u}_{i,i} = 0. \quad (3)$$

We consider the global non-parallel flow stability, yielding global eigenmodes. None of the spatial direction is distinguished. In particular, we do not assume any *dominating flow direction* or *weakly non-parallel flow*. This is the most general assumption of linear stability theory. Under non-degenerate conditions, the evolution of any infinitesimal disturbance is composed of normal solutions with product ansatz for space and time dependency:

$$\begin{aligned} \acute{u}_i(x, y, z, t) &= \tilde{u}_i(x, y, z) e^{\lambda t}, \\ \acute{p}(x, y, z, t) &= \tilde{p}(x, y, z) e^{\lambda t}. \end{aligned} \quad (4)$$

A traveling wave may appear as a *solution* of the problem but its form is not pre-assumed.

To formulate a differential eigenvalue problem, we linearize the equation (2), i.e. we ignore the quadratic term $\bar{u}_j \bar{u}_{i,j}$. In this linearized disturbance equation, we separate the time and space dependence according to (4).

Introducing (4) into the linearized form of (2) results in a linear system of partial differential equations:

$$\begin{aligned} \lambda \tilde{u}_i + \tilde{u}_j \bar{u}_{i,j} + \bar{u}_j \tilde{u}_{i,j} + \tilde{p}_{,i} - \frac{1}{Re} \tilde{u}_{i,jj} &= 0, \\ \tilde{u}_{i,i} &= 0. \end{aligned} \quad (5)$$

Equation (5) represents the generalized differential eigenvalue problem.

3 Finite Element Method discretization of the global flow stability problem

We use the Finite Element Method with its penalty formulation for discretization of the Navier-Stokes equation (1) and for the eigenvalue problem (5). Fluid velocity is expressed by sums of the quadratic interpolation functions:

$$u_i = \Phi_k u_{ik}. \quad (6)$$

The index sets for i, k are $i = 1, 2$; $k = 1, \dots, 6$ for 2D and $i = 1, 2, 3$; $k = 1, \dots, 10$ for 3D. The interpolation function is defined on a 6-node triangular or 10-node tetrahedral element depicted in Fig. 1.

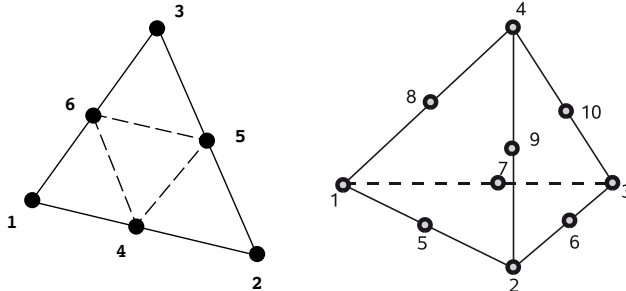


Figure 1. Natural coordinate triangular and tetrahedral element with quadratic interpolation function

The penalty method eliminates the pressure from governing equations via:

$$\frac{1}{\epsilon} p = u_{i,i}. \quad (7)$$

The penalty FEM approach is described in detail in (Baker, 1983; Chung, 2002). The penalty parameter ϵ is usually chosen to be a large number, related to computer word length. Sometimes it is varied within the iteration process to increase the convergence rate. Numerical experiments show that variation of ϵ in the range of 10^3 – 10^7 has negligible influence on the steady flow solutions. In the calculations presented in the following sections, we assume $\epsilon = 10^5$ and keep it constant in the iteration process. In mixed (velocity-pressure) FEM formulation poor conditioning of the linear equation system can be avoided with an interpolation function for pressure of lower order as compared to the velocity one. In penalty formulation, we apply a similar technique and assume linear interpolation of velocity in the penalty term and a quadratic interpolation in all other terms.

First, we have to find the steady solution for the flow eigenanalysis. We present the FEM procedure in detail, since it is very similar to the eigensolver one. The approximation residual $R_i^{(1)}$ of the steady Navier-Stokes equation with FEM approximation (6) reads:

$$u_{i,j} u_j + p_{,i} - \frac{1}{Re} u_{i,jj} = R_i^{(1)}. \quad (8)$$

We introduce a set of weighting functions w_i and evaluate the standard inner product $(R_i^{(1)}, w_i)$ on each triangular or tetrahedral volume element. With the Galerkin method

$$(R_i^{(1)}, w_i) = 0, \quad (9)$$

we formulate the FEM discretization:

$$\int_{\Omega} \left(u_{i,j} u_j + p_{,i} - \frac{1}{Re} u_{i,jj} \right) \Phi_m d\Omega = 0. \quad (10)$$

We employ the interpolation functions for the velocity field and obtain

$$\int_{\Omega} \left(\Phi_{k,j} u_{ik} \Phi_o u_{jo} + p_{,i} - \frac{1}{Re} \Phi_{k,jj} u_{ik} \right) \Phi_m d\Omega = 0. \quad (11)$$

The equation (11) is used to calculate the element matrices. Further, we exploit the weak formulation of the problem. This allows a lower differentiation order of weighting and interpolation functions and delivers a very

convenient stress-free natural boundary condition. In this formulation, we apply the Gauss-Green theorem to the diffusion term:

$$\int_{\Omega} u_{ik} \Phi_{k,jj} \Phi_m d\Omega = \int_{\Gamma} \Phi_m u_{i,j} n_j d\Gamma - \int_{\Omega} u_{ik} \Phi_{k,j} \Phi_{m,j} d\Omega. \quad (12)$$

The same procedure is applied to the pressure term:

$$\int_{\Omega} p_{,i} \Phi_m d\Omega = \int_{\Gamma} p \Phi_m \delta_{ij} n_j d\Gamma - \int_{\Omega} p \Phi_{m,i} d\Omega. \quad (13)$$

With the penalty function given by (7), we obtain the final version of the FEM equation:

$$\begin{aligned} & u_{ik} u_{jo} \int_{\Omega} \Phi_{k,j} \Phi_o \Phi_m d\Omega - \epsilon u_{jk} \int_{\Omega} \Phi_{k,j} \Phi_{m,i} d\Omega - \\ & \int_{\Gamma} \Phi_m \left(-p \delta_{ij} + \frac{1}{Re} u_{i,j} \right) n_j d\Gamma + \frac{1}{Re} u_{ik} \int_{\Omega} \Phi_{k,j} \Phi_{m,j} d\Omega = 0. \end{aligned} \quad (14)$$

For triangular and tetrahedral elements it is possible to integrate the FEM matrix exactly with formulas given in FEM textbooks (see, e.g., (Chung, 2002; Baker, 1983)). For this purpose, we use the symbolic manipulation program REDUCE. For example, element $A(1,1)$ for the 3D case is given by:

```
a(1,1)=(re*vol*(2*ux(10)*b1+4*ux(10)*b3+4*ux(10)*b4+2*ux(9)*b1
. +4*ux(9)*b2+4*ux(9)*b4+8*ux(8)*b1+12*ux(8)*b4+8*ux(7)*b1+12*ux
. (7)*b3+2*ux(6)*b1+4*ux(6)*b2+4*ux(6)*b3+8*ux(5)*b1+12*ux(5)*b2
. -ux(4)*b1-2*ux(4)*b4-ux(3)*b1-2*ux(3)*b3-ux(2)*b1-2*ux(2)*b2+
. 12*ux(1)*b1+2*uy(10)*c1+2*uy(9)*c1+4*uy(8)*c1+4*uy(7)*c1+2*uy(
. 6)*c1+4*uy(5)*c1-uy(4)*c1-uy(3)*c1-uy(2)*c1+6*uy(1)*c1+2*uz(10
. )*d1+2*uz(9)*d1+4*uz(8)*d1+4*uz(7)*d1+2*uz(6)*d1+4*uz(5)*d1-uz
. (4)*d1-uz(3)*d1-uz(2)*d1+6*uz(1)*d1+252*b1**2*eps)+252*vol*(b1
. **2+c1**2+d1**2))/420
```

The equation (14) is nonlinear. We define the residual vector as:

$$R_i(u) := F_{ij}(u)u_j \quad (15)$$

We solve the nonlinear steady-state equation with the Newton-Raphson method for the linearized equation. Introducing the Jacobian $J_{ij}^{(0)}$ and the guess solution $u^{(0)}$:

$$J_{ij}^{(0)} = \frac{\partial R_i(u^{(0)})}{\partial u_j}, \quad (16)$$

we obtain the expression for the correction of the solution in the subsequent iteration:

$$J_{ij}^{(0)} \Delta u_j = -R_i(u^{(0)}). \quad (17)$$

This linear equation is solved iteratively until the desired accuracy is obtained.

By analogy with the steady flow equation, we can derive the penalty-formulation FEM equation for the eigenvalue problem:

$$\lambda \int_{\Omega} \Phi_k \tilde{u}_i d\Omega + \int_{\Omega} \Phi_k [\tilde{u}_j \bar{u}_{i,j} + \bar{u}_j \tilde{u}_{i,j} + \tilde{p}_{,i}] d\Omega - \frac{1}{Re} \int_{\Omega} \Phi_k \tilde{u}_{i,jj} d\Omega = 0.$$

After integration we obtain:

$$\begin{aligned} & \lambda \tilde{u}_{im} \int_{\Omega} \Phi_k \Phi_m d\Omega + (\tilde{u}_{ik} \bar{u}_{jo} + \bar{u}_{ik} \tilde{u}_{jo}) \int_{\Omega} \Phi_{k,j} \Phi_o \Phi_m d\Omega \\ & \quad - \epsilon \tilde{u}_{jk} \int_{\Omega} \Phi_{k,j} \Phi_{m,i} d\Omega \quad (18) \\ & - \int_{\Gamma} \Phi_m (-\tilde{p} \delta_{ij} + \frac{1}{Re} \tilde{u}_{i,k}) n_j d\Gamma + \tilde{u}_{ik} \frac{1}{Re} \int_{\Omega} \Phi_{k,j} \Phi_{m,j} d\Omega = 0. \end{aligned}$$

This equation represents the generalized complex, non-Hermitian eigenvalue problem:

$$\mathbf{Ax} - \lambda \mathbf{Bx} = \mathbf{0} \quad (19)$$

4 Numerical techniques to solution of the eigenvalue problem

Before attempting to solve equation (19), let us consider the possible approaches for the linearized equation (2). We intend to identify the eigenmodes and eigenvalues for this dynamical system. Model (2) is a *white-box* system and we can use a discretized eigenvalue problem (19) to find an eigensolution. The alternative method of system identification is known as the *black-box* method. One can exemplify these approaches considering identification of eigenmodes in aeroelasticity. If the structural model of the airplane is available, we can use the FEM (*white-box* model) to compute the normal modes necessary for aeroelastic analysis. However, an alternative procedure is often used in the ground tests. We have the airplane but the complete technical documentation is unavailable. The modes for aeroelastic analysis are needed to assess the necessary modifications, e.g. change of the stores. Now, in the ground test, we force the (*black-box*) system and record the answers. Postprocessing of these measurements gives the required eigensolutions. The latter method also be used also for the linearized equation (2). We concentrate then on the flow snapshots generated by unsteady integration of this equation and try to identify the empirical

eigenmodes of the system. The results presented in following chapters are based only on solution of the algebraic eigenvalue system. As this black-box method is intensively developed recently (Rowley et al., 2009; Schmid and Sesterhenn, 2008), the time domain system identification is presented briefly in § 4.4.

4.1 Solution of Algebraic Eigenvalue Problem

Equation (19) represents a non-Hermitian, generalized eigenvalue problem. The matrices are unsymmetrical, not positive definite, large and sparse. The solution of large eigenproblems is not trivial, even in case of Hermitian matrices. Here, the solution is even more difficult. The algorithms (e.g. QZ) of library routines (like EISPACK) are not suitable for solution, even in two-dimensional case. We can rely only on iterative solvers. Iterative methods are based on determination of both the eigenvalue and the eigenvector at the same time. The simplest power method for the eigenproblem

$$\mathbf{A}\mathbf{x} = \lambda\mathbf{x} \quad (20)$$

starts the solution from the random vector \mathbf{x} . Computation of $\mathbf{A}^2\mathbf{x} = \mathbf{A}(\mathbf{A}\mathbf{x}) \sim \lambda^2\mathbf{x}$ then $\mathbf{A}^3\mathbf{x} = \mathbf{A}(\mathbf{A}^2\mathbf{x}) \sim \lambda^3\mathbf{x}$ and finally, $\mathbf{A}^n\mathbf{x} = \mathbf{A}(\mathbf{A}^{n-1}\mathbf{x}) \sim \lambda^n\mathbf{x}$ enables determination of the largest eigenvalue λ of the matrix \mathbf{A} .

If we are interested in several eigenvalues we can reduce the system (19) exactly in the same way as model reduction of large linear dynamic systems is performed. We define a projection of the high dimensional space to a lower dimensional one for which we intend to build a model which preserves principal dynamics properties:

$$\boldsymbol{\Theta}^T \mathbf{B} \boldsymbol{\Theta} \dot{\mathbf{x}}_r = \boldsymbol{\Theta}^T \mathbf{A} \boldsymbol{\Theta} \mathbf{x}_r \quad (21)$$

where $\mathbf{x} = \boldsymbol{\Theta} \mathbf{x}_r$ and r denotes the reduced system having a dimension m which is much smaller than the original one (19). For the projection, we use the Krylov subspace, spanned by m vectors and defined as:

$$\mathbf{K}_m = [\mathbf{x}, \mathbf{A}\mathbf{x}, \mathbf{A}^2\mathbf{x}, \dots \mathbf{A}^{m-1}\mathbf{x}] \quad (22)$$

To assure that the vectors constituting the Krylov subspace are linearly independent, Gram–Schmidt orthogonalization is usually used. Instead of a single vector in the power method, we compute now several vectors simultaneously. The vectors of Krylov subspace converge now to n dominating eigenvectors of \mathbf{A} . The stabilized version of the Krylov subspace algorithm is Arnoldi method, the most often used eigensolver procedure for the global flow stability.

The power method converges to the largest eigenvalue of \mathbf{A} while we are interested in the smallest one, more precisely in the rightmost having the smallest real part of the complex eigenvalue. If we substitute \mathbf{A} with \mathbf{A}^{-1} the power method is now the inverse iteration method and gives us the desired eigensolution. In practice we do not invert matrix \mathbf{A} but use the LU decomposition. For subspace iteration the procedure is similar, but now we compute m eigenvalues and eigenvectors simultaneously.

4.2 Subspace iteration method

Technically, the subspace iteration is a natural extension of the power method to m eigensolutions instead of one. We can iterate in direct or inverse mode finding the largest or the smallest eigenvalues.

Physically, the concept of the method is to reduce the system for which the eigenvalues have to be calculated to another one, with less degrees of freedom, for which eigensolution can be found much easier.

In subspace iteration, the first step is to assign initial values to the elements of m linearly independent vectors. In practice we use the orthogonal vectors obtained by setting unit value to a zero vector. In this way the orthogonality condition is easily fulfilled:

$$\mathbf{R}^{(0)} = \left[\mathbf{R}_1^{(0)}, \mathbf{R}_2^{(0)}, \mathbf{R}_3^{(0)}, \dots, \mathbf{R}_m^{(0)} \right]. \quad (23)$$

It should be noted that the procedure described above is — from CFD point of view — equivalent to forcing of the system. The base Ritz matrix is most often calculated as:

$$\mathbf{A} \Theta^{(n)} = \mathbf{R}^{(n-1)} \quad (24)$$

where n is a number of the iteration. With a given initial set of $\mathbf{R}^{(0)}$, the set of $\Theta^{(0)}$ vectors is found. The LU-decomposition of the \mathbf{A} matrix can be done only once and several back-substitutions involving \mathbf{R} vectors are quite effective, but requirements of storage for the decomposed matrix is rising dramatically with the number of degrees of freedom. In this work, the penalty method with the Finite Element Method and effective Quasi-Minimal-Residual Lanczos solver was adopted. We re-use the incomplete LU (ILU) decomposed matrix in each step. ILU decomposition is a compromise between the efficiency of back-substitution and memory limitations. To increase the numerical stability, the $\Theta^{(i)}$ vectors are normalized after each step. The matrices for the reduced problem are calculated according to:

$$\begin{aligned} \hat{\mathbf{A}}^{(n)} &= \Theta^{(n)^T} \mathbf{A} \Theta^{(n)} = \Theta^{(n)^T} \mathbf{R}^{(n-1)} \\ \hat{\mathbf{B}}^{(n)} &= \Theta^{(n)^T} \mathbf{B} \Theta^{(n)}. \end{aligned} \quad (25)$$

The matrix $\Theta^{(n)}$ multiplication with matrices \mathbf{A} , \mathbf{B} and the right-hand side reduces the eigenvalue problem to a smaller one. Matrices $\hat{\mathbf{A}}^{(n)}$ and $\hat{\mathbf{B}}^{(n)}$ have the assumed range of m . The value of m has to be a compromise between the computational resources as the eigenvalues for generalized eigenvalue problem for the $m \times m$ matrices has to be solved and the accuracy of the adequate representation of the physical problem.

The reduced generalized eigenvalue problem can be written as:

$$\left(\hat{\mathbf{A}}^{(n)} - \hat{\Omega}^{(n)} \hat{\mathbf{B}}^{(n)} \right) \hat{\varphi}^{(n)} = 0. \quad (26)$$

Here, $\hat{\Omega}$ is a diagonal matrix containing the eigenvalues of the reduced problem. This eigenvalue problem can be easily solved using any existing library algorithm. The eigenvectors for n -th iteration can be recalculated from the equation:

$$\varphi^{(n)} = \Theta^{(n)^T} \hat{\varphi}^{(n)}. \quad (27)$$

If the convergence is not obtained, the new set of vectors $\mathbf{R}^{(n)}$ is calculated from

$$\mathbf{R}^{(n)} = \mathbf{B} \varphi^{(n)} \quad (28)$$

and the iteration has to be repeated.

4.3 Preconditioning

In the subspace iteration process, the subspace $\text{span} \left[\Theta_1^{(k)}, \Theta_2^{(k)}, \dots, \Theta_m^{(k)} \right]$ tends to the subspace spanned by the eigenvectors corresponding to the eigenvalues having the smallest modulus. This is the so-called dominant subspace of the problem (19). The computed eigenpairs $(\lambda_i^k, \mathbf{x}_i^k)$, $i = 1, \dots, m$ approximate the dominant eigensolution of the problem (19). The larger the difference (in sense of modulus) between the computed eigenvalues, the better is the convergence of the process. Because of this, we calculate more (m) to increase the convergence, even if we need only one eigenvalue. The convergence ratio is different for different eigenvalues To speed up the iteration we have to transform the rightmost eigenvalues into the dominant ones. For symmetrical eigenvalue problem already the real shift α is very effective if we know that α approximates the eigenvalue μ :

$$(\mathbf{A} - \alpha \mathbf{B}) \mathbf{x} - \mu \mathbf{B} \mathbf{x} = 0. \quad (29)$$

In the case of the unsymmetrical eigenvalue problem, the eigenvalues are complex. This forces us to use a complex shift. However, a complex shift leads to complex matrices and thus increases significantly the computational costs. In order to avoid this complication, the inverse Cayley transformation

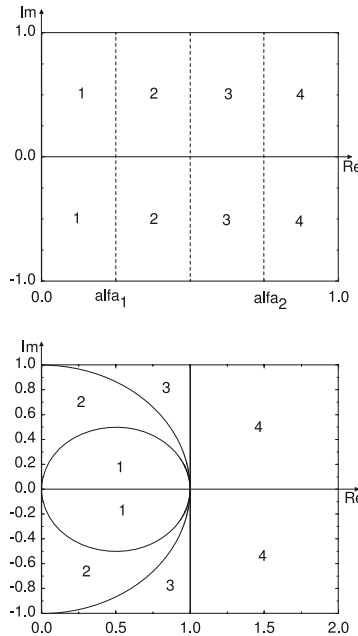


Figure 2. Spectrum mapping before (top) and after (bottom) the inverse Cayley transformation

with the real shift can be applied. Fig. 2 explains the transformation. The transformation of the problem (19) with the Cayley method results in:

$$((1 - \alpha_3)\mathbf{A} - (\alpha_1 - \alpha_2\alpha_3)\mathbf{B})\mathbf{x} - \mu(\mathbf{A} - \alpha_2\mathbf{B})\mathbf{x} = 0. \quad (30)$$

The eigenvalues of the base problem (19) can be recalculated from the eigenvalues of (30) via the following formula:

$$\lambda = (\alpha_2(\mu + \alpha_3) - \alpha_1)/(\mu + \alpha_3 - 1). \quad (31)$$

The parameters $\alpha_1, \alpha_2, \alpha_3$ are real and enable us to deal only with the real system of equations. The uninteresting eigenvalues can be removed by manipulation of the subspace dimension and appropriate choice of shift parameters. The convergence rate can be significantly increased with the α_3 shift (α_3 has the same meaning as α in (29)). The rule is to set α_3 so that the modulus of the leftmost eigenvalue is smaller than all remaining eigenvalue moduli.

4.4 Eigensolution via system identification

The procedure based on snapshots starts with formulation of Hankel matrix (32), also called trajectory matrix:

$$\begin{bmatrix} u_0 & u_1 & \cdots & u_n \\ u_1 & u_2 & \cdots & u_{n+1} \\ \vdots & \vdots & \ddots & \vdots \\ u_n & u_{n+1} & \cdots & u_{2n-1} \end{bmatrix} = \begin{bmatrix} \tilde{u}_{11} & \tilde{u}_{12} & \cdots & \tilde{u}_{1n} \\ \tilde{u}_{21} & \tilde{u}_{22} & \cdots & \tilde{u}_{2n} \\ \vdots & \vdots & \ddots & \vdots \\ \tilde{u}_{n1} & \tilde{u}_{n2} & \cdots & \tilde{u}_{nn} \end{bmatrix} \begin{bmatrix} e^{\lambda_1 t_1} & e^{\lambda_1 t_2} & \cdots & e^{\lambda_1 t_n} \\ e^{\lambda_2 t_1} & e^{\lambda_2 t_2} & \cdots & e^{\lambda_2 t_n} \\ \vdots & \vdots & \ddots & \vdots \\ e^{\lambda_n t_1} & e^{\lambda_n t_2} & \cdots & e^{\lambda_n t_n} \end{bmatrix}. \quad (32)$$

It consists of values characterizing the flow, e.g. velocity, shifted by one position for subsequent time steps. The elements of Hankel matrix can be vectors consisting of values in a 'window' (block) over the flow.

The second matrix in (32) can be simplified assuming that $t_1 = 0$, having in mind that $t_n = t_1 + (n - 1)\Delta t$ and denoting $\Lambda_n = e^{\lambda_n n \Delta t}$:

$$\begin{bmatrix} 1 & \Lambda_1 & \cdots & \Lambda_1^{n-1} \\ 1 & \Lambda_2 & \cdots & \Lambda_2^{n-1} \\ \vdots & \vdots & \ddots & \vdots \\ 1 & \Lambda_n & \cdots & \Lambda_n^{n-1} \end{bmatrix}. \quad (33)$$

This is called Vandermonde matrix. Now we construct another Hankel matrix, starting from the snapshot at $t = t_1 + \Delta t$. If we write the equation (32) in the form:

$$\mathbf{u} = \tilde{\mathbf{u}} e^{\lambda t}, \quad (34)$$

the new equation will have the form:

$$\mathbf{u}_{t+1} = \tilde{\mathbf{u}} \Lambda e^{\lambda t}. \quad (35)$$

The shift to the left is equivalent to adding Δt to the exponents in (32), or, equivalently, the multiplication of the Vandermonde matrix with the diagonal matrix:

$$\begin{bmatrix} \Lambda_1 & 0 & \cdots & 0 \\ 0 & \Lambda_2 & \cdots & 0 \\ \vdots & \vdots & \ddots & \vdots \\ 0 & 0 & \cdots & \Lambda_n \end{bmatrix}. \quad (36)$$

With equations (34) and (35), the eigenvalue problem can be re-stated:

$$\mathbf{A}\tilde{\mathbf{u}} = \tilde{\mathbf{u}}\Lambda \quad \text{with} \quad \mathbf{A} = \mathbf{u}_{t+1}\mathbf{u}^{-1}. \quad (37)$$

The \mathbf{A} matrix can be also formulated in a more complex way employing $\mathbf{u}_{t+1}, \mathbf{u}_{t+2}$ etc. Important factors are, however, not the formulation but the eigensolutions of the (37). The mentioned similarity to POD approach would suggest the Singular Value Decomposition (SVD) method. The algorithm of SVD, which consists mainly of the eigensolver, could be potentially used also in this case. The \mathbf{A} matrix is now real but non-Hermitian. Hence, a complex procedure has to be applied and complex eigenvalues and eigenvectors are the result, as in case of eigenproblem resulting from linearized Navier–Stokes equations (§ 4.1). In the form (37) the matrix is large but we can apply reduction of the large-dimensional space similarly to methods applied in § 4.1. We can also formulate the trajectory matrix for the part of the domain- ‘window’ only. There are also more serious numerical challenges. \mathbf{A} matrix is a product of weighting $\mathbf{u}_{t+1}\mathbf{u}^{-1}$ and forms a companion matrix, with only one non-zero column and unit values below main diagonal:

$$C(p) = \begin{bmatrix} 0 & 0 & \dots & 0 & -c_0 \\ 1 & 0 & \dots & 0 & -c_1 \\ 0 & 1 & \dots & 0 & -c_2 \\ \vdots & \vdots & \vdots & \vdots & \vdots \\ 0 & 0 & \dots & 1 & -c_{n-1} \end{bmatrix}. \quad (38)$$

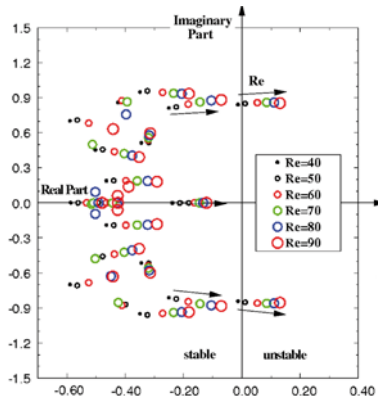
Performing the SVD on the product may introduce catastrophic round-off errors. In case of wide range of singular values of both matrices, the small singular values of the product can be either not computed accurately or not found at all. To compute the SVD of (37) $\mathbf{AB}^{-1} = \mathbf{U}\Sigma\mathbf{V}^*$, two decompositions of \mathbf{A} and \mathbf{B} are performed: $\mathbf{A} = \mathbf{U}\Sigma_A\mathbf{X}$ and $\mathbf{B} = \mathbf{V}\Sigma_B\mathbf{X}$. The generalized singular values of \mathbf{A} and \mathbf{B} are computed with diagonal matrices $\Sigma = \Sigma_A\Sigma_B^{-1}$. The keywords for solution of the problem (37) is PSVD (for Product SVD), QSVD (for Quotient SVD). The details of the algorithms are provided in numerous papers of G.H. Golub.

5 Stability results for the cylinder wake

5.1 Steady flow global stability

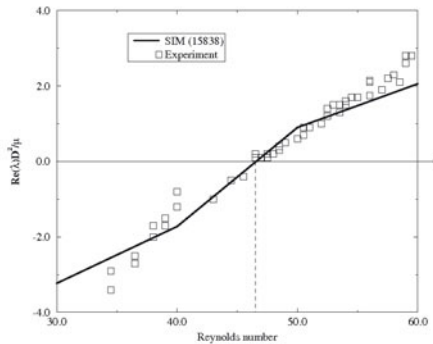
A solution of the eigenvalue problem (19) consists of the leading eigenvalues depicted in Fig. 3 and eigenvectors shown in Fig. 7. The eigenvalues are mostly complex with the real part being the growth rate and the imaginary part being the angular frequency, i.e. $2\pi \times St$ (St : Strouhal number).

Figure 3. The eigenvalue spectrum for a circular cylinder flow and its change with the increasing Reynolds number



Complex eigenvalues are characteristic for oscillatory flow. Non-oscillatory modes, with the eigenvalues laying on the imaginary axis are characterized by vanishing frequency. The dominant non-oscillatory flow is typically related to base flow changes, and thus to the shift mode explained later. With increasing Reynolds number, the flow becomes unstable, i.e. the leading eigenvalue moves from the left into the right-half plane of Fig. 3. For wake behind a circular cylinder, the critical Reynolds number is about $Re_c = 47$. At larger (smaller) Reynolds numbers any disturbance present in the flow is amplified (decaying).

Figure 4. Comparison of the disturbance growth-rate obtained in computation (SIM) and experiment (Schumm, 1991)



The critical Reynolds number determined by the global stability analy-

Figure 5. Strouhal number of circular cylinder flow obtained with the stability analysis of the steady flow and of the averaged solution. In addition, experimental values for periodic vortex shedding are shown.

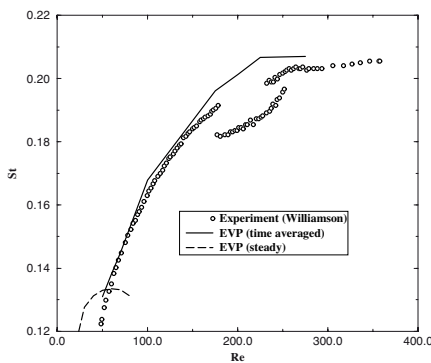
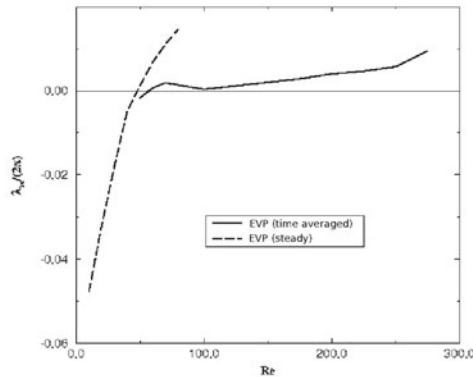


Figure 6. Comparison of the growth-rate based on the steady solution and averaged periodic one.



sis compare (Tab. 1) is in very good agreement with the experiment. Also the growth rate, Fig. 4, agrees with the experimental values by Schumm (Schumm, 1991) in the neighborhood of the critical Reynolds number. The values of the Strouhal number and growth rate deviate from the experiment as the Reynolds number increases above the critical value as shown in Figs. 5 and 6. The Strouhal number at larger Reynolds numbers is unphysically decreasing, while the growth rate is monotonically increasing, even for Reynolds number higher than the critical one. This feature is the consequence of linearization of our flow model.

The eigenanalysis of the flow is targeting the determination of the physical modes — as opposed to numerical ones. The leading complex eigenvector

Table 1. Critical values for circular cylinder flow

Critical value	Re_c	St_c
Jackson (Jackson, 1987)	45.4	0.1363
Zebib (Zebib, 1987)	39 – 43	0.11 – 0.13
Strykowski (Strykowski and Sreenivasan, 1990)	46.0	-
Schumm (Schumm, 1991)	46.6	
global stability analysis	47.00	0.1320

relates to von Kármán vortex shedding for the flow around circular cylinder and is shown in Fig. 7 at various Reynolds numbers. The eigenvector patterns of Fig. 7 are similar for a large class of wake flows. The modes can be determined even for stable flows at small Reynolds numbers. At larger Reynolds number, the maximum intensity of disturbance energy is moving toward the cylinder. The disturbance structures are getting smaller as the wavenumber increases with the flow Reynolds number. Fig. 8 depicts the result of the computation for much larger computational domain ($x = 45D$) and $Re = 100$. It shows the streamlines in the domain, with maximum intensity of the fluctuation behind the cylinder and decaying in the direction of the outflow. Fig. 8 confirms that computations depicted in Fig. 7 are not significantly effected by the far-field boundary conditions at $x = 15$.

5.2 Time-averaged flow stability

We observe that ROM with the stability eigenmodes can be accurate at the Reynolds numbers close to the critical one. See also the results presented in § 5. The results presented in § 7.4 for the airfoil corroborate that statement. The stability analysis of the mean flow is an interesting alternative to the one of the steady solution. One can expect that a linearization of the Navier-Stokes equation at the center of the flow attractor may, in some sense, be more accurate than at the steady solution, which is further away. The base flow has frequently been observed to be marginally stable corroborating a conjecture by Malkus (Malkus, 1956). Under mean-field assumptions, marginal stability of time-averaged (mean) flow was proven by Noack et al. (Noack et al., 2003). The plots in Fig. 5 and 6 showing that indeed the time-averaged flow has physically correct, nearly zero growth rate (is marginally stable). Moreover, the stability-inferred frequency approximates the true Strouhal number for the whole laminar Reynolds number

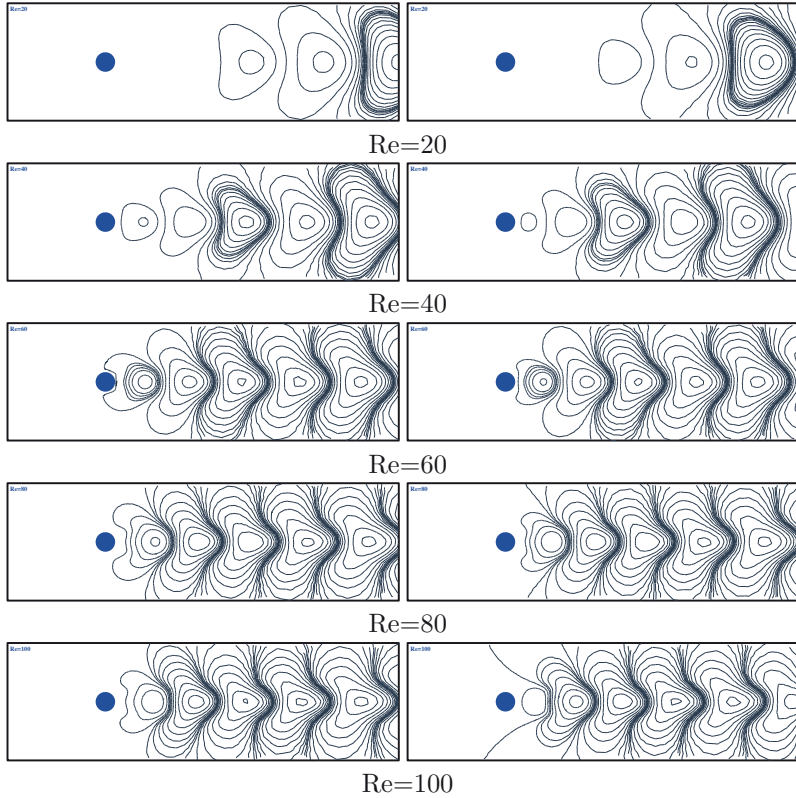


Figure 7. Leading complex eigenvector for the flow around a circular cylinder at $Re = 20, 40, 60, 80$ and 100 from top to bottom, respectively. The real (imaginary) part is shown in the left (right) column.

range. This was first presented in 1999 in (Morzyński et al., 1999a). Also the eigenmodes of time-averaged flow are more 'POD-like' (Fig. 9), suggesting that these modes can be a better alternative than the classical, steady flow based ones at supercritical Reynolds numbers. The theory and results are not presented here, the results in (Morzyński et al., 2006a) show the implementation of time-averaged eigenmodes in construction of the *a priori* flow model.

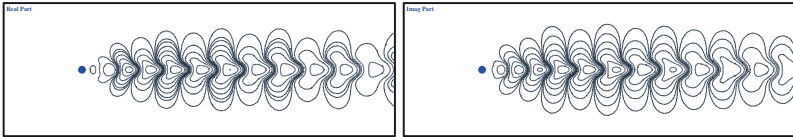


Figure 8. Same as Fig. 7 but at $Re = 100$ in larger computational domain.

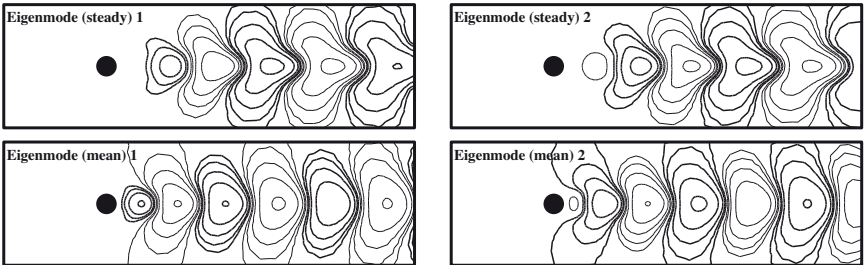


Figure 9. Flow around a circular cylinder at $Re = 100$. Streamlines of real (left) and imaginary (right) parts of the leading pair of eigenmodes for linearization around steady solution (top) and time-averaged one (bottom).

6 Wake control

6.1 General philosophy of flow control for stabilization

In the following, we show how flow control for stabilization can be guided by CFD and the global stability analysis presented earlier.

Any spatial discretization (FDM, FEM, FVM) of the linearized disturbance equation (2) yields a finite-dimensional evolution equation of the form

$$\frac{d}{dt} \mathbf{a} = \mathbf{A} \mathbf{a}, \quad (39)$$

where \mathbf{a} is a vector of state variables. State variables are dependent on the formulation, for instance, the velocity components at the grid nodes, stream function, stream function and vorticity.

The matrix \mathbf{A} has a natural spectrum of eigenvalues similar to depicted in Fig. 10. A conjugate pair of eigenvalues laying in the right-hand side of the imaginary axes of the complex plane represent the flow instability. Flow control techniques are targeting suppression of the instability.¹

¹Enhancement of instability for instance to increase mixing is also possible but not in the scope of this chapter.

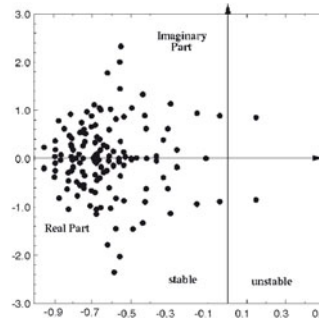


Figure 10. Stability spectrum of steady flow around a circular cylinder at $Re = 100$

Suppression of instability implies an actuator leading to a *small* change of matrix \mathbf{A} which moves the unstable eigenvalues to the left-hand (stable) half of the complex plane. A general control approach can be expressed by adding to the Navier-Stokes equations a volume force term. This leads to a finite-dimensional evolution equation of the form

$$\frac{d}{dt} \mathbf{a} = \mathbf{A} \mathbf{a} + \mathbf{B} \mathbf{b}. \quad (40)$$

Here \mathbf{b} represents a vector for the volume force amplitudes and the matrix \mathbf{B} is the gain from the corresponding local force fields. The volume force \mathbf{Bb} can substantially change the solution of the Navier-Stokes equations. It can mimic active or passive control devices. An active proportional controller $\mathbf{b} = -\mathbf{K} \mathbf{a}$, for instance, gives rise to the forced dynamics

$$\frac{d}{dt} \mathbf{a} = \mathbf{A}^c \mathbf{a}, \quad (41)$$

with the modified linear term $\mathbf{A}^c = \mathbf{A} - \mathbf{B} \mathbf{K}$. Here, the design parameter \mathbf{K} may be used to stabilize or destabilize the system. With this assumption, (41) has the same form as (39) and the control goal becomes once more the desired manipulation of the eigenvalue spectrum of a matrix.

Besides volume forces, also models with wall-mounted actuators can be written in the form (40) (Rediniotis et al., 2002).

In the penalty method of CFD, obstacles are modeled by time-dependent volume forces which lead to vanishing velocity inside the obstacle. This corresponds to a local actuation term \mathbf{Bb} and a strongly stabilizing controller $\mathbf{b} = -\mathbf{Ka}$. Thus, the actuation term of (41) may model passive control with control wires, splitter plates, riblets or other devices. Here, \mathbf{A}^c describes the effect of the device and optimization of a passive device may be guided by global stability analysis. An example is provided in § 6.2.

6.2 Wake stabilization using model-based passive control

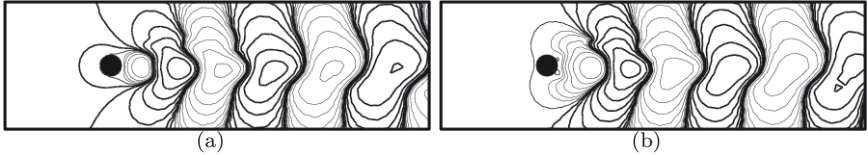


Figure 11. Real (a) and imaginary (b) part of the most unstable eigenmode of the passively manipulated cylinder wake at $Re = 100$. The control cylinder ($d/D = 0.1$) is placed at $x = 1.2, y = 1.2$. The cylinder is indicated by the solid circle and the flow field is visualized with streamlines. Thick (thin) lines correspond to positive (negative) stream-function values.

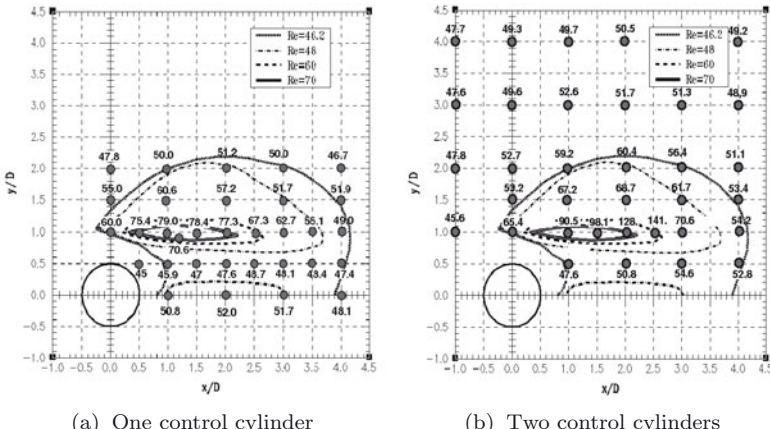


Figure 12. Optimization of passive control with one and two Strykowsky wires employing global flow stability analysis. The dots and numbers in the field denote the control cylinder position and respective critical Reynolds numbers. The second control cylinder in subfigure (b) is placed symmetrically with respect to the x -axis.

Passive suppression of vortex shedding may be achieved with splitter plates (Unal and Rockwell, 1987; Mittal, 2003) or small control cylinders

(Strykowski and Sreenivasan, 1990). In this case, the \mathbf{A}^c matrix of (41) is computed in terms of parameters of passive actuators. The no-slip conditions on the surface of a control cylinder or a splitter plate can be imposed with a penalization of the surface velocities with time- and space-dependent volume forces. Thus, we can study how the geometry of passive actuators is related to the flow stability varying the parameters of the actuator (like position or size). In this way, the linear model can be employed to optimize passive control. This approach is demonstrated for the Strykowski control cylinder (Strykowski and Sreenivasan, 1990). The critical Reynolds number is determined at different locations of the control cylinder with global nonparallel flow stability analysis (Fig. 11). The eigenanalysis (see Fig. 12) yields the optimal position for one and two symmetrically placed control cylinders. Isolines in that figure denote the critical Reynolds number values found experimentally in (Strykowski and Sreenivasan, 1990), small circles denote analyzed positions of the control cylinder, and the numbers represent critical values obtained by global stability analysis.

The critical Reynolds number is largest for control wire positions in a narrow shear-layer region behind the cylinder. Global stability analysis predicts also that any non-symmetrical configuration is less effective for stabilization than the optimal symmetrical one.

The passive control optimization with Strykowski wires depicted in Fig. 12 shows good agreement with experiment. Below the position-dependent critical Reynolds number, the steady solution is at least locally stable. The agreement of the largest achievable critical Reynolds number in experiment and in the current study suggests the domain of attraction of the steady solution contains at least the periodic shedding state and may even contain all flows. We can also extend the investigation and solve the *sensitivity* problem for the flow to determine the regions most sensitive to passive actuation. Technically, one has to solve the adjoint eigenvalue problem (Giannetti and Luchini, 2007) with similar techniques as used for the regular one (19).

7 Weakly non-linear models

7.1 Mean-field correction

We can use real and imaginary part of the eigenvector to build a Galerkin model of the flow. For the flow around a circular cylinder, the initial growth rate $\sigma = 0.1439$ and Strouhal number $St = 0.1346$ are in good agreement with the simulation. Apart from exponential divergence of the Galerkin solution, the stability modes can resolve only about 41% of the turbulent kinetic energy of the periodic vortex shedding. The reason is the changing

structure of vortex shedding at the limit cycle. The maximum fluctuation level moves from far downstream, as predicted by the stability modes, to close to the cylinder, as resolved by the first POD modes.

The alternative, a ROM obtained with the POD Galerkin method (see chapter of B.R. Noack et al.) is highly efficient and resolves nearly perfectly the kinematics of the flow. At the same time, it is highly fragile and sensitive to changes in the parameters or operating conditions. For the circular cylinder wake, the first two POD modes capture about 95% of the fluctuation energy. Yet, a Galerkin model (GM) based on these two modes alone is unstable for physical reasons. The inclusion of eight POD modes, capturing the first four harmonics of the attractor, suffices to achieve nearly perfect resolution and weakly stable Galerkin model. Yet, the correct prediction of the system dynamics with this model is limited to a small neighborhood of the attractor and to relatively small Reynolds number changes. In particular, the oscillatory dynamics associated with linear instability from the steady solution is not well resolved. Further increase in number of POD modes does not cure the problem and violates the targeted low dimensionality of the model. Hence, we have to find other ways of stabilization.

Stabilization of the GM can be obtained with the shift mode (Noack et al., 2003) as suggested by the mean-field theory. The shift mode is a normalized difference $\mathbf{u}_0 - \mathbf{u}_s$ where \mathbf{u}_0 is mean flow solution and \mathbf{u}_s is (unstable) steady solution. Figure 13 illustrates the concept. The vertical axis is referring to the base flow state. The radius of the paraboloid is the amplitude of the fluctuation for natural transient between instability and the limit cycle at the top of the paraboloid. The bottom fixed point on the paraboloid represents the unstable steady flow solution shown at the left part of the figure. Fluctuations at this point are well approximated by the stability eigenmodes. One of the modes is shown at the right part of the figure. The center of the limit cycle corresponds the the mean flow (left) with associated POD modes (right). The difference between the steady flow solution and the mean flow of the limit cycle is characterized by the length of the recirculation bubble. Evidently, this base flow change cannot be resolved by the oscillatory eigenmodes obtained with global stability analysis.

For robustness, we have to add to the Galerkin system the missing direction, connecting both states of the flow. It is the shift mode depicted in the middle of the figure. The inclusion of the shift mode reduces significantly the model sensitivity to parameter variations.

Up to now, we only defined the kinematic shift mode and pointed out its importance for flow modeling. In (Tadmor et al., 2010), the dynamic role of mean-field variations and transient energy flow analysis is presented. It is proven that the shift mode is indispensable to represent that contri-

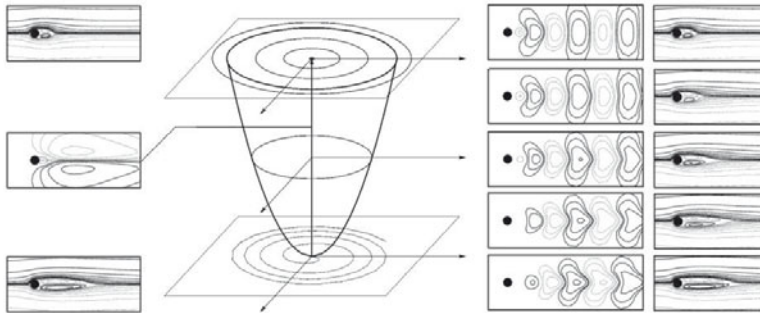


Figure 13. Principal sketch of the transient wake dynamics. The left side displays the mean flow (top), shift-mode (middle) and steady solution (bottom). The right side illustrates interpolated modes and vortex streets on the mean-field paraboloid. The flow fields are depicted as the streamline plots.

bution. The shift mode can be computed with many methods as presented in (Tadmor et al., 2010). We show only the shift mode derived from the Reynolds-Averaged Navier-Stokes (RANS) equation:

$$\bar{u}_j \bar{u}_{i,j} + \bar{p}_{,i} - \frac{1}{Re} \bar{u}_{i,jj} + (\bar{u}_j \bar{u}_i)_{,j} = 0. \quad (42)$$

The Reynolds stress term is well approximated by:

$$(\bar{u}_j \bar{u}_i)_{,j} = \mathcal{K} \nabla \cdot (\tilde{\mathbf{u}}_1 \otimes \tilde{\mathbf{u}}_1 + \tilde{\mathbf{u}}_2 \otimes \tilde{\mathbf{u}}_2), \quad (43)$$

where $\mathcal{K}(t)$ is the mean fluctuation energy averaged over one period T , and $\tilde{\mathbf{u}}_{1,2}$ is the dominant POD mode pair.

Figure 14 shows the kinematic and an *a priori* shift mode computed with (42), in virtually good agreement. It may be worthwhile to note that higher-order modes can be derived from the non-linear Navier-Stokes term and utilizing harmonic expansions (Dušek et al., 1994), considering each POD mode pair as one harmonic. Hence, refined *a priori* models are in reach, too.

The dynamics of the least-order (3-dimensional) Galerkin model enriched with a shift mode is compared with a DNS in Fig. 15. The shift mode is the first step and the key enabler for construction of transient, control-oriented models. This subject will be elaborated in the chapter by G. Tadmor et al. The reader should refer for more details there.

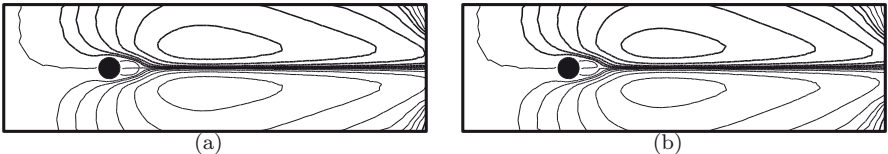
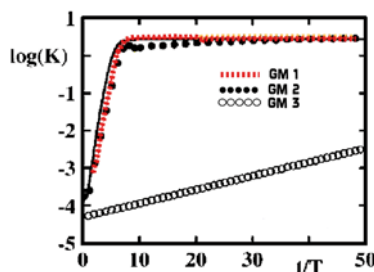


Figure 14. Empirical (left) and a priori (right) shift mode. The empirical mode is computed from the mean flow and steady solution as described in (Noack et al., 2003). The a priori shift mode is derived from the Reynolds equation using the POD representation of the Reynolds stress tensor.

7.2 Hybrid model employing stability modes

Further improvement of the model dynamics can be obtained with a hybrid model employing POD *and* stability modes (Morzyński et al., 1999b). In this model, POD resolves the attractor and stability eigenmodes resolve the linearized dynamics. Thus, dynamic transient and post-transient flow behavior is accurately predicted. The concept of hybrid model reduces significantly the number of necessary degrees of freedom of the system in comparison to the purely POD-based one. The hybrid approach is demonstrated for benchmark problem of the flow around circular cylinder in (Noack et al., 2003). The transients of the hybrid models are compared with DNS in Fig. 15. The hybrid model combines the advantages of both reduced models. It converges to the limit cycle preserving initially the growth rate predicted by global stability analysis.

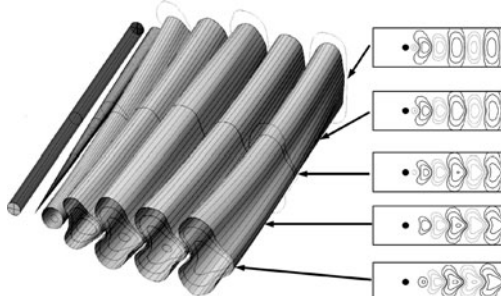
Figure 15. Transients of various Galerkin models. The logarithm of the fluctuation energy over time nondimensionalized with the period T . Galerkin model: GM 1 - with shift mode and 2 interpolated modes, GM 2 - as GM 3 with shift mode and leading stability mode added, GM 3 - with 8 POD modes.



7.3 Continuous mode interpolation

Additive interpolation procedures, based on the superposition of two modes ensembles like the one described in section § 7.2 may resolve different operating conditions. For model-based control the modes need to be additionally 'flexible' and smoothly change at different operating conditions (Luchtenburg et al., 2006)(Siegel et al., 2006). Let us consider the interpolation problem of periodic cylinder wakes at two operating conditions. The resulting vortex streets look similar but may have slightly different wavenumbers, frequencies, and fluctuation envelopes. The states may, for instance, be near the onset of vortex shedding and the asymptotic state (Noack et al., 2003)(Siegel et al., 2006). Other pairs of states are the natural and forced wake (Luchtenburg et al., 2006), or the natural flow at two different Reynolds number (Deane et al., 1991). We are looking for a method which smoothly interpolates the modes of different states in the way shown schematically in Fig. 16. The straightforward idea of 'morphing' used in image processing could be an inspiration but we shall use here a more advanced method and interpolate the discrete operators for different operating conditions, to generate the modes for a continuum of intermediate states.

Figure 16. Principal sketch of continuous mode interpolation. Left: Transition between stability eigenmodes and POD modes. Right: streamlines of the intermediate states



In the following, we outline a continuous interpolation technique which will yield modes with all intermediate wavenumbers and frequencies.

For example, the most amplified stability eigenmodes of the linearized Navier-Stokes equation at two base flows can be interpolated. We assume one dominant oscillatory eigenmode, like for the flow around a bluff cylinder (Morzyński et al., 1999b). Then, the associated two sets of modes constitute complex eigenmodes $\mathbf{f}^\kappa = \mathbf{u}_1^\kappa + i\mathbf{u}_2^\kappa$ of the eigenvalue problem

$$\mathbf{A}^\kappa \mathbf{f}^\kappa = \lambda^\kappa \mathbf{f}^\kappa, \quad \kappa = 0, 1, \quad (44)$$

where λ^κ are the associated eigenvalues. Here, \mathbf{A}^κ is the linearized FEM

discretization of the Navier-Stokes operator forming the stability matrix. The stability matrix may be linearly interpolated for $\kappa \in [0, 1]$,

$$\mathbf{A}^\kappa = \mathbf{A}^0 + \kappa (\mathbf{A}^1 - \mathbf{A}^0), \quad (45)$$

thus giving rise the intermediate eigenproblems of the form (44) and intermediate complex eigenmodes $\mathbf{f}^\kappa = \mathbf{u}_1^\kappa + i\mathbf{u}_2^\kappa$. A smooth connection between both eigenmodes is not guaranteed per se but can be expected for the most unstable stability modes of shear flows.

The example presented here represents the simplest case of continuous mode interpolation. More advanced problems of interpolation of stability and POD bases, characterized by matrices of different size, mode extrapolation to new operating conditions or building of *a priori* flow models with stability eigenmodes are described in (Morzyński et al., 2006a) and (Morzyński et al., 2006b).

7.4 Mean field correction and Galerkin Model for NACA-0012 flow

We aim at designing a flow model for feedback flow control. Low-dimensionality and simplicity is required for the online-capable feedback laws. Robustness of flow control models implies even stronger limitations on 'superfluous' degrees of freedom. A frequent observation is that observers and controllers derived from higher-fidelity models are less robust.

A low-dimensional representation of the natural flow should be the first test of such a model. We first construct a ROM using the Galerkin method, presented in the chapter of B.R. Noack et al. in this volume. As mode basis, we can use POD and stability eigenmodes. We apply the technique of continuous mode interpolation to connect both types of modes smoothly.

We continue our ROM flow consideration for the example of a flow around a NACA-0012 airfoil having the angle of attack of 30 degrees. This typical wake flow can be treated as representative for 'real life' one, for which we intend to build the Galerkin model. With standard procedure, described in § 4 we determine the base flow, Fig. 17, and eigenmodes of the steady and time-averaged solutions, Fig. 18.

Figure 17. Flow around NACA-0012 airfoil - streamlines of the steady solution.

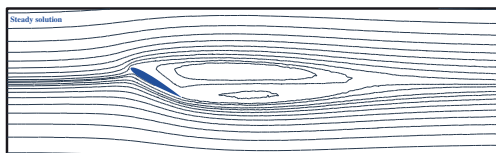
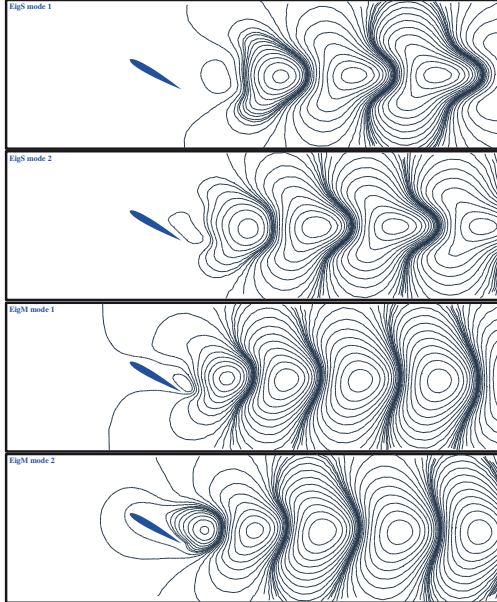


Figure 18. The most dominant eigenmodes pairs based on the steady solution (top two figures, $\lambda = -0.147 \pm 0.720i$) and time-averaged solution (bottom two figures, $\lambda = 0.018 \pm 0.915i$)



We also compute the first four POD modes with the snapshot POD method (Sirovich, 1987). (Fig. 19).

With the determined mode basis and POD Galerkin method, we construct the Galerkin model of the flow. The conclusions from this numerical experiment can be expected to representative for all Galerkin models of the wake flow. In Fig. 21, the shift-mode amplitude is shown as a function of fluctuation amplitude, both, for the Galerkin model and for the DNS. The deviation of the curves from the values for DNS is a measure of the model quality.

The first observation is that for all presented models, we have to employ the mean-field correction (shift mode) to avoid the structural instability and thus fragility of the ROM.

It can be seen in Fig. 21 that POD modes allow the reconstruction of Navier-Stokes attractor (limit cycle), but they are unable to reproduce the dynamical properties of transitional flow. For the flow states close to fixed point (steady solution, small values of shift-mode coefficient), the kinetic energy of the flow is overestimated — especially in POD-2 Galerkin model.

The models based on the two most unstable eigenmodes (Fig. 20, middle) reconstruct the flow states close to fixed-point (steady solution) and the

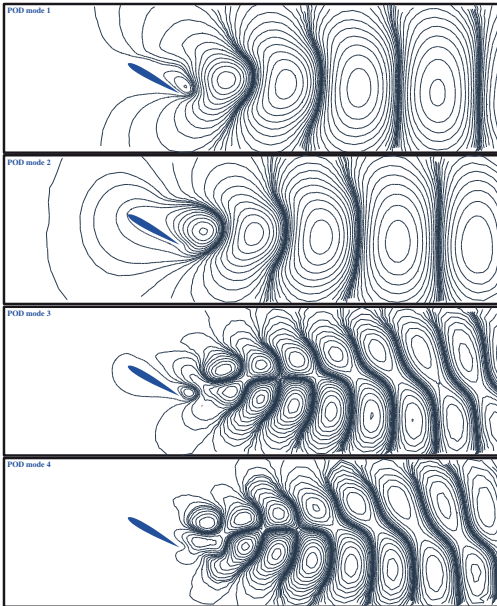


Figure 19. First 4 POD modes for the NACA-0012 airfoil flow

transition to limit cycle better than POD Galerkin models. On the other hand the limit-cycle disturbance kinetic energy and shift-mode coefficients of periodic flow are significantly underestimated with these mode bases.

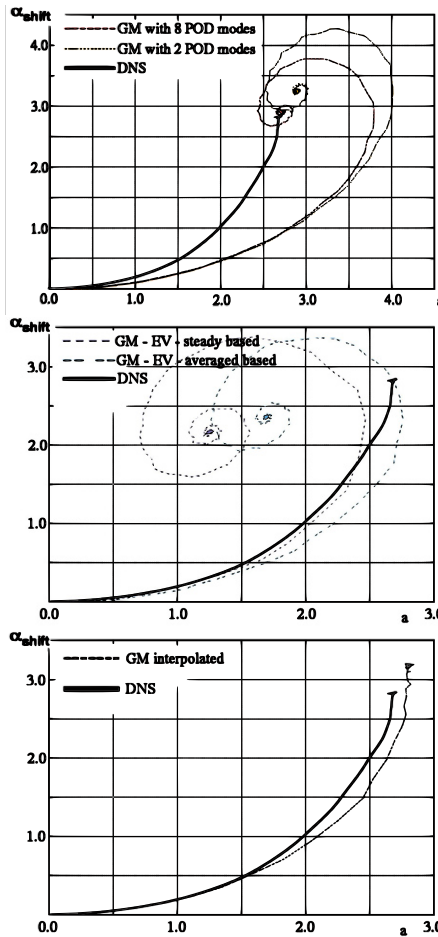
The last of the models presented here is the least-dimensional model of continuous interpolated mode pair using the technique described in section § 7.3.

The comparison shows that dynamical properties of simple ROMs can be unsatisfactory. At the same time, special techniques allows construction of least-dimensional model having very good dynamical properties. This study demonstrates that not only the appropriate expansion mode basis but also modeling skills are a necessary ingredient in ROM design.

8 Summary and perspectives - 3D flow stability analysis

We have presented the foundations of global flow stability analysis and its role in fluid dynamics. An interested reader should be able to adapt his own numerical code or any of the open source ones to compute the global stability eigensolutions and use the results for ROM modeling, possibly employing

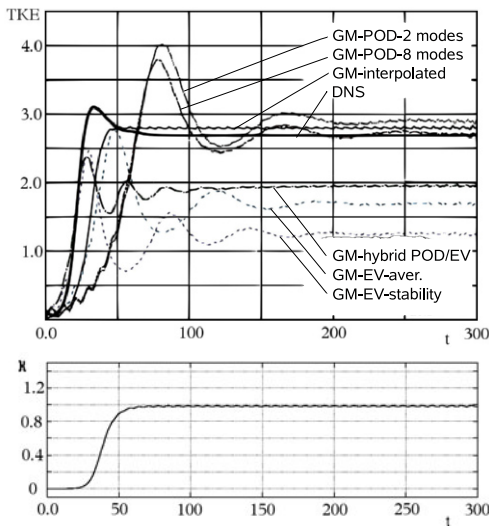
Figure 20. Shift-mode amplitude as a function of fluctuation amplitude for POD-based models (top), eigenmode-based models (middle), and interpolated model (bottom). The solid black line corresponds to the CFD benchmark.



further detailed descriptions.

The global stability analysis begun in late 80's of the last century. Recent interest in feed-back control using ROM enhanced also investigations in this direction. Stability modes are characterized by a single frequency for each mode pair and may thus constitute a 'clean' piano with 'pure tones'. By construction, stability modes are the optimal mode basis for modeling the transients near the onset of instability. As alternative, Galerkin expansion piano may be build from POD modes of given solutions. By construction, POD resolves the energy of the fluctuation in optimal way but may mix

Figure 21. The variation of disturbance kinetic energy (TKE) for different Galerkin models and interpolation parameter κ as a function of time. The flow transitions from steady state to the limit cycle oscillation. The displayed Galerkin model can be inferred from the legend.



several frequencies in a single mode (Rowley et al., 2009). Combination of the POD mode basis with stability modes is shown to improve the ROM dynamics. In a more refined approach, the evolution of stability eigenmodes towards POD modes is parameterized by a continuous mode interpolation, thus removing unnecessary degrees of freedom in the modal expansion. In this case, the interpolation employs also a solution of the eigenvalue problem.

The computational aspects of the eigensolution computation has been explained in detail. The formulation of the problem was presented for 2D and 3D case. We interpreted the eigenvalue solution procedure from the point of view of CFD methods, speaking in terms of practical numerics. Particularly noteworthy is the similarity between state space reduction for solution of the eigenvalue problem and other methods employed in model reduction. The computational methods of global flow stability analysis have benefitted from recent developments in global flow stability from physical methods employed for ROMs, from signal processing, from system identification and from CFD.

The computational challenges of 2D global flow stability are now trivial in comparison with problems of early development of the method. At the same time, the 3D global flow stability is still a challenge, no matter what method is used for eigensolution. In Figs. 22 and 23 we show that also for 3D geometry it is possible to extract eigenmodes with the described method.

The solution of these computational problems are a key enabler for ROMs of 3D flows of practical importance. Other methods, as described in this chapter and in this book can be expected to serve as further catalyzers.

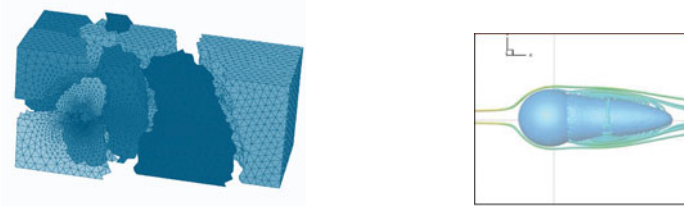


Figure 22. Left: Unstructured, 3D computational grid with partitioning for parallel computation; Right: Steady flow solution for the 3D flow around the sphere - zero velocity isosurface is shown for $Re = 300$.



Figure 23. Real parts of two higher eigenmodes for the 3D flow around the sphere at $Re = 300$. Isosurfaces indicate constant streamwise (V_x) velocity. The grayscale shows the positive and negative sign of the velocity.

Bibliography

- E. Åkervik, J. Høppffner, U. Ehrenstein, and D. S. Henningson. Optimal growth, model reduction and control in a separated boundary-layer flow using global eigenmodes. *J. Fluid Mechanics*, 579:305–314, 2007.
- D. Amsallem and C. Farhat. Interpolation method for adapting reduced-order models and application to aeroelasticity. *AIAA Journal*, 46(7):1803–1813, 2008.
- S. Bagheri, D. S. Henningson, J. Høppffner, and P. J. Schmid. Input-output analysis and control design applied to a linear model of spatially developing flows. *Applied Mechanics Reviews*, 62:020803, 2009.
- A. J. Baker. *Finite Element Solution Algorithm for Viscous Incompressible Fluid Dynamics*. John Wiley and Sons, New York, 1983.

- R. Becker, M. Garwon, C. Gutknecht, G. Bärwolff, and R. King. Regelung aerodynamischer Strömungen am Beispiel einer rückwärtsgewandten Stufe (transl.: Control of aerodynamics flows exemplified for the backward-facing step). *Automatisierungstechnik*, 50:79–86, 2002.
- M. Bergmann, L. Cordier, and J. P. Branger. Optimal rotary control of the cylinder wake using proper orthogonal decomposition reduced order model. *Phys. Fluids*, 17:097101–097121, 2005.
- T. J. Chung. *Computational Fluid Dynamics*. Cambridge University Press, Cambridge, U.K., 2002.
- A. E. Deane, I. G. Kevrekidis, G. E. Karniadakis, and S. A. Orszag. Low-dimensional models for complex geometry flows: Application to grooved channels and circular cylinders. *Phys. Fluids A*, 3(10):2337–2354, 1991.
- J. Dušek, P. Le Gal, and P. Fraunie. A numerical and theoretical study of the first Hopf bifurcation in a cylinder wake. *J. Fluid Mech.*, 264:59–80, 1994.
- F. Giannetti and P. Luchini. Structural sensitivity of the first instability of the cylinder wake. *J. Fluid Mechanics*, 581:167–197, 2007.
- C. P. Jackson. A finite-element study of the onset of vortex shedding in flow past variously shaped bodies. *J. Fluid Mech.*, 182:23–45, 1987.
- B. H. Jørgensen, J. N. Sørensen, and M. Brøns. Low-dimensional modeling of a driven cavity flow with two free parameters. *Theoret. Comput. Fluid Dynamics*, 16:299–317, 2003.
- A. I. Khibnik, S. Narayanan, C. A. Jacobson, and K. Lust. Analysis of low dimensional dynamics of flow separation. In *Continuation Methods in Fluid Dynamics. Notes on Numerical Fluid Mechanics*, vol. 74, pages 167–178. Vieweg, 2000. Proceedings of ERCOFTAC and Euromech Colloquium 383, Aussois, France, September 6–9, 1998.
- T. Lieu, C. Farhat, and M. Lesoinne. Reduced-order fluid/structure modeling of a complete aircraft configuration. *Computer Meth. Appl. Mech. Engr.*, 195(41-43):5730–5742, 2006.
- D. M. Luchtenburg, G. Tadmor, O. Lehmann, B. R. Noack, R. King, and M. Morzyński. Tuned POD Galerkin models for transient feedback regulation of the cylinder wake. In *44th AIAA Aerospace Sciences Meeting and Exhibit*, Reno, Nevada, USA, 2006. AIAA-Paper 2006-1407.
- X. Ma and G. E. Karniadakis. A low-dimensional model for simulating three-dimensional cylinder flow. *J. Fluid Mech.*, 458:181–190, 2002.
- W. V. R. Malkus. Outline of a theory of turbulent shear flow. *J. Fluid Mech.*, 1:521–539, 1956.
- S. Mittal. Effect of a “slip” splitter plate on vortex shedding from a cylinder. *Phys. Fluids*, 9:817–820, 2003.

- M. Morzyński, K. Afanasiev, M. Braza, and F. Thiele. Eigenmodes and empirical eigenmodes in flow stability and control. In *Proceedings IS-CFD'99, All Contributions*, 1999a. International Symposium Computational Fluid Dynamics, Bremen, 5-10 September 1999.
- M. Morzyński, K. Afanasiev, and F. Thiele. Solution of the eigenvalue problems resulting from global non-parallel flow stability analysis. *Comput. Meth. Appl. Mech. Engrg.*, 169:161–176, 1999b.
- M. Morzyński, W. Stankiewicz, B. R. Noack, R. King, F. Thiele, and G. Tadmor. Continuous mode interpolation for control-oriented models of fluid flow. In R. King, editor, *Active Flow Control*, pages 260–278. Springer-Verlag, 2006a.
- M. Morzyński, W. Stankiewicz, B. R. Noack, F. Thiele, and G. Tadmor. Generalized mean-field model with continuous mode interpolation for flow control. In *3rd AIAA Flow Control Conference*, San Francisco, Ca, USA, 2006b. AIAA-Paper 2006-3488.
- B. R. Noack, K. Afanasiev, M. Morzyński, G. Tadmor, and F. Thiele. A hierarchy of low-dimensional models for the transient and post-transient cylinder wake. *J. Fluid Mech.*, 497:335–363, 2003.
- O. K. Rediniotis, J. Ko, and A. J. Kurdila. Reduced order nonlinear Navier-Stokes models for synthetic jets. *J. Fluids Engrg.*, 124(2):433–443, 2002.
- C. Rowley, I. Mezić, S. Bagheri, P. Schlatter, and D. S. Henningson. Reduced-order models for flow control: balanced models and Koopman modes. Seventh IUTAM Symposium on Laminar-Turbulent Transition, 23-26 June 2009, Stockholm, Sweden, 2009.
- P. Schmid and J. Sesterhenn. Dynamic mode decomposition of numerical and experimental data. In *61st Annual Meeting of the Division of Fluid Dynamics of the American Physical Society*, 2008.
- M. Schumm. *Experimentelle Untersuchungen zum Problem der absoluten und konvektiven Instabilität in Nachlauf zweidimensionaler stumpfer Körper*. PhD thesis, HFI, TU-Berlin, 1991.
- S. Siegel, K. Cohen, J. Seigel, and T. McLaughlin. Proper orthogonal decomposition snapshot selection for state estimation of feedback controlled flows. In *AIAA Aerospace Sciences Meeting and Exhibit*, January 9–12, 2006, Reno/NV, 2006. Paper 2006-1400.
- L. Sirovich. Turbulence and the dynamics of coherent structures, Part I: Coherent structures. *Quart. Appl. Math.*, XLV:561–571, 1987.
- P. J. Strykowski and K. R. Sreenivasan. On the formation and suppression of vortex ‘shedding’ at low Reynolds numbers. *J. Fluid Mech.*, 218:71–107, 1990.
- G. Tadmor, O. Lehmann, B. R. Noack, and M. Morzyński. Mean field representation of the natural and actuated cylinder wake flow. *Phys. Fluids* 22 (3), 034102-1...22, 2010.

- V. Theofilis. Advances in global linear instability analysis of nonparallel and three-dimensional flows. *Progress in Aerospace Sciences*, 39(4):249–315, 2003.
- M. F. Unal and D. Rockwell. On the vortex formation from a cylinder; Part2. control by a splitter-plate interference. *J. Fluid Mech.*, 190:513–529, 1987.
- D. Wolter, M. Morzyński, H. Schütz, and F. Thiele. Numerische Untersuchungen zur Stabilität der Kreiszylinderumströmung. *Z. Angew. Math. Mech.*, 69:T601–T604, 1989.
- A. Zebib. Stability of viscous flow past a circular cylinder. *J. Engr. Math.*, 21:155–165, 1987.

Galerkin Method for Nonlinear Dynamics

Bernd R. Noack ^{*}, Michael Schlegel [†], Marek Morzynski [‡]
and Gilead Tadmor ⁺

^{*} Institut Pprime, CNRS – Université de Poitiers – ENSMA, UPR 3346,
Département Fluides, Thermique, Combustion, CEAT, 43, rue de l’Aérodrome,
F-86036 Poitiers cedex, France

[†] Berlin Institute of Technology MB1, Department of Fluid Dynamics and
Engineering Acoustics, Straße des 17. Juni 135, D-10623 Berlin, Germany

[‡] Technical University of Poznań, Institute of Combustion Engines and
Transportation, ul. Piotrowo 3, PL 60-965 Poznań, Poland

⁺ Northeastern University, Department of Electrical and Computer Engineering,
440 Dana Research Building, Boston, MA 02115, USA

Abstract A Galerkin method is presented for control-oriented reduced-order models (ROM). This method generalizes linear approaches elaborated by M. Morzyński et al. for the nonlinear Navier-Stokes equation. These ROM are used as plants for control design in the chapters by G. Tadmor et al., S. Siegel, and R. King in this volume. Focus is placed on empirical ROM which compress flow data in the proper orthogonal decomposition (POD). The chapter shall provide a complete description for construction of straight-forward ROM as well as the physical understanding and teste

1 Introduction

In the previous chapter by M. Morzyński et al., stability analysis was introduced as one foundation for control-oriented reduced-order models (ROM). These ROM constitute least-order descriptions optimized for linear flow dynamics. Here, the mathematical framework is extended to traditional Galerkin methods employing a larger class of expansion modes and resolving fully the nonlinear dynamics. The following chapters by G. Tadmor et al. and R. King in this volume will provide control studies based on the Galerkin method.

The current chapter is organized as follows: First (§2), the traditional Galerkin method is elaborated. This includes dynamic models based on the stability eigenmodes and the proper orthogonal decomposition (POD). In §3, a modal refinement of statistical fluid mechanics is outlined. This includes a novel closure for the first and second statistical moments based on

finite-time thermodynamics (Andresen, 1983). The resulting modal balance equations give important insights in the modal interactions and serve as design tool in model development. In §4, key enablers for control-oriented Galerkin models of turbulent flows are revisited. The conclusions (§5) summarize the previous chapters and outline challenges for future research.

2 Galerkin method as foundation

Focus of this section is a traditional *Galerkin method* for incompressible flow (Fletcher, 1984). This method shall approximately solve an initial boundary value problem which is formulated in §2.1. The postulates of the method are outlined in §2.2. The approximation ansatz is a finite *Galerkin expansion* in terms of global modes (§2.3). The derivation of the evolution equation for the mode amplitudes, the *Galerkin system*, is described in §2.4. In §2.5, we revisit this derivation for stability eigenmodes elaborated by M. Morzyński et al. in his chapter. A popular empirical realization is the proper orthogonal decomposition (POD), which minimizes a residual for a given data ensemble (§2.6). In general, this Galerkin method can approximate the flow evolution over a finite time horizon and may even reproduce the main characteristics of the long-term behavior.

2.1 Problem formulation

The incompressible, viscous flow is described in a Cartesian coordinate system $\mathbf{x} = (x, y, z)$ in the finite steady domain Ω . The x -, y - and z -axes are described by unit vectors \mathbf{e}_x , \mathbf{e}_y , \mathbf{e}_z , respectively. For the cylinder wake, the x -axis is aligned with the flow, the y -axis parallel to the shear and the z -axis parallel to cylinder axis. The velocity $\mathbf{u} = (u, v, w)$ has the components u , v and w in x -, y -and z -direction, respectively. The time is denoted by t and considered in the interval $[0, T]$. The pressure field is represented by p . The Cartesian components may also be indicated by indices, e.g. $\mathbf{x} = (x_1, x_2, x_3)$ or $\mathbf{u} = (u_1, u_2, u_3)$. An analogous convention applies to the unit vectors \mathbf{e}_1 , \mathbf{e}_2 , \mathbf{e}_3 .

Kinematically, the flow is characterized by D , a characteristic length of the geometry, and U , a characteristic velocity. For the flow around the cylinder, D is chosen to be the diameter and U the oncoming velocity. The Newtonian fluid has constant density ρ and dynamic viscosity μ . In the following, we assume that all dependent and independent variables are non-dimensionalized with D , U , ρ and μ . The flow is characterized by the Reynolds number $Re = \rho U D / \mu$ or, equivalently, by its reciprocal denoted by $\nu := 1/Re$.

For the formulation of the initial boundary value problem (IBVP), we introduce ∂_x , ∂_y , ∂_z , and ∂_t for derivatives with respect to x , y , z and t . Alternatively, ∂_α indicates a derivate in the α -th Cartesian direction. Second derivatives are denoted similarly, e.g. ∂_{xx}^2 for the second derivative with respect to x . The Nabla operator $\nabla := (\partial_x, \partial_y, \partial_z)$ comprises first derivatives in a vector. The Laplace operator $\Delta := \partial_{xx}^2 + \partial_{yy}^2 + \partial_{zz}^2$ can act on a scalar or on a vector by acting on each Cartesian component.

We employ tensor algebra for products of scalars (0-th order tensors), vectors (1st order tensors) and matrices (representing 2nd-order tensors). The product between two tensors is by default an outer product, e.g. $\nabla \mathbf{u} = (\partial_\alpha u_\beta)$ represents the Jacobian of the velocity field. Similarly, $\mathbf{u}\mathbf{u} := (u_\alpha u_\beta)$ denotes the dyadic product (a matrix). Inner products are denoted by \cdot and contract the inner indices. Let \mathbf{a} and \mathbf{b} be two vectors, then $\mathbf{a} \cdot \mathbf{b} := \sum_{\alpha=1}^3 a_\alpha b_\alpha$ represents the standard Euclidean product yielding a scalar. Let

\mathbf{A} be a matrix, then $\mathbf{A} \cdot \mathbf{b} := \sum_{\alpha=1}^3 \mathbf{e}_\alpha \left(\sum_{\beta=1}^3 A_{\alpha\beta} b_\beta \right)$. For later reference, we introduce the double contraction ':'. Let \mathbf{A} and \mathbf{B} two matrices, then $\mathbf{A} : \mathbf{B} := \sum_{\alpha=1}^3 \sum_{\beta=1}^3 A_{\alpha\beta} B_{\beta\alpha}$. Details can be inferred from any text book of tensor algebra.

It should be emphasized that tensor algebra and linear algebra have quite different notations. In tensor algebra the indices are tied to physical space and imply well-defined behavior for physical coordinate transformations. In linear algebra, vectors and matrices are just book-keeping quantities and the elements having no a priori meaning or transformation properties. Also the mathematics is different. Let \mathbf{A} be a matrix and \mathbf{b} a vector. Then \mathbf{Ab} represents an outer product leading to a 3-rd order tensor in tensor algebra and inner product yielding a vector in matrix algebra. To cleanly separate both worlds, we keep round brackets for tensors and introduce square brackets for elements of linear algebra.

The evolution of the flow obeys mass and momentum balance, i.e. the equation of continuity and Navier-Stokes equation:

$$\nabla \cdot \mathbf{u} = 0, \tag{1a}$$

$$\partial_t \mathbf{u} + \nabla \cdot (\mathbf{u} \mathbf{u}) = -\nabla p + \nu \Delta \mathbf{u} + \mathbf{g} b \tag{1b}$$

The flow is actuated with a simple volume force $\mathbf{g}(x) b(t)$ with a steady carrier field \mathbf{g} and time-dependent amplitude b . An example is a Lorentz force of magnetohydrodynamics or a buoyancy term in the Boussinesq approximation.

A unique solution of (1) is expected when completed with an initial condition at time $t = 0$ and a boundary condition on the domain boundary $\partial\Omega$ in the integration time interval $[0, T]$. These conditions typically read

$$\mathbf{u}(\mathbf{x}, 0) = \mathbf{u}_{IC}(\mathbf{x}) \quad \forall \mathbf{x} \in \Omega, \quad (2)$$

$$\mathbf{u}(\mathbf{x}, t) = \mathbf{u}_{BC}(\mathbf{x}) \quad \forall \mathbf{x} \in \partial\Omega, t \in [0, T]. \quad (3)$$

We assume $\mathbf{u}_{IC} = \mathbf{u}_{BC}$ for $\mathbf{x} \in \partial\Omega$. The Dirichlet boundary condition (3) may be the no-slip condition on the wall or the free-stream condition at infinity. The following considerations can easily be applied also to periodic boundary conditions in nominally homogeneous directions or convective outflow conditions. The initial boundary value problem (1),(2),(3) defines flows around obstacles, like spheres, cylinders and airfoils, in uniform stream as well as most internal flows.

Typically, the pressure is considered as a Lagrange multiplier ensuring incompressibility (1a). The pressure can be computed from the velocity field by taking the divergence of (1b) and exploiting (1a). This yields the pressure-Poisson equation,

$$\Delta p = -(\nabla \mathbf{u})^\top : \nabla \mathbf{u}. \quad (4)$$

Here, the superscript \top denotes a transpose (exchange of indices) in the velocity Jacobian. At the boundary, the multiplication of (1b) with the wall normal \mathbf{n} yields a Robins boundary condition for p . This condition and (4) define p uniquely up to an arbitrary constant. The constant does not affect the velocity field. Hence, we can consider the Navier-Stokes residual

$$\mathbf{R}(\mathbf{u}) := \partial_t \mathbf{u} + \nabla \cdot (\mathbf{u} \mathbf{u}) + \nabla p - \nu \Delta \mathbf{u} - \mathbf{g} b \quad (5)$$

as a function of the velocity field only.

The above consideration apply to low-Mach number flows of Newtonian fluids in steady domains. The consideration does not include compressibility (e.g. transonic or supersonic flows), wall motion (e.g. aeroelastics) and combustion (or other multi-physics phenomena).

2.2 Traditional Galerkin method

The Galerkin method (Fletcher, 1984) approximates the solution of the IBVP (1), (2), (3) in the form

$$\mathbf{u}^{[0\dots N]}(\mathbf{x}, t) = \mathbf{u}_0(\mathbf{x}) + \sum_{i=1}^N a_i(t) \mathbf{u}_i(\mathbf{x}) \quad (6a)$$

$$\frac{d}{dt} \mathbf{a} = \mathbf{f}^{[0\dots N]}(\mathbf{a}, b). \quad (6b)$$

Here, the velocity field is approximated by $\mathbf{u}^{[0\dots N]}$, a finite expansion in terms of the base flow \mathbf{u}_0 , N space-dependent modes \mathbf{u}_i and corresponding time-dependent mode amplitudes a_i . The evolution equation is compressed in a system of ordinary differential equations for the mode amplitudes $\mathbf{a} := [a_1, \dots, a_N]^\top$ via the propagator $\mathbf{f}^{[0\dots N]} = [f_1^{[0\dots N]}, \dots, f_N^{[0\dots N]}]^\top$. The control command b is included in (6b) to match (1b). The bulky superscript $[0\dots N]$ shall remind which index set of modes is employed in the approximation and may be omitted without warning.

Almost any computational solution method of the Navier-Stokes equation can be framed in the form (6). The particularity of the *traditional* Galerkin method is aiming at a low dimension N as first priority. This method is deeply rooted in functional analysis and has following properties:

GM1: The incompressibility (1a) is exactly fulfilled for all choices of mode amplitudes.

GM2: The boundary condition (3) is exactly fulfilled for all choices of mode amplitudes.

GM3: The modes are a subset of a complete orthonormal system (ONS) $\{\mathbf{u}_i\}_{i=0}^\infty$ of the Hilbert space of square integrable vector fields $L^2(\Omega)$, or an Hilbert subspace $H(\Omega) \subset L^2(\Omega)$ guaranteeing a problem-specific, sufficiently high regularity of the considered functions. The Hilbert space $L^2(\Omega)$ is equipped with an inner product between two vector fields \mathbf{v} and \mathbf{w}

$$(\mathbf{v}, \mathbf{w})_\Omega := \int_{\Omega} d\mathbf{x} \mathbf{v} \cdot \mathbf{w} \quad (7)$$

and the associated norm

$$\|\mathbf{v}\|_\Omega := \sqrt{(\mathbf{v}, \mathbf{v})_\Omega}. \quad (8)$$

Orthonormality of the modes reads

$$\forall i, j \in \{1, \dots, N\} \quad : \quad (\mathbf{u}_i, \mathbf{u}_j)_\Omega = \delta_{ij}. \quad (9)$$

The completeness of the ONS implies that an arbitrary accuracy of (6a) is achievable by increasing the mode number N .

GM4: The ansatz should be compatible with the weak solution of the Navier-Stokes equation, i.e.

$$\forall \mathbf{v} \in H(\Omega) \quad : \quad (\mathbf{v}, \mathbf{R}(\mathbf{u}))_\Omega = 0, \quad (10)$$

where \mathbf{R} represents the Navier-Stokes operator based on generalized derivatives.

The numbering of the postulate reflects its relative importance in the traditional Galerkin method. Property *GM3* implies that the resolution accuracy is controlled by the number of global modes, defined on the whole domain Ω . No existence of grid is implied or necessary in this analytical framework. Property *GM3* discriminates the traditional Galerkin method from grid-based discretizations of the Navier-Stokes equation, like finite-difference, finite-volume or finite-element schemes. Here, the local modes are tied to the grid and an increasing grid resolution requires a new set of modes. A rigorous mathematical theory detailing *GM4* and other aspects is outside the scope of this book. Instead, we refer to the classics by Ladyzhenskaya (1963).

2.3 Galerkin expansion

In this section, properties of the Galerkin expansion (6a) are derived. The first property *GM1* of the previous section implies

$$\nabla \cdot \mathbf{u}_i = 0, \quad i = 0, 1, \dots, N. \quad (11)$$

This condition liberates us from re-considering the mass balance (1a) in future considerations.

The second property *GM2* yields

$$\forall \mathbf{x} \in \partial\Omega : \quad \mathbf{u}_0(\mathbf{x}) = \mathbf{u}_{BC}(\mathbf{x}) \quad \text{and} \quad \mathbf{u}_i(\mathbf{x}) = 0, \quad i = 1, \dots, N. \quad (12)$$

Now, the boundary conditions are incorporated.

The third property *GM3* allows to determine the mode amplitudes for a given velocity field \mathbf{u} by minimizing the residual $\|\mathbf{u} - \mathbf{u}^{[0\dots N]}\|_\Omega$:

$$a_i = (\mathbf{u} - \mathbf{u}_0, \mathbf{u}_i)_\Omega. \quad (13)$$

It should be noted that the mode amplitude a_i is not distorted by the orthogonal residual $\sum_{i=N+1}^{\infty} a_i \mathbf{u}_i$ of the Galerkin expansion, i.e. is independent of N .

The energy content of the fluctuation $\mathbf{u}' := \mathbf{u} - \mathbf{u}_0 = \sum_{i=1}^{\infty} a_i \mathbf{u}_i$ is quantified by the instantaneous fluctuation energy

$$K(t) = \frac{1}{2} \|\mathbf{u}'\|_\Omega^2. \quad (14)$$

In statistical fluid mechanics, K is also termed turbulent kinetic energy (*TKE*). The orthogonality of the modes allows to partition K into modal

energies $K_i(t)$, the energy content of each modal subspace contribution $\mathbf{u}^{[i]} = a_i \mathbf{u}_i$:

$$K(t) = \sum_{i=1}^{\infty} K_i(t), \quad \text{where} \quad K_i(t) := \frac{1}{2} \left\| \mathbf{u}^{[i]} \right\|_{\Omega}^2 = \frac{1}{2} a_i^2. \quad (15)$$

For later reference, we note that (14) and (15) refer to the instantaneous values of the energies. By default, K and K_i represent averaged values if the argument ' (t) ' is omitted.

2.4 Galerkin system

Finally, we derive the evolution equation of the mode amplitudes. The finite Galerkin expansion (6a) cannot be expected to yield an exact solution of (10) under general conditions. However, (10) can be exactly satisfied for all test functions from the same subspace as the Galerkin expansion. Without loss of generality, we choose the N expansion modes as test functions:

$$\left(\mathbf{u}_i, \mathbf{R}(\mathbf{u}^{[0\dots N]}) \right)_{\Omega}, \quad i = 1, \dots, N. \quad (16)$$

This step is called *Galerkin projection*, we project the Navier-Stokes equation on the subspace of the Galerkin expansion.

To simplify the Galerkin projection, we re-write (6a) as

$$\mathbf{u}^{[0\dots N]} = \sum_{i=0}^N a_i \mathbf{u}_i, \quad (17)$$

where $a_0 \equiv 1$. Moreover we introduce $(F)_{\Omega} := \int_{\Omega} d\mathbf{x} F$ as notation for the volume integral of F over the domain. $[F]_{\partial\Omega} := \oint_{\partial\Omega} d\mathbf{A} \cdot F$ represents the surface integral of F over the boundary of the domain. F is typically a scalar, like pressure, but could also be a vector or higher-order tensor.

The projection of the local acceleration term reads

$$\left(\mathbf{u}_i, \partial_t \left[\sum_{j=0}^N a_j \mathbf{u}_j \right] \right)_{\Omega} = \sum_{j=1}^N \dot{a}_j (\mathbf{u}_i, \mathbf{u}_j)_{\Omega} = \dot{a}_i, \quad (18)$$

exploiting the steadiness of a_0 and the orthonormality of the modes (9). The Galerkin projection of the viscous term yields

$$\left(\mathbf{u}_i, \nu \Delta \left[\sum_{j=0}^N a_j \mathbf{u}_j \right] \right)_{\Omega} = \nu \sum_{j=0}^N l_{ij}^{\nu} a_j, \quad (19a)$$

$$l_{ij}^{\nu} = (\mathbf{u}_i, \Delta \mathbf{u}_j)_{\Omega} = [\mathbf{u}_i \cdot \nabla \mathbf{u}_j]_{\partial\Omega} - (\nabla \mathbf{u}_i : \nabla \mathbf{u}_j)_{\Omega} \quad (19b)$$

The transformation of l_{ij}^ν to a term with first derivatives has been performed employing Green's identity. Numerically, the transformed term generally leads to more accurate values of l_{ij}^ν and is hence preferred. For Dirichlet boundary conditions, the surface integral vanishes, since $\mathbf{u}_i \equiv 0$ on the domain boundary. In this case, l_{ij}^ν represents a negative semi-definite matrix.

Note that (19) is linear ('pseudo-linear') in $[a_0, \dots, a_N]^\top$ but contains a constant term at $j = 0$ with respect to the non-trivial mode amplitudes $[a_1, \dots, a_N]^\top$.

The Galerkin projection of the convective term leads to a pseudo-quadratic form

$$\begin{aligned} \left(\mathbf{u}_i, -\nabla \cdot \left(\left[\sum_{j=0}^N a_j \mathbf{u}_j \right] \left[\sum_{k=0}^N a_k \mathbf{u}_k \right] \right) \right)_\Omega &= \sum_{j=0}^N \sum_{k=0}^N q_{ijk}^c a_j a_k \quad (20a) \\ q_{ijk}^c &= -(\mathbf{u}_i, \nabla \cdot (\mathbf{u}_j \mathbf{u}_k))_\Omega. \quad (20b) \end{aligned}$$

For the Galerkin projection of the pressure term, we first construct a solution of the pressure-Poisson equation with respect to p . Let p_{jk} , termed 'partial pressures' in the sequel, satisfy

$$\Delta p_{jk} = -(\nabla \mathbf{u}_j)^\top : \nabla \mathbf{u}_k. \quad (21)$$

Then, the pseudo-quadratic Galerkin ansatz of the pressure

$$p^{[0\dots N]}(\mathbf{x}, t) = \sum_{j=0}^N \sum_{k=0}^N p_{jk}(\mathbf{x}) a_j(t) a_k(t) \quad (22)$$

satisfies the pressure-Poisson equation (4) neglecting the residual of the Galerkin expansion. Employing (22), the Galerkin projection of the pressure term becomes

$$\left(\mathbf{u}_i, -\nabla p^{[0\dots N]} \right)_\Omega = \sum_{j=0}^N \sum_{k=0}^N q_{ijk}^p a_j a_k \quad (23a)$$

$$q_{ijk}^p = -(\mathbf{u}_i, \nabla \cdot p_{jk})_\Omega = -[\mathbf{u}_i p_{jk}]_{\partial\Omega}. \quad (23b)$$

In the second transformation of q_{ijk}^p , the incompressibility of the modes and Gauss integral formula is exploited. Note that this surface integral vanishes for Dirichlet boundary conditions (3), implying (12) for the modes. In this case, the pressure-term representation vanishes identically in the Galerkin projection. This behavior is consistent with the interpretation of pressure as a Lagrange multiplier for incompressibility. The pressure has no role to

play on the solenoidal affine space spanned by the Galerkin expansion (6a). The same statement applies also to periodic boundary conditions, as proven in Holmes et al. (1998).

In case of open flows with convective boundary conditions, the modes do not vanish identically on the boundary and the pressure term may play an important role (Noack et al., 2005; Noack, 2006). We refer to these original papers for the details on the incorporation of the boundary conditions in (4), (21).

In practice, the computation of partial pressures p_{jk} is numerically delicate and expensive. Past studies (Noack et al., 2005; Noack, 2006) indicate that the effect of the pressure term is well accounted by a linear term. In fact, most authors employ a calibrated linear term to account for the pressure term — starting with Galletti et al. (2004). We decompose the pressure in a constant part $p^c = p_{00}$, a linear (so called 'fast') term $p^l = \sum_{j=1}^N (p_{j0} + p_{0j}) a_j$, and a quadratic (so called 'slow') contribution $p^q = \sum_{j,k=1}^N p_{jk} a_j a_k$, respectively:

$$p = p^c + p^l + p^q. \quad (24)$$

The constant component may drive internal flows, like the pressure gradient in pipe flow. For open flows, the Galerkin representation of this part tends to be negligible. The quadratic component tends to be small compared to linear pendant (Noack, 2006), justifying *a posteriori* the calibrated linear term.

As a historical note, the pioneering work of Aubry et al. (1988) emphasized already the potentially important role of the pressure term, but did not propose a physics-based model. Rempfer and Fasel (1994) bypassed the modeling problem by projection on the pressure-free vorticity equation. This projection lumps the effect of the convection- and the pressure-term in a single term

$$q_{ijk} = q_{ijk}^c + q_{ijk}^p \quad j, k = 0, \dots, N. \quad (25)$$

Finally, the Galerkin projection of the volume force term reads

$$(\mathbf{u}_i, \mathbf{g} b)_\Omega = g_i b, \quad \text{where} \quad g_i = (\mathbf{u}_i, \mathbf{g})_\Omega. \quad (26)$$

Summarizing, the projection (16) yields following Galerkin system:

$$\dot{a}_i = \underbrace{\nu \sum_{j=0}^N l_{ij}^\nu a_j}_{\substack{\text{local} \\ \text{acceleration}}} + \underbrace{\sum_{j,k=0}^N q_{ijk}^c a_j a_k}_{\substack{\text{viscous} \\ \text{term}}} + \underbrace{\sum_{j,k=0}^N q_{ijk}^p a_j a_k}_{\substack{\text{convective} \\ \text{term}}} + \underbrace{g_i b}_{\substack{\text{pressure} \\ \text{gradient}}} + \underbrace{\text{volume force}}_{\substack{\text{force}}} . \quad (27)$$

The form elegantly allows to trace back each term from the corresponding Navier-Stokes pendant. However, dynamical system analyses are complicated by the inclusion of $a_0 \equiv 1$. Examples include finding the fixed point and performing a stability analysis. Hence, we re-write (27) in the form

$$\dot{a}_i = c_i + \sum_{j=1}^N l_{ij} a_j + \sum_{j,k=1}^N q_{ijk} a_j a_k + g_i b, \quad (28)$$

where $c_i = \nu l_{i0} + q_{i00}^c + q_{i00}^p$, $l_{ij} = \nu l_{ij}^\nu + q_{ij0}^c + q_{ij0}^c + q_{ij0}^p + q_{ij0}^p$, and q_{ijk} is defined by (25). Note that the constant term c_i would vanish if \mathbf{u}_0 is chosen to be a steady Navier-Stokes solution.

2.5 Non-orthogonal modes

The eigenmodes of stability analysis are generally not orthogonal to each other. In this case, we introduce a mass matrix $\mathbf{M} = (m_{ij})$, where $m_{ij} := (\mathbf{u}_i, \mathbf{u}_j)_\Omega$ and the Galerkin projection leads to

$$\sum_{j=1}^N m_{ij} \dot{a}_j = \nu \sum_{j=0}^N l_{ij}^\nu a_j + \sum_{j,k=0}^N q_{ijk}^c a_j a_k + \sum_{j,k=0}^N q_{ijk}^p a_j a_k + g_i b. \quad (29)$$

The local acceleration term on the left-hand side is generalized, but all terms on the right-hand side remain unaltered. This equation can be solved for \dot{a}_i by multiplication with the inverse mass matrix. An alternative yet equivalent trick is the use of adjoint modes \mathbf{v}_i as test functions in the Galerkin projection (Haken, 1983):

$$\left(\mathbf{v}_i, \mathbf{R}(\mathbf{u}^{[0 \dots N]}) \right)_\Omega, \quad i = 1, \dots, N. \quad (30)$$

The adjoint and original modes satisfy the orthogonality relationship $(\mathbf{u}_i, \mathbf{v}_j)_\Omega = \delta_{ij}$. Thus, Galerkin projection leads to (27), again.

2.6 POD models

The main art of Galerkin modeling is constructing a good low-dimensional ‘modal piano.’ The modes should span a subspace in which the attractor and nearby transients are well resolved.

Common choices of the basic mode \mathbf{u}_0 are the steady solution or the mean flow. Both fulfill the incompressibility (1a) and the boundary conditions (3). In principle, any velocity field satisfying these conditions serve the purpose. In practice, the choice of the basic mode is not overly critical if the expansion modes can compensate for deviations of the base flow.

In contrast, the performance of the Galerkin method depends quite sensitively on the choice of the expansion modes. In principle, the Hilbert space of square-integrable solenoidal velocity fields guarantees the existence of a complete orthonormal system. This property is exploited by *mathematical* approaches which are successfully applied to geometrically simple internal flows (Lorenz, 1963; Busse, 1991) but also to open flows (Noack and Eckelmann, 1994a,b). The method poses severe analytical and numerical challenges for general 3D geometries. These challenges have excluded an application for most engineering tasks. Moreover, the advantage of the mathematical modes, guaranteed completeness independently of the evolution equation to be approximated, is at the same time a weakness in terms of the required low dimensions.

A more problem-tailored *physical* method is a Galerkin model based on stability eigenmodes of a linearized Navier-Stokes related equation, like Stokes equation (Joseph, 1976), a modified Stokes equation (Batcho, 1994), or the constitutive equation of stability analysis (see the chapter of M. Morzyński et al.). This approach can be expected to lead to lower-order expansions since it includes properties of the evolution equation. However, the property of completeness of the stability eigenmodes has only been proven for very few highly symmetrical configurations (Joseph, 1976; Grosch and Salwen, 1978; Salwen and Grosch, 1981) and may be questionable for open flows. Physical Galerkin models have been constructed for internal flows (Rummel, 2000), for wakes (Afanasiev, 2003) and for the flow over a cavity (Åkervik et al., 2007).

A third *empirical* ansatz employs experimental or simulation flow data from the target configuration. Often, the most energetic directions are extracted from snapshots \mathbf{u}^m , $m = 1, \dots, M$ in the observation domain Ω . A canonical approach, is called principle axis, Karhunen-Lòeve or *proper orthogonal decomposition* (POD). Let $\langle \cdot \rangle_M$ denote the average over these snapshots. Then, POD optimizes the averaged residual with respect to the L_2 -norm. In other words, any other N -dimensional expansion $\mathbf{w}^{[0\dots N]} =$

$\sum_{i=0}^N c_i \mathbf{w}_i$ of which the modes $\{\mathbf{w}_i\}_{i=0}^N$ satisfy incompressibility (11), the boundary conditions (12) and orthonormality (9) cannot have a smaller residual:

$$\langle \|\mathbf{u}^m - \sum_{i=0}^N c_i^m \mathbf{u}_i\|_\Omega^2 \rangle_M \leq \langle \|\mathbf{u}^m - \sum_{i=0}^N c_i^m \mathbf{w}_i\|_\Omega^2 \rangle_M. \quad (31)$$

Here, the superscript m of the snapshot is transferred to the mode amplitudes. Apart from there usefulness for data compression, the POD modes have no inherent physical meaning. For the soft onset of oscillatory fluctuations, mean-field theory derives that the first 2 POD modes span the real and imaginary part of the unstable complex stability eigenmode. Similarity between selected POD modes and stability eigenmodes has been observed for several configurations. In general, POD does not extract pure frequency modes, like stability eigenmodes. Dynamic mode decomposition (DMD) is another data-driven flow decomposition designed to match stability eigenmodes under suitable conditions (Rowley et al., 2009; Schmid, 2010). DMD trades the optimal resolution efficiency of POD against distillation of pure eigenfrequencies in short-time sampled data.

The construction of POD modes can be inferred from many excellent sources (Holmes et al., 1998). The modes are best conceptualized as principle axes of a Gaussian distribution fitted to the snapshots representing the first and second moments (Cordier and Bergmann, 2003). Typically, the number of POD modes is chosen much smaller than the number of snapshots, $N \ll M$. The maximum of number of modes reads $N = M - 1$, since M points span a $M - 1$ -dimensional manifold.

Snapshot-based POD consists of 5 steps (Sirovich, 1987):

1. Compute the mean flow,

$$\mathbf{u}_0 := \frac{1}{M} \sum_{m=1}^M \mathbf{u}^m. \quad (32)$$

2. Compute the correlation matrix $\mathbf{C} = (C^{mn})$ of the fluctuations,

$$C^{mn} := \frac{1}{M} (\mathbf{u}^m - \mathbf{u}_0, \mathbf{u}^n - \mathbf{u}_0)_\Omega. \quad (33)$$

Note that \mathbf{C} is a symmetric positive semi-definite gramian matrix.

3. Perform the spectral analysis of this matrix, i.e. find the first N eigenvectors $\mathbf{e}_i = [e_1^i, \dots, e_M^i]^\top$ and sorted eigenvalues $\lambda_1 \geq \lambda_2 \geq \dots \geq \lambda_N \geq 0$,

$$\mathbf{C}\mathbf{e}_i = \lambda_i \mathbf{e}_i, \quad i = 1, \dots, N. \quad (34)$$

Without loss of generality, the eigenvectors are assumed to be orthonormalized, $\mathbf{e}_i \cdot \mathbf{e}_j = \delta_{ij}$, thanks to the symmetry of \mathbf{C} .

4. Compute each POD mode as linear combination of the snapshot fluctuations,

$$\mathbf{u}_i := \frac{1}{\sqrt{M \lambda_i}} \sum_{m=1}^M e_m^i (\mathbf{u}^m - \mathbf{u}_0), \quad i = 1, \dots, N. \quad (35)$$

The POD modes satisfy the orthonormality condition (9).

5. Compute the mode amplitudes,

$$a_i^m := \sqrt{\lambda_i M} e_m^i, \quad i = 1, \dots, N. \quad (36)$$

These amplitudes vanish on average and are uncorrelated (orthogonal in time),

$$\langle a_i \rangle_M = 0, \quad \langle a_i a_j \rangle_M = \lambda_i \delta_{ij}, \quad i, j \in \{1, \dots, N\}. \quad (37)$$

POD defines a second-order statistics providing the mean flow \mathbf{u}_0 and the two-point autocorrelation function

$$\overline{\mathbf{u}'(\mathbf{x}, t) \mathbf{u}'(\mathbf{y}, t)} = \sum_{i=1}^N \lambda_i \mathbf{u}_i(\mathbf{x}) \mathbf{u}_i(\mathbf{y}). \quad (38)$$

Hence, a minimum requirement to the snapshot ensemble is the accuracy of the derived mean flow and the second moments. Accuracy of the statistics for a given number of snapshots is increased by uncorrelated snapshots as required in the original paper on the snapshot POD method (Sirovich, 1987).

POD is optimal for the given data set in the sense of (31), but is generically not complete (violates *GM3*). Applicability for other Reynolds numbers, for transients and for actuation is very restricted (Deane et al., 1991). Numerous suggestions have been made to improve or augment POD for several operating conditions. We refer the interested reader to the literature (Ma and Karniadakis, 2002; Noack et al., 2003; Jørgensen et al., 2003; Siegel et al., 2008).

The Galerkin projection can be effected on any orthonormal(ized) set of modes. It has become increasingly common to add calibrated corrections to the constant and linear terms (Galletti et al., 2004; Tadmor and Noack, 2004). These corrections shall account for the pressure term, the neglected modes, mode deformations or other diseases of the Galerkin method. The calibration of the whole Galerkin system with constant, linear, and quadratic terms is generally badly conditioned and should invoke a penalization procedure for the quadratic terms (Cordier et al., 2010).

POD Galerkin models have been constructed for practically all flow configurations. Examples are Couette flow (Moehlis et al., 2002), transitional (Rempfer and Fasel, 1994) and turbulent boundary layers (Aubry et al., 1988; Podvin, 2009), wakes (Deane et al., 1991; Noack et al., 2003), mixing layers (Ukeiley et al., 2001; Noack et al., 2005; Wei and Rowley, 2009), jets (Schlegel et al., 2009). The vast amount of published successful POD models should not mislead the reader to assume that they can be easily constructed with the standard approach, or that they are robust. Most models are fragile and critically dependent on additional enablers, such as discussed in §4.

3 Statistical fluid mechanics as design tool

POD can be considered as a refinement of the Reynolds decomposition of velocity field. The fluctuation is decomposed in modal compartments,

$$\mathbf{u} = \mathbf{u}_0 + \mathbf{u}', \quad \mathbf{u}' = \sum_{i=1}^{\infty} \mathbf{u}^{[i]}, \quad \mathbf{u}^{[i]} = a_i \mathbf{u}_i. \quad (39)$$

In this section, we refine some well-known equations of statistical fluid mechanics for the fluctuation (Monin and Yaglom, 1971, 1975) into the modal pendants. First (§3.1), the principles of global and modal balance equations are revisited. The modal pendants of the Reynolds and TKE equation are presented in §3.2. Finally, a novel closure for the first and second moments of Galerkin systems is outlined (§3.3). The balance equations of this section can be employed as powerful analysis and design tool. Examples are understanding the modal interactions, checking the accuracy of the numerical data, evaluating the (reduced) Galerkin models, deriving free calibration parameters, and determining the analytical form of the subgrid turbulence models.

3.1 Principles of balance equations

Statistical fluid mechanics is based on a Reynolds average, denoted by an overbar $\overline{}$ or $\langle \rangle$. This average may be the infinite time mean, an ensemble average, a spatial average over one or more homogeneous directions, or any other filter satisfying the Reynolds properties (Monin and Yaglom, 1971). A large class of global balance equations for the domain Ω can be derived from the average of (10)

$$\overline{(\mathbf{v}, \mathbf{R}(\mathbf{u}))}_{\Omega} = 0. \quad (40)$$

The weak form of the Reynolds equation is obtained by substituting the Reynolds decomposition in (40), and allowing any test function \mathbf{v} . Choosing

$\mathbf{v} = \mathbf{u}$, \mathbf{u}_0 , or \mathbf{u}' leads to global balance equation for the total kinetic energy, the mean flow or the TKE, respectively. The drag or lift formulae are derived by setting $\mathbf{v} = \mathbf{e}_x$ or $\mathbf{v} = \mathbf{e}_y$, respectively. As a slight variation, the Reynolds stress balance equations are inferred from the symmetric matrix valued equation:

$$\overline{(\mathbf{u}' \mathbf{R}(\mathbf{u}) + \mathbf{R}(\mathbf{u}) \mathbf{u}')_\Omega} = 0, \quad (41)$$

representing the special case $\mathbf{v} = \mathbf{u}'$ of a larger class of balance equations given by

$$\overline{(\mathbf{v} \mathbf{R}(\mathbf{u}) + \mathbf{R}(\mathbf{u}) \mathbf{v})_\Omega} = 0. \quad (42)$$

Modal pendants of the above mentioned global equations are obtained by substituting the POD (39) as argument in the Navier-Stokes residual and, if necessary, by replacements of the test function. The i -th modal Reynolds equation is obtained by setting $\mathbf{v} = \mathbf{u}_i$ in (40).

The i -th modal energy balance equation employs $\mathbf{v} = \mathbf{u}^{[i]}$ instead of $\mathbf{v} = \mathbf{u}'$ for the TKE equation. Note that the linearity of (40) in \mathbf{v} allows to derive the original TKE from the modal compartments.

Similarly, the modal Reynolds stress balance equation is based on the similar trick: insert $\mathbf{v} = \mathbf{u}^{[i]}$ in (42). The global pendant is obtained by the sum of the original equation.

The effect of the modes on the energy of the mean flow, on the drag or on the lift can be assessed when the Reynolds decomposition is replaced by the POD in the original equation. Tab. 1 summarizes the discussion.

3.2 Modal balance equations

Detailing the discussion of the last section, we derive the modal Reynolds and TKE equation for POD modes. This derivation can be based on the Navier-Stokes equation or the Galerkin system (27), since there is a one-to-one correspondence between Navier-Stokes and Galerkin-system terms (see Tab. 2). We pursue the easier task based on deriving the balance equation from the dynamical system. Moreover, we assume accuracy of the finite Galerkin expansion with N modes and shall, at the moment, not pause to discuss the effect of the residual.

The Reynolds decomposition of the POD mode amplitudes reads

$$a_0 \equiv 1, \quad a'_0 \equiv 0 \quad (43a)$$

$$a_i = a'_i, \quad \bar{a}_i = 0 \quad i = 1, \dots, N. \quad (43b)$$

The modal Reynolds equation is obtained by Reynolds-averaging the Galerkin system and exploiting (37). We chose the dynamical systems (28) for rea-

Table 1. Constitutive equations for selected global and modal balances.

quantity	global balance equation	modal balance equation
argument of $\mathbf{R}(\mathbf{u})$	$\mathbf{u} = \mathbf{u}_0 + \mathbf{u}'$	$\mathbf{u} = \sum_{j=0}^{\infty} \mathbf{u}^{[j]}$
Reynolds equation	(40) for all test functions \mathbf{v}	(40) for $\mathbf{v} = \mathbf{u}_i$
kinetic energy	(40) for $\mathbf{v} = \mathbf{u}_0 + \mathbf{u}'$	(40) for $\mathbf{v} = \sum_{j=0}^{\infty} \mathbf{u}^{[j]}$
mean flow kinetic energy	(40) for $\mathbf{v} = \mathbf{u}_0$	(40) for $\mathbf{v} = \mathbf{u}_0$
TKE / modal energy	(40) for $\mathbf{v} = \mathbf{u}'$	(40) for $\mathbf{v} = \mathbf{u}^{[i]}$
Reynolds stress	(42) for $\mathbf{v} = \mathbf{u}'$	(42) for $\mathbf{v} = \mathbf{u}^{[i]}$
drag	(40) for $\mathbf{v} = \mathbf{e}_x$	(40) for $\mathbf{v} = \mathbf{e}_x$
lift	(40) for $\mathbf{v} = \mathbf{e}_y$	(40) for $\mathbf{v} = \mathbf{e}_y$

sons of brevity:

$$0 = c_i + \sum_{j=1}^N 2q_{ijj} K_j. \quad (44)$$

Here, c_i comprises the \mathbf{u}_i -projected Navier-Stokes residual of \mathbf{u}_0 and right term resolves the effect of the Reynolds stress and of the quadratic pressure term. There is only one energy distribution $K_i = \lambda_i/2$ consistent with the mean flow (N equations for N energy values). The linear term is averaged out and hence immaterial for POD modes.

The modal TKE equation is derived from the dynamical system by multiplying (28) with $a'_i = a_i$ and averaging:

$$\begin{aligned} \frac{d}{dt} K_i &= Q_i + T_i, \\ Q_i &:= 2l_{ii} K_i, \\ T_i &:= \sum_{j,k=1}^N T_{ijk}, \quad T_{ijk} := q_{ijk} \overline{a_i a_j a_k}. \end{aligned} \quad (45)$$

Table 2. Derivation diagram of the Galerkin system. In each column, all Navier-Stokes terms are listed. From top to bottom, the local acceleration, convective viscous and pressure gradient term are shown. From left to right, the Navier-Stokes equation is processed from the original form, to a form employing the Reynolds decomposition, and to a Galerkin projected form. Note that the Galerkin system on the right-most column can be aggregated form (27). with $a_0 \equiv 1$.

NSE	NSE with $\mathbf{u} = \mathbf{u}_0 + \mathbf{u}'$	Galerkin- projection	Galerkin- system
$\partial_t \mathbf{u} =$	$\partial_t \mathbf{u}' =$	$(\mathbf{u}_i, \partial_t \mathbf{u}')_\Omega =$	$\frac{d}{dt} a_i =$
$-\nabla \cdot [\mathbf{u} \mathbf{u}]$	$-\nabla \cdot [\mathbf{u}_0 \mathbf{u}_0]$ $-\nabla \cdot [\mathbf{u}' \mathbf{u}_0]$ $-\nabla \cdot [\mathbf{u}_0 \mathbf{u}']$ $-\nabla \cdot [\mathbf{u}' \mathbf{u}']$	$-(\mathbf{u}_i, \nabla \cdot [\mathbf{u}_0 \mathbf{u}_0])_\Omega$ $-(\mathbf{u}_i, \nabla \cdot [\mathbf{u}' \mathbf{u}_0])_\Omega$ $-(\mathbf{u}_i, \nabla \cdot [\mathbf{u}_0 \mathbf{u}'])_\Omega$ $-(\mathbf{u}_i, \nabla \cdot [\mathbf{u}' \mathbf{u}'])_\Omega$	q_{i00}^c $+ \sum_{j=1}^N q_{ij0}^c a_j$ $+ \sum_{j=1}^N q_{i0j}^c a_j$ $+ \sum_{j,k=1}^N q_{ijk}^c a_j a_k$
$+\nu \Delta \mathbf{u}$	$+\nu \Delta \mathbf{u}_0$ $+\nu \Delta \mathbf{u}'$	$+\nu (\mathbf{u}_i, \Delta \mathbf{u}_0)_\Omega$ $+\nu (\mathbf{u}_i, \Delta \mathbf{u}')_\Omega$	$+\nu l_{i0}$ $+\nu \sum_{j=1}^N l_{ij}^\nu a_j$
$-\nabla p$	$-\nabla p_0$ $-\nabla p'$	$-(\mathbf{u}_i, \nabla p_0)_\Omega$ $-(\mathbf{u}_i, \nabla p')_\Omega$	$+q_{i00}^p$ $+ \sum_{j,k=0}^N q_{ijk}^p a_j a_k$ $\max\{j,k\} > 0$

The time-derivative of K_i does not generally vanish for finite POD snapshot ensembles. Q_i lumps the effect of all Navier-Stokes terms which are linear in \mathbf{u}' . A look on Tab. 2 and the pressure model will reveal that these terms contain either \mathbf{u}_0 or ν , i.e. describe interactions with the mean flow or with the molecular chaos. Hence, Q_i lumps the effect of *external* interactions with respect to the mode ensemble. In contrast, T_i aggregates the energy flow of *internal* triadic interactions T_{ijk} from the convection term and the

quadratic pressure term $p^{(2)}$. Hence, T_i is not effected by mean flow or viscosity.

A refined physical resolution of the modal TKE equation is obtained by repeating the operations for the Galerkin system (27). We shall refer to the Navier-Stokes equation. Tab. 3 elucidates the origin of the TKE terms, namely the production P , the convection C , the transfer T , the dissipation D and the pressure power F . Tab. 4 contains the modal pendant. Neglecting pressure terms, the external energy flow comprises production, convection and dissipation $Q_i = P_i + C_i + D_i$ while the transfer term T_i remains unaltered. In (45), the linear pressure term p^l of (24) contributes to Q_i and the quadratic term p^q to T_i .

Table 3. Derivation scheme of the global TKE equation.

NSE with $\mathbf{u} = \mathbf{u}_0 + \mathbf{u}'$	Galerkin projection on \mathbf{u}'	global energy flow balance (averaged)	do. (short form)
$\partial_t \mathbf{u}' =$	$(\mathbf{u}', \partial_t \mathbf{u}')_\Omega =$	$dK/dt =$	$dK/dt =$
$-\nabla \cdot [\mathbf{u}_0 \mathbf{u}_0]$	$-(\mathbf{u}', \nabla \cdot [\mathbf{u}_0 \mathbf{u}_0])_\Omega$		
$-\nabla \cdot [\mathbf{u}' \mathbf{u}_0]$	$-(\mathbf{u}', \nabla \cdot [\mathbf{u}' \mathbf{u}_0])_\Omega$	$-(\overline{\mathbf{u}' \mathbf{u}'} : \nabla \mathbf{u}_0)_\Omega$	P
$-\nabla \cdot [\mathbf{u}_0 \mathbf{u}']$	$-(\mathbf{u}', \nabla \cdot [\mathbf{u}_0 \mathbf{u}'])_\Omega$	$-\left[\mathbf{u}_0 \frac{1}{2} \ \mathbf{u}'\ ^2\right]_{\partial\Omega}$	$+C$
$-\nabla \cdot [\mathbf{u}' \mathbf{u}']$	$-(\mathbf{u}', \nabla \cdot [\mathbf{u}' \mathbf{u}'])_\Omega$	$-\left[\mathbf{u}' \frac{1}{2} \ \mathbf{u}'\ ^2\right]_{\partial\Omega}$	$+T$
$+\nu \Delta \mathbf{u}_0$	$+\nu (\mathbf{u}', \Delta \mathbf{u}_0)_\Omega$		
$+\nu \Delta \mathbf{u}'$	$+\nu (\overline{\mathbf{u}' \Delta \mathbf{u}'})_\Omega$	$+\nu (\mathbf{u}' \cdot \Delta \mathbf{u}')_\Omega$	$+D$
$-\nabla p$	$-(\mathbf{u}', \nabla p)_\Omega$	$-\left[\mathbf{u}' p'\right]_{\partial\Omega}$	$+F$

Table 4. Derivation scheme of the modal energy flow balance analog to Tab. 3 following the recipe of Tab. 1.

projection on $a_i \mathbf{u}_i$	Galerkin- representation	modal energy- flow balance (averaged)	do. (short form)
$(a_i \mathbf{u}_i, \partial_t \mathbf{u}')_\Omega =$	$\frac{d}{dt} \left(\frac{1}{2} a_i^2 \right) =$	$dK_i/dt =$	do.
$-(a_i \mathbf{u}_i, \nabla \cdot [\mathbf{u}_0 \mathbf{u}_0])_\Omega$	$q_{i00}^c a_i$		
$-(a_i \mathbf{u}_i, \nabla \cdot [\mathbf{u}' \mathbf{u}_0])_\Omega$	$+ \sum_{j=1}^N q_{ij0}^c a_i a_j$	$+ 2q_{ii0}^c K_i$	P_i
$-(a_i \mathbf{u}_i, \nabla \cdot [\mathbf{u}_0 \mathbf{u}''])_\Omega$	$+ \sum_{j=1}^N q_{i0j}^c a_i a_j$	$+ 2q_{i0i}^c K_i$	$+ C_i$
$-(a_i \mathbf{u}_i, \nabla \cdot [\mathbf{u}' \mathbf{u}''])_\Omega$	$+ \sum_{j,k=1}^N q_{ijk}^c a_i a_j a_k$	$+ \sum_{j,k=1}^N q_{ijk}^c \bar{a}_i \bar{a}_j \bar{a}_k$	$+ T_i$
$+\nu (a_i \mathbf{u}_i, \Delta \mathbf{u}_0)_\Omega$	$+\nu l_{i0} a_i$		
$+\nu (a_i \mathbf{u}_i, \Delta \mathbf{u}')_\Omega$	$+\nu \sum_{j=0}^N l_{ij} a_i a_j$	$+ 2\nu l_{ii} K_i$	$+ D_i$
$-(a_i \mathbf{u}_i, \nabla p)_\Omega$	$+ \sum_{j,k=0}^N q_{ijk}^p a_i a_j a_k$	$+ \sum_{j,k=0}^N q_{ijk}^p \bar{a}_i \bar{a}_j \bar{a}_k$	$+ F_i$

3.3 Finite-time thermodynamics as closure model

In the following, we propose a closure for the first and second moments of a Galerkin system, inspired by finite-time thermodynamics (FTT) (Andresen, 1983). The modal balance equation for momentum and for energy constitute consistency conditions for Galerkin modeling process. The FTT closure of these equations can provide further insights and make predictions. These predictions may include intermodal dependencies, the behavior of a reduced system, auxiliary terms needed for the reduced system, a good way to aggregate mode groups in single 'quasi modes', or transient behavior.

The consideration of transients may require the inclusion of non-POD modes in the Galerkin model. Hence, we formulate the closure for general orthogonal modes. The general Reynolds decomposition of the mode

amplitudes read

$$a_i = m_i + a'_i, \quad m_i := \langle a_i \rangle, \quad K_i = \langle (a'_i)^2 \rangle / 2. \quad (46)$$

The closure shall determine the mean values m_i and fluctuation levels K_i , both for $i = 1, \dots, N$. We exploit the energy preservation of the quadratic Galerkin-system term (Kraichnan and Chen, 1989). The main closure assumptions are that the i -th external energy flow is only a function of the i -th energy, $Q_i = Q_i(K_i)$ and that the triadic interaction is only a function of the involved modal energies $T_{ijk} = T_{ijk}(K_i, K_j, K_k)$, i.e. not higher or lower moments.

The FTT modeled modal Reynolds and modal TKE equations read

$$\dot{m}_i = c_i + \sum_{j=1}^N l_{ij} m_j + \sum_{j,k=1}^N q_{ijk} m_j m_k + \sum_{j=1}^N 2q_{ijj} K_j, \quad (47a)$$

$$\dot{E}_i = Q_i + T_i, \quad \text{where} \quad Q_i = q_i K_i, \quad T_i = \sum_{j,k=1}^N T_{ijk}, \quad (47b)$$

$$q_i = \chi_i + \sum_{j=1}^N \chi_{ij} m_j, \quad (47c)$$

$$T_{ijk} = \alpha \chi_{ijk} \sqrt{K_i K_j K_k} \left(1 - \frac{3K_i}{K_i + K_j + K_k} \right), \quad (47d)$$

where χ_i , χ_{ij} and χ_{ijk} are functions of the Galerkin system coefficients and α is derived from an energetic consistency condition. For the details, the reader is referred to the original publications (Noack et al., 2008, 2010).

Note that (47) represent $2N$ equations for $2N$ unknowns. The FTT framework (47) includes, for instance, the amplitude equations for transient and post-transient behavior of generalized mean-field models with one or more incommensurable frequencies (Noack et al., 2003; Luchtenburg et al., 2009a). Another implication is the absolute equilibrium ensemble (Lesieur, 1993) for Hamiltonized equations. In other words, a condition for equipartition of energy between the modes is defined.

The statistical moments m_j and K_j are searched as the fixed point of the equation (47). Currently, the closure has been successfully applied to a mathematical Galerkin model of the modified Burgers' equation, a POD model of the cylinder wake, and a physical Galerkin model mimicking homogeneous turbulence (Noack et al., 2008). More applications of this closure are actively pursued by the authors.

4 Auxiliary models as key enablers

In previous sections, we have outlined the POD Galerkin method (§2) and associated balance equations (§3). More often than not this method may fail to yield robust, control-oriented models. Root causes are the lack of completeness of POD modes or the intended compression of the physics into few modes. This section shall serve as trouble shooting guide, showing physics-based generalizations of the Galerkin expansion and helpful modifications of the Galerkin system.

First (§4.1), the main challenges are enumerated. Cures are presented in form of general modeling principles addressing the root causes of the challenges. In the following, these principles are detailed as enablers for the Galerkin expansion (§4.2), for the natural dynamics (§4.3), and for the actuation effect (§4.4).

4.1 Challenges and modeling principles

Mathematical Galerkin models can be proven to converge to the Navier-Stokes solution with increasing mode number under suitable conditions (Ladyzhenskaya, 1963). The POD expansion can be expected to converge against the original data in averaged L_2 sense. However, the corresponding hierarchy of Galerkin systems may fail to resolve the Navier-Stokes equation in important aspects. Moreover, the kinematic resolution of the POD expansion may become unsuitable away from the design condition, e.g. at another Reynolds number or with actuation applied. The reason of these challenges can be traced back to the generic incompleteness of the POD in $L^2(\Omega)$.

Incompleteness of POD may lead to following challenges of the corresponding Galerkin method:

1. If the Navier-Stokes solution depends sensitively on small variations of the configuration or the initial condition, the model solution can be expected to be correspondingly strongly effected by modeling errors, even for direct numerical simulations. In the sequel, we assume that the flow dynamics is robust, i.e. we can target a robust reduced-order model as well.
2. The stability property of the Navier-Stokes solution is not conserved during Galerkin projection, even if the Galerkin expansion is 100% accurate. A stable Navier-Stokes solution may lead to an unstable Galerkin solution or the other way round. Simple 3-dimensional models reveal that the omission of a single non-energetic mode may drastically change the stability property of the remaining dynamics (Rempfer, 2000; Noack et al., 2003). Even worse, mean-field models

show that low-energy mean-field modes (shift-modes) lead to cubic stabilizing terms in the Galerkin system (Aubry et al., 1988; Ukeiley et al., 2001; Podvin, 2009), i.e. cannot be cured by re-calibrating the constant, linear or quadratic term.

3. The solution of the Navier-Stokes equation will be a solution of the Galerkin model if the Galerkin basis is accurate. But the Galerkin system may have more unphysical solutions (Rempfer, 1995; Noack et al., 2003). In other words, the Galerkin system may have a narrow region of validity, possibly only the attractor.
4. Turbulent flows are by definition high-dimensional and the Galerkin model shall by construction resolve only the gist, the coherent structures. These structures may contain only a fraction of the turbulent kinetic energy, say 20–50% in case of highly visible coherency. Hence, the effect of the Galerkin expansion residual on the dynamics cannot be ignored and must be modeled. The general recipe to resolve 90% of the fluctuation energy is typically not doable and misses the very goal of reduced-order models.
5. The purpose of actuation is generally to change the coherent structures not only in amplitude but also in shape. One example is to delay vortex shedding behind a bluff body further downstream. Hence, the application of control may invalidate the Galerkin model design at natural conditions.
6. Local small-scale actuation may distort coherent structures from small to large-scale structures. This multi-scale effect can generally not be resolved in the standard POD Galerkin method — like in unsteady RANS methods as well.

The challenges look intimidating. A rich kaleidoscope of seemingly unrelated cures can be found for numerous individual configurations. Fortunately, the root causes for ailing POD models can easily be explained and can often be cured by corresponding simple principles. We mentally partition the flow in coherent structures with characteristic dominant frequency ω_c , a base flow with slow variations $\omega \ll \omega_c$, and small-scale stochastic turbulent fluctuations at high frequencies $\omega \gg \omega_c$. By construction, the POD model may well resolve the coherent structures and associated instabilities and nonlinearities. The coherent structures are continually ‘nurtured’ by the mean flow. The energy growth is limited by base flow variations and by the turbulence cascade, i.e. by the low- and high-frequency side of the spectrum. By construction, a POD model will fail to resolve the turbulence cascade as energy sink and is not guaranteed to resolve stabilizing base flow variations. Hence, the Galerkin model will be much stabler if the POD bases is augmented by additional modes for the base flow variations and a

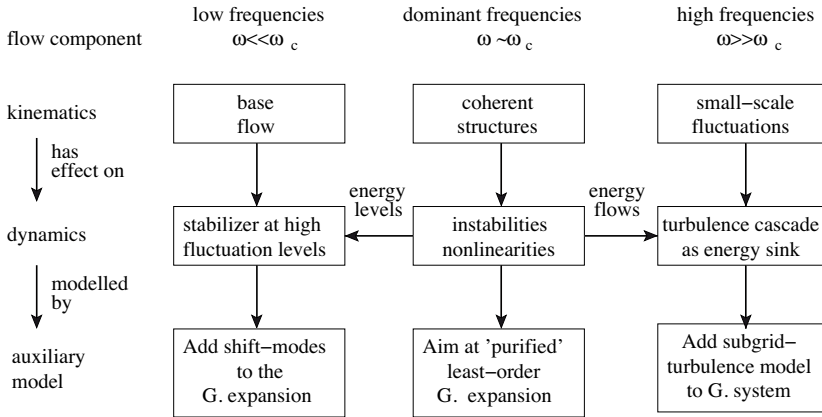


Figure 1. Simplified flow physics and modeling principles. 'G.' stands for Galerkin. The figure is explained in the text.

good auxiliary model for unresolved fine-scale turbulence. Fig. 1 summarizes these principles. In other words, there is no reason to hope for a stable Galerkin model if the physical stabilizing effects are not resolved. Historically, the first pioneering POD model by Aubry et al. (1988) includes a base flow model and an auxiliary turbulence model, i.e. is consistent with these recipes.

4.2 Generalizations of the Galerkin expansion

We outline generalizations of the POD expansion, derived from the evolution equation or resolving multiple operating conditions. First (§4.2), a simple example demonstrates how the evolution equation can be used to construct a dynamically important missing mode. Sections §4.2 and §4.2 address fluctuations with one varying frequency or multiple incommensurable frequencies. Finally (§4.2), general approaches are enumerated.

Shift mode For reasons of simplicity, we consider a simple system of ordinary differential equation illustrating the dynamic incompleteness of POD and showing a necessary cure. This system is derived from the Navier-Stokes equation under assumptions of mean-field theory, i.e. the soft onset

of an oscillatory fluctuation (Noack et al., 2003):

$$\dot{u} = (\sigma_1 - \beta w) u - (\omega_1 + \gamma w) v \quad (48a)$$

$$\dot{v} = (\sigma_1 - \beta w) v + (\omega_1 + \gamma w) u \quad (48b)$$

$$\dot{w} = -\sigma_\Delta w + \alpha (u^2 + v^2) \quad (48c)$$

The roles of the parameters $\sigma_1 > 0$, $\sigma_\Delta > 0$, $\alpha > 0$, $\beta > 0$, and γ are described below. The flow of (48) is illustrated in a phase portrait (Fig. 2). The dynamic behavior is easily inferred from a transcription to cylindrical coordinates r , θ , where $r e^{i\theta} = u + iv$, $i = \sqrt{-1}$ being the imaginary unit:

$$\dot{r} = (\sigma_1 - \beta w) r, \quad (49a)$$

$$\dot{\theta} = (\omega_1 + \gamma w), \quad (49b)$$

$$\dot{w} = -\sigma_\Delta w + \alpha r^2. \quad (49c)$$

We introduce $\mathbf{u} = [u, v, w]^\top$. Evidently, $\mathbf{u}_s = 0$ is the unstable fixed point of the system (48). The neighboring infinitesimal fluctuation spirals outwards in the $w = 0$ plane with growth rate σ_1 and frequency ω_1 . The fluctuation level r^2 shifts the stable mean flow parameter w away from the origin. Typically, the mean flow immediately adjusts to the fluctuation level (Noack et al., 2003; Tadmor and Noack, 2004), $\sigma_\Delta \gg \sigma_1$, showing the slaving to the parabolic mean-field manifold,

$$w = \frac{\alpha}{\sigma_\Delta} r^2. \quad (50)$$

This slaving (Haken, 1983) in (49a), (49b) yields the famous Landau equations for the onset of a supercritical Hopf bifurcation:

$$\dot{r} = \sigma_1 r - \beta^* r^3, \quad \dot{\theta} = \omega_1 + \gamma^* r^2, \quad (51)$$

with $\beta^* = \alpha\beta/\sigma_\Delta$ and $\gamma^* = \alpha\gamma/\sigma_\Delta$. As a result of changing w , the growth rate (frequency) is reduced (changed) via the β (γ) term. Saturation happens at $\dot{r} = 0$ or, equivalently, at fluctuation level r_∞^2 , height w_∞ and frequency ω_∞ given by

$$r_\infty^2 = \frac{\sigma_1 \sigma_\Delta}{\alpha \beta}, \quad w_\infty = \frac{\sigma_1}{\beta} \quad \omega_\infty = \omega_1 + \frac{\sigma_1 \gamma}{\beta} \quad (52)$$

The periodic solution reads

$$\mathbf{u} = \mathbf{u}_0 + a_1 \mathbf{u}_1 + a_2 \mathbf{u}_2, \quad (53)$$

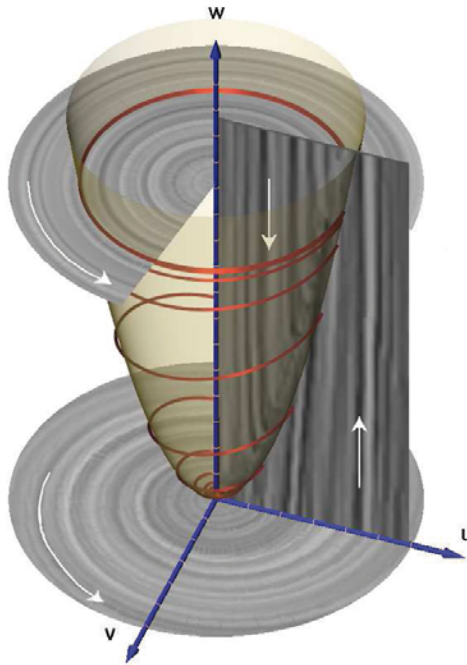


Figure 2. Phase portrait of (48). The red curve shows a transient from the unstable fixed point to the stable limit cycle on the mean-field paraboloid which is indicated by a semi-transparent surface. In the planes, the tangential flow component is visualized. Selected white arrows indicate the direction of the flow. The lower (middle) plane contains the fixed point (limit cycle). The half-plane $v = 0, u > 0$ displays the transient towards the mean-field paraboloid.

where $\mathbf{u}_0 = [0, 0, w_\infty]^\top$ represents the mean, and $\mathbf{u}_1 = [1, 0, 0]^\top$, $\mathbf{u}_2 = [0, 1, 0]^\top$, $a_1 = r_\infty \cos \omega_\infty t$, $a_2 = r_\infty \sin \omega_\infty t$ the harmonic oscillation modulo a phase shift. Not incidentally, (53) is the exact POD of the limit cycle with \mathbf{u}_1 and \mathbf{u}_2 as POD modes and $\lambda_1 = \lambda_2 = r_\infty^2/2$ as eigenvalues. A straight-forward Galerkin projection of the mean-field system (48) on these 2 POD modes yields a marginally stable center

$$\dot{a}_1 = -a_2 \quad \dot{a}_2 = a_1. \quad (54)$$

The Galerkin system (54) illustrates the challenges 2 and 3 of §4.1. The limit cycle is stable in the original 3-dimensional system (48), but only marginally stable in the POD system (54). The POD system contains the periodic solution (53), but also a continuum of unphysical solutions. The truncated dynamics do not resolve the amplitude selection mechanism on the mean-field paraboloid (50) described by the cubic (!) Landau equation (51).

From this example, we can easily infer possible cures for the poorly performing POD Galerkin method. We kinematically include the steady solution in (53) by adding $a_3 \mathbf{e}_3$ to the expansion, i.e. the direction from steady solution \mathbf{u}_s to the mean flow \mathbf{u}_0 . Thus, we restore the full dynamics and associated damping mechanism. The direction may be called *shift-mode* as it shifts the center of the attractor (here: limit cycle). The shift-mode from the mean flow \mathbf{u}_0 and steady solution \mathbf{u}_s is normalized:

$$\mathbf{u}_\Delta = \frac{\mathbf{u}_0 - \mathbf{u}_s}{\|\mathbf{u}_0 - \mathbf{u}_s\|_\Omega}. \quad (55)$$

We assume orthogonality with the POD modes, or enforce orthogonality with a Gram-Schmidt orthonormalization.

The steady unstable Navier-Stokes solution may be difficult to compute. Hence, we search for another approach. Reynolds-averaging of (48) yields only one nontrivial equation, namely the average of the third equation (49c)

$$0 = \sigma_\Delta \bar{w} + \alpha \bar{r^2}.$$

From this equation, we see that a change in the fluctuation level $\bar{r^2}$ immediately affects \bar{w} , i.e. shifts the limit cycle 'up' or 'down' in \mathbf{e}_3 direction. This dynamic consideration also indicates that \mathbf{e}_3 is an important direction to be included in the generalized POD expansion. The pendant for the Navier-Stokes discussion is the Reynolds equation and POD decomposition of the Reynolds stress tensor:

$$\nabla \cdot (\mathbf{u}_0 \mathbf{u}_0) = -\nabla p_0 + \nu \Delta \mathbf{u}_0 - \nabla \cdot \left(\sum_{i=1}^{\infty} \lambda_i \mathbf{u}_i \mathbf{u}_i \right) \quad (56)$$

Evidently, \mathbf{u}_0 varies with changes in each eigenvalue λ_i . This ansatz is elaborated and exploited by Morzyński et al. (2006); Tadmor et al. (2010). For nominally 1-dimensional channel, Couette, or mixing layer flows, the Reynolds equation (56) can be solved directly (Aubry et al., 1988; Ukeiley et al., 2001; Podvin, 2009). The slaving between mean-flow modes and fluctuations leads to cubic terms, like in the Landau equation as an especially simple slaving example.

Deformable oscillatory modes In this section, we address a root cause of the frequently observed narrow dynamic bandwidth of POD models, outlined first by Deane et al. (1991). Let us consider a 1-dimensional, slowly spatially decaying traveling wave

$$u(x, t) = e^{-x/100} \cos [\kappa x - t], \quad x \geq 0, t \geq 0 \quad (57)$$

with wave number $\kappa > 0$ and unit circular frequency. We keep the discussion at a qualitative level. The analytics is presented in Noack (2006); Luchtenburg et al. (2009b). This wave motion is spanned by 2 POD modes $u_{1,2}^\kappa$ of similar energy.

$$u(x, t) = a_1(t) u_1^\kappa(x) + a_2(t) u_2^\kappa(x). \quad (58)$$

This POD is an exact representation for the chosen wave number, say $\kappa = 1$ but quickly deteriorates if κ is slightly, say 10%, of.

Suppose we want to capture a slow transient as κ increases from 1 to 1.5. A first idea may be a 4-dimensional expansion with POD mode pairs at $\kappa = 1$ and $\kappa = 1.5$, targeting a resolution at intermediate wavenumbers. However, superposition leads to an unphysical beat phenomena. A well resolving POD of the transient requires a large number of modes. Examples of this type are POD modes of the cylinder wake under chirp forcing (Bergmann et al., 2005). This large POD basis may lead to suitable models targeting full-information control (Bergmann et al., 2005), i.e. when state estimation is not an issue. For robust sensor-based control, the preservation of least-order representation is a must, since each state space direction can act as noise amplifier.

Strategies to preserve the least-order expansion (58) for variable parameter κ are abundantly offered in literature, mostly for the cylinder wake. A straight-forward example is a look-up table with a 'stack' of expansions at different κ and κ -estimator (Lehmann et al., 2005). Double POD (see the chapter of S. Siegel in this volume) follows a similar logic. Continuous mode (Morzyński et al., 2007) and geodesic interpolation are continuous interpolation variants.

Tracking mode changes is crucial if the model-based control is based on sensors and actuators at different locations (Gerhard et al., 2003), i.e. if POD modes communicate phase differences between input and output. In some cases, slow variations of frequencies and wavenumbers can or shall be ignored in the POD model, e.g. if only the near-wake region is of interest. In this case, POD-based phase averaging techniques (Depardon et al., 2007) can be employed.

Modes for different frequencies Some flows display simultaneously two or more distinct oscillatory structures at different locations. One example is high-frequency forcing to mitigate von Kármán vortex shedding (Thiria et al., 2006; Pastoor et al., 2008). In this case, modes based on extraction of pure frequencies are desirable. Numerous straight-forward techniques are available. Examples are frequency filtering, phase-averaging for natural flow, or linear stochastic estimation (Bonnet et al., 1998) connecting the flow to actuation signal. Corresponding 4-dimensional models for flows with two dominant frequencies have been used for open- and closed-loop control of wakes (Luchtenburg et al., 2010) and flow around airfoils (Luchtenburg et al., 2009a).

General approaches Here, we discuss generalizations of POD comprising multiple operating conditions. Consider, for instance, a flow actuated at 5 different frequencies.

A POD of all operating conditions may be obtained by putting all snapshots in the same 'basket', i.e. performing POD from this enlarged data set. This approach has severe drawbacks: (1) The weighting of each operating condition depends on the number and energy of the individual snapshots at each operating condition. (2) There is no guaranteed minimal resolution at each operating condition. (3) The POD may show unphysical beat phenomena (see §4.2) or the number of modes is unnecessarily large.

Sequential POD (Jørgensen et al., 2003) addresses the first two drawbacks. Here, a minimal resolution at all operating conditions is prescribed. In the first iteration, POD resolves the first data ensemble at prescribed accuracy. In the second iteration, POD modes are added based on the residual of the first expansion with respect to second data ensemble. The new enlarged data set has prescribed accuracy at the first two operating conditions. The procedure is continued until all operating conditions are included.

The mentioned POD generalizations assume given 'off-line' data. Elegant 'online' corrections of POD bases during a simulation or an experiment are obtained with a trust-region (TR) approach (Fahl, 2000; Bergmann and Cordier, 2008). This POD-TR approach is well aligned with the search for least-order representations.

4.3 Modeling natural dynamics

In this section, we model the effect of unresolved fluctuations in the Galerkin system. Periodic flows may be fully resolved by 4 to 10 modes (Deane et al., 1991; Noack et al., 2003, 2005). Transitional flows may require

thousands of modes for a 90% resolution of turbulent kinetic energy (TKE) and a much smaller percentage of the dissipation. The number of modes for fully turbulent flows may be estimated by the Kolmogorov dimension $N \sim Re^{9/4}$ (see, e.g., Landau and Lifshitz (1987)).

The computational load for one time-step integration of a Galerkin system (28) increases with N^3 due to the quadratic term, while the load of grid-based Navier-Stokes solvers increases only linearly with the number of grid points. This limits the practicality of the Galerkin method to $N \sim 100$ or $N \sim 1000$. Robust sensor-based control design poses more severe restrictions on the dimension, say $N \sim 10$. Hence, the Galerkin expansion with N modes will have a non-negligible residual $\delta\mathbf{u}$ for most non-periodic flows:

$$\mathbf{u} = \mathbf{u}_0 + \sum_{i=1}^N a_i \mathbf{u}_i + \delta\mathbf{u}, \quad \text{where} \quad \delta\mathbf{u} = \sum_{i=N+1}^{\infty} a_i \mathbf{u}_i. \quad (59)$$

The error $\delta\mathbf{u}$ leads to a corresponding propagator residual δf_i in the dynamical system (28)

$$\dot{a}_i = c_i + \sum_{j=1}^N l_{ij} a_j + \sum_{j,k=1}^N q_{ijk} a_j a_k + \delta f_i, \quad (60a)$$

$$\delta f_i = \sum_{j=N+1}^{\infty} l_{ij} a_j + \sum_{\substack{j,k=1 \\ \max\{j,k\} > N}}^{\infty} q_{ijk} a_j a_k. \quad (60b)$$

Model development for δf_i is guided by the picture that first N modes represent low to dominant frequencies $\omega \lesssim \omega_c$, while the residual describes large frequencies $\omega \gg \omega_c$. The linear term of δf_i in (60b) contributes with higher frequencies in (60a) and can loosely be interpreted as noise. The quadratic term of δf_i in (60b) will show the whole frequency spectrum.

First, we estimate the average of the propagator residual from the Galerkin-Reynolds equation (39)

$$0 = c_i + \underbrace{\sum_{j=1}^N 2q_{ijj} K_j}_{\text{resolved}} + \underbrace{\sum_{j=N+1}^{\infty} 2q_{ijj} K_j}_{\text{from } \delta f_i}. \quad (61)$$

The last term can be considered negligible with respect to the middle term, assuming that the coherent structures resolved by N modes characterize the Reynolds-stress tensor.

Secondly, we investigate the energetic effect of the propagator residual and make the ansatz $\delta f_i = d_i a_i$. From turbulence theory, we expect a

dissipative effect of the small-scale structures, i.e. a negative growth rate d_i . The modal energy equation (45) implies for (60b) following consistency condition for the modal power $a_i \delta f_i$

$$2d_i K_i = \sum_{\substack{j,k=1 \\ \max\{j,k\} > N}}^{\infty} q_{ijk} \overline{a_i} \overline{a_j} \overline{a_k}. \quad (62)$$

Note that the linear term of the propagator residual does not contribute to that balance. On the attractor, (62) defines a unique (constant) value d_i^∞ .

Rempfer and Fasel (1994) reason that the propagator residual has a similar effect than a 'modal eddy viscosity' ν_i^T , i.e. $\delta f_i = \nu_i^T \sum_{j=0}^N l_{ij}^\nu a_j$, following the very ideas of Boussinesq, Prandtl and Smagorinsky adopted in computational fluid mechanics. The value ν_i^T is obtained from the modal TKE equation. This ansatz yields $d_i = \nu_i^T l_{ii}^\nu$. In fact, most authors employ a linear term representing the nonlinear effect of small-scale turbulence. This ansatz appears to work well for small-bandwidth dynamics, e.g. laminar and transitional flows, without additional stabilizers.

For broadband turbulence, diverging Galerkin solutions are frequently observed (yet rarely published). One reason can be attributed to the fact that the nonlinearities have a stronger damping effect at high fluctuation levels than the postulated linear term. We estimate the correct scaling by assuming that the modal energies $K_i = \kappa_i K$ have a constant non-negative share $\kappa_i \geq 0$ in the total TKE K . Here, $\sum_{i=1}^N \kappa_i = 1$ and K is considered as a free parameter. The right-hand side of (62) can be approximated with the FTT closure equation (47d). Thus, (62) becomes after division by $2\kappa_i K$

$$d_i = \frac{1}{2\kappa_i} \left[\sum_{\substack{j,k=1 \\ \max\{j,k\} > N}}^{\infty} \alpha \chi_{ijk} \sqrt{\kappa_i \kappa_j \kappa_k} \left(1 - \frac{3\kappa_i}{\kappa_i + \kappa_j + \kappa_k} \right) \right] K^{1/2}.$$

The term in the square brackets is independent of K . Hence, this equation implies that the growth-rate d_i scales with $K^{1/2}$. In other words, the identified attractor value d_i^∞ should be corrected with a corresponding factor

$$d_i = d_i^\infty \sqrt{\frac{K}{K^\infty}}, \quad (63)$$

where K^∞ is total TKE on the Navier-Stokes attractor. In practice and without loss of generality, K can be assumed to be the resolved fluctuation energy. A POD model of a turbulent jet (Schlegel et al., 2009) was found to be stable when using the new scaling (63) and diverging during some

corona bursts when assuming a constant value. Similarly, an FTT-based eddy viscosity (Noack et al., 2010) is derived for periodic flows leading to $d_i \sim K$ scaling. The ad-hoc reasoning leading to (63) may be subject to numerous concerns and refinements. At minimum, a new potential direction for future 'subgrid' turbulence representations δf_i is offered.

4.4 Modeling actuation effects

We derive the forcing term in Galerkin system (27) for volume force actuation §4.4 and for boundary actuation §4.4. Finally (§4.4), a recipe is given for identifying a forcing term from data.

Volume force actuation The flow may be actuated with volume force. Examples are magnetohydrodynamic (MHD) forces, the buoyancy term in the Boussinesq approximation, and fictitious forces from choosing a body-fixed coordinate system of a moving body.

In general, the volume force can be expressed or approximated by a modal expansion in space-dependent carrier fields \mathbf{g}_i and time-dependent actuation amplitudes b_i ,

$$\mathbf{g}(\mathbf{x}, t) = \sum_{i=1}^{N_V} b_i(t) \mathbf{g}_i(\mathbf{x}). \quad (64)$$

The Galerkin representation for $N_V = 1$ is derived in §2.4. For larger number of volume force modes N_V , superposition yields

$$\dot{a}_i = f_i(\mathbf{a}) + \sum_{j=1}^N g_{ij} b_j, \quad (65)$$

where f_i is the propagator for the unactuated dynamics and $g_{ij} := (\mathbf{u}_i, \mathbf{g}_j)_\Omega$ are the gains from the volume force modes.

Boundary actuation The flow may be manipulated with suction and blowing at the boundary $\partial\Omega$. Contrary to the stationary boundary condition (3), we now impose a time-dependent velocity. A Galerkin-type expansion with N_A modes shall represent this distribution,

$$\mathbf{u}_{BC}(\mathbf{x}, t) = \sum_{i=-N_A}^{-1} a_i(t) \mathbf{u}_i(\mathbf{x}), \quad \mathbf{x} \in \partial\Omega. \quad (66)$$

Here, \mathbf{u}_i may characterize the exit profile of a local actuator and a_i denotes the amplitude. Straightforward POD Galerkin method will slave actuation

and flow dynamics, i.e. the actuation is reconstructed from the Galerkin system. One example is a Galerkin model for the Kelvin-Helmholtz vortices excited by a stability eigenmode at the inlet (Noack et al., 2005). The Galerkin model 'sees' that only one actuation is consistent with the POD and Navier-Stokes equation. The same observation applies to any Galerkin model on subdomains with inflow and outflow.

However, a straight-forward Galerkin projection will not reveal the effect of this forcing as free input, since only a zero-set of the whole domain is affected. This input can be 'freed' as follows. (66) is generalized for the whole domain Ω by introducing incompressible actuation modes \mathbf{u}_i , $i < 0$,

$$\mathbf{u}^{[-N_A \dots -1]}(\mathbf{x}, t) = \sum_{i=-N_A}^{-1} a_i(t) \mathbf{u}_i(\mathbf{x}). \quad (67)$$

(66) and (67) coincide on the boundary. The choice of the actuation mode is largely a design parameter. One example is a potential vortex representing rotations of a circular cylinder (Bergmann et al., 2005). A more general strategy is offered by Kasnakoglu et al. (2008). Now, POD retaining N modes is performed on the remainder $\mathbf{u} - \mathbf{u}^{[-N_A \dots -1]}$. The resulting expansion reads

$$\mathbf{u}(\mathbf{x}, t) = \sum_{i=-N_A}^N a_i(t) \mathbf{u}_i(\mathbf{x}). \quad (68)$$

Note that $a_0 \equiv 1$, a_i with $i < 0$ are predetermined actuation amplitudes and a_i with $i > 0$ represent POD mode amplitudes. (68) fulfills exactly the incompressibility condition (*GM1*) and the new unsteady boundary conditions for any choice of the a_i , $i > 0$ (*GM2*) of §2.2.

Galerkin projection of (1b) on (68) yields

$$\dot{a}_i = \nu \sum_{j=-N_A}^N l_{ij}^\nu a_j + \sum_{j,k=-N_A}^N \left(q_{ijk}^c + q_{ijk}^p \right) a_j a_k - \sum_{j=-N_A}^{-1} m_{ij} \dot{a}_j. \quad (69)$$

The terms of dynamical system generalize (27) by a larger index set of modes. The last new term with the mass matrix $m_{ij} = (\mathbf{u}_i, \mathbf{u}_j)_\Omega$, $i > 0$, $j < 0$ arises from the local acceleration term and the non-orthonormality between actuation and POD modes.

POD Galerkin models with actuation modes have been constructed for wakes behind rotating (Graham et al., 1999; Bergmann et al., 2005), oscillating circular cylinders (Noack et al., 2004), and local actuation (Weller et al., 2009).

Identification of a forcing term In aerodynamic flow control applications, small actuators may effect large-scale coherent structures. In principle, such actuation can be derived from a priori consideration. In practice, a low-order Galerkin model is expressly designed to ignore the kinematics of small-scale phenomena. For the effect on the large-scale dynamics, a forcing term needs to be identified. The *structure identification* of the analytical form of this term may be based on the Navier-Stokes equation. The *parameter identification* utilizes available data.

In the sequel, we outline a simple identification technique which has been employed in a number of turbulence control studies with periodic forcing (Luchtenburg et al., 2009a, 2010; John et al., 2010). Let f_i be the propagator of the natural dynamics and b be the amplitude of a local actuator. Then, we postulate a forced system of the form

$$\dot{a}_i = f_i(\mathbf{a}) + g_{1i}b + g_{2i}\dot{b}. \quad (70)$$

This form can be derived from a priori considerations (Luchtenburg et al., 2009a). The forcing term may be considered as two pseudo volume forces. The last term with \dot{b} is often neglected but nevertheless important. This term allows the actuation b to 'hit' each mode with the right phase. The gains can be inferred from the mode amplitudes $t \mapsto \mathbf{a} = \mathbf{a}^a$ and control $t \mapsto b$ of the reference simulation or experiment with actuation. Substituting this actuated solution in (70), multiplication with b or \dot{b} , averaging, and exploiting $\overline{b\dot{b}} = 0$ for long time intervals yields the formula for the gains:

$$g_{1i} = \overline{(\dot{a}_i^a - f_i(\mathbf{a}^a))\overline{b}/\overline{b^2}}, \quad (71a)$$

$$g_{2i} = \overline{(\dot{a}_i^a - f_i(\mathbf{a}^a))\dot{b}/\dot{b^2}}. \quad (71b)$$

For periodic actuation $b = B \cos \omega^a t$, this procedure implies dynamical system consistency with respect to the first actuated harmonics, i.e. projections on $\cos \omega^a t$ and $\sin \omega^a t$.

5 Conclusions and Outlook

We have outlined the mathematical frame-work for reduced-order Galerkin models, particularly for empirical variants based on POD. In §2, we elaborated a standard operating procedure. This should allow an interested reader to build a corresponding model for his/her data. Important physics insights for modeling and control are gained from refined statistical analyses of the Navier-Stokes equation, as outlined in §3. In §4, we have attempted to give a trouble shooting guide for ROM of turbulent flows and its control. This guide starts with physical mechanisms which may not be resolved

for a particular configuration and ends with recipes which have proven to work for many cases. The next chapter by G. Tadmor et al. will outline applications for nonlinear laminar wake stabilization.

Reduced-order modeling is under rapidly evolving development in an increasing number of institutes involving more and more interdisciplinary research initiatives. Its potential is far from being exploited. The low dimension of the Galerkin model makes it

- an ultimate testbed of the gained physical understanding,
- a link to nonlinear dynamics analyses,
- a numerically tractable framework for mathematical turbulence theory,
- a necessity for many control designs, and
- an exciting door-opener to many system-reduction methods of theoretical physics.

Current turbulence control applications indicate a pressing need for understanding the nonlinearities of the turbulence cascade and actuation effects — transcending the current possibilities of available knowledge. ROM offer an ideal plant for these investigations (Luchtenburg et al., 2010).

As word of warning, we mention that the Galerkin method is an essentially elliptic approach for often hyperbolic Navier-Stokes dynamics. The very ansatz, the Galerkin expansion with global modes, assumes a globally synchronized flow dynamics. This may be a good approximation of internal flows or of the neighborhood of a recirculation bubble in open flows. On contrary, the Galerkin model is not well suited for transient shear flows with nearly uni-directional 'hyperbolic' convection of vortices (Noack et al., 2005). A cure may be provided in form of local modes or coupled Galerkin models. As alternative, vortex methods (Cottet and Koumoutsakos, 2000; Pastoor et al., 2008) provide more robust reduced-order models. However, the hybrid nature of vortex models challenges control design methods due to continuous injection, removal or merging of states (vortices).

Bibliography

- K. Afanasiev. *Stabilitätsanalyse, niedrigdimensionale Modellierung und optimale Kontrolle der Kreiszylinderumströmung* (transl.: *Stability analysis, low-dimensional modelling, and optimal control of the flow around a circular cylinder*). PhD thesis, Fakultät Maschinenwesen, Technische Universität Dresden, 2003.
- E. Åkervik, J. Hoepffner, U. Ehrenstein, and D. S. Henningson. Optimal growth, model reduction and control in separated boundary-layer flow using global eigenmodes. *J. Fluid Mech.*, 579:305–314, 2007.

- B. Andresen. *Finite-Time Thermodynamics*. Physics Laboratory II, University of Copenhagen, Copenhagen, 1983.
- N. Aubry, P. Holmes, J. L. Lumley, and E. Stone. The dynamics of coherent structures in the wall region of a turbulent boundary layer. *J. Fluid Mech.*, 192:115–173, 1988.
- P. F. Batcho. *Global Spectral Methods for the Solution of the Incompressible Navier-Stokes Equations in Complex Geometries: The Generalized Stokes Eigensystem*. PhD thesis, Princeton University, 1994.
- M. Bergmann and L. Cordier. Optimal control of the cylinder wake in the laminar regime by Trust-Region methods and POD Reduced Order Models. *J. Comp. Phys.*, 227:7813–7840, 2008.
- M. Bergmann, L. Cordier, and J.-P. Branger. Optimal rotary control of the cylinder wake using proper orthogonal decomposition reduced order model. *Phys. Fluids*, 17:097101–1...21, 2005.
- J.-P. Bonnet, D.R. Cole, J. Delville, M. N. Glauser, and L. S. Ukeiley. Stochastic estimation and proper orthogonal decomposition — complementary techniques for identifying structure. *Exp. Fluids*, 17:307–314, 1998.
- F. H. Busse. Numerical analysis of secondary and tertiary states of fluid flow and their stability properties. *Appl. Sci. Res.*, 48:341–351, 1991.
- L. Cordier and M. Bergmann. Proper orthogonal decomposition: An overview. In P. Millan and M.L. Riethmuller, editors, *Post-Processing of Experimental and Numerical Data*, VKI Lecture Series 2003-03. Von Kármán Institut for Fluid Dynamics, 2003.
- L. Cordier, B. Abou El Majd, and J. Favier. Calibration of POD reduced-order models by Tikhonov regularization. *Internat. J. Numer. Meth. Fluids*, 63(2), 269–296, 2010.
- G. H. Cottet and P. Koumoutsakos. *Vortex Methods — Theory and Practice*. Cambridge University Press, Cambridge, 2000.
- A. E. Deane, I. G. Kevrekidis, G. E. Karniadakis, and S. A. Orszag. Low-dimensional models for complex geometry flows: Application to grooved channels and circular cylinders. *Phys. Fluids A*, 3:2337–2354, 1991.
- S. Depardon, J. J. Lasserre, L. E. Brizzi, and J. Borée. Automated topology classification method for instantaneous velocity fields. *Exp. Fluids*, 42: 697–710, 2007.
- M. Fahl. *Trust-region methods for flow control based on reduced order modeling*. PhD thesis, Universität Trier, 2000.
- C. A. J. Fletcher. *Computational Galerkin Methods*. Springer, New York, 1st edition, 1984.
- G. Galletti, C. H. Bruneau, L. Zannetti, and A. Iollo. Low-order modelling of laminar flow regimes past a confined square cylinder. *J. Fluid Mech.*, 503:161–170, 2004.

- J. Gerhard, M. Pastoor, R. King, B. R. Noack, A. Dillmann, M. Morzyński, and G. Tadmor. Model-based control of vortex shedding using low-dimensional Galerkin models. *AIAA-Paper 2003-4262, 33rd AIAA Fluids Conference and Exhibit*, 2003.
- W. R. Graham, J. Peraire, and K. Y. Tang. Optimal control of vortex shedding usind low-order models. Part I — Open-loop model development. *Int. J. Numer. Meth. Engrng.*, 44:945–972, 1999.
- C. E. Grosch and H. Salwen. The continuous spectrum of the Orr-Sommerfeld equation. Part I. The spectrum and the eigenfunctions. *J. Fluid Mech.*, 87:33–54, 1978.
- H. Haken. *Synergetics, An Introduction. Nonequilibrium Phase Transitions and Self-Organizations in Physics, Chemistry, and Biology*. Springer, New York, 3rd edition, 1983.
- P. Holmes, J. L. Lumley, and G. Berkooz. *Turbulence, Coherent Structures, Dynamical Systems and Symmetry*. Cambridge University Press, Cambridge, 1st paperback edition, 1998.
- C. John, B. R. Noack, M. Schlegel, F. Tröltzsch, and D. Wachsmuth. Optimal boundary control problems related to high lift configurations. In R. King, editor, *Active Flow Control II, Notes on Numerical Fluid Mechanics and Multidisciplinary Design*, Vol. 108, pages 405–419. Springer-Verlag, 2010.
- B. H. Jørgensen, J. N. Sørensen, and M. Brøns. Low-dimensional modeling of a driven cavity flow with two free parameters. *Theoret. Comput. Fluid Dynamics*, 16:299–317, 2003.
- D. D. Joseph. *Stability of Fluid Motions I & II*. Springer Tracts in Natural Philosophy - Vol. 26 & 27. Springer, Berlin, Heidelberg, New York, 1976.
- C. Kasnakoglu, A. Serrani, and M. O. Efe. Control input separation by actuation mode expansion for flow control problems. *Internat. J. Control.*, 81(9):1475–1492, 2008.
- R. H. Kraichnan and S. Chen. Is there a statistical mechanics of turbulence? *Phys. D*, 37:160–172, 1989.
- O. A. Ladyzhenskaya. *The Mathematical Theory of Viscous Incompressible Flow*. Gordon and Breach, New York, London, 1st edition, 1963.
- L. D. Landau and E. M. Lifshitz. *Fluid Mechanics*. Course of Theoretical Physics, Vol. 6. Pergamon Press, Oxford, 2nd engl. edition, 1987.
- O. Lehmann, M. Luchtenburg, B. R. Noack, R. King, M. Morzyński, and G. Tadmor. Wake stabilization using POD Galerkin models with interpolated modes. Invited Paper MoA15.2 of the *44th IEEE Conference on Decision and Control and European Control Conference ECC*, 2005.
- M. Lesieur. *Turbulence in Fluids*. Kluwer Academic Publishers, Dordrecht, Boston, London, 2nd edition, 1993.

- E. N. Lorenz. Deterministic nonperiodic flow. *J. Atm. Sci.*, 20:130–141, 1963.
- D. M. Luchtenburg, B. Günter, B. R. Noack, R. King, and G. Tadmor. A generalized mean-field model of the natural and actuated flows around a high-lift configuration. *J. Fluid Mech.*, 623:283–316, 2009a.
- D. M. Luchtenburg, B. R. Noack, and M. Schlegel. An introduction to the POD Galerkin method for fluid flows with analytical examples and MATLAB source codes. Technical Report 01/2009, Chair in Reduced-Order Modelling for Flow Control, Department of Fluid Dynamics and Engineering Acoustics, Berlin Institute of Technology, Germany, 2009b.
- D. M. Luchtenburg, M. Schlegel, B. R. Noack, K. Aleksić, R. King, G. Tadmor, and B. Günther. Turbulence control based on reduced-order models and nonlinear control design. In R. King, editor, *Active Flow Control II*, Notes on Numerical Fluid Mechanics and Multidisciplinary Design, Vol. 108, pages 341–356. Springer-Verlag, 2010.
- X. Ma and G. E. Karniadakis. A low-dimensional model for simulating three-dimensional cylinder flow. *J. Fluid Mech.*, 458:181–190, 2002.
- J. Moehlis, T. R. Smith, P. Holmes, and H. Faisst. Models for turbulent plane Couette flow using the proper orthogonal decomposition. *Phys. Fluids*, 14:2493–2507, 2002.
- A. S. Monin and A. M. Yaglom. *Statistical Fluid Mechanics I*. The MIT Press, Cambridge, Massachusetts, and London, 1971.
- A. S. Monin and A. M. Yaglom. *Statistical Fluid Mechanics II*. The MIT Press, Cambridge, Massachusetts, and London, 1975.
- M. Morzyński, W. Stankiewicz, B. R. Noack, F. Thiele, and G. Tadmor. Generalized mean-field model for flow control using continuous mode interpolation. Invited AIAA-Paper 2006-3488 of the *3rd AIAA Flow Control Conference*, 2006.
- M. Morzyński, W. Stankiewicz, B. R. Noack, R. King, F. Thiele, and G. Tadmor. Continuous mode interpolation for control-oriented models of fluid flow. In R. King, editor, *Active Flow Control*, Notes on Numerical Fluid Mechanics and Multidisciplinary Design, Vol. 95, pages 260–278. Springer-Verlag, 2007.
- B. R. Noack. *Niederdimensionale Galerkin-Modelle für laminare und transitionelle freie Scherströmungen* (transl.: *low-dimensional Galerkin models of laminar and transitional free shear flows*). Habilitation thesis, Berlin Institute of Technology, Germany, 2006.
- B. R. Noack and H. Eckelmann. A global stability analysis of the steady and periodic cylinder wake. *J. Fluid Mech.*, 270:297–330, 1994a.
- B. R. Noack and H. Eckelmann. A low-dimensional Galerkin method for the three-dimensional flow around a circular cylinder. *Phys. Fluids*, 6: 124–143, 1994b.

- B. R. Noack, K. Afanasiev, M. Morzyński, G. Tadmor, and F. Thiele. A hierarchy of low-dimensional models for the transient and post-transient cylinder wake. *J. Fluid Mech.*, 497:335–363, 2003.
- B. R. Noack, G. Tadmor, and M. Morzyński. Actuation models and dissipative control in empirical Galerkin models of fluid flows. Paper **FrP15.6** of the *The 2004 American Control Conference*, 2004.
- B. R. Noack, P. Papas, and P. A. Monkewitz. The need for a pressure-term representation in empirical Galerkin models of incompressible shear flows. *J. Fluid Mech.*, 523:339–365, 2005.
- B. R. Noack, M. Schlegel, B. Ahlborn, G. Mutschke, M. Morzyński, P. Comte, and G. Tadmor. A finite-time thermodynamics of unsteady fluid flows. *J. Non-Equilibr. Thermodyn.*, 33:103–148, 2008.
- B. R. Noack, M. Schlegel, M. Morzyński, and G. Tadmor. System reduction strategy for Galerkin models of fluid flows. *Internat. J. Numer. Meth. Fluids*, 63(2), 231–248, 2010.
- M. Pastoor, L. Henning, B. R. Noack, R. King, and G. Tadmor. Feedback shear layer control for bluff body drag reduction. *J. Fluid Mech.*, 608: 161–196, 2008.
- B. Podvin. A proper-orthogonal-decomposition based for the wall layer of a turbulent channel flow. *Phys. Fluids*, 21:015111–1...18, 2009.
- D. Rempfer. *Empirische Eigenfunktionen und Galerkin-Projektionen zur Beschreibung des laminar-turbulenten Grenzschichtumschlags* (transl.: *Empirical eigenfunctions and Galerkin projection for the description of the laminar-turbulent boundary-layer transition*). Habilitation thesis, Fakultät für Luft- und Raumfahrttechnik, Universität Stuttgart, 1995.
- D. Rempfer. On low-dimensional Galerkin models for fluid flow. *Theoret. Comput. Fluid Dynamics*, 14:75–88, 2000.
- D. Rempfer and F. H. Fasel. Dynamics of three-dimensional coherent structures in a flat-plate boundary-layer. *J. Fluid Mech.*, 275:257–283, 1994.
- C. W. Rowley, I. Mezić, S. Bagheri, P. Schlatter and D.S. Henningson. Spectral analysis of nonlinear flows. *J. Fluid Mech.*, 641:115–127, 2009.
- B. Rummel. *Zur Lösung der instationären inkompressiblen Navier-Stokes-Gleichungen in speziellen Gebieten* (transl.: *On the solution of the incompressible Navier-Stokes equations in some domains*). Habilitation thesis, Fakultät für Mathematik, Otto-von-Guericke-Universität Magdeburg, 2000.
- H. Salwen and C. E. Grosch. The continuous spectrum of the Orr-Sommerfeld equation. Part 2. Eigenfunction expansions. *J. Fluid Mech.*, 104:445–465, 1981.
- M. Schlegel, B. R. Noack, P. Comte, D. Kolomenskiy, K. Schneider, M. Farge, J. Scoutingen, D. M. Luchtenburg, and G. Tadmor. *Reduced-order*

-
- modelling of turbulent jets for noise control*, pages 3–27. In C. Brun, D. Juvé, M. Manhart, and C.-D. Munz, editors, *Numerical Simulation of Turbulent Flows and Noise Generation*, Notes on Numerical Fluid Mechanics and Multidisciplinary Design (NNFM), Vol. 104, pages 3–27. Springer-Verlag, 2009.
- P. J. Schmid. Dynamic mode decomposition for numerical and experimental data. *J. Fluid. Mech.* (in press), 2010.
- S. G. Siegel, J. Seidel, C. Fagley, D. M. Luchtenburg, K. Cohen, and T. McLaughlin. Low dimensional modelling of a transient cylinder wake using double proper orthogonal decomposition. *J. Fluid Mech.*, 610:1–42, 2008.
- L. Sirovich. Turbulence and the dynamics of coherent structures, Part I: Coherent structures. *Quart. Appl. Math.*, XLV:561–571, 1987.
- G. Tadmor and B. R. Noack. Dynamic estimation for reduced Galerkin models of fluid flows. Paper **WeM18.1** of the *The 2004 American Control Conference*, 2004.
- G. Tadmor, O. Lehmann, B. R. Noack, and M. Morzyński. Mean field representation of the the natural and actuated cylinder wake. *Phys. Fluids* 22 (3), 034102-1...22, 2010.
- B. Thiria, S. Goujon-Durand, and J. E. Wesfreid. The wake of a cylinder performing rotary oscillations. *J. Fluid Mech.*, 560:123–147, 2006.
- L. Ukeiley, L. Cordier, R. Manceau, J. Delville, J. P. Bonnet, and M. Glauser. Examination of large-scale structures in a turbulent plane mixing layer. Part 2. Dynamical systems model. *J. Fluid Mech.*, 441: 61–108, 2001.
- M. Wei and C. W. Rowley. Low-dimensional models of a temporally evolving free shear layer. *J. Fluid Mech.*, 618:113–134, 2009.
- J. Weller, E. Lombardi, and A. Iollo. Robust model identification of actuated vortex wakes. *Physica D*, 238:416–427, 2009.

Galerkin Models Enhancements for Flow Control

Gilead Tadmor[†], Oliver Lehmann[†],
Bernd R. Noack[‡], and Marek Morzyński[§]

[†]Electrical & Comp. Engineering Department, Northeastern University, Boston,
MA 02115, USA, tadmor@coe.neu.edu, olehmann@coe.neu.edu

[‡]Institute Pprime, CNRS – Université de Poitiers – ENSMA, UPR 3346,
Département Fluides, Thermique, Combustion, CEAT, 43, rue de l'Aérodrome,
F-86036 Poitiers cedex, France, bernd.noack@univ-poitiers.fr

[§]Poznań University of Technology, Institute of Combustion Engines and
Transportation, PL 60-965 Poznań, Poland, marek.morzynski@put.poznan.pl

Abstract Low order Galerkin models were originally introduced as an effective tool for stability analysis of fixed points and, later, of attractors, in nonlinear distributed systems. An evolving interest in their use as low complexity dynamical models, goes well beyond that original intent. It exposes often severe weaknesses of low order Galerkin models as dynamic predictors and has motivated efforts, spanning nearly three decades, to alleviate these shortcomings. Transients across natural and enforced variations in the operating point, unsteady inflow, boundary actuation and both aeroelastic and actuated boundary motion, are hallmarks of current and envisioned needs in feedback flow control applications, bringing these shortcomings to even higher prominence. Building on the discussion in our previous chapters, we shall now review changes in the Galerkin paradigm that aim to create a mathematically and physically consistent modeling framework, that remove what are otherwise intractable roadblocks. We shall then highlight some guiding design principles that are especially important in the context of these models. We shall continue to use the simple example of wake flow instabilities to illustrate the various issues, ideas and methods that will be discussed in this chapter.

1 Introduction

The essence of feedback control is the ability to utilize realtime sensing, decision making and actuation, to manipulate the unsteady dynamics of a system subject to disturbances, uncertainties and time variations in the

operating regime over a wide range of time scales. One of a multitude of pertinent examples that come to mind is the aerodynamic control of a small unmanned air vehicle (UAV / MAV): Indeed, the UAV may have to track far more complex flight trajectories, and face changes in wind speed and orientation, let alone the impact of irregular gusts on aerodynamic forces, that are far higher, in relative terms, than in the case of larger aircraft. This example therefore brings into sharp relief the significance of unsteadiness in feedback control applications that are the subject matter of the yet nascent field of feedback flow control.

Models used in feedback design and implementation reflect the need to reconcile the conflicting demands of precision, time horizon and dynamic envelope, on the one hand, and complexity restrictions imposed by analytic design methods and feasible realtime computations, on the other hand. An ensemble of mathematically rigorous methods to address this balancing act has been developed within mainstream linear systems theory: With a high fidelity, high order model as a starting point, operator theoretic model reduction procedures are associated with provable error bounds that quantify the tradeoff between simplicity, precision and closed loop performance (Antoulas, 2005; G. Obinata, 2000; Sánchez-Peña and Sznaier, 1998). The feasibility of that level of rigor is largely lost in complex, nonlinear systems. In fact, even the computations required by linear reduced order models, e.g., the solution of Lyapunov and Riccati equations, become a formidable task at very high nominal dimension, requiring an appeal to simulation based approximations (Rowley, 2005). Adaptation of linear methods to nonlinear systems, analytical methods based on differential-geometric, energy and stochastic dynamical systems considerations, are often based on asymptotic convergence arguments, heuristics and, at best, on local error bounds (Nijmeijer and van der Schaft, 1990; Rowley et al., 2003; Mezić, 2005; Homescu et al., 2005; Gorban et al., 2006; Schilders et al., 2008).

The combined effects of nonlinearity, high dimension and the rich dynamic repertoire of fluid mechanical systems, bring the tension between model precision, dynamic envelope and simplicity demands to an extreme. This tension has lead to the evolution of low order models, identified directly from experimental or simulation models, as alternatives to the top-down, model reduction approach. Notable examples include black box linear models (Cattafesta et al., 2008), low order Galerkin models (Holmes et al., 1998), and more sporadically, Lagrangian vortex models (Protas, 2008). Yet these alternative approaches lack a rigorous supportive theory that explicitly quantifies the tradeoff between model fidelity and its complexity. Indeed, despite decades of efforts, low order models of natural and actuated fluid flow systems often fail to meet the needs of viable engineering design.

Following on the authors' previous two chapters, we maintain our focus on Galerkin models, and direct the reader to those chapters for a discussion motivating this focus. Our purpose here is to further elucidate the root causes for pronounced shortcomings and failures of prevalent low order Galerkin modeling methods, and to use these observations as a basis for the development of an extended framework of Galerkin models on nonlinear manifolds. Specifically, we shall review inherent conflicts between the traditional Galerkin paradigm and the requirements of flow control applications, which give rise to persistent failures, and develop the proposed framework, expressly, to remove these inconsistencies. Finally, we will highlight essential guidelines for the utilization of the new paradigm in flow control design. The discussion will cover aspects of mean field theory, turbulence models, mode deformation, actuation models and forced and elastic boundary motion.

Nomenclature and formalism. Unless otherwise stated, the mathematical formalisms and nomenclature used in this chapter follow those set in the appendix and used in our previous chapter, by Noack et al. To facilitate reading we shall nonetheless remind the reader, of some of these conventions when using them.

2 Benchmark Model Systems

We shall use two model systems to illustrate the discussion in this chapter: The laminar wake flow behind a two dimensional cylinder at the Reynolds number $Re = 100$, will continue to be used as the main running example. The separated, turbulent flow over a two dimensional airfoil at a high angle of attack, at $Re = 10^6$, will be used as a supplementary example, to illustrate peculiar aspects of high frequency actuation. This section reviews the geometry, the postulated actuators, and some basic facts regarding the dynamics of these two examples. It also serves as a reminder of some of our basic nomenclature.

2.1 The Cylinder Wake

The two dimensional flow in the wake of a circular cylinder is an extensively studied canonical configuration. A systematic analysis of the instability of the steady flow and of the nature of a characteristic periodic attractor were first introduced in the celebrated work of von Kármán (von Kármán and Rubach, 1912), a century ago, with numerous subsequent studies in diverse natural and actuated contexts, continuing to the present day. The general interest and our own selection of this configuration stem from the

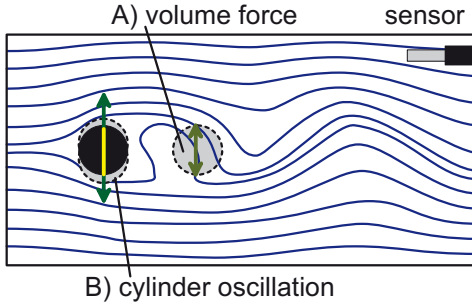


Figure 1. The actuated cylinder wake: The cylinder is represented by the black disk. The downstream circle and arrows indicate the location and orientation of a volume-force actuator. The vertical arrows across the cylinder represent controlled vertical oscillations as an alternative, second form of actuation. Streamlines represent a snapshot of the natural flow.

fact that it is one of the simplest possible examples of the bifurcations from potential to vortical flow, at $Re \approx 4$, and then, to periodic instability with the emergence of vortex shedding and the von Kármán vortex street, at $Re \approx 47$ (Noack and Eckelmann, 1994; Williamson, 1996; Barkley, 2006).

2.2 The Actuated Cylinder Wake Configuration

Figure 1 depicts the key elements of this example. As in previous discussions, the incoming flow and the transverse direction are aligned with the x and y coordinates, respectively. The cylinder is represented by the black disk, in that figure:

$$\Omega_D = \{\mathbf{x} \in \mathcal{R}^2 : \|\mathbf{x}\| \leq 1/2\}. \quad (1)$$

The flow is represented by streamlines over the area of the computational domain surrounding the cylinder:

$$\Omega = \{\mathbf{x} = (x, y) \in \mathcal{R}^2 \setminus \Omega_D : x \in [-5, 15], y \in [-5, 5], x \notin \Omega_D\}. \quad (2)$$

As in the previous chapter, the velocity field is $\mathbf{u} = (u, v)$. Length and velocity are normalized with respect to the cylinder diameter and the horizontal incoming flow velocity U . We consider this configuration at the Reynolds number of $Re = 100$, well above the transition to instability and yet well within the laminar regime.

Periodic vortex shedding leads to often undesirable mechanical vibrations and a generic control objective is to attenuate this instability. Figure 1 includes two forms of actuation that can be used to that end:

One is a vertical volume-force, defined over a downstream disk Ω_{vf} :

$$\begin{aligned} \mathbf{f}(\mathbf{x}, t) &= b(t) \mathbf{g}(\mathbf{x}), \quad \text{where} \\ \mathbf{g}(\mathbf{x}) &= \begin{cases} (0, 1) & \mathbf{x} \in \Omega_{vf} \\ (0, 0) & \text{otherwise,} \end{cases} \\ \Omega_{vf} &= \{\mathbf{x} \in \mathcal{R}^2 : \|\mathbf{x} - (0, 2)\| \leq 1\}, \end{aligned} \quad (3)$$

The volume force may be viewed as mimicking an electro-hydrodynamic (EHD) actuator (D'Adamo et al., 2009). Volume force representations are also commonly used as a simple way to include boundary actuation, such as pulsating jets and zero-net-flux actuators (Glezer and Amitay, 2002) in both CFD and reduced order models (Ahuja et al., 2007; Joe et al., 2008). We shall revisit this point in the discussion of outstanding modeling challenges. The discussion of volume force actuation will refer to a number of studies by our group, including Gerhard et al. (2003); Noack et al. (2004b); Tadmor et al. (2004); Noack et al. (2004a); Tadmor and Noack (2004); Lehmann et al. (2005); Luchtenburg et al. (2006); Tadmor et al. (2010).

To attenuate vortex shedding, actuation policies will be designed to dissipate the kinetic energy of the oscillatory flow field as an opposing force. Actuation will therefore be periodically modulated, taking the form

$$b(t) = B \cos(\psi(t)). \quad (4)$$

Under such a policy, the oscillations phase ψ is assigned by a feedback controller to apply a decelerating force on the oscillatory vertical component of the flow field \mathbf{u} over Ω_{vf} . The actuation frequency $\dot{\psi}$ must therefore match the shedding frequency.

The second form of forcing shown in Figure 1 is the vertical oscillation of the cylinder. Once again, this is a simple example of a broad array of dynamic fluid body interactions that range from controlled boundary motion to elastic deformations and disturbance driven boundaries, under diverse scenarios of engineered and natural systems. The particular example of the oscillatory-actuated cylinder has been studied by our team, in Noack et al. (2004b); Tadmor et al. (2004); Noack et al. (2004a); Tadmor and Noack (2004), and by this volume's co-author, S. Siegel and collaborators, as described in Siegel et al. (2008).

A postulated sensor is also shown in Figure 1. The sensor measures one or two components of the velocity field, and represents one of several

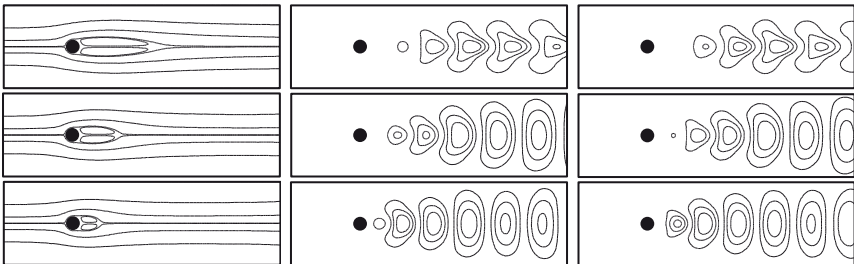


Figure 2. Least order local representations of the unsteady cylinder wake flow at $Re = 100$, from a small perturbation the unstable, steady solution \mathbf{u}_s (top row), through a mid-transient period (mid-row), to the natural attractor (bottom row). From left to right: The mean flow and a mode-pair resolving flow unsteadiness at the dominant, vortex shedding frequency.

standard physical implementations, including hot wire sensors and, as in an increasing number of studies, a real time digital particle image velocimetry (Yu et al., 2006) or laser Doppler anemometry. Sensor readings will provide a representation of a realistic feedback flow control implementation.

2.3 Dominant Coherent Structures of the Natural Flow

The transition to instability at $Re_c \approx 47$ is a supercritical Hopf bifurcation: Considering small fluctuations from the steady solution, \mathbf{u}_s , the real part of a complex conjugate pair of eigenvalues of the linearized NSE becomes positive once $Re > Re_c$, giving rise to an oscillatory instability and the inception of periodic vortex shedding. The exponential growth of these oscillatory fluctuations saturates as the flow settles at a periodic attractor. As will be further elaborated in § 6, at least 94% of the TKE¹ can be resolved by an operating-point-dependent mode-pair, throughout the natural transient from the steady solution to the attractor (Noack et al., 2003; Lehmann et al., 2005; Morzyński et al., 2007). These local modes and the local mean flow can be computed as slowly varying, distributed Fourier coefficients of the flow field, a perspective we shall also elucidate in short order. In this particular case, the same modes can be computed by application of the proper orthogonal decomposition (POD) procedure, reviewed in the

¹As defined in the previous chapter, the TKE is the period-averaged turbulent kinetic energy of the unsteady flow.

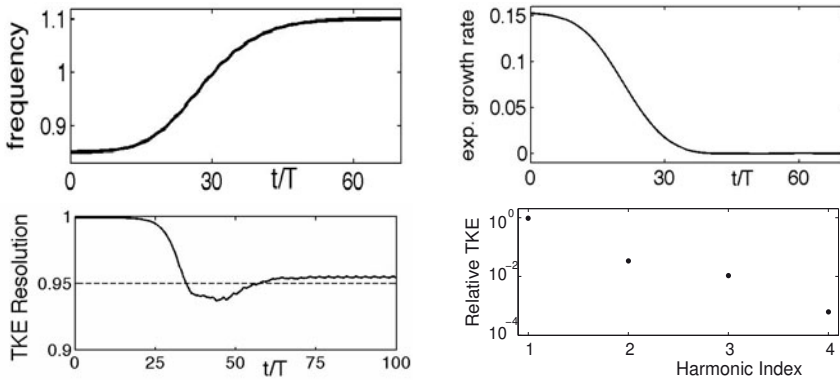


Figure 3. Dynamic characteristics of the cylinder wake flow at $Re = 100$, as they vary along the natural transient from the steady solution to the attractor: The instantaneous shedding frequency (top, left), the instantaneous exponential growth rate of the fluctuation amplitude (top, right), and the feasible TKE resolution with an expansion by a single mode pair (bottom, left). Attractor TKE levels of the first 4 mode-pairs (8 modes), resolving the first 4 harmonics of the shedding frequency, normalized by the TKE at the leading harmonic, are also shown (bottom, right).

previous chapter, to a single vortex shedding period².

Figure 2 depicts³ the mean fields and the dominant mode-pair at the beginning of the natural transient, at a mid-point, and following the convergence to the natural attractor. Figure 3 shows the feasible TKE resolution by a single mode-pair and the gradually changing shedding frequency, along the natural transient. It also provides the distinct TKE levels of each of the first four harmonics of the shedding frequency over the attractor. Figures 2 and 3 highlight two complementary properties of the flow: On the one hand, key quantitative properties of the flow change substantially along the transient: The mean flow's near wake recirculation bubble is drastically reduced as the flow approaches the attractor, the vortical structures of the leading two modes move closer to the cylinder, the characteristic wave-length of these vortices reduces and the shedding frequency grows by nearly 25%. A single mode-pair would therefore provide a far poorer resolution of the entire transient, when compared with what is feasible with operating-point-

²The property that POD modes are each associated with distinct frequencies is generic only when the flow is dominated by a single frequency and its harmonics.

³Here and throughout, velocity fields are represented by streamlines.

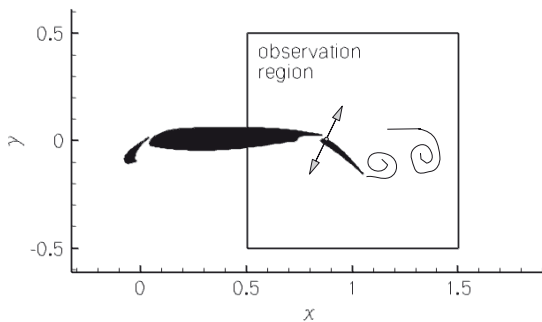


Figure 4. A sketch of the three element high-lift configuration and the observation region for the model. Periodic excitation (\leftrightarrow) is implemented at the upper part of the trailing edge flap.

dependent expansions. For example, the attractor POD modes resolve less than 50% of the early transient's TKE (Noack et al., 2003). The flip side of this observation is that the overall qualitative nature of the flow, including the topology of the mean flow and the leading modes, the dominance of a single frequency, etc., are preserved, and their quantitative manifestations change gradually. Both these observations are generic and characterize natural and actuated non-bifurcating transients in fluid flow systems.

2.4 A High Lift Configuration

Figure 4 shows a simplified, two dimensional representation of generic wing extensions, used by transport airplanes to increase lift during takeoff and landing. It includes the main wing section, a leading edge slat and a trailing edge flap. The incompressible flow is considered at $Re = 10^6$, where velocity and length are scaled with respect to the incoming flow velocity U and the wing chord length c , measured when the high lift mechanism is retracted. The chord lengths of the slat and flap are $c_{sl} = 0.158 c$ and $c_{fl} = 0.254 c$, and their deployed deflection angles are 26.5° and 37° , respectively. The angle of attack of the main wing section is 6° . At these conditions the flow separates only from the trailing edge flap. The two-way arrow in Figure 4 represents an oscillating jet that is used as the control actuator, with the purpose to reattach the flow to the flap and thus, increase

the lift gain. The actuated jet is simulated by imposing a flow velocity, orthogonal to the airfoil, and is located at $0.04 c$ from the flap's leading edge. Some additional technical details will be provided during discussion and the complete description can be found in (Luchtenburg et al., 2009).

This configuration has been the subject of several experimental and numerical flow control studies the Berlin Institute of Technology and our group, including (Günther et al., 2007; Schatz et al., 2007; Kaepernick et al., 2005; Luchtenburg et al., 2009). We shall use this example only in an open loop mode. The imposed periodic velocity will be the open loop counterpart of (4):

$$b(t) = B \cos(\omega_a t), \quad (5)$$

where ω_a is the actuation frequency and B the amplitude of actuation.

2.5 The Natural and the Actuated Flows

The natural, massively separated flow around and behind the flap is characterized by alternating shedding of the leading and trailing edge vortices. The average shedding frequency is $\omega_n = 1.875$ (equiv. $St_n = 0.32$) and the fluctuation peak TKE area is in the wake.

The open loop actuated jet, in this example oscillates at the frequency $\omega_n = 3.75$ (equiv. $St_a = 0.6$), with the maximal momentum coefficient $C_\mu = 4 \times 10^{-3}$. Actuation leads to a substantial reattachment of the flow, a near complete attenuation of shedding at ω_n , the emergence of a new periodic attractor, locked-in to the actuation frequency ω_a , and, indeed, a 19% increase of the average lift coefficient. The actuated fluctuations are concentrated above and near the trailing edge flap.

Kinematically, once again, both the natural and the actuated attractors are well resolved, each, each by a single POD mode pair. Figure 5, taken from (Luchtenburg et al., 2009), shows the mean flow, the first POD mode and a generic snapshot of the respective natural and the actuated attractors.

3 Low Order Galerkin Models: Some Added Concepts

This section sets the ground for the main developments, including the extension of the Galerkin framework, in § 4, § 5, § 6 and § 7, and the discussion of actuation and control design, in § 8. This review begins with a reminder of the basic ingredients of the Galerkin model. It continues with a discussion of the triple Reynolds decomposition (TRD) in relation to Galerkin models, and of an interpretation of that decomposition in terms of harmonic

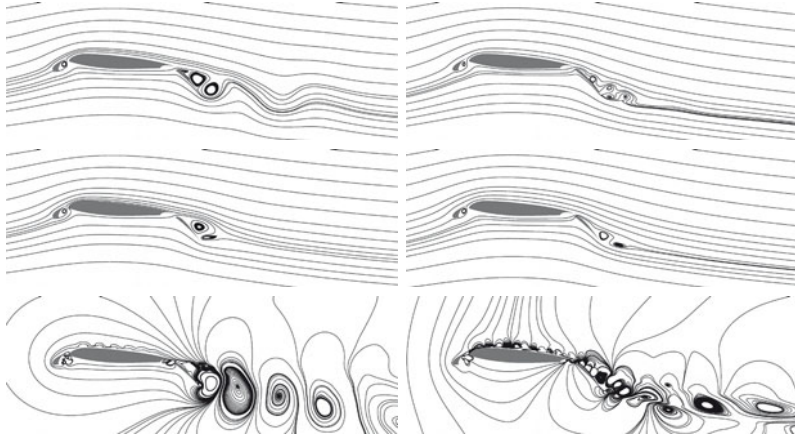


Figure 5. Comparison of a natural (left) and the actuated (right) attractors of the separated flow over the deployed rear flap of the high lift configuration example. Visualized flow fields include characteristic snapshots (top), the mean flows (center) and instantaneous fluctuation (bottom) of the two respective attractors, as detailed in Luchtenburg et al. (2009).

Galerkin expansions. A review of basic concepts of power and energy dynamics completes this set of preliminaries. To motivate the rather lengthy but essential preparatory work, we interrupt the presentation, early on, with a simple illustrative example of the gamut of failures one may encounter when applying the existing Galerkin paradigm to transient modeling.

3.1 The Constitutive First Principles Model

For ease of reference we display again the incompressible Navier-Stokes equations (NSE), the constitutive model underlying the entire discussion:

$$\begin{aligned} \partial_t \mathbf{u} &= \mathcal{N}(\mathbf{u}) + \mathbf{f} = -\nabla \cdot (\mathbf{u} \otimes \mathbf{u}) - \nabla p + \nu \Delta \mathbf{u} + \mathbf{f}, \\ \nabla \cdot \mathbf{u} &= 0. \end{aligned} \quad (6)$$

Low order Galerkin models were developed as efficient computational tools to analyze fixed points and, later on, attractors of partial differential equations (PDEs), such as the NSE. The Galerkin framework was therefore traditionally designed for handling steady domain geometry and boundary conditions. In fluid dynamics contexts, an increasing interest in cases where both these restrictions fail is an outgrowth of generic flow control applica-

tions, e.g., boundary actuators by jets, suction and membranes, active and elastic walls, flapping flight and wind gusts. being able to incorporate these challenges in a systematic modeling framework is a central component of the discussion of this chapter.

The distributed force field, \mathbf{f} , may represent an actuation, such as the volume force $\mathbf{f} = b\mathbf{g}$ in (3), where the signal $b(t)$ represents the control command. Boundary forcing is not represented by terms in (6), but rather, they are formulated as time varying inputs into the domain of the infinitesimal generated of the semi-flow, associated with a controlled PDE (Lasiecka and Triggiani, 2000).

3.2 The Galerkin Modeling Framework

The Galerkin model is determined by a choice of a base flow, \mathbf{u}^B , defining the origin of a state space hyperplane, and of an expansion mode set $\{\mathbf{u}_i\}_{i \geq 1} \subset \mathcal{L}^2(\Omega)$. The Galerkin approximations of the velocity and the force fields in a fluid dynamic system are then

$$\begin{aligned}\mathbf{u}(\mathbf{x}, t) &= \mathbf{u}^B(\mathbf{x}) + \sum_{i \geq 1} a_i(t) \mathbf{u}_i(\mathbf{x}), \\ \mathbf{f}(\mathbf{x}, t) &= \mathbf{f}^B(\mathbf{x}) + \sum_{i \geq 1} f_i(t) \mathbf{u}_i(\mathbf{x}),\end{aligned}\quad (7a)$$

where the generic case of zero-mean steady state forcing means that $\mathbf{f}^B = 0$. The time coefficients $a_i(t)$ and $f_i(t)$ are defined by the projection of the flow field, $\mathbf{u}(\mathbf{x}, t)$, and the force field, $\mathbf{f}(\mathbf{x}, t)$, on the expansion hyperplane. When the expansion set is orthonormal (e.g., when \mathbf{u}_i are POD modes), the projection formulae reduce to the inner products

$$a_i = (\mathbf{u}, \mathbf{u}_i)_\Omega, \quad f_i = (\mathbf{f}, \mathbf{u}_i)_\Omega.$$

When \mathbf{f} is a modulated volume force such as (3) we have $f_i(t) = g_i b(t)$ where g_i are defined by the time invariant projections of $\mathbf{g}(\mathbf{x})$ and the modulation signal $b(t)$ represents the control command. (Notice that this formulation includes multivariable control, where both $\mathbf{g}(\mathbf{x})$, hence g_i , and $b(t)$ are vector valued, and “ $g_i b(t)$ ” stands for the Euclidean inner product.)

The Galerkin dynamical system is the compression of the constitutive NSE to the approximation hyperplane. It comprises of ordinary differential equations, governing the time evolution of the coefficients a_i , and is obtained by the projection of the NSE (6) on the approximation hyperplane. Thus, with an orthonormal expansion, we have

$$\begin{aligned}\dot{a}_i &= (\partial_t \mathbf{u}, \mathbf{u}_i)_\Omega \\ &= (\mathcal{N}(\mathbf{u}), \mathbf{u}_i)_\Omega + (\mathbf{f}, \mathbf{u}_i)_\Omega \\ &= c_i + \sum_{j \geq 1} l_{ij} a_j + \sum_{j,l \geq 1} q_{ijk} a_j a_k + f_i, \quad i \geq 1.\end{aligned}\quad (7b)$$

An, ideal, infinite set of incompressible modes that forms a complete orthonormal sequence in $\mathcal{L}^2(\Omega)$ leads to an exact model, which is equivalent to the NSE. In the context of feedback flow control, however, one's interest is rather in the other extreme, i.e., in the lowest possible model order: The term *least order* will thus be understood in reference to designated quantitative and qualitative system properties that the model needs to resolve. For example, in the context of the cylinder wake stabilization problem, these properties will include the instability of the steady solution, existence of a periodic attractor, the TKE growth rate along natural and actuated transients between \mathbf{u}_s and the attractor, and the vortex shedding frequency along such transients and over the attractor. Additionally, the model should be able to correctly represent the actuation force and the sensor signal.

We recall the following fundamental Galerkin model requirements, made to ensure that any flow field generated by (7) satisfies both the incompressibility and boundary conditions:

- Both the base flow and the modes are divergence-free:

$$\nabla \cdot \mathbf{u}^B = 0, \quad \nabla \cdot \mathbf{u}_i = 0, \quad i \geq 1.$$

- The base flow \mathbf{u}^B absorbs the boundary conditions (in particular, only steady boundary conditions are allowed).
- The modes \mathbf{u}_i satisfy homogeneous boundary conditions.

Our discussion will highlight the way these requirements conflict with key modeling needs in generic flow control applications, and delineate the changes needed in the Galerkin paradigm to remove such conflicts.

3.3 A Simple Example of an Utter Failure

The litany of definitions and technicalities occupying the remainder of this section provide the foundation for our subsequent extension of the Galerkin framework. As a motivation we present first a brief, illustrative preview, using the cylinder wake flow to highlight the sever modeling issues that the traditional Galerkin modeling framework gives rise to.

As a matter of basic dynamic principles, a dynamic model capable to resolve oscillatory fluctuations requires at least two states. In particular, a meaningful Galerkin model of the unsteady cylinder wake flow requires at least two modes. As mentioned earlier, this lower bound is kinematically attainable over the natural attractor, where at least 94% of the TKE is resolved by a Galerkin approximation that employs the attractor's mean flow, denoted $\mathbf{u}_{*,0}$, as the base flow, and a single mode-pair (e.g., the leading POD modes), to resolve the fluctuations. As shown in Noack et al. (2003),

the Galerkin projection of the NSE on the chosen expansion is⁴ a linear system of the form:

$$\frac{d}{dt} \begin{bmatrix} a_1 \\ a_2 \end{bmatrix} = \begin{bmatrix} \sigma & -\omega \\ \omega & \sigma \end{bmatrix} \begin{bmatrix} a_1 \\ a_2 \end{bmatrix}. \quad (8)$$

The excellent kinematic approximation and the simplicity of this dynamical model certainly make it very appealing. Alas, this model suffers from severe flaws, listed right below, that make it of little, if any use.

Instability. The Galerkin projection yields the values of the growth rate $\sigma \approx 0.05$ and the frequency $\omega \approx 1.1$ in (8). The predicted frequency is a good approximation of the shedding frequency. However, with $\sigma > 0$, (8) is linearly anti-stable, which precludes the existence of an attractor, i.e., the key characterization of this flow configuration.

Poor transient prediction. The model also grossly mis-predicts the early transient dynamics, near the unstable steady solution, \mathbf{u}_s : The correct growth rate of small perturbations from \mathbf{u}_s is $\sigma_s \approx 0.44$, i.e., it is nearly nine folds larger than the Galerkin projection value of σ . The early transient shedding frequency is < 0.9 , much smaller than the nominal ω .

Model structure inconsistency. Accepting the validity of the NSE, model parameter mismatch is often attributed to aspects of low order models, such as the truncation of the energy cascade to neglected, higher order modes. A common approach to remedy poor dynamic predictions is to employ a posteriori parameter estimation from simulation or experimental data. This procedure, known in our field as *calibration*, is based on the implicit assumption that the NSE-based structure of the dynamical systems is correct, and that the desired predictive power will be achieved once coefficients are appropriately adjusted, e.g., ensuring stability by adding identified eddy viscosities (Aubry et al., 1988; Rempfer, 1991). Figure 3 refutes this assumption: The substantial drift in both the exponential growth rate and in the shedding frequency along the transient is a property of the exact NSE solution. Therefore no constant values of the coefficients σ and ω can match the entire natural transient!

⁴To be precise, (8) is the *phase-averaged Galerkin system*: Due to the slight difference between the oscillation amplitudes of the first and second POD modes, the oscillations in the (a_1, a_2) plane would be along an ellipse, rather than a circle. The model (8) is obtained by averaging the model coefficients over all rotational changes of coordinates.

Modal expansion inconsistency. The inherent inconsistency of the dynamical system structure with the entire transient is paralleled by the Galerkin approximation: As seen in Figure 2, the flow structures that dominate early transients, starting at small perturbations of the steady solution, are substantially different from their counterparts over the attractor. The implications on feedback flow control of using the same expansion throughout the transient can be severe: A Galerkin approximation of the early transient with an expansion based on the attractor’s mean, $\mathbf{u}_{*,0}$, and on attractor POD modes is guaranteed to fail in the near wake. Likewise, predictions based on an approximation by \mathbf{u}_s and the stability eigenmodes will be misleading as the flow approaches the attractor. As mentioned earlier, the quality of TKE resolution, in both cases, drops to as low as 50%, when the flow state is considered away from the nominal operating condition at which the modes were obtained. These discrepancies can become manifest both in state estimation by dynamic observers and in the anticipated impact of actuation, based on any fixed pair of expansion modes. Poor closed-loop performance will then be inevitable (Gerhard et al., 2003; Lehmann et al., 2005; Luchtenburg et al., 2006).

Failure to predict an attractor. The observation above highlighted the failure at modeling the entire transient. Here we note that the shortcomings of the model persist even when one’s interest is restricted to a single operating point, e.g., the generic focus on small fluctuations from the attractor: Calibrating the growth rate to the observed marginal stability value of $\sigma = 0$, the model becomes a representation of an ideal linear oscillator, consistent with the attractor’s periodic orbit. Yet this model has no preferred oscillation amplitude and therefore cannot recover from disturbance-induced drift. That is, the existence of periodic orbits does not translate to the existence of a true attractor.

Inconsistency with moving boundaries. The inclusion of actuation requires adding a control term to the model, reflecting the effect of the actuated force field. The description of the cylinder wake benchmark includes two forms of actuation: A volume force and cylinder oscillations. The inclusion of the former is, at least conceptually, straightforward. That is not the case when actuated cylinder oscillations are considered. One difficulty is due to the fact that some points in the computational domain are alternately occupied by a solid body (the cylinder) and by moving fluid. The Galerkin projection of the NSE is ill defined at these points, and the model is not capable to produce meaningful dynamic predictions in their neighborhood. A second difficulty is due to the fact that, since boundary motion does not

involve a body force, it does not lead to a first principles based control term in the Galerkin system.

As the discussion of this chapter unfolds, we shall demonstrate that the difficulties we have just identified are not unfortunate peculiarities of a specific example. Rather, they are the results of generic inconsistencies between the very structure of the traditional Galerkin model and of modeling practices. The existence of many successful Galerkin models is typically the results of implicit or explicit structural corrections. Even then, the dynamic envelope and operational range of low order Galerkin models are mostly severely limited. Our goal is to expose these generic inconsistencies and to propose solutions at the structural level. The technical discussion in this section, starting with the triple Reynolds decomposition, right below, provide the necessary tools to do so.

3.4 The Triple Reynolds Decomposition (TRD)

The discussion of impediments to the success of standard low order Galerkin models and of suggested remedies will employ the concepts and notations of the TRD, which is formalized in Eq. (B.9) of Appendix B.3. For convenience we present this formalism here, including both the standard and the triple Reynolds decomposition:

$$\mathbf{u} = \mathbf{u}^B + \mathbf{u}' = \mathbf{u}^B + \mathbf{u}^C + \mathbf{u}^S. \quad (9)$$

The middle expression in (9) is the standard Reynolds decomposition of the velocity field \mathbf{u} as the sum of a *base flow* \mathbf{u}^B and an *unsteady fluctuations* field \mathbf{u}' . Associated with this decomposition is the concept of the *fluctuation energy*

$$K' := \frac{1}{2} \overline{\|\mathbf{u}'\|_{\Omega}^2}, \quad (10)$$

where the bar indicates the ensemble average. In the generic ergodic case, ensemble and time averages are equivalent, the latter providing the computationally accessible option we shall use in this chapter. The *turbulent kinetic energy*, and the abbreviation *TKE* are identified with K' . We alert the reader to the fact that this notation is a slight modification of the nomenclature listed in the appendix and used in the previous chapter, where the TKE is denoted simply by K , i.e., without a prime. The reason for this change is our explicit reference to the *total kinetic energy* of the flow field, including the non-oscillatory base flow, which we shall denote by K :

$$K := \frac{1}{2} \overline{\|\mathbf{u}\|_{\Omega}^2}. \quad (11)$$

The TRD is shown following the second equality in (9). Here the unsteady fluctuation field \mathbf{u}' is partitioned into a *coherent velocity field* \mathbf{u}^C and a remainder \mathbf{u}^S . The coherent component \mathbf{u}^C is understood as the part of \mathbf{u} that one is interested to resolve by a low order Galerkin approximation. The superscript notation of \mathbf{u}^S is motivated by the conceptual parallel to the stochastic flow component that is represented in CFD simulations only indirectly, by subgrid, turbulence models. We will categorize state-related modeling issues by their relations to each of the three components of (9).

As an illustration, in a two states attractor POD approximation of the cylinder wake flow, the base flow is the attractor's mean flow, and the coherent fluctuations are defined by the projection of $\mathbf{u}' = \mathbf{u} - \mathbf{u}^B$ on the dominant POD mode pair:

$$\mathbf{u}^B := \mathbf{u}_{*,0} := \bar{\mathbf{u}} \quad \text{and} \quad \mathbf{u}^C := \sum_{i=1}^2 a_i \mathbf{u}_i \quad \text{with} \quad a_i := (\mathbf{u}', \mathbf{u}_i)_\Omega, \quad i = 1, 2.$$

The remainder, \mathbf{u}^S , comprises of higher frequency components of the flow.

3.5 Harmonic Modes and Harmonic Expansions

Here we provide an explicit mathematical definition of the three components of the Reynolds decomposition.

As the unsteady flow component that is sought to be resolved by a low order Galerkin approximation, \mathbf{u}^C is implicitly defined in terms of certain ranges of length-scales and time-scales. In this chapter we focus on frequency bandwidth characterizations of \mathbf{u}^C . That focus is motivated by the observation that the dynamics of interest in phase-dependent feedback flow control studies are invariably dominated by a finite set of distinct, slowly varying frequencies. This description applies, in particular, to the two illustrating examples we have introduced in § 2.

Dynamical systems featuring a distinct set of slowly varying frequencies match each frequency with a pair of states. It therefore appears prudent to construct the reduced order model of frequency-specific expansion modes, to begin with. In that case, the Galerkin expansion provides an explicit definition for \mathbf{u}^B , \mathbf{u}^C and \mathbf{u}^S in terms of participating frequencies:

$$\begin{aligned} \mathbf{u} = & \underbrace{\mathbf{u}_* + A_0 \mathbf{u}_0}_{\mathbf{u}^B} \\ & + \underbrace{\sum_{i=1}^{N_h} A_{2i-1} \cos(\phi_i) \mathbf{u}_{2i-1} + A_{2i} \sin(\phi_i) \mathbf{u}_{2i}}_{\mathbf{u}^C} \\ & + \underbrace{\sum_{i=N_h+1}^{\infty} A_{2i-1} \cos(\phi_i) \mathbf{u}_{2i-1} + A_{2i} \sin(\phi_i) \mathbf{u}_{2i}}_{\mathbf{u}^S}, \end{aligned} \quad (12)$$

where the distinct participating frequencies are $\frac{d}{dt}\phi_i = \omega_i$. In what follows we add some needed details on the technical assumptions made regarding the components of (12), on ways to compute them, on the meaning of the equality in this expansion, and indeed, on its utility.

Starting with formalisms, the flow fields \mathbf{u}_i are assumed to be normalized, $\|\mathbf{u}_i\|_{\Omega} = 1$. This way $\{\mathbf{u}_i\}_{i \geq 1}$ is viewed as playing the role of a Galerkin expansion set, and the Galerkin expansion is defined by the scalar coefficients $a_{2i-1} := A_{2i-1} \cos(\phi_i)$ and $a_{2i} := A_{2i} \sin(\phi_i)$. In particular, w.l.o.g., we require that $A_i \geq 0$, $i \geq 1$. In preparation for the discussion of mean field models, in § 4, the 0^{th} mode in (12), defining the slowly varying base flow, \mathbf{u}^B , includes a constant component, denoted \mathbf{u}_* and a slowly time varying component, $A_0 \mathbf{u}_0$. Following common practice, one may define the fixed component \mathbf{u}_* as either a steady NSE solution, \mathbf{u}_s , or as the mean flow of a studied attractor, which we denote by $\mathbf{u}_{*,0}$, throughout this chapter.

We shall adopt the convention that the participating frequencies are organized in an ascending order, $\omega_i < \omega_{i+1}, \dots$. In the particular case in which these frequencies are commensurate, when the flow is dominated by a single base frequency and by its harmonics, $\omega_i = i\omega$, then (12) is a temporal Fourier expansion and the distributed coefficients of that expansion are $A_i \mathbf{u}_i$. Regardless of whether the participating frequencies are commensurate or not, we postulate that the flow component \mathbf{u}^C that we want resolved by the Galerkin model is defined by the lower frequencies, ω_i , $i = 1, \dots, N_h$. The high frequencies ω_i , $i > N_h$, are included merely in order to formalize the definition of \mathbf{u}^S . These frequencies are not used in computational realizations, but they can be clearly selected in a way that ensures the possibility of an equality in the restriction of (12) to time windows $[t - \frac{1}{2}t_p, t + \frac{1}{2}t_p]$, $t \geq \frac{1}{2}t_p$, for some fixed $t_p \geq 2\pi/\omega_1$.

The definitions above are obvious in “steady state”, i.e., when the frequencies ω_i , expansion modes \mathbf{u}_i and amplitudes A_i are time invariant. What makes (12) useful in transient flows, as well, is the assumption that the flow field \mathbf{u} is band limited, allowing only slow time variations in these harmonic characteristics. We interpret this assumption in terms of a time scale $\tau \gg 2\pi/\omega_1$ (equivalently, $\tau/t_p \gg 1$) and the following smooth time dependencies:

$$\mathbf{u}_i(\mathbf{x}, t/\tau), \quad A_0(t/\tau), \quad \omega_i(t/\tau). \quad (13)$$

By this assumption, the expansion modes remain essentially constant over the short time windows $[t - \frac{1}{2}t_p, t + \frac{1}{2}t_p]$, and the infinite sum equality in (12) may be interpreted in the $\mathcal{L}^2(\Omega \times [t - \frac{1}{2}t_p, t + \frac{1}{2}t_p])$ sense, over such intervals. The truncated series for $\mathbf{u}^B + \mathbf{u}^S$ is then a smooth, periodically dominated function of time, justifying the point-wise, mid-window interpretation of the original $\mathcal{L}^2(\Omega \times [t - \frac{1}{2}t_p, t + \frac{1}{2}t_p])$ approximation.

We note Models based on slowly varying harmonic coefficients are commonplace, e.g., *dynamic phasor* models in power engineering (DeMarco and Verghese, 1993; Lev-Ari and Stanković, 2008; Tadmor, 2002). The use of harmonic mode sets and *harmonic balancing* has been motivated in flow applications as an effective and relatively simple computational approach to system identification of otherwise complex phenomena, such as separated flows (Tadmor et al., 2008), vortex breakdown (Mishra et al., 2009), and aeroelastic fluid-body interactions (Attar et al., 2006).

The harmonic modes at the time t are computed by the straightforward but generally oblique projection of the time function

$$r \mapsto \mathbf{u}(\cdot, r) - \mathbf{u}_* : \left[t - \frac{t_p}{2}, t + \frac{t_p}{2} \right] \mapsto \mathcal{L}^2(\Omega)$$

on the temporal expansion set $\{1, \cos(\phi_i), \sin(\phi_i), i \geq 1\} \subset \mathcal{L}^2\left[t - \frac{t_p}{2}, t + \frac{t_p}{2}\right]$. In the particular case of commensurate frequencies, where $\omega_i = i\omega$, these modes are computed by the standard Fourier series formulae, with $t_p = 2\pi/\omega$:

$$\tilde{\mathbf{u}}_0(\mathbf{x}, t) = \frac{1}{t_p} \int_{t - \frac{t_p}{2}}^{t + \frac{t_p}{2}} \mathbf{u}(\mathbf{x}, r) dr, \quad \mathbf{u}_0 := \frac{1}{\|\tilde{\mathbf{u}}_0\|_\Omega} \tilde{\mathbf{u}}_0, \quad (14a)$$

and for $i = 1, 2, \dots$,

$$\tilde{\mathbf{u}}_{2i-1}(\mathbf{x}, t) := \frac{2}{t_p} \int_{t - \frac{t_p}{2}}^{t + \frac{t_p}{2}} \mathbf{u}(\mathbf{x}, r) \cos(i\omega r) dr, \quad \mathbf{u}_{2i-1} := \frac{1}{\|\tilde{\mathbf{u}}_{2i-1}\|_\Omega} \tilde{\mathbf{u}}_{2i-1}, \quad (14b)$$

$$\tilde{\mathbf{u}}_{2i}(\mathbf{x}, t) := \frac{2}{t_p} \int_{t - \frac{t_p}{2}}^{t + \frac{t_p}{2}} \mathbf{u}(\mathbf{x}, r) \sin(i\omega r) dr, \quad \mathbf{u}_{2i} := \frac{1}{\|\tilde{\mathbf{u}}_{2i}\|_\Omega} \tilde{\mathbf{u}}_{2i}. \quad (14c)$$

To maintain notational simplicity, the remainder of this discussion is presented for the case of harmonically related frequencies. We note that the only difference in the general case is in the need to compute the temporal correlation of the temporal basis, and use the inverse of that matrix to “de-correlate” the modes.

Although convergence to an exact equality in the infinite expansion (12) is guaranteed by standard harmonic analysis, an important distinction of the harmonic modes is that spatial orthogonality is not generic. Nonetheless, we

shall now demonstrate that these modes share useful advantages of spatially orthogonal modes.

One such advantage is the simplicity of the computation of the time coefficients, $a_i(t)$, by a straightforward extension of the projection formulae for spatially orthogonal expansion sets, i.e. $a_i = (\mathbf{u}, \mathbf{u}_i)_\Omega$, which is no longer valid in its original form. The harmonic time coefficients a_i are completely determined by the amplitudes A_i . The latter are computed by the Fourier series based spatio-temporal projections on the base functions $\mathbf{u}_{2i-1}(\mathbf{x}) \cos(\phi_i(t))$ and $\mathbf{u}_{2i}(\mathbf{x}) \sin(\phi_i(t))$ in $\mathcal{L}^2\left(\Omega \times \left[t - \frac{t_p}{2}, t + \frac{t_p}{2}\right]\right)$. Specifically:

$$\begin{aligned} A_{2i-1}(t/\tau) &= \frac{2}{t_p} \int_{t - \frac{t_p}{2}}^{t + \frac{t_p}{2}} (\mathbf{u}(\cdot, r), \mathbf{u}_{2i-1}(\cdot, t/\tau))_\Omega \cos(\phi_i(r)) dr \\ &= \frac{2}{t_p} \int_{-\frac{t_p}{2}}^{\frac{t_p}{2}} (\mathbf{u}(\cdot, t+r), \mathbf{u}_{2i-1}(\cdot, t/\tau))_\Omega \cos(\phi_i(t+r)) dr \end{aligned} \quad (15a)$$

$$\begin{aligned} A_{2i}(t/\tau) &= \frac{2}{t_p} \int_{t - \frac{t_p}{2}}^{t + \frac{t_p}{2}} (\mathbf{u}(\cdot, r), \mathbf{u}_{2i}(\cdot, t/\tau))_\Omega \sin(\phi_i(r)) dr \\ &= \frac{2}{t_p} \int_{-\frac{t_p}{2}}^{\frac{t_p}{2}} (\mathbf{u}(\cdot, t+r), \mathbf{u}_{2i}(\cdot, t/\tau))_\Omega \sin(\phi_i(t+r)) dr \end{aligned} \quad (15b)$$

A second appealing property is the Pythagorean property of the TKE. The *modal energy* (for $i \geq 1$, the *modal TKE*) at the time t is the period averaged kinetic energy of the respective mode:

$$\begin{aligned} K_0(t/\tau) &:= \frac{1}{2} \|A_0(t/\tau) \mathbf{u}_0(\cdot, t/\tau)\|_\Omega^2 = \frac{1}{2} A_0(t/\tau)^2, \\ K_{2i-1}(t/\tau) &:= \frac{1}{2t_p} \int_{t - \frac{t_p}{2}}^{t + \frac{t_p}{2}} \|a_{2i-1}(r) \mathbf{u}_i(\cdot, t/\tau)\|_\Omega^2 dr \end{aligned}$$

The latter term is simplified as follows:

$$\begin{aligned}
K_{2i-1}(t/\tau) &:= \frac{1}{2t_p} \int_{t-\frac{t_p}{2}}^{t+\frac{t_p}{2}} a_{2i-1}(r)^2 dr \underbrace{\|\mathbf{u}_i(\cdot, t/\tau)\|_\Omega^2}_{=1} \\
&= \frac{1}{2t_p} \int_{t-\frac{t_p}{2}}^{t+\frac{t_p}{2}} (A_{2i-1}(t/\tau) \cos(\phi_i(r)))^2 dr \\
&= \frac{A_{2i-1}(t/\tau)^2}{4i\pi} \int_{\phi_i(t)-i\pi}^{\phi_i(t)+i\pi} \cos(i\omega r)^2 dr \\
&= \frac{1}{4} A_{2i-1}(t/\tau)^2.
\end{aligned}$$

Likewise we obtain

$$K_{2i}(t/\tau) = \dots = \frac{1}{4} A_{2i}(t/\tau)^2.$$

Having selected an index set $\mathcal{I} \subset \mathbb{N}_0$ and denoted

$$\mathbf{u}^\mathcal{I} = \sum_{i \in \mathcal{I}} a_i \mathbf{u}_i,$$

the temporal orthogonality of the distinct components of a harmonic expansion with a single base frequency now leads to the desired equality, which is a distributed version of Plancharel's theorem according to which

$$K^\mathcal{I}(t/\tau) := \frac{1}{2t_p} \int_{t-\frac{t_p}{2}}^{t+\frac{t_p}{2}} \|\mathbf{u}^\mathcal{I}(\cdot, r)\|_\Omega^2 dr$$

becomes

$$\begin{aligned}
K^{\mathcal{I}}(t/\tau) &= \frac{1}{2t_p} \int_{t-\frac{t_p}{2}}^{t+\frac{t_p}{2}} (\mathbf{u}^{\mathcal{I}}(\cdot, r), \mathbf{u}^{\mathcal{I}}(\cdot, r))_{\Omega} dr \\
&= \frac{1}{2t_p} \int_{t-\frac{t_p}{2}}^{t+\frac{t_p}{2}} \left(\sum_{i \in \mathcal{I}} a_i(r) \mathbf{u}_i(\cdot, t/\tau), \sum_{i \in \mathcal{I}} a_j(r) \mathbf{u}_j(\cdot, t/\tau) \right)_{\Omega} dr \\
&= \sum_{i,j \in \mathcal{I}} (\mathbf{u}_i, \mathbf{u}_j)_{\Omega} \frac{1}{2} \overline{a_i(t + \cdot) a_j(t + \cdot)} \\
&= \underbrace{\frac{1}{2} A_0(t/\tau)^2}_{\text{if } 0 \in \mathcal{I}} + \sum_{1 \leq i \in \mathcal{I}} \frac{1}{4} A_i(t/\tau)^2 \\
&= \underbrace{K_0(t/\tau)}_{\text{if } 0 \in \mathcal{I}} + \sum_{1 \leq i \in \mathcal{I}} K_i(t/\tau)^2
\end{aligned} \tag{16}$$

It is noted that this version of the Pythagorean rule exceeds what is generically valid for standard, spatially orthogonal Galerkin expansion, where it is valid only for K' and its components, but generally *not* for the total kinetic energy. It is also noted that while (16) does not extend as an exact equality when the various frequencies are not harmonically related, an arbitrarily good approximation is achievable when the t_p is selected sufficiently large.

It is easy to see that should a Krylov-Bogoliubov phase averaging hypothesis be applicable, the oscillation amplitudes and the TKE become a functions of the frequency alone and can be determined by the instantaneous state of the Galerkin approximation. Thus

$$A_{2i-1} = A_{2i}, \quad \text{and} \quad K_{2i-1} = K_{2i} = \frac{1}{4} A_{2i-1}^2 = \frac{1}{4} (a_{2i-1}^2 + a_{2i}^2). \tag{17}$$

The cylinder wake flow is an example of a case where the Krylov-Bogoliubov hypothesis is a good approximation of the exact dynamics (Noack et al., 2003; Tadmor et al., 2010).

3.6 The Harmonically Dominated Galerkin System

Time variations in the modes \mathbf{u}_i and the frequencies ω_i will be assumed negligible, or recoverable from an exogenous, measurable parameter, which we shall discuss in § 6. The components of the time evolution of the Galerkin coefficients that need to be included in a reduced order dynamical system are thus those involving the slowly varying amplitudes A_i and the locally linear evolution of the phases ϕ_i . That is, we consider a polar coordinates counterpart of the Galerkin system.

The phase equations are straightforward:

$$\dot{\phi}_i = \omega_i, \quad i = 1, \dots, N_h. \quad (18a)$$

We present the computation of the time derivatives of A_i only for commensurate frequencies, allowing us to appeal to the Fourier coefficient formulae (15). For the time being we also assume that short time variations in \mathbf{u}_i , $i \geq 1$, are negligible, deferring treatment of faster modal variations to § 6. Then,

$$\begin{aligned} \frac{d}{dt} A_{2i-1}(t/\tau) &= \frac{d}{dt} \frac{2}{t_p} \int_{-\frac{t_p}{2}}^{\frac{t_p}{2}} (\mathbf{u}(\cdot, t+r), \mathbf{u}_{2i-1})_\Omega \cos(\phi_i(t+r)) dr \\ &= \frac{2}{t_p} \int_{-\frac{t_p}{2}}^{\frac{t_p}{2}} \frac{d}{dt} ((\mathbf{u}(\cdot, t+r), \mathbf{u}_{2i-1})_\Omega \cos(\phi_i(t+r))) dr \\ &= \frac{2}{t_p} \int_{-\frac{t_p}{2}}^{\frac{t_p}{2}} (\partial_t \mathbf{u}(\cdot, t+r), \mathbf{u}_{2i-1})_\Omega \cos(\phi_i(t+r)) dr \\ &\quad - i \omega \frac{2}{t_p} \int_{-\frac{t_p}{2}}^{\frac{t_p}{2}} (\mathbf{u}(\cdot, t+r), \mathbf{u}_{2i-1})_\Omega \sin(\phi_i(t+r)) dr \\ &= \frac{2}{t_p} \int_{-\frac{t_p}{2}}^{\frac{t_p}{2}} (\mathcal{N}(\mathbf{u}(\cdot, t+r) + \mathbf{f}(\cdot, t+r), \mathbf{u}_{2i-1})_\Omega \cos(\phi_i(t+r)) dr \\ &\quad - \omega_i (\mathbf{u}_{2i}, \mathbf{u}_{2i-1})_\Omega A_{2i}. \end{aligned}$$

Likewise,

$$\begin{aligned} \frac{d}{dt} A_{2i-1}(t/\tau) &= \frac{2}{t_p} \int_{-\frac{t_p}{2}}^{\frac{t_p}{2}} (\mathcal{N}(\mathbf{u}(\cdot, t+r) + \mathbf{f}(\cdot, t+r), \mathbf{u}_{2i-1})_\Omega \sin(\phi_i(t+r)) dr \\ &\quad + \omega_i (\mathbf{u}_{2i}, \mathbf{u}_{2i-1})_\Omega A_{2i-1}. \end{aligned}$$

We note that the only difference in the case where incommensurate frequencies are involved is the need for a left division of the vector formed by these expressions by a slowly varying correlation matrix.

For later reference and in order to stress the simple structure of these equations we rewrite them in a compressed form, in terms of the modified

frequencies

$$\tilde{\omega}_i := \omega_i (\mathbf{u}_{2i-1}, \mathbf{u}_{2i})_{\Omega}.$$

Then:

$$\begin{aligned} \frac{d}{dt} A_{2i-1} + \tilde{\omega}_i A_{2i} &= \text{the cos}(\phi_i) \text{ phasor of } (\mathcal{N}(\mathbf{u}) + \mathbf{f}, \mathbf{u}_{2i-1})_{\Omega}, \\ \frac{d}{dt} A_{2i} - \tilde{\omega}_i A_{2i-1} &= \text{the sin}(\phi_i) \text{ phasor of } (\mathcal{N}(\mathbf{u}) + \mathbf{f}, \mathbf{u}_{2i})_{\Omega}. \end{aligned} \quad (18b)$$

The left hand side terms of (18b) adhere to the generic form of *dynamic phasor models* (DeMarco and Verghese, 1993; Tadmor, 2002; Lev-Ari and Stanković, 2008). Dynamic phasor models are widely used in power engineering, where they were introduced to predict the slowly varying transients of the harmonic coefficients (termed dynamic phasors) of AC voltages and currents. The right hand side terms in (18b) are affine-plus-quadratic expressions in the amplitudes A_i . These equations therefore adhere to the general pattern of Galerkin models.

It is noted that the presence of the $\tilde{\omega}_i$ -proportional terms on the left hand side of (18b) gives rise to an oscillatory homogeneous dynamics at the frequency $\tilde{\omega}_i$. Therefore, validity of the underlying hypothesis that the amplitudes A_i are slowly varying means that these terms are either small, e.g., when $\mathbf{u}_{2i-1} \perp \mathbf{u}_{2i}$, or that they are (nearly) cancelled by the right hand side terms of (18b).

We revisit the two modes POD expansion and the Galerkin system (8), as the simplest illustration of (18). Due to the particular structure of the cylinder wake flow, it has the non-generic property that the two dominant POD modes are also harmonic modes at the shedding frequency, over the attractor. Given the scope and objective of this example, we are satisfied with the fact that flow state trajectories initiated at small perturbations of attractor states are well approximated as

$$\begin{aligned} \mathbf{u}(\mathbf{x}, t) &= \mathbf{u}_{*,0}(\mathbf{x}) + a_1(t)\mathbf{u}_1(\mathbf{x}) + a_2(t)\mathbf{u}_2(\mathbf{x}) \\ &= \mathbf{u}_{*,0}(\mathbf{x}) + A_1(t/\tau)(\cos(\phi(t))\mathbf{u}_1(\mathbf{x}) + \sin(\phi(t))\mathbf{u}_2(\mathbf{x})), \end{aligned} \quad (19a)$$

and ignore the issue of the merit (or lack of merit) of (8) for dynamic predictions. Let us consider now the ingredients of (18) in this example:

- The fact that the harmonic modes we use are POD modes means that they are spatially orthogonal. Thus, in this example, $\tilde{\omega}_1 = 0$ in (18).
- The fact that (8) is the Galerkin projection of the NSE over the expansion (19a) means that:

$$\begin{aligned} (\mathcal{N}(\mathbf{u}_{*,0} + a_1 \mathbf{u}_1 + a_2 \mathbf{u}_2, \mathbf{u}_1)_\Omega &= \sigma a_1 - \omega a_2 \\ &= A_1 (\sigma \cos(\phi) - \omega \sin(\phi)), \end{aligned} \quad (19b)$$

$$\begin{aligned} (\mathcal{N}(\mathbf{u}_{*,0} + a_1 \mathbf{u}_1 + a_2 \mathbf{u}_2, \mathbf{u}_2)_\Omega &= \sigma a_2 + \omega a_1 \\ &= A_1 (\sigma \sin(\phi) + \omega \cos(\phi)). \end{aligned} \quad (19c)$$

The $\cos(\phi)$ phasor of the right hand side of (19b) is σA_1 , and the $\sin(\phi)$ phasor of the right hand side of (19c), is σA_2 . Thus, (8) gives rise to a dynamic phasor model, comprising of the equations

$$\frac{d}{dt} A_i = \sigma A_i, \quad i = 1, 2. \quad (20)$$

This model isolates and highlights the exponential instability of the oscillation amplitude under (8).

3.7 Interim Comments

The preceding discussion provided an explicit interpretation of the TRD in terms of harmonic expansions and dynamic phasors. The focus of the discussion has been on periodically dominated flows. The same focus will be maintained throughout this chapter. It is noted however that the rationale and definitions of Galerkin expansions in terms of harmonically specific modes extend, mutatis mutandis, to flows that involve multiple, non-commensurate frequencies, on which we commented in the text.

While harmonic modes are generically *not* mutually orthogonal in the state space $\mathcal{L}^2(\Omega)$, Galerkin expansions by harmonic modes do retain useful properties of Galerkin expansions with spatially orthogonal mode sets. Those properties include simple projection formulae to compute time coefficients of distinct modes, the equality of the TKE stored in the i^{th} mode to the respective Galerkin state TKE, and the pythagorean law by which the total TKE of a harmonic expansion is the sum of the respective modal TKE levels.

An explicit TRD interpretation as a frequency band partition of the flow field is provided by the (generalized) harmonic expansion: The base flow, the coherent unsteadiness and the unresolved flow field represent the slowly varying mean flow, the intermediate bandwidth and the high bandwidth components of the harmonic expansion.

A side benefit of the formalism (12) that will prove extremely useful later on, is that the continuity of the harmonic modes with respect to gradual

changes in the flow provide a simple and consistent framework to represent the continuous deformation of dominant coherent structures along transients (Lehmann et al., 2005; Morzyński et al., 2007). This enables to maintain a relatively small expansion set without any loss in model accuracy. Defining counterpart concepts of deformable mode sets is a far greater challenge in the POD framework, due to the lack of a firm generic dependence between indices of POD modes and intrinsic dynamic characteristics, such as frequencies and phases, as illustrated in Tadmor et al. (2007a, 2008); Mishra et al. (2008, 2009). We shall revisit this issue when we discuss mode deformation, in § 6.

Till then, the discussion of *mean field models* in § 4, and of *turbulence subgrid models*, in § 5, will be based on the use of time invariant mode sets. The one exception will be the 0th harmonic mode, which is the core of the Galerkin mean field theory.

3.8 Dynamic Power Balancing

As in any physical system, the time evolution of the energy content of distinct components state components, e.g., K^B , K^C and K^S , is key to understanding the dynamics of a fluid flow system. The last component of the preliminaries concerns these concepts which we discuss first in the context of exact NSE model, and then in the Galerkin model.

Dynamic Power Balancing: NSE Definitions The dynamic law governing the time evolution of the TKE, K' , is derived from the NSE (Noack et al., 2002, 2005, 2008). We use the following nomenclature to refer to the contributions of distinct components of the (actuated) NSE to the *energy supply rate* (i.e., the *power*) in the flow:

$$\frac{d}{dt} K' = P + D + C + T + F + G, \quad (21)$$

where P , D , C , T , F , G are the respective *production*, *dissipation*, *convection*, *transfer*, *pressure* and *actuation* components of the power $\frac{d}{dt} K'$, and are defined as:

$$P = -\overline{(\mathbf{u}', \nabla \cdot (\mathbf{u}' \otimes \mathbf{u}^B))_\Omega}, \quad (22a)$$

$$C = -\overline{(\mathbf{u}', \nabla \cdot (\mathbf{u}^B \otimes \mathbf{u}'))_\Omega}, \quad (22b)$$

$$T = -\overline{(\mathbf{u}', \nabla \cdot (\mathbf{u}' \otimes \mathbf{u}'))_\Omega}, \quad (22c)$$

$$D = \frac{1}{Re} \overline{(\mathbf{u}', \Delta \mathbf{u}')_\Omega}, \quad (22d)$$

$$F = -\overline{(\mathbf{u}', \nabla p')_\Omega} . \quad (22e)$$

$$G = \overline{(\mathbf{u}', \mathbf{f})_\Omega} , \quad (22f)$$

The power provided by the actuation force field \mathbf{f} is included for later reference and will not be discussed in this section. With a continued focus on periodically dominated systems, averaging at the time t is carried over the period $[t - \frac{t_p}{2}, t + \frac{t_p}{2}]$. Effects on the supplied power of changes in any of the harmonic modes, and in any of the amplitudes A_i , are assumed negligible.

As we have already demonstrated, the total energy of periodically dominated flows is the sum of the modal contributions, i.e., $K = \sum_i K_i$. When computing power terms in the context of the Galerkin system, we shall therefore focus on modal contributions. Modal power contributions can be derived from (22). For example, the combined contributions of the $(2i-1)^{st}$ and $(2j-1)^{st}$ modes to the production power component is computed by substituting $A_0 \mathbf{u}_0$ for \mathbf{u}^B and $A_{2i-1} \cos((2i-1)\omega r) \mathbf{u}_{2i-1}$ and $A_{2j-1} \cos((2j-1)\omega r) \mathbf{u}_{2j-1}$ for \mathbf{u}' in (22a). This leads to the following expression:

$$\begin{aligned} & -A_{2i-1} A_{2j-1} A_0 \left((\mathbf{u}_{2i-1}, \nabla \cdot (\mathbf{u}_{2j-1} \otimes \mathbf{u}_0))_\Omega \right. \\ & \quad \left. + (\mathbf{u}_{2j-1}, \nabla \cdot (\mathbf{u}_{2i-1} \otimes \mathbf{u}_0))_\Omega \right) \cdot \\ & \quad \cdot \overline{\cos((2i-1)\omega \cdot) \cos((2j-1)\omega \cdot)} \\ &= -\delta(i-j) \frac{1}{2} (\mathbf{u}_{2i-1}, \nabla \cdot (\mathbf{u}_{2i-1} \otimes \mathbf{u}_0))_\Omega A_0 A_{2i-1}^2 \\ &= -\delta(i-j) 2\sqrt{2} (\mathbf{u}_{2i-1}, \nabla \cdot (\mathbf{u}_{2i-1} \otimes \mathbf{u}_0))_\Omega \sqrt{K_0} K_{2i-1}. \end{aligned} \quad (23)$$

Similar expressions are obtained, by an obvious analogy, for the modal contributions to the remaining power components.

Dynamic Power Balancing: Galerkin System Definitions As discussed in previous chapters, the inner product terms following the last two equalities in (23) are the Galerkin projection definitions of coefficients of the Galerkin system (7b). The same will hold for the modal contributions to other power components. In other words, the total modal power contributions are *equivalently* computed in terms of the time coefficients in the ideal, infinite Galerkin system. Motivated by our concentration on the Galerkin

system, we continue our analysis with a focus on the Galerkin formulation:

$$\frac{d}{dt} K_i = \frac{d}{dt} \frac{1}{2} \overline{a_i^2} = c_i \overline{a_i} + \sum_{j=1}^{\infty} l_{ij} \overline{a_i a_j} + \sum_{j,k=1}^{\infty} q_{ijk} \overline{a_i a_j a_k} + g_i \overline{a_i b}. \quad (24)$$

Considering harmonic Galerkin expansions, let us examine each of the terms in (24):

The contribution of the constant terms vanishes.

$$c_i \overline{a_i} = 0.$$

This is a consequence of the sinusoidal nature of a_i for $i \geq 1$.

Only the diagonal linear terms make a nonzero power contribution. This is simply a restatement of Plancharel's theorem. Thus,

$$Q_i := \sum_{j=1}^{\infty} l_{ij} \overline{a_i a_j} = \frac{1}{2} l_{ii} A_i^2 = 2 l_{ii} K_i, \quad Q' = \sum_{i=1}^{\infty} Q_i, \quad Q = Q_0 + Q'. \quad (25)$$

This expression includes the combined contribution of the production, convection and dissipation to the modal power. We say that the i^{th} mode is *productive* when $l_{ii} > 0$, that it is *dissipative* when $l_{ii} < 0$, and term the marginal case, where $l_{ii} = 0$, as *neutral*. Productive modes are typically a dominant component of \mathbf{u}' . They are therefore included in \mathbf{u}^C and in the expansion mode set of the Galerkin model. Modes spanning \mathbf{u}^S , are invariably dissipative.

It is noted that the annihilation of off-diagonal linear terms by windowed time averages remains a good approximation well beyond the periodically dominant case. For example, assuming that a POD model is obtained over a statistically representative interval, the time coefficients will remain orthogonal over sufficiently long time windows.

Triadic energy exchanges represent the transfer power in the NSE and their cumulative contributions are conservative (lossless). This means that the sum total of the rate of energy exchanges between any three modes through the quadratic terms of the Galerkin system is zero. Denoting the (order dependent) rate of energy supplied by the j^{th} and k^{th} modes to the i^{th} mode by

$$T_{ijk} = q_{ijk} \overline{a_i a_j a_k}, \quad (26)$$

the lossless nature of the triadic exchanges is a formal consequence of the equality

$$q_{ijk} + q_{ikj} + q_{ikj} + q_{jik} + q_{jki} + q_{kij} + q_{kji} = 0.$$

Evaluating each T_{ijk} is generally an unsolved problem. Indeed, this issue is at the core of what continues to keep the problem of turbulence closure a Grand Challenge, even as we enter a second century of relentless efforts to address it. The difficulty in the general case arises from the lack of explicit expressions for phase relationships between the oscillations in the three modes. For completeness we shall shortly discuss a simple axiomatic finite time thermodynamics (FTT) framework that we proposed in Noack et al. (2008), as an approximate solution, tailored specifically for Galerkin systems. However, in the particular but important class of periodically dominated flows, on which we focus here, an explicit computation is possible. Starting with the products $a_j(t)a_k(t)$, one has:

$$a_j(t)a_k(t) = \frac{1}{2}A_j(t/\tau)A_k(t/\tau) \cdot \begin{cases} \cos(\phi_j - \phi_k) + \cos(\phi_j + \phi_k) & j = 2\ell - 1 \\ & k = 2m - 1 \\ \cos(\phi_j - \phi_k) - \cos(\phi_j + \phi_k) & j = 2\ell \\ & k = 2m \\ \sin(\phi_j + \phi_k) + \sin(\phi_j - \phi_k) & j = 2\ell \\ & k = 2m - 1 \\ \sin(\phi_j + \phi_k) - \sin(\phi_j - \phi_k) & j = 2\ell - 1 \\ & k = 2m. \end{cases} \quad (27)$$

Multiplying by a_i and taking period averages, as in (26), we obtain:

$$\begin{aligned} T_{ijk} &= q_{ijk}\overline{a_i a_j a_k} \\ &= \sigma_{ijk} \begin{cases} \frac{1}{4}q_{ijk}A_i A_j A_k = 2q_{ijk}\sqrt{K_i K_j K_k} & i = |j \pm k| \\ 0 & \text{else.} \end{cases} \end{aligned} \quad (28)$$

where $\sigma_{ijk} = \pm 1$ depending on i, j, k . Summing over all pertinent input pairs, the net TKE flow rate to the i^{th} mode is

$$T_i = \sum_{\substack{j,k \\ i=|j\pm k|}} 2\sigma_{ijk} q_{ijk} \sqrt{K_i K_j K_k}. \quad (29)$$

We defer the discussion of the actuation power to §8. Ideally, the contribution of the pressure term to the power balance in the Galerkin system is zero. In cases where that is not the case, this term is approximated by the linear and quadratic terms of the Galerkin system, and is therefore subsumed by the terms discussed right above.

A Finite Time Thermodynamics Variant The analytic form of the transfer terms in (28)-(29) relied heavily on the near periodicity assumption, which provided for the phase relations (27). The lack of such models in more general cases motivated our development of the axiomatic framework of *finite time thermodynamics (FTT)* (Noack et al., 2008). The FTT axioms lead to an identical formulation of the contributions of linear Galerkin system terms, in (25). The FTT estimates of triadic energy exchange rates are of the form:

$$\widehat{T}_{ijk} = \chi_{ijk} \sqrt{K_i K_j K_k} \left(1 - \frac{3K_i}{K_i + K_j + K_k} \right). \quad (30)$$

This form indicates that the respective phases of modal oscillations will be aligned in a way that, on average, energy will flow “downhill”, i.e., from TKE rich to low TKE modes. The expressions (30) match (28) when the rational scaling term in (30) is nearly constant. That happens, e.g., when the modal TKE levels are rapidly decaying, making the scaling term equal to either 1, 0, -0.5 or -2.

3.9 Closing Comments

The following comment is made in anticipation of the review of mean field models in § 4, below. Discussions of the kinetic energy in the flow and of its time variations, including those by the present authors in Noack et al. (2002, 2005, 2008, 2010); Tadmor et al. (2010), is typically focused on the unsteady component of the flow, ideally \mathbf{u}' , and on its energy content, the K' . In anticipation of the discussion of Galerkin mean field models, in § 4, it is useful to highlight the implications of the preceding analysis on the non-oscillatory base flow, and on the triadic energy exchanges between the base flow and the fluctuations:

$$q_{0jj} \overline{a_0 a_j^2} = q_{0jj} A_0 A_j^2 = 2q_{0jj} \sqrt{K_0} K_j, \quad (31)$$

This expression is analogous to the Reynolds stress term

$$\overline{(\mathbf{u}^B, \nabla \cdot (\mathbf{u}' \otimes \mathbf{u}'))_\Omega}, \quad (32)$$

which is left out in the TKE focused (21), is obvious. This parallel, and the importance of the *bilateral* energy transfer between fluctuating modes and the base flow, is the basis of the Galerkin mean field theory that we shall discuss next.

4 Broadband Galerkin Models: Mean Field Models

With an eye on low and least order models suitable for the design of flow control, the sections spanning the remainder of this chapter, elaborate on the challenges mentioned in the review of the spectacular failure of (8). The first category of modeling challenges and solutions that we discuss occupies this section and the following § 5. It can be broadly explained in terms of the TRD (9), its explicit harmonic realization (12), and the trilateral energy flow between \mathbf{u}^B , \mathbf{u}^C and \mathbf{u}^S .

With \mathbf{u}^C at the focus of attention, and with a usual concentration on observed steady state dynamics, traditional low order Galerkin models use an attractor's mean flow as a time invariant definition of \mathbf{u}^B . Slow variations in the base flow, and small structures that we conceptually aggregate in \mathbf{u}^S , are both truncated and ignored. The adverse effects of this practice, including the potential for utter failures, such as we have seen in the case of (8), were explained In the seminal article by Aubry et al. (1988). Using the vocabulary of the present discussion, the exposition highlighted the need to include at least a lumped representation of the dynamic energy exchanges between \mathbf{u}^C , \mathbf{u}^B and \mathbf{u}^S , to regain the stabilizing effects of changes in the base flow and of energy transfer to turbulence, in the exact NSE solution.

The methods proposed by Aubry et al. (1988) defined the beginning of efforts, continued to the present day, to effectively represent the contributions of truncated flow structures in a way that is simple enough to meet sought complexity bounds. Directly or indirectly, investigations alongare particularly Widely applicable solutions are yet to be developed.

The purpose of this section is to seek insight into the problem from an analysis the very structure of the underlying physical mechanisms, at the NSE and the Galerkin levels. That analysis will then reveal the root causes of observed difficulties in structural inconsistencies in the traditional framework, and guide us in the systematic development of viable alternatives. The first part of the discussion addresses the need for and the form of mean field representations, and the second part addresses the issue of turbulence modeling.

4.1 The Need for a Mean Field Model: An NSE Perspective

The discussion of mean field representations summarizes key components of the expositions in Noack et al. (2003); Tadmor et al. (2010), where the interested reader will find additional details.

Let us apply the filters on the right hand sides of (14) to the entire NSE.

The averaging of (14a) yields the familiar Reynolds averaged equation:

$$\partial_t \mathbf{u}^B + \nabla \cdot (\mathbf{u}^B \otimes \mathbf{u}^B) + \overline{\nabla \cdot (\mathbf{u}' \otimes \mathbf{u}')} = -\nabla p^B + \nu \Delta \mathbf{u}^B, \quad (33a)$$

where the time derivative $\partial_t \mathbf{u}^B$ scales with $1/\tau$ and is commonly ignored. The Reynolds averaged equation highlights the impact of the fluctuations \mathbf{u}' on the base flow, via the slowly varying Reynolds stress $\nabla \cdot (\mathbf{u}' \otimes \mathbf{u}')$.

The dynamical system explanation of this effect, via the Reynolds averaged equation, is complemented by an energy flow interpretation, which was discussed right above. That is, the Reynolds stress is the term responsible for the energy flow rate (32) between \mathbf{u}' and \mathbf{u}^B .

An appeal to the combined higher order harmonic filters in (14b) and (14c), would similarly yield a high-pass filtered harmonic counterpart of the Reynolds equation:

$$\begin{aligned} \partial_t \mathbf{u}' + \nabla \cdot (\mathbf{u}^B \otimes \mathbf{u}') + \nabla \cdot (\mathbf{u}' \otimes \mathbf{u}^B) \\ + \nabla \cdot (\mathbf{u}' \otimes \mathbf{u}')' = -\nabla p' + \nu \Delta \mathbf{u}', \end{aligned} \quad (33b)$$

where the prime ' $'$ indicates the high-pass filtered component of a time function. Thus $\nabla \cdot (\mathbf{u}' \otimes \mathbf{u}')'$ is the high-pass filtered component of $\nabla \cdot (\mathbf{u}' \otimes \mathbf{u}')$, and the term $\nabla \cdot (\mathbf{u}^B \otimes \mathbf{u}^B)$ is eliminated by a high-pass filter. A critical observation, in this equation, is that the component of (33b) that is linear in \mathbf{u}' includes the base flow dependent terms $\nabla \cdot (\mathbf{u}^B \otimes \mathbf{u}') + \nabla \cdot (\mathbf{u}' \otimes \mathbf{u}^B)$. Changes in \mathbf{u}^B will therefore modify the linear growth rate of the \mathbf{u}' .

Here too, the stabilizing mechanism is reflected by a power term, which is the counterpart of (32) in (33b). That term is

$$\overline{(\mathbf{u}', \nabla \cdot (\mathbf{u}^B \otimes \mathbf{u}') + \nabla \cdot (\mathbf{u}' \otimes \mathbf{u}^B))_\Omega}, \quad (34)$$

Once again, it captures the energy transfer rate between the base flow and the fluctuations. The conservatism of this flow rate means that (34) has the negative value of (32).

This bilateral interdependence is precisely what enables the transition from an unstable steady solution to a marginally stable attractor in the NSE solution: Small perturbations of the steady solution experience high production rate. As the base flow approaches the attractor's mean, that rate declines, and with it, the growth in K' , saturating over the attractor.

This mechanism explains the structural failure of (8), where a constant base flow is used and where the said change in the production rate cannot take place. A detailed examination of the dynamic energy balancing along the transient in the cylinder wake example, verifying this explanation, can

be found in Tadmor et al. (2010). That analysis demonstrates that, *regardless of the precision of the Galerkin approximation of \mathbf{u}'* , a substitution of the slowly varying \mathbf{u}^B by a fixed field, e.g. by the steady NSE solution or by the attractor's mean flow, will lead to a drastic mis-match of energy production and dissipation along the natural transient. For example the use of the attractor's mean field leads to the non-physical prediction of decay of small fluctuations from the steady solution.

The conclusion at this point is therefore that, in order to provide a close approximation of modal energy production and consumption, a reduced order model must account for the interactions between the fluctuations and a (slowly varying) dynamic mean field.

4.2 Simple Galerkin-Reynolds Mean Field Models

The preceding analysis exposes the sources of observed model failures in both energy flow and dynamical system terms. By the same token, it also suggests a clear solution path: Just as the NSE comprises of the bilaterally interacting (33a) and (33b), a least order Galerkin model should include approximations of both these NSE components. The coherent flow \mathbf{u}^C and the fluctuations equation (33b) are already addressed by the standard Galerkin modeling framework of (7). A Galerkin-Reynolds equation needs to be added to the model, targeting the time variations in the base flow component $\mathbf{u}^B = \mathbf{u}_* + a_0 \mathbf{u}_0$ in (12), and serving as the counterpart of the Reynolds averaged NSE (33a).

The previous chapter by Noack et. al. suggested a very simple recipe for a least order Galerkin approximation of base flow variations

$$\mathbf{u}^B \approx \mathbf{u}_{*,0} + a_\Delta \mathbf{u}_\Delta. \quad (35a)$$

in terms of a single *shift mode*:

$$\mathbf{u}_\Delta := \frac{1}{\|\mathbf{u}_s - \mathbf{u}_{*,0}\|_\Omega} (\mathbf{u}_s - \mathbf{u}_{*,0}), \quad (35b)$$

where we return to the erstwhile interpretation of $\mathbf{u}_* = \mathbf{u}_{*,0}$ as the time-independent attractor's mean flow. By this definition, $a_\Delta = 0$ over the attractor and $a_{\Delta,s} < 0$ near the steady solution. This definition arises naturally when one is focused on the dynamic envelope of the flow between an unsteady attractor and an unstable fixed point. As shown in Lehmann et al. (2005); Tadmor et al. (2010), the relative TKE error in (35), in the cylinder wake example, is $\leq 30\%$. The term *shift mode* was coined in Noack et al. (2003) to indicate the role of mean field variations in determining the rate of energy shifted from the base flow to the attractor. The cylinder wake version of the shift mode (35b) is depicted in Figure 6.

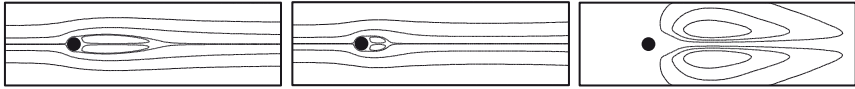


Figure 6. The shift mode as defined in (35b) for the cylinder wake flow (right). For ease of reference we present here again the steady solution (left) and the mean of the attractor flow (center).

Extensions are readily obtained in cases where a wider dynamic envelope renders the approximation (35) insufficient. One example, continuing the empirical approach underlying this chapter, is to approximate the trajectory of the 0th harmonic component of the transient flow, $a_0 \mathbf{u}_0 = \mathbf{u}^B - \mathbf{u}_*$, over the dynamic envelope of interest, e.g., using a POD basis. The incremental base flow is captured by period averaging $\mathbf{u}^B - \mathbf{u}_*$ for a choice of \mathbf{u}_* , the base flow at a nominal operating point (e.g., an attractor). Alternatives with a stronger first principle flavor appeal to evaluation(s) of the local orientation of the mean field correction, as defined by the local period-averaged NSE. Such definitions require also an approximation of the fluctuation field, \mathbf{u}' , e.g., by a (local or global) Galerkin expansion. Details can be found in Tadmor et al. (2010) (cf. Tadmor et al. (2007b, 2008)). We shall revisit and extend these ideas in our discussion of nonlinear manifold embedding and parameterized Galerkin models on nonlinear manifolds, in § 6.

To illustrate the transformative power of these idea we apply the least order approximation (35) to the failing example of the two state cylinder wake model (8). The least order Galerkin expansion of the cylinder wake flow that approximates time variations of both \mathbf{u}^C and \mathbf{u}^B employs the modes $\{\mathbf{u}_i\}_{i=1}^2$, as in (8), and the shift mode from (35b), \mathbf{u}_Δ . The Galerkin projection on this extended basis substitutes the faulty (8) by a three equations Stewart-Landau system, comprising of two components, derived in Noack et al. (2003): The new, Galerkin-Reynolds equation, is a counterpart of (33a):

$$\frac{d}{dt} a_\Delta = -\sigma^B a_\Delta + \beta^B (a_1^2 + a_2^2). \quad (36a)$$

The Galerkin-Reynolds stress counterpart is the term $\beta^B (a_1^2 + a_2^2) = 2\beta^B K$. The Galerkin counterpart of the fluctuations equation (33b) is a nonlinear variant of (8):

$$\frac{d}{dt} \begin{bmatrix} a_1 \\ a_2 \end{bmatrix} = \begin{bmatrix} \sigma^C - \beta^C a_\Delta & -(\omega + \gamma a_\Delta) \\ \omega + \gamma a_\Delta & \sigma^C - \beta^C a_\Delta \end{bmatrix} \begin{bmatrix} a_1 \\ a_2 \end{bmatrix}. \quad (36b)$$

The constant coefficients β^B , β^C , σ^C and σ^B , and the constant term c , in

this model, are all positive.

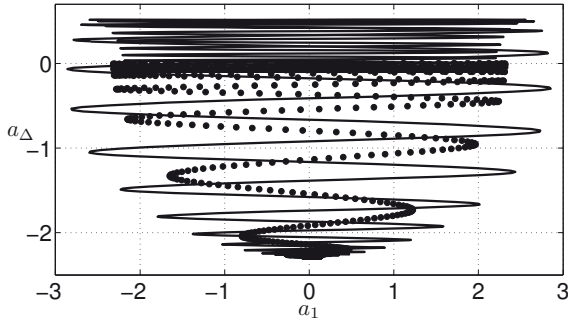


Figure 7. Natural transient of a DNS simulation (dotted line) and the three states Galerkin model (36), that includes the two leading attractor POD modes and the shift mode (35b) (solid curve). The added shift mode enables the recovery of key qualitative aspects of the NSE solution, including the existence of an attractor and the paraboloid manifold connecting the steady solution, \mathbf{u}_s , with the attractor. Reasons for the quantitative difference between the Galerkin and the NSE predictions include the lack of adequate turbulence representation, which will be discussed next, and mode deformation, which is the subject of § 6.

When compared with the faulty two states model (8), the effect of the added shift mode and the Galerkin-Reynolds equation in (36) is no less than dramatic. The model now supports the the existence of *both* a marginally stable attractor, where $a_\Delta = \sigma^C/\beta^C$ and $a_1^2 + a_2^2 = (c + \sigma^B a_\Delta)/2\beta^B$, and a linearly unstable fixed point, a counterpart of \mathbf{u}_s , where $a_1 = a_2 = 0$, $a_\Delta = -c/\sigma^B$, and where the positive fluctuation growth rate is $\sigma^C - \beta^C a_\Delta = \sigma^C + \beta^C c/\sigma^B > 0$. As shown in Figure 7, this new least order model captures key dynamic qualitative features the NSE solution, as well as a decent, albeit imperfect approximation of the paraboloid transient manifold that is defined by the projection of the NSE solution on the expansion modes. In fact, this approximation is a substantial improvement over the prediction achievable by Galerkin model that employs four times as many modes in the expansion of \mathbf{u}^C , but does not (explicitly) includes a mean field representation, other than by trace components in the POD modes (Deane et al., 1991; Noack et al., 2003). The residual mismatch is nonetheless conspicuous: The oscillations amplitude is over-predicted, both throughout

the transient and over the attractor, while the growth rate near the fixed point is under-predicted. Our task in the following sections is to identify and remove the key structural obstacles that cause model inaccuracies such as this.

5 Broadband Galerkin Models: Subgrid Models

Continuing with the discussion of neglected scales, that we begun in the previous section, we now turn our attention from the adverse effects of suppressing \mathbf{u}^B to the impact of neglecting \mathbf{u}^S .

5.1 The Need for Subgrid Models

The language of dynamic energy balancing continues to be central. TKE production, i.e., the extraction of energy from \mathbf{u}^B , occurs in the most dominant modes which are therefore included in \mathbf{u}^C . Any remaining modes in the expansion set that defines \mathbf{u}^C , and the entire \mathbf{u}^S , are dissipative. TKE dynamics balances the net production and dissipation with the growth or decay rate of modal energies. As follows from our previous discussion of energy dynamics, the conduits for triadic intermodal energy flow are formed by the quadratic term of the NSE, and by its representation by the quadratic terms of the ideal, infinite Galerkin system. The suppression of these conduits, when the dissipative modes spanning \mathbf{u}^S are truncated, therefore creates a non-physical imbalance between energy production and dissipation. That imbalance leads to a net over-prediction of the TKE in the Galerkin system. This includes the modes aggregated in \mathbf{u}^C , and when a mean field model is included, in the combined modes spanning \mathbf{u}^B and \mathbf{u}^C . In the extreme, the imbalance may lead to global instability.

This phenomenon is manifest in both of the models we have previously considered for the cylinder wake flow:

The two states model (8). The instability of this model is the consequence of the suppression of all the quadratic terms, hence all the conduit for inter-modal energy exchanges. This includes both conduits that lead to energy balance with the base flow and those that allow energy flow to modes capturing higher temporal harmonics. With no component capable to drain the TKE generated by the first two modes, the TKE level of \mathbf{u}^C grows at an exponential rate.

The three states model (36). The Galerkin-Reynolds stress $\beta^B(a_1^2 + a_2^2)$, in (36a), and the quadratic terms $-\beta^C a_\Delta a_i$, in (36b), create lossless energy

links between \mathbf{u}^C and \mathbf{u}^B . Their presence eliminates the possibility of global instability and enables an energy balance over an attractor. Nonetheless, the suppression of quadratic terms linking the dominant frequency with modes representing higher harmonics causes the energy absorbed by those modes, in the exact NSE solution, to remain trapped in the three states representing $\mathbf{u}^B + \mathbf{u}^C$. The resulting over prediction by the Galerkin model of both the transient and attractor amplitudes features prominently in Figure 7.

The significance of the distorting effects of truncated energy cascades in low order Galerkin models was brought to attention by the aforementioned article by Aubry et al. (1988). The solution approach suggested in that article is to correct the energy imbalance by increasing the kinematic viscosity ν with an added *eddy viscosity* ν_t . The added dissipation is set to balance the rate by which energy is transferred from \mathbf{u}^C to \mathbf{u}^S over the NSE attractor. Distinct *modal eddy viscosities* ν_{ti} were introduced shortly thereafter (Rempfer, 1991), motivated by difficulties to tune a single ν_t . Mounting examples of tuning difficulties continue to accumulate since.

We use the cylinder wake example to elucidate structural reasons for these difficulties and to motivate the class of solutions we shall present shortly. To simplify the discussion we exploit some particular properties of the cylinder wake flow. First, a Krylov-Bogoliubov phase averaging hypothesis, whereby $A_{2i-1} = A_{2i}$ for all $i = 1, 2, \dots$ is nearly accurate (Noack et al., 2003). The fact that modal TKE levels in the first several harmonics decline geometrically, with a factor of some 20-30 folds and higher between successive harmonics, allows additional simplifications. Considering the ideal, infinite Galerkin system (7b) and the explicit expressions (27), for $i = 1, \dots, 4$, we then have the following restrictions on pertinent quadratic terms:

- For $i \in \{1, 2\}$, non-negligible quadratic terms $q_{ijk}a_ja_k$ can only be those where either
 - $j \in \{1, 2\}$ and $k \in \{3, 4\}$
 - $j \in \{3, 4\}$ and $k \in \{1, 2\}$
 - $j \in \{1, 2\}$ and $k = 0$,
 - $j = 0$ and $k \in \{1, 2\}$,

Likewise, using the convention that a_0 is the coefficient of the 0^{th} harmonic, namely, the shift mode coefficient, we have:

- For $i \in \{3, 4\}$, non-negligible quadratic terms $q_{ijk}a_ja_k$ can only be those where $j, k \in \{1, 2\}$.

These observations will be used to estimate the rate of energy transfer from \mathbf{u}^C to \mathbf{u}^S , denoted T^{SC} in two ways: One estimate will be based directly

on the dynamic equations. The other will be based on a postulated eddy viscosity model.

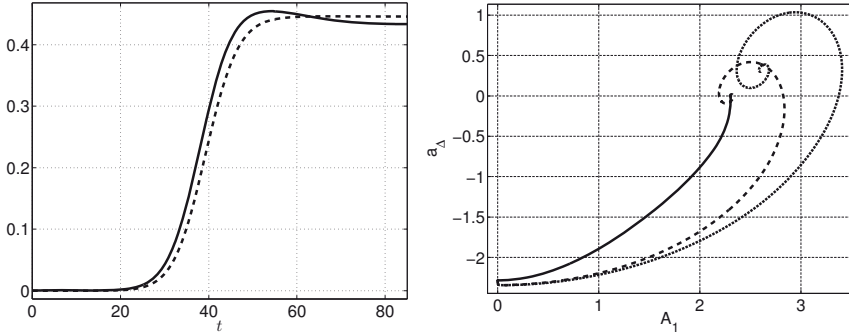


Figure 8. The proposed turbulence model is evaluated in a three states Galerkin model of the cylinder wake flow, comprising of the leading attractor POD mode pair and the shift mode (35b). The second harmonic amplitude A_3 is used as a surrogate for $a_S = \sqrt{K^S}$. The projection of the exact NSE solution (solid curve, left), is well approximated by the estimate obtained by slaving A_3 to A_1^2 , as in (37) (there, dashed). The effect of including this turbulence model in the Galerkin system is illustrated by transient plots in the (A_1, a_Δ) plane. The bold line continues to represent the exact NSE solution. The dissipation coefficient of the turbulence model (dashed curve) is determined by energy balance over the attractor, whereas the remaining coefficients are derived by the Galerkin projection of the NSE. The advantage of adding the turbulence model is evident in eliminating the over-prediction of the attractor amplitude and in reducing the transient overshoot of the original three states Galerkin model (dotted curve). That said, the remaining transient overshoot is nonetheless significant. It is the result of mode deformation, as will be discussed in § 6.

A direct estimate of T^{SC} . By the simplifications, above, the differential equations governing a_i , $i \in \{3, 4\}$, comprise linear (and stable) homogeneous parts and sinusoidal quadratic forcing terms at amplitudes that are proportional to $A_1^2 = A_2^2 (= 2K_1 = 2K_2)$. Consequently, $A_3 = A_4$ is linearly slaved to A_1^2 . A time scale separation between the response times in the first and second harmonics allows to approximate this property in algebraic, rather than dynamic terms:

$$A_3 = \kappa A_1^2. \quad (37)$$

This dependence can be seen in the left plot, in Figure 8.

The conclusion concerning $q_{ijk}a_ja_k$ with $i \in \{3, 4\}$ is that the TKE transfer rate from $K^C := K_1 + K_2 = \frac{1}{2}A_1^2$ to $K^S \approx K_3 + K_4 = \frac{1}{2}A_3^2$ is captured by

$$T^{SC} = \sum_{i=3}^4 \sum_{j,k=1}^2 q_{ijk}\bar{a}_i \bar{a}_j \bar{a}_k =: \lambda A_1^2 A_2 = \underbrace{\lambda \kappa}_{=: \frac{1}{4}v} A_1^4 = v K_1^2. \quad (38)$$

The same conclusion is obtained in complete analogy by evaluation of the terms $q_{ijk}\bar{a}_i \bar{a}_j \bar{a}_k$ with $i \in \{1, 2\}$, in order to estimate the same energy flow rate.

An eddy viscosity estimate of T^{SC} . A subgrid (modal) eddy viscosity suggests that the suppression of the energy flow from \mathbf{u}^C to \mathbf{u}^S can be compensated by adding dissipative terms of the form $-\nu_t a_i$, $i = 1, 2$, to the first two equations in the Galerkin system. The average rate of TKE loss, i.e., $T^{CS} = -T^{SC}$, due to these terms is

$$\hat{T}^{CS} := \sum_{j=1}^2 \nu_t \bar{a}_j^2 = \nu_t A_1^2 = 2 \nu_t K_1. \quad (39)$$

To be valid, the eddy viscosity estimate (39) needs to be reconciled with (38). Denoting attractor related values by the subscript “ $*$ ”, the selection of

$$\nu_t := \frac{1}{2} v K_* \quad (40)$$

achieves that objective over the attractor. Yet along transients and near \mathbf{u}_s , the discrepancy between (39) and (38) grows indefinitely. The root cause for the discrepancy is the very *structure* of the eddy viscosity compensation by a linear dissipative term, instead of the quadratic nonlinearity of the transfer terms in the exact Galerkin system.

Commenting on the discussion to this point, we stress that while the approximate relations (37) and (38) were obtained under conditions that extend beyond the specific example of the cylinder wake, these conditions are not generic. Nonetheless, the illustrated causes for the mismatch between the eddy viscosity estimate and the correct value of T^{SC} are generic indeed. Specifically, the mismatch is due to the generic situation where K^S cannot be estimated at a constant level, and that the actual value of T^{SC} , arising from the sum of pertinent triadic terms $q_{ijk}\bar{a}_i \bar{a}_j \bar{a}_k$, cannot be approximated by a term proportional to K_i alone.

5.2 The Structure of Valid Subgrid Models

We seek a consistent, low complexity scheme for adding dissipation to the Galerkin system, in a way that can compensate for the severance of energy flow from $\mathbf{u}^B + \mathbf{u}^C$ to \mathbf{u}^S in the exact model. We shall derive that scheme in two steps: In the first step, termed **the energy balancing step**, we focus on the slower, non-oscillatory dynamics of the energy flow equation (24). Here we shall formulate an added phase invariant dissipative term with the goal of reconciling the energy levels of the truncated system with those of the ideal model, as derived from NSE simulations. In the second step will translate the expressions obtained for the energy dynamics equation to phase dependent correction terms in the truncated Galerkin system (7b).

Energy Balance. The truncated energy conduits from \mathbf{u}^C to \mathbf{u}^S are the triadic terms that involve at least one unresolved mode in (24):

$$T_i^S := \sum_{\substack{j, k \geq 1 \\ \max\{j, k\} > N}} q_{ijk} \bar{a}_i a_j a_k. \quad (41)$$

The terms contributing to the summation in (41) have been analytically computed in (28) for periodically dominated flows, yielding

$$T_i^S := \frac{1}{4} \sum_{\substack{j, k \geq 1 \\ \max\{j, k\} > N \\ i = |j \pm k|}} \sigma_{ijk} q_{ijk} A_i A_j A_k, \quad i = 1, \dots, N, \quad (42)$$

In a more general setting, lacking the rigid phase information of periodically dominant dynamics, an estimate can be based on the FTT terms (30):

$$T_i^S := \sum_{\substack{j, k \geq 1 \\ \max\{j, k\} > N}} \chi_{ijk} A_i A_j A_k \left(1 - \frac{3K_i}{K_i + K_j + K_k} \right). \quad (43)$$

The challenge in a reduced order model that suppresses a detailed resolution of \mathbf{u}^S , is that T_i^S needs to be estimated without explicit knowledge of the amplitudes A_j , $j > N$. We shall base our estimates from two variants of a simple axiom, motivated by generic power laws for the distribution of modal energy as a function of the modal frequency:

Axiom 5.1 (A Global Algebraic Power Rule).

$$K^S = \kappa (K^C)^\lambda$$

for some $\kappa > 0$ and $\lambda > 1$.

In the cylinder wake example we used the equality $K^C = 2K_1$ and the approximation $K^S = 2K_3$ to show in (37) that this axiom is a good approximation with $\lambda = 2$. Variants may include distinct *effective* modal TKE levels K_i^S , which allows the energy of the turbulence flow field that interacts with \mathbf{u}_i to vary with i . In that case, K^C substituted by K_i and mode-dependent κ_i and λ_i need to be used.

For simplicity we focus first on periodically dominated flows satisfying Axiom 5.1. In that case, the expression (41) is approximated by an expression of the form

$$T_i^S \approx (K^C)^{\frac{\lambda}{2}} A_i \sum_{j=0}^N \xi_{ij} A_j, \quad i = 0, \dots, N. \quad (44)$$

The sum thus approximates contributions of terms in (42) that include a single A_j , $j > N$, in the ideal, infinite system, but neglects the products of two such terms, which are assumed small. The unresolved amplitudes are substituted by $(K^C)^{\frac{\lambda}{2}}$.

The terms T_i^S are added to the truncated energy equation. In nearly periodic, un-actuated systems, that will be

$$\frac{d}{dt} K_i = \sum_{j=1}^N 2l_{ii} K_i + \sum_{\substack{1 \leq j, k \leq N \\ i = |j \pm k|}} \frac{1}{4} \sigma_{ijk} q_{ijk} A_i A_j A_k + T_i^S, \quad (45)$$

where $\sigma_{ijk} = \pm$ is determined by which harmonic functions are involved. Using NSE simulations data, the free parameters of the dissipative term, i.e., η_i and ξ_{ij} , are estimated by the requirement that (45) be satisfied by that data. An additional simplification is this formulation is attained by a focus only on energy exchanges between a single resolved mode and \mathbf{u}^S , whereby $\xi_{ij} = \delta(i - j) \xi_i$.

The Galerkin Subgrid Terms. The translation of a phase invariant estimate of T_i^S in (44) into phase dependent terms in the Galerkin system (7b), will be based on our previous derivation of the translation of terms in (7b) into terms in the Galerkin energy equations (24): The quadratic term $q_{ijk} a_j a_k$, in the former, gives rise to the term $\frac{1}{4} q_{ijk} A_i A_j A_k$ (or $\frac{1}{2} q_{ijk} A_i A_j A_k$ when one index is 0) in the latter. The conclusion, in the reversed translation, the terms T_i^S need to be multiplied by 2, that one copy of A_i should be eliminated, and that the terms A_j should be substituted by

$\mp a_j$, where, once again, the sign is determined by which harmonic functions are involved. Thus, T_i^S from (44) gives rise to Galerkin system terms of the form

$$d_i^S := \frac{1}{2} \sum_{j=0}^N \xi_{ij} (K^C)^{\frac{\lambda}{2}} a_j. \quad (46)$$

In a simplified version, those terms reduce to *nonlinear modal eddy viscosity* terms

$$d_i^S = \frac{1}{2} \xi_{ij} (K^C)^{\frac{\lambda}{2}} a_i =: -\nu_{t,i}(K^C) a_i. \quad (47)$$

Considering this approach in the context of the cylinder wake example and the three states model (36), we recall the estimates (37) and thus, (38). The former agrees with Axiom 5.1 with $\lambda = 2$. The latter agrees with the simplified version (47) with $\xi_{11} = \xi_{22} = v$. The added dissipative terms in (36b) will thus be proportional to $-K^c a_i$. With that subgrid representation added to (36), we obtain the system

$$\frac{d}{dt} \begin{bmatrix} a_1 \\ a_2 \end{bmatrix} = \begin{bmatrix} \sigma^C - \beta^C a_\Delta - \nu_t a_S & -(\omega + \gamma a_\Delta + \zeta a_S) \\ \omega + \gamma a_\Delta + \zeta a_S & \sigma^C - \beta^C a_\Delta - \nu_t a_S \end{bmatrix} \begin{bmatrix} a_1 \\ a_2 \end{bmatrix}. \quad (48a)$$

$$\frac{d}{dt} a_\Delta = -\sigma^B a_\Delta + \beta^B (a_1^2 + a_2^2) - c, \quad (48b)$$

$$a_S = \kappa (a_1^2 + a_2^2). \quad (48c)$$

We also note that slaving the shift mode to the fluctuations will make (48b) an algebraic counterpart of (48c). The improvement in the dynamic prediction due to the inclusion of this subgrid model is visualized in the right plot, in Figure 8.

An alternative, substitutes the algebraic dependencies in Axiom 5.1 by dynamic dependencies:

Axiom 5.2 (Global Dynamic Power Rule). The modal TKE level K^S , satisfies

$$\frac{d}{dt} a_S = -\sigma^S a_S + \kappa (K^C)^\lambda.$$

for some $\kappa, \sigma^C > 0$ and $\lambda > 1$.

Returning to our running example, with the dynamic variant, a fourth dynamic state is added to (36), leading to the system:

$$\frac{d}{dt} \begin{bmatrix} a_1 \\ a_2 \end{bmatrix} = \begin{bmatrix} \sigma^C - \beta^C a_\Delta - \nu_t a_S & -(\omega + \gamma a_\Delta + \zeta a_S) \\ \omega + \gamma a_\Delta + \zeta a_S & \sigma^C - \beta^C a_\Delta - \nu_t a_S \end{bmatrix} \begin{bmatrix} a_1 \\ a_2 \end{bmatrix}. \quad (49a)$$

$$\frac{d}{dt} a_\Delta = -\sigma^B a_\Delta + \beta^B (a_1^2 + a_2^2) - c, \quad (49b)$$

$$\frac{d}{dt} a_S = -\sigma^S a_S + \kappa (a_1^2 + a_2^2), \quad (49c)$$

5.3 Closing Comments

Lumped force models: A low order alternative to the binary resolve-or-neglect choice. Low order models are differentiated from detailed models by a clear focus on an application-specific set of dynamic properties that need to be resolved, and by the high premium put on low complexity. The amplitude and phase of certain flow structures, e.g., the amplitudes and phases associated with von Kármán vortices in wake control, the leading and trailing edge vortices in separation control, are examples. This focus labels as “uninteresting” significant portions of the flow’s dynamic characteristics, and an inherent dilemma: Neglecting these structures, hence their impact on retained flow structures, hinders effective and accurate dynamic predictions. Including additional states increases complexity and sensitivity, and therefore erodes a model’s utility in realtime applications. Motivated by the universal significance and mean field and subgrid representations, we have suggested a third path: Representing the lumped forces effected by neglected structures on retained states. Time scale separations enables to model such impact by few slow states that interact with similarly slow properties, e.g., oscillations amplitudes, of retained states.

An analogy between mean field and subgrid representations. The structure of (49c) in the augmented system (49), and the stabilizing role played by the added state, a_S , in that system, are completely analogous to the structure and of the Galerkin-Reynolds equation (49b) and the role of the shift mode coefficient a_Δ . The same parallelism applies to the algebraic variant, i.e., to (48), and an obvious slaved mean field model counterpart. This similarity is by no means accidental: Although \mathbf{u}^B and \mathbf{u}^S aggregate altogether different frequency ranges and length scales in the flow, the focus in both models is on representations of slow mechanisms for time averaged energy exchanges with \mathbf{u}^C . This analogy is easily seen when stated in terms of period averaged energy exchanges between states in ideal harmonic expansions.

The structural analogy to the mean field model may reduce in more complex configurations, when $\lambda \neq 2$ provides the best fit, or when non-periodic flows require an appeal to an FTT representation, based on (43), as explained in the previous chapter, and in more detail, in Noack et al. (2010). Nonetheless, the main ingredients of the big picture will remain essentially

unchanged: The centerpiece of the added viscosity in the i^{th} equation will remain of the form of $-\nu_t(K_1, \dots, K_N)a_i$. The fundamental difference from the standard linear eddy viscosity approach is the explicit dependence of the positive dissipation coefficient ν_t on the resolved TKE, as a monotonously increasing, algebraic or dynamic function. The viscosity coefficient vanishes at the steady solution, and it grows indefinitely with the growth of K^S . In complete analogy to the state dependent stabilizing effect of the mean field model, this functional dependence reflects the changes in the dissipative effects of turbulence on large coherent structures along the modeled dynamic manifold.

A conceptual departure from the Galerkin framework. The introduction of the mean field model may have constituted a new focus in low order Galerkin models, but did not deviate from the traditional Galerkin framework. In contrast, the Galerkin subgrid framework outlined here introduces a significant conceptual departure from the Galerkin framework. To this point, the state of the Galerkin system state has been the time varying vector $\mathbf{a} = (a_1, \dots, a_N)$ of coefficients of an approximation of the NSE state \mathbf{u} by a modal expansion (7a). The modeling premise is that the compression of the NSE to the state space hyperplane that is defined by these expansions is a good approximation, and the dynamical system was based on the NSE as the constitutive equation. None of these ingredients applies to (49c): Here a_S is an estimated surrogate for the unresolved TKE component, K^S . The constitutive equation is not the distributed NSE, but the lumped energy dynamics equation (21). A first principles derivation of the coefficients of (49c) and of the added dissipative term in equations governing the unsteady states (49a) now has to be derived by balancing empirical energy flow rates, i.e., balancing (24) with empirical time trajectories of a_i , $i = 1, \dots, N$, and not by a projection of the NSE.

Is the subgrid model simply a calibration method? Attractor energy flow analysis in Galerkin models was developed in (Rempfer, 1991) and expanded in (Noack et al., 2002, 2005) and is the foundation of our FTT framework (Noack et al., 2008). This useful tool was recently adapted to the analysis of transient dynamics, and played a central role in establishing the necessity of a mean field model by energy flow considerations, in Tadmor et al. (2010). Energy balancing grew to become an important component of what is known as *calibration*, i.e., parameter tuning in low order Galerkin flow models, aiming to compensate for dynamic distortions such as those described here (Manhart, 1998; Tadmor et al., 2004; Tadmor and Noack, 2004; Noack et al., 2005; Couplet et al., 2005; Attar et al., 2006; Galletti

et al., 2007; Cordier et al., 2010; Bourguet et al., 2009; Navon, I. M. Navon).

One may thus argue that once system parameters are calibrated by empirical data, there might not be any need for a subgrid model. For example, in Tadmor et al. (2004); Tadmor and Noack (2004); we have demonstrated that a properly calibrated three states model (36) can provide a near perfect representation of the natural transient. In effect, here the subgrid model is absorbed into (36), exploiting the identical structures of the mean field and the subgrid equations. While that may well be the case in some examples, even then we see a significance in the very understanding of the correct structure of the subgrid model, in general, as well as in the ability to derive a model from constitutive equations. Absent the rigorous hard error bounds one has in linear systems theory, the reliance on the physical fundaments is as important to ensure robustness and reliability of the model, as are, the often very limited empirical validation experiments.

6 Mode Deformation and Models on Nonlinear Manifolds

The very objective of flow control can be stated in terms of the deformation of leading flow structures (Prabhu et al., 2001). Such deformations are also characteristic of short and long term changes in the ambient operating conditions, such as in the incoming flow velocity and orientation, and during any significant transient, whether controlled or in response to disturbances and ambient changes (Prabhu et al., 2001; Lehmann et al., 2005; Morzyński et al., 2007). To be useful in flow control, models must accommodate these changes over the intended dynamic envelope, loosing neither their predictive power, simplicity and robustness. Here we discuss structural issues that stand in the way of meeting these conflicting demands by standard Galerkin flow models, and suggest a framework of Galerkin models on nonlinear manifolds as a promising alternative.

Bifurcations, where small parameter changes lead to abrupt and drastic realignment of the large scale topology of the flow are associated with model discontinuity (Marsden and McCracken, 1976; Guckenheimer and Holmes, 2002; Aref et al., 2007). Most feedback flow control tasks, however, address flow regulation at a level of resolution where one encounters gradual, continuous modification of dynamic and topological characteristics⁵.

⁵To further elaborate this point, note that while the supercritical bifurcation in the wake flow at $Re_c \approx 47$ marks a transition to instability and the emergence of a periodic attractor, key flow characteristics are qualitatively preserved and undergo only a gradual quantitative change during that bifurcation: A pair of least-stable (equiv.

These changes preserve *qualitative* topological and dynamic properties but may have significant cumulative *quantitative* effects. So much so, that the representation capability of a Galerkin model derived at a single nominal operating point may be seriously deteriorated over large portions of the desired dynamic range, and with it, the utility of control design, based on that model (Gerhard et al., 2003; Lehmann et al., 2005; Luchtenburg et al., 2006).

Following a summary of key aspects of the effects of mode deformation and a review of possible paths to address them, right below, the purpose of this section is to describe a class of nonlinear Galerkin models, defined over nonlinear manifolds and expressly geared to meet the challenge associated with dynamic deformation of leading flow structures. In § 7 we shall utilize the proposed framework to address yet another outstanding modeling challenge, the representation of flow over unsteady boundary geometries.

Finally, we mention a recent elegant account of similar ideas in Sapsis and Lermusiaux (2009) developed in the context of stochastic nonlinear PDEs.

6.1 Adverse Effects of Deforming Coherent Structures

We highlight three aspects of the adverse cumulative effects of the deformation of dominant flow structures, that we have already briefly mentioned in the previous section, illustrated by properties of the cylinder wake flow.

Poor resolution of the flow field by the Galerkin expansion. To illustrate this issue we revisit our previous observation that the quantitative differences between stability and attractor POD modes, and between an unstable steady NSE solution and the mean flow of an attractor, can both be substantial. As seen in Figure 2, these differences are especially manifest in the near wake of a cylinder, where the recirculation bubble of \mathbf{u}_s is over three times longer than that of the attractor's mean, $\mathbf{u}_{*,0}$. As a consequence,

most unstable) eigenmodes dominates the dynamics of perturbations from \mathbf{u}_s , these modes are associated with a complex conjugate pair of eigenvalues of the linearized NSE, and changes in both these modes and eigenvalues are continuous as functions of the Reynolds number. Moreover, while the suppression of mean field representation in the Galerkin model will not entail an instability when $Re < Re_c$, the arguments heretofore regarding the significance of mean field variations to accurate dynamic predictions remain valid, motivating a model of the form (36) or (49) to predict the dynamic response to large initial perturbations, or in the use of dynamic models in branch continuation, as in Mishra et al. (2009). The point we make here is therefore that structure of the model is preserved and the expansion modes undergo only a gradual change, even during changes in flow conditions that entail stability related bifurcations.

if the Galerkin approximation employs \mathbf{u}_s and the modulated two dominant eigenmodes, to resolve the unsteady flow, then attractor oscillations of the significant unsteadiness of the velocity field cannot be adequately resolved within that near wake area that is contained in the recirculation bubble of \mathbf{u}_s . Conversely, the use of the attractor mean, $\mathbf{u}_{*,0}$, and of the two leading attractor POD modes, in the Galerkin approximation, will lead to gross over prediction of the oscillations amplitude in the near wake area, at the beginning of the transient leading from \mathbf{u}_s to the attractor. In fact, the TKE resolution, in both cases, will deteriorate to $\leq 50\%$. In this example, this poor resolution compares with the excellent resolution feasible by a locally extracted two modes expansion of the same flow, seen in Figure 3. Figure 5 provides an additional illustration of mode deformation, showing changes between the actuated and the natural attractors of the high lift configuration example.

Poor dynamic predictions. The prediction of dynamic properties of the flow by the Galerkin system, including the growth rate and oscillation frequencies, are determined by the Galerkin projection of the NSE on the expansion hyperplane. The accuracy of the approximation of the NSE by the Galerkin system critically depends on the resolution of the velocity and the acceleration fields by the Galerkin approximation. The level of prediction will therefore deteriorate, away from the operating point at which the model was derived. This fact is vividly illustrated in Figure 3, where we ignore for the moment the overshoot issue, which is caused by the lack of a subgrid model, which we discussed previously. Comparing the trajectories of the exact NSE solution and of the Galerkin model we see that many more periods are needed in the latter to reach comparable changes in the mean field, and eventually, to reach the attractor level. This difference is due to an order of magnitude difference between the Galerkin projection evaluation of σ^B , in (36) and (48), and the real part of the leading eigenvalue of the linearized NSE, at \mathbf{u}_s . A careful observation will also reveal the cumulative phase difference between the two trajectories, reflecting a nearly 25% difference between the POD-based Galerkin projection's evaluation of the oscillation frequency, and the imaginary parts of the said eigenvalues. These qualitative changes are quantitatively visualized in the plots of the time variations of the instantaneous vortex shedding frequency and of the exponential growth rate of the fluctuations, along the natural transient of the cylinder wake flow, in Figure 3.

Distorted phase predictions. As will be further elaborated in § 8, the information about the phase of flow oscillations is critical in dissipative

feedback control. Intuitively, in order to stabilize an unsteady flow by TKE dissipation, the actuation must act as an opposition force and oscillate at the same frequency and at an opposing phase to the oscillatory velocity field it aims to attenuate. A correct prediction of both the relevant phase of the flow and thus, of the effective phase of the actuation, are therefore essential to the success of a stabilizing opposition control policy. The loss of resolution of oscillations at the dominant frequency by expansion modes, away from the operating conditions at which these modes were derived, leads to the subsequent deterioration in the model based definition of the correct actuation phase. As a consequence, control will become ineffective; not only may it lose its dissipative effect, but it may actually become destabilizing (Gerhard et al., 2003; Lehmann et al., 2005; Luchtenburg et al., 2006).

Existing Remedies The issues reviewed above are widely recognized roadblocks, and have motivated considerable efforts to mitigate their impact. Approaches to address these issues can be categorized as follows:

Limiting the operational envelope. A simple way to avoid the distortions caused by mode deformation is to stick to the classical restriction of Galerkin models to a single operating point and thus, the narrow validity region of the expansion set, such as near an attractor or a fixed point. Yet this approach gives up on the very purpose of low order models in flow control applications: As stated in the introduction, the essence of feedback control is to enable a system to operate properly through time varying assignments of the operating conditions and in unsteady ambient environments.

Extended mode sets. Representing the obvious flip side of the same idea, mode deformations can be addressed by including in the expansion set modes obtained at multiple operating conditions. This approach has been adapted, in multiple variants by many research groups. In our own work, Noack et al. (2003), we demonstrated that using both the stability and the attractor POD modes, along with the shift mode (35b), the Galerkin system recaptures a nearly exact dynamic representation.

The common denominator in the wide range of proposed versions of this approach, is the goal to minimize the overall size of the extended expansion set. Examples of variants are the double POD (Siegel et al., 2008) and interval based POD (Borggaard et al., 2007), adding modes extracted by sensitivity analysis (Hay et al., 2009), and informing snapshot selection by computed probability densities and uncertainty quantification (Mathelin and Maitre, 2009).

One obvious downside of this approach is an eventual loss on the model

complexity front. A second issue that is perhaps less obvious at first glance, is the possible raise of the numerical sensitivity associated with the design of dynamic observers for the extended state space. This observation too is illustrated by Figure 2: While modes obtained at different points that reflect the continuous deformation of a distinct flow structure, along a transient, may be different enough to cause the obstructions described right above, these modes may still be far from mutually orthogonal, raising the specter of numerical sensitivity in any effort to distinguish between their respective contributions to a single noisy sensor signal.

Online mode set adaptation. To mitigate the proliferation of the expansion set for wide validity envelopes, yet another family of solutions is based on the adaptation of the expansion set on the fly. Examples include an iterative, simulation based search for an optimal state trajectory and an optimal control, or an iterative optimal state estimation, using an adaptive reduced order model, along with a periodic appeal to the NSE. These methods include, e.g., adaptive control methods (Ravindran, 2000), the *trust region* approach (Fahl, 2000; Arian et al., 2000; Bergmann et al., 2007; Bergmann and Cordier, 2008; Chen et al., 2009), and the *episodal POD* technique (Mokhasi and Rempfer, 2008; Mokhasi et al., 2009). The advantage of this class of methods is that the size of the expansion set remains equal to that of a local model, avoiding both the aforementioned issues of complexity and numerical sensitivity, which can be critical in nonlinear dynamic optimization. Yet the need to repeatedly re-derive the modes and model coefficients, as the operating conditions changes, would typically render adaptive low order models far more computationally taxing than their nonadaptive counterparts. So much so, that such procedures become effective, primarily in off line computations, where they still enable substantial computational savings when compared with using the NSE alone.

Offline mode set adaptation. The topic of this section is a third option: The adaptation of the model and mode set using a pre-computed correction scheme. This approach aims to realize the advantages of adaptation and address the hurdles listed above, without sacrificing the potential for realtime implementation. The ingredients of solutions in this class must include a parameterization of the dynamic envelope, a method to utilize sensor readings to determine changes in the operating point, within that envelope, and characterization of changes in the expansion modes and the dynamical system, as a function of the operating point parametrization. Next we shall formalize these ingredients in terms of nonlinear manifold embedding, and a Galerkin dynamical system, defined on that manifold, as an extension to

the affine embedding of the classical Galerkin framework (7). Early versions of these ideas have been presented in Lehmann et al. (2005); Luchtenburg et al. (2006); Morzyński et al. (2007); Stankiewicz et al. (2008). Related work on deformable modes in reduced order models in fluid dynamics can be found in Amsallem and Farhat (2008); Amsallem et al. (2009); Sapsis and Lermusiaux (2009). We also note that concepts of mode deformation and interpolation have long been a mainstay in video processing and in the generation of animation videos, including animation of fluid motion (Chiang et al., 2008; Amanatiadis and Andreadis, 2009). Finally, nonlinear manifold embedding is at the core of center and approximate inertial manifold models, including fluid dynamic and flow control applications (Foias et al., 1988; Foiaş et al., 1988; Holmes, 1985; Du and Gunzburger, 2003; Noack et al., 2003; Kasnakoğlu et al., 2009). The framework presented below bears both similarities and points of departure from the center / inertial manifold formalism that we will highlight in the closing comments, at the end of this section.

6.2 Deformable modes and accurate low order models

Instead of adding modes in order to resolve mode deformation over the entire operating envelope, the proposed solution is to employ a low dimensional parametrization $\alpha \in \mathcal{A}$ of the operating point, allowing the modes to deform as nonlinear functions of α , and the approximation, to take values over a nonlinear manifold, parametrized by α :

$$\mathbf{u}(\mathbf{x}, t) \approx \mathbf{u}^B(\mathbf{x}, \alpha) + \sum_{i=1}^N a_i(t) \mathbf{u}_i(\mathbf{x}, \alpha). \quad (50a)$$

The dimension N of the local tangent space of the nonlinear manifold embedding is lower than that of the linear subspace span by the ensemble of all local tangent spaces of the form (50a), for all $\alpha \in \mathcal{A}$, which is the required dimension of an affine approximation with the same resolution. The difference is reflected in the order of the dynamical system, governing the evolution of the state $\mathbf{a} = [a_i]_{i=1}^N$. This advantage comes at the obvious cost of higher structural complexity. We will revisit this point along the discussion.

To derive the form of the dynamical system component of the model we first observe that the time derivative of the approximation (50a) now includes an $\dot{\alpha}$ -proportional force field, in addition to the traditional ex-

pansion by the time derivatives of the coefficients a_i :

$$\begin{aligned} \partial_t \mathbf{u}(\mathbf{x}, t) &\approx \sum_{i=1}^N \dot{a}_i(t) \mathbf{u}_i(\mathbf{x}, \alpha) \\ &+ \left(\frac{\partial}{\partial \alpha} \mathbf{u}_0(\mathbf{x}, \alpha) + \sum_{i=1}^N a_i(t) \frac{\partial}{\partial \alpha} \mathbf{u}_i(\mathbf{x}, \alpha) \right) \dot{\alpha}(t). \end{aligned} \quad (50b)$$

The projection of the NSE on (50a) will therefore include both α -dependent coefficients and $\dot{\alpha}$ -proportional terms:

$$\begin{aligned} \dot{a}_i &= c_i(\alpha) + \sum_{j=1}^N l_{ij}(\alpha) a_j + \sum_{j,k=1}^N q_{ijk}(\alpha) a_j a_k \\ &+ \left(c'_i(\alpha) + \sum_{j=1}^N l'_{ij}(\alpha) a_j \right) \dot{\alpha}, \quad i = 1, \dots, N. \end{aligned} \quad (50c)$$

The $\dot{\alpha}$ -dependent terms can be neglected when the time constant of changes in the operating condition is small relative to the oscillation period. This is fairly generic during natural transients. It is also a standard requirement in on line adaptation schemes. Yet the significance of including $\dot{\alpha}$ -dependent terms is precisely in allowing fast transitions. Conceptually, these terms define a spatially global force field that realizes the effect of the deformation of leading flow structures. In this way, (50) provides a critical enabler to representing intrinsically transient effects, such as the dynamic morphing of a leading edge vortex over a rapidly pitching airfoil into a stagnant separation bubble, hence the hysteresis in lift loss. This effect cannot be captured by the prediction of aerodynamic forces in terms of the state of a traditional, low order Galerkin expansion. As we shall see in the discussion of unsteady boundaries, in § 7, this mechanism is also critical for Galerkin modeling of flow interactions with moving boundaries.

Illustrating these ideas, we have shown (cf. Figure 2) that the topology of both the respective mean fields and of the pairs of local modes representing the oscillatory field, gradually morph from one set of velocity fields to the other along the transient, naturally lending themselves to smooth parametrization. We have also shown (cf. Figure 3) that the unsteady cylinder wake flow is well approximated near any point along the natural transient by a Galerkin expansion, defined by a parametrized representation of the local mean field and a single pair of locally derived modes. The excellent kinematic approximation is paralleled at the dynamic model level by the agreement of the Galerkin projection values of system coefficients with observed dynamic properties of the exact NSE solution for the natural transient of the cylinder wake flow (cf. Figure 9). The Galerkin model employs interpolated modes of the form (52). A practical computational method to explicitly realize the parameterization, including the one showed in Figure 9, will be discussed next.

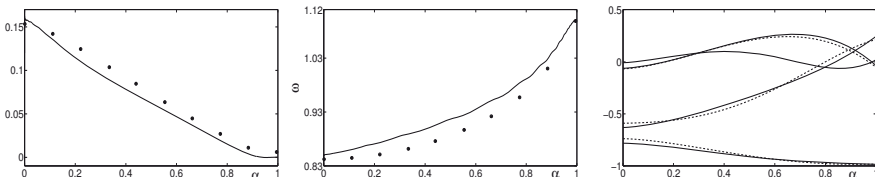


Figure 9. To illustrate the quality of the parametrized Galerkin model, we compare the transient values of \dot{A}_1/A_1 along the natural transient of the exact NSE solution (left, solid) with the Galerkin projection evaluation of the expression $\sigma^C - \beta^C a_\Delta$, using the local bases at several intermediate operating points (left, dots). The parametrization is by $\alpha = K_1^{1.5}$. The small positive residual illustrates both the need for a turbulence model and the agreement between the empirical and theoretical observations. A similar comparison is made in the center figure between the observed and predicted shedding frequency. Once again the quality of the approximation is a vast improvement of what is achieved with a single basis. The right figure depicts the interpolation coefficients $b_{i,k}(\alpha)$ for $i = 0$ and $i = 1, 2$, when the local bases are defined by the interpolation scheme (52), with $L_0 = 4$ and $L_1 = L_2 = 3$.

6.3 Computational Aspects of Parametrized Mode Sets

The success of nonlinear Galerkin models of the form (50) depends on several key ingredients. Those include the ability to derive a smooth, low sensitivity mapping

$$\alpha \mapsto \mathbf{u}_i(\cdot, \alpha) : \mathcal{A} \mapsto \mathcal{L}^2(\Omega), \quad i = 0, 1, \dots, N.$$

that covers the desired range; the ability to derive a computationally simple and robust approximation of these mappings; and the ability to robustly estimate the parameter α from measurable quantities. Conceptually, there are two interdependent facets to each of these issues. One facet concerns the rate and extent of changes in the leading coherent flow structures along transients, covered by the dynamic envelope. The smoothness and rate of mode deformation along such transients is a measure of the feasibility of the proposed framework, and can be determined by direct analysis of such transients. The other facet concerns the existence of a simple α parametrization of the operating condition.

Parametrize the operating point. Externally determined components of α include the incoming flow velocity and its orientation, the parameters

of pulsatile actuation with slowly varying frequency, amplitude and phase shift relative to a fixed reference frame (time) or to flow oscillations. Also included in this category are parameters of a varying boundary geometry, ranging from flapping flight through membrane actuators, to elastic fluid body interactions. As noted earlier, the discussion of moving boundaries is deferred to § 7. State dependent parameter components need to be robustly estimated from measured surrogates. Examples include the TKE of the unsteady flow, the TKE captured in a frequency band, and the dominant oscillations frequency and the choice should be driven by minimizing the numerical sensitivity of dynamic estimation from sensor data.

The examples we used to illustrate the discussion, above, were all restricted to relatively slow deformations and straightforward parametrization. That said, our studies experimental and simulation based studies of 2D and 3D wake stabilization, in Lehmann et al. (2005); Pastoor et al. (2008), demonstrate the ability of the suggested framework to produce easily, robustly implementable and effective control strategies. In the cylinder wake example, Lehmann et al. (2005), both the shift mode coefficient a_Δ and the instantaneous TKE can be used to parametrize the operating point and both can be inferred from appropriately positioned point-wise flow velocity sensing. In the experimental 3D bluff body stabilization, Pastoor et al. (2008), an even simpler, implicit parametrization underlies a phase feedback that depends on the incoming flow velocity and the phase of vortex shedding from a single lip of the bluff body. A very similar phase feedback strategy, successfully applied to the dynamic state estimates and feedback control of shear layer vortices, in Pastoor et al. (2005), and to separation control of the flow over an airfoil at a high AOA, in Joe et al. (2008); Joe and Colonius (2010).

The dynamics of operating point parametrization. A central outstanding challenge is the potential for *dynamic* interconnections between measurable parameters and deformable flow structures. As an illustration, consider the *dynamic stall* phenomenon (McCroskey, 1982). The dynamic nature of the deformation of dominant flow structures that determine the aerodynamic forces over a rapidly pitching airfoil is at the essence of this phenomenon. To account for the dynamic dependence of lift and drag on the angle of attack (AOA), Theodorsen's classic model incorporates the pitch rate into a functional representation of these forces. Later extensions, e.g., McCroskey (1982); DeLaurier (1993); Goman and Khrabrov (1994); Peters et al. (2007)), include in the lift model a simple dynamic system representation of the dependence of aerodynamic forces on the AOA. The goal is to account for such phenomena as the substantial delay in the gradual

changes of the lift, following the end of a pitching motion, i.e., when the AOA is already constant. Despite some experimental demonstration in the cited articles, our experience⁶ clearly shows that this type of models is very sensitive to changes in the characteristics of the pitching maneuvers. The approach proposed in this chapter is to regain robustness by basing the said dynamic model on the key physical aspects that come to play: Forces generated by the moving boundary, which will be discussed in the following section, and the dynamics mode deformation. By this approach, a successful model will be able to correctly couple the parametrization (50a) of mode deformation by α , with an identified auxiliary model that determines α dynamically, in terms of the AOA and other characteristics of the ambient flow. This remark will be further clarified by our next discussion of moving and bending boundaries.

The form and computation of deformable modes. The simplest option is to use (local) linear approximations:

$$\begin{aligned}\mathbf{u}_i(\mathbf{x}, \alpha) &\approx \mathbf{u}_{*,i}(\mathbf{x}) + \kappa_i(\alpha)\mathbf{u}_{\Delta,i}(\mathbf{x}), \\ \partial_\alpha \mathbf{u}_i(\mathbf{x}, \alpha) &\approx (\partial_\alpha \kappa_i(\alpha)) \mathbf{u}_{\Delta,i}(\mathbf{x}).\end{aligned}\quad (51a)$$

Here $\mathbf{u}_{*,i}$ is the value of the i^{th} mode at a nominal operating point, such as over an attractor, and $\mathbf{u}_{\Delta,i}$ approximates the gradient (or the Jacobian, when α is vector valued) $\partial_\alpha \mathbf{u}_i$. The nonlinearity of the dependence on α is absorbed in the mappings $\alpha \mapsto \kappa_i$. As in the case of the shift mode definition, (35b), the simplest way to define the approximate gradients $\mathbf{u}_{\Delta,i}$ is via

$$\mathbf{u}_{\Delta,i} := \frac{1}{\|\mathbf{u}_{*,i} - \mathbf{u}_{s,i}\|_\Omega} (\mathbf{u}_{*,i} - \mathbf{u}_{s,i}), \quad , i = 0, 1, \dots, N, \quad (51b)$$

where the attractor is the selected nominal operating point and the steady solution defines the maximal intended range of the approximation. The evaluation of the interpolation coefficients κ_i as functions of $\alpha \in \mathcal{A}$ can then be identified and tabulated from transient numerical or experimental data. Figure 10 illustrates these ideas with depictions of $\mathbf{u}_{\Delta,i}$, $i = 1, 2$, calculated for the natural transient of the cylinder wake flow. The figure thus complements Figure 6 which showed $\mathbf{u}_\Delta := \mathbf{u}_{\Delta,0}$.

Refined approximations are achievable by a projection of POD approxi-

⁶Here we refer to observation made during joint experimental work with D. R. Williams and associates on flow control of a pitching 3D airfoil Williams et al. (2009).

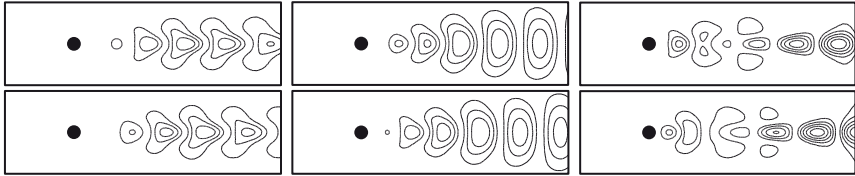


Figure 10. The “shift modes” in a least order approximation of the deforming mode pair that resolves the shedding frequency along the natural transient of the cylinder wake flow. The two shift modes, as defined in (51b), are depicted in the right column. For ease of reference we present here again the corresponding stability eigenmodes, (left column), resolving the 1st harmonic near the steady solution, and the mode pair that resolves that harmonic over the attractor (center column).

mations of each of the “trajectories” $\alpha \mapsto \mathbf{u}_i$ onto the unit sphere in $\mathcal{L}^2(\Omega)$:

$$\mathbf{u}_i(\cdot, \alpha) \approx \sum_{\ell=1}^{L_i} \tilde{a}_{i,\ell}(\alpha) \mathbf{u}_{i,\ell}, \quad \sum_{\ell=1}^{L_i} \tilde{a}_{i,\ell}^2 \equiv 1. \quad (52)$$

The application of this option to the natural transient of the cylinder wake flow is illustrated in Figure 9, depicting the flow fields $b_{i,\ell}$ in POD approximations (52) of \mathbf{u}_i , $i = 0, 1, 2$. The smoothness of the α dependencies illustrate the robustness and simplicity of these approximations. An illustration focused on the 0th harmonic can be found in Tadmor et al. (2010).

The expressions (51) represent the interpolation of $\mathbf{u}_i(\cdot, \alpha)$ between evaluations at the two ends of a transient. Yet another natural refinement is thus the interpolation between sampled values of $\mathbf{u}_i(\cdot, \alpha)$ at multiple intermediate points. This approach, in conjunction with POD modeling, gave rise to the use of geodesic curves over the Grassmann manifold of orthonormal bases, e.g., in Amsallem and Farhat (2008); Amsallem et al. (2009). The use of geodesic interpolation, formalized in Edelman et al. (1998), is common in image and video processing. Since the geodesic is defined in terms of the interpolation hyperplane, rather than individual base vectors, it requires an additional of extracting the explicit basis realization. The advantage of the POD based interpolation (52) over the interpolation approach is that as a POD approximation, (52) optimizes the approximation with respect to bounds on the number of representative flow fields $\mathbf{u}_{i,\ell}$, using the entire data regarding the α -dependence of the expansion modes. In contrast, the starting point of an interpolation scheme is the a priori selection of these fields, as determined by the interpolation points.

While geodesic interpolation over a Grassmann manifold concerns the entire interpolation plane, the hierarchical significance of expansion modes, indicated by their index, is a fundamental albeit implicit tenet of the Galerkin framework. There is therefore an advantage to parametrization approaches that retain the index references to the modes. The harmonic expansion has this advantage, as modes are identified by both the harmonic number and the phase alignment with respect to a common phase trajectory and slowly varying frequencies. An advantage of harmonic modes over POD modes is the instability of the indexing with respect to changes in the operating points: POD approximations can experience significant state space rotations between modes representing similar energy levels in response to small variations in the operating point.

6.4 Closing Comments

Parametrized modes vs. higher dimension. Our first comment revisits the important distinction between higher state dimension and the inclusion of a dependence on the parameter α . This is called for because, at a first glance, an approximations such as (52) may appear as equivalent to the use of the larger expansion set, $\{\mathbf{u}_{i,\ell}\}_{\ell=1}^{L_i} \}_{i=1}^N$, which is precisely what we tried to avoid, in the first place. We therefore recall that the coefficients $\tilde{a}_{i,\ell}(\alpha)$ in the parametrization (52) are not states of the dynamical system. As functions of α , these coefficients are determined either by an external input, including control commands and the ambient conditions, or as functions of the Galerkin system state, $\mathbf{a} = [a_i]_{i=1}^N$. In the latter case, this slaving of $\{\tilde{a}_{i,\ell}\}_{i,\ell}$ is conceptually analogous to the slaving of higher modes to few dominant modes in center and approximate inertial manifold models. The distinction is that here, the goal is the resolution of mode deformation between operating points, and not the not the resolution of smaller and faster structures, as in center and approximate inertial manifold models.

Parametrized modes vs. center and inertial manifold models. Expanding on this point, the center / approximate manifold approximation of the flow field (and generally, the exact state of the high order system), is by expansions of the form

$$\mathbf{u} = \mathbf{u}_* + \sum_{i=1}^N a_i \mathbf{u}_i + \sum_{i=N+1}^{N+M} \tilde{a}_i(\mathbf{a}) \mathbf{u}_i,$$

where $\mathbf{a} = [a_i]_{i=1}^N$ is the state of the low order Galerkin system, \mathbf{u}_i , $i = N+1, \dots, N+M$, are the slaved modes of a higher order model, resolving finer spatial and temporal resolution.

In contrast, when the formalism of (52) is used, the flow field reconstruction in the proposed framework is

$$\begin{aligned}\mathbf{u} &= \mathbf{u}_* + \sum_{i=1}^N a_i \mathbf{u}_i(\alpha) \\ &= \mathbf{u}_* + \sum_{i=1}^N a_i \sum_{\ell=1}^{L_i} \tilde{a}_{i,\ell}(\alpha) \mathbf{u}_{i,\ell}, \\ \alpha &= f(\mathbf{a}, \text{inputs}).\end{aligned}\quad (53)$$

What changes is therefore the purpose of using $\sum_{i=1}^N L_i > N$ modes, which is the resolution of mode deformation, rather than smaller scales. The two approaches are therefore complementary, rather than overlapping.

Analytic construction of the parametrized expansion set. The ability to compute the deforming expansion modes by direct appeal to the NSE and stability eigenmodes, as an alternative to the empirical / post processing approach we described earlier, is an interesting observation, previously pursued in relation to base flow corrections (Tadmor et al., 2007b, 2010). This approach is based by an extension of the use of the Reynolds equation and a close variant can be found in the aforementioned independent and elegant study by Sapsis and Lermusiaux (2009). A brief outline of key aspects of the procedure is presented here for harmonic expansions.

A useful observation. The computations is greatly facilitated by the observation that the local deformation of the mode \mathbf{u}_i must be orthogonal to that mode. The reason is simply the fact that the normalized modes vary over the unit sphere in $\mathcal{L}^2(\Omega)$, whereby the correction term, which is proportional to the tangent vector $\partial_\alpha \mathbf{u}_i$, must be orthogonal to the sphere at \mathbf{u}_i :

$$\partial_\alpha \mathbf{u}_i \perp \mathbf{u}_i. \quad (54)$$

Expansions of small fluctuations from \mathbf{u}_s : Small fluctuations from a fixed point are approximated by eigenmode expansions

$$\mathbf{u} = \mathbf{u}_s + A_0 \mathbf{u}_0 + \sum_{i=1}^{N_h} A_i (\cos(\phi_i) \mathbf{u}_{2i-1} + \sin(\phi_i) \mathbf{u}_{2i}). \quad (55)$$

Here N_h is the number of frequencies we aim to resolve and $\{\mathbf{u}_{2i-1}\}_{i=1}^{N_h}$ are the respective stability eigenmodes, at \mathbf{u}_s is the fixed point. The linear mean field correction mode, \mathbf{u}_0 , is the eigenvector for the largest real eigenvalue. It may be difficult to compute when that eigenvalue represents fast decay. In that case $A_0 = 0$ and \mathbf{u}_0 can be ignored when very small fluctuations are considered. To simplify this brief discussion, we shall nonetheless

assume that \mathbf{u}_0 is known. The rationale presented here will allow the reader to extend the observations we make to the case where we use $\mathbf{u}_0 = 0$ near α_s .

Generalized Reynolds averaged equations. Let us recall the spatio-temporal projections we used in the discussion of harmonic expansions, in § 3.

The period averaged projection of the NSE on the expansion (55) is the Reynolds equation, (33a). That equation determines the (quadratically dominated) algebraic relationships between A_0 and A_i , $i = 1, \dots, N_h$. However, as A_1 is increased, so will the residuum in the period averaged NSE. That residuum can be corrected by correcting both A_0 and \mathbf{u}_0 , i.e., by defining

$$\begin{aligned} A_0(\alpha_s + \delta\alpha\partial_\alpha)\mathbf{u}_0(\alpha_s + \delta\alpha\partial_\alpha) \\ \approx A_0(\alpha_s)\mathbf{u}_0(\alpha_s) + (\partial_\alpha A_0\mathbf{u}_0(\alpha_s) + A_0(\alpha_s)\partial_\alpha\mathbf{u}_0) \delta\alpha, \end{aligned}$$

where α_s is the parameter value at the steady solution and $\delta\alpha$ reflects the change in the operating condition. The orthogonality property (54) allows us to partition the residuum equation into two independent linearized equations, one for the component of the mean field correction that is aligned with $\mathbf{u}_0(\alpha_s)$, yielding the amplitude correction $\partial_\alpha A_0$, and one for the component orthogonal to $\mathbf{u}_0(\alpha_s)$, yielding the orientation $\partial_\alpha\mathbf{u}_0$ of the $\dot{\alpha}$ -proportional mode deformation.

As in the computation of Fourier coefficients, (14), sinusoidally weighted period averages distill the NSE components that are pertinent to each participating frequency and phase. In precisely the same manner, and by precisely the same rationale as for the 0^{th} harmonic, right above, these weighted averages create equations that define the dependence of the incremental amplitudes and modes as functions of $\delta\alpha$. That is, they allow us to solve for $\partial_\alpha A_i$ and for $\partial_\alpha \mathbf{u}_i$, for all i . Moreover, a Galerkin projection of the NSE, using the corrected modes and amplitudes, will yield the corrected value of the dominant frequency $\omega(\alpha_s + \delta\alpha)$.

Incremental marching. There is no conceptual difference between the computation of $\partial_\alpha A_i$ and $\partial_\alpha \mathbf{u}_i$, near α_s , and between the computation of such increments near any other operating point. Key to this observation is the fact that the computations are based on period averaging, whether near α_s or near any other value of α . The conclusion is that expansion modes, coefficients and frequency can (ideally) be computed along the entire operational range in terms of solutions of a succession of incremental equations.

7 Galerkin Models for Flows in Unsteady Geometry

Fluid interactions with moving and deforming boundaries are part and parcel of key fluid mechanics issues, from flow control challenges in engineered systems through bio-flyers and swimmers, to plants. Familiar examples in engineered systems include damaging vibrations in turbine engines (Russell, 1950; Hall et al., 2006; Boyce, 2006), wind turbines (Andersen et al., 2007; Barlas and van Kuik, 2009; Wilson et al., 2009; Berg et al., 2009), helicopter blades (Leishman, 2006) and civil infrastructure (Clark et al., 2004; Strømmen, 2006; Stathopoulos and Baniotopoulos, 2007), full-structure bending and torsional forces on light, high-altitude long-endurance (HALE) flying wings, such as DARPA’s Vulture and NASA’s ill-fated Helios (Noll et al., 2007; Patil, 2007; Raghavan and Patil, 2010), and both damaging flutter and buffeting and the currently pursued potential for lift enhancement and drag reduction by active aero/hydroelastic and boundary actuation mechanisms (Theodorsen, 1935; Livne, 2003; Ho et al., 2003; Kamakoti and Shyy, 2004; Clark et al., 2004; Ansari et al., 2006; de C. Henshaw et al., 2007; Kota et al., 2009; Carruthers et al., 2007; Liang et al., 2006; Lopez and Sarigul-Klijn, 2010; Dong et al., 2010). Equally interesting, elastic fluid body interactions are central to bio-swimmers and bio-flyers (Pendleton, 2000; Ho et al., 2003; Fish and Lauder, 2006; Carruthers et al., 2007; Kato and Kamimura, 2008; Lauga and Powers, 2009; Dong et al., 2010; Shyy et al., 2010), and even plant-wind interactions (de Langre, 2008). In addition to their critical roles in crisply encapsulating an accessible understanding of the physics of fluid-body interactions, and in the design of feedback controllers, low order models are increasingly sought as computational tools, used to accelerate numerical simulations in these highly demanding configurations (Schuster et al., 2003; FFAST, 2010). This section addresses the conceptual challenge of a consistent definition of LOGMs for these flow configurations, and the means to compute such models.

7.1 A Galerkin Modeling Conundrum and Existing Solutions

In applications such as the examples listed above, the Galerkin modeler faces yet another, seemingly insurmountable conceptual conundrum: Unsteady geometry requires that (Eulerian) global expansion modes satisfy at once the mutually exclusive dynamic properties of body and of fluid, over subdomains that are alternately occupied by body and by fluid. This inherent contradiction precludes the physical credibility and consistency that are at the very foundation of the Galerkin approach to model reduction. Here we review existing approaches and set the ground for a solution path.

Most prevalent solution categories. Reviewing today’s state of the art (Dowell and Hall, 2001; Livne, 2003; Schuster et al., 2003; Clark et al., 2004; Peters et al., 2007; Demasi and Livne, 2009; Silva et al., 2009), most existing solutions may be broadly classified in one of two general categories:

In one category, low oscillation amplitudes justify a sole focus on the generated acceleration forces acting on the fluid at the boundary. Boundary displacements and domain variations are ignored, the ambiguity regarding the governing dynamic laws is eliminated, and the Galerkin method can be used in its traditional form. Methods that employ linearized elasticity models are quintessential examples of this approach.

The primary focus of methods of the second category is on the elastic body. Fluid dynamic representation is reduced to low order models of aerodynamic forces, induced by the flow. Tracing to Theodorsen (1935), such models may postulate potential flows, with or without a periodic train of vortices over an airfoil, and or calibrate aerodynamic forces by harmonic balancing. Methods in this category provide effective computational and analytical tools in (nearly) steady or in predictably periodic flows.

These broad-brush descriptions do not do ample justice to the rich and diverse pools of ideas in each of the two categories. Nonetheless, they provide a “birds-eye view” of the limitations of both, when the targeted fluid-body system displays large scale, unsteady, transient dynamics.

Actuation modes. Yet a third direction, applicable primarily to rigid body motion, is based on two complementary ideas:

- (i) Transition to body-locked coordinates. This is straightforward in an external flow around a single moving rigid body. Resulting variations of far field geometry are viewed as negligible and handled by domain truncation to a uniform, time invariant subdomain.
- (ii) An unsteady coordinate change induces an unsteady addition to the velocity field, including the boundary velocity. The unsteady velocity at the boundary is absorbed by a modulated Galerkin expansion, using (incompressible) *actuation / boundary modes* $\mathbf{u}_{act,i}$, so that the velocity field

$$\mathbf{u} - \mathbf{u}_{act} := \mathbf{u} - \sum_{i=1}^{N_{act}} b_i \mathbf{u}_{act,i}, \quad (56)$$

is steady along the boundary. When this correction follows a transition to a steady domain, then $\mathbf{u} - \mathbf{u}_{act}$, has the properties required by the traditional Galerkin framework: A steady domain with steady boundary conditions.

We illustrate these ideas, right below, with two simple examples: The oscillating cylinder (Noack et al., 2004b; Tadmor et al., 2004; Siegel et al., 2008; Liberge and Hamdouni, 2010), and the rotating cylinder (Graham et al., 1999a,b; Bergmann et al., 2005, 2007). Other pertinent examples include the lid-driven cavity (Fitzpatrick et al., 2005), and the flow around a heaving and pitching airfoil (Lewin and Haj-Hariri, 2005; Stankiewicz et al., 2008). Finally, we mention also actuation modes arising in the context of an unsteady inflow which does not involve boundary motion, but does invoke very similar ideas (Kasnakoğlu et al., 2008). We shall revisit these examples throughout this section.

* *The vertically oscillating cylinder.* Referring to the description in § 2, we use α to denote the instantaneous vertical coordinate of the center of the cylinder, whereby the unsteady domain is

$$\Omega(\alpha) = \{ \mathbf{x} = (x, y) \in [-5, 15] \times [-5, 5], : \| (x, y - \alpha) \| \geq 1/2 \},$$

and the point-wise parametrization of the boundary is

$$\Omega'(\alpha) = \left\{ \mathbf{x}_b(\alpha, \kappa) := 1/2 \begin{pmatrix} \cos(\kappa) \\ \sin(\kappa) \end{pmatrix} + \alpha \begin{pmatrix} 0 \\ 1 \end{pmatrix}, \quad \kappa \in [0, 2\pi) \right\}.$$

Moving to a body locked coordinates, the cylinder center is used as origin. Vertical fluctuations of the upper and lower boundaries, now located at $y = \pm 5 + \alpha$, are ignored and $\Omega_c := \Omega(0)$ is used as a fixed computational domain. Ignoring the far field unsteady boundary is justified since the spatial development of flow unsteadiness near the upper and lower boundaries is negligible.

The transition to a body locked coordinates induces a global addition of a vertical velocity $-\dot{\alpha} \begin{pmatrix} 0 \\ 1 \end{pmatrix}$. This addition cancels the original vertical velocity of points along Ω'_c , where a standard zero velocity boundary condition now holds. Yet the added unsteadiness is felt away from the cylinder, and in particular, the far field boundary velocity is now unsteady. The actuation mode used to cancel this unsteadiness in Noack et al. (2004b); Tadmor et al. (2004), is depicted in Figure 11 (left plot). It is a viscous potential flow around the cylinder, with a vertical unit amplitude inflow.

* *The rotating cylinder.* This effects of cylinder rotation on lift, drag, and wake stability have been studied extensively in both experimental and numerical studies (Hu et al., 1996; Mittal and Kumar, 2003; Lo Jacono et al., 2008). Flow control studies (Graham et al., 1999a,b; Bergmann et al., 2005, 2007; Bergmann and Cordier, 2008) employed low order Galerkin models

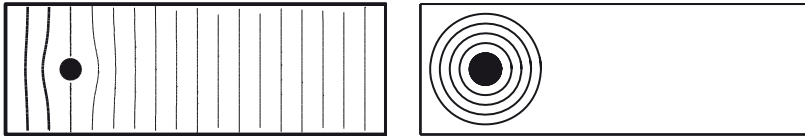


Figure 11. Left: An actuation mode \mathbf{u}_{act} for the vertically oscillating cylinder is defined as a potential flow with a vertical inflow. Right: An actuation mode for the rotating cylinder is a potential vortex flow with a zero far field azimuthal velocity.

and required a method to address boundary unsteadiness. The solution proposed by these authors is the use of an actuation mode depicted in the right plot, in Figure 11, formed as a potential vortex flow, driven by the rotating cylinder with a no-slip boundary condition, and a zero azimuthal velocity on a larger, concentric circle. Notice that while this example involves an unsteady boundary, the geometry of the flow domain is steady, to begin with.

Lagrangian- Eulerian methods and deformable grids. Shortcomings of the actuation / boundary modes approach include the lack of systematic guidelines for generating actuation modes and, more significantly, a quantum leap in the challenge of the transition to steady coordinates of elastic and multiple bodies. To address the latter, a number of pioneering studies (Epureanu et al., 2002; Anttonen et al., 2003, 2005; Feng and Soulaimani, 2007; Liberge et al., 2008) endeavored to adapt Eulerian-Lagrangian dynamic mesh adaptation methods, that are commonly used in CFD models of aeroelasticity (Batina, 1990; Farhat et al., 1998; Blom, 2000; Schuster et al., 2003; Ishihara and Yoshimura, 2005; Hsu and Chang, 2007; Xie et al., 2007; Braun et al., 2008; Roszak et al., 2009). The objective in these methods is to continuously deform the fluid simulation's grid, in a way that agrees with the deforming fluid-body interface and that obeys pertinent geometric properties, including incompressibility. Identifying the flows state not with the Eulerian location but rather, with the index of a Lagrangian grid point, these methods achieve the equivalent of a transition to a canonical computational domain. An analogy of the deforming fluid domain to the boundary-driven equilibrium of an elastic body allows the developer of a numerical method to draw on a vast body of knowledge in theoretical and numerical solid mechanics. Developments along these lines are still vibrant, not only in CFD and computational elasticity (Bijelonja et al., 2006; Persson and Peraire, 2009) but also in other areas of applied geometry, notably, in diverse areas of computer graphics (Hong et al., 2006; Irving et al., 2007;

Adams et al., 2008; Dizioli and Bayer, 2009).

Our objective in this section is to review a broadly applicable methodology that integrates these ideas with the observation underlying the actuation modes approach, regarding the two ingredients of a successful solution: The transition to a steady computational domain, where the ambiguity between body and fluid is removed, and the cancellation of residual unsteady velocity at the boundary, to enable the space-time separation of variables, at the essence of the Galerkin paradigm. In what follows we use two subsections to derive the characteristics of each of these two components, preparing for the subsequent constructive integration of the two. Setting the ground for these technical discussions, we begin with a brief review of basic formalism and assumptions that will be used, and introduce the concept of the *complete flow domain*, for flows over unsteady boundaries.

7.2 Canonical Embedding Preliminaries

Nomenclature and assumptions. To simplify notations, throughout this section we use $\alpha \in \mathcal{A}$ only to define a smooth *point-wise* parametrization of the boundary⁷ $\Omega'(\alpha)$ of the compact domain $\Omega(\alpha)$. That is, we assume that boundary points are defined by a smooth function $\mathbf{x}_b(\alpha, \kappa) \in \Omega'(\alpha)$, where κ is a local coordinates parametrization (in the differential geometric sense) of the boundary curve or surface, for each α .

The boundary $\Omega'(\alpha)$ may include both walls of bodies immersed in, or bounding the flow, and free, far field inflow and outflow boundaries of the studied domain. Restricting this discussion to incompressible flows, we assume that the volume (or area) of $\Omega(\alpha)$ is constant, and independent of α . Where needed, the constant volume assumption can be easily enforced by α -dependent far field, inflow and outflow boundaries.

The velocity conditions along the boundary include steady or unsteady inflow and outflow conditions, and *no-penetration* and *no-slip* conditions along body walls. The latter require that, along these sections, fluid velocity must agree with wall velocity.

We treat α as an exogenous input. Control mechanisms and elastic fluid-body interactions are represented by feedback laws, determining α .

The augmented domain and velocity field. While the ambiguity regarding the applicable dynamic rule at points in space that are alternately

⁷We bear in mind, however, that the need to parametrize mode deformations may only rise in the presence of deforming boundaries, and that viable models should incorporate parametrization of mode deformation, as discussed in § 6.

occupied by fluid and structure is clear, we argue that essentially the same ambiguity exists throughout the spatial domain: The dynamic rule at a point \mathbf{x} is determined by the location of \mathbf{x} relative to the boundary. A complete description of a point in the domain thus requires the specification of the pair (\mathbf{x}, α) , whereby the *complete flow domain* is the manifold:

$$\mathcal{M}_\Omega := \{(\mathbf{x}, \alpha) : \alpha \in \mathcal{A}, \mathbf{x} \in \Omega(\alpha)\}. \quad (57)$$

Vector fields over \mathcal{M}_Ω comprise of pairs (\mathbf{u}, ν) , so that

$$\frac{d}{dt}(\mathbf{x}, \alpha) = (\mathbf{u}, \nu). \quad (58)$$

The concept of the complete domain, \mathcal{M}_Ω , will enable the use of compact and unambiguous formalism, throughout this discussion. For example, in stating the prescribed wall velocity, by (58).

Should we develop LOGMs over \mathcal{M}_Ω ? The derivation of expansion modes by the methods considered heretofore requires a succession of snapshots of the flow. Among other issues (e.g., the nonlinearity of \mathcal{M}_Ω) we note that a LOGM for the flow over \mathcal{M}_Ω stipulates that a snapshot is a vector field (\mathbf{u}, ν) , which needs to be defined for all $(\mathbf{x}, \alpha) \in \mathcal{M}_\Omega \mathcal{M}_\Omega$. Yet the time trace of a simulation or an experiment defines the fluid velocity $\mathbf{u}(\cdot, t)$ as a vector field over $\Omega(\alpha(t))$, for the single value of $\alpha(t)$. This gap can be closed in a way that conceptually parallels what will be described here. Considering the complexity of this option, however, our choice is to limit the use of the augmented domain and vector fields to the notational and conceptual simplifications they will enable along the discussion. LOGMs will be developed more traditionally, either over a canonical computational domain, or equivalently, in an Eulerian-Lagrangian setting, over an unsteady grid in the physical domain, as will be explained below.

7.3 Canonical Embedding for Deforming Boundaries

Admissible embedding in a canonical computational domain. The transition to a steady (canonical) computational domain, Ω_c , is made by an *admissible mapping*, ψ ,

$$\psi : (\mathbf{x}, \alpha) \mapsto (\mathbf{x}_c, \alpha) : \mathcal{M}_\Omega \mapsto \Omega_c \times \mathcal{A}, \quad (59)$$

which is required to satisfy the following basic properties:

- ψ is a diffeomorphism. This is clearly necessary to enable an unambiguous correspondence between the flow over the physical domain and its

representation over the canonical domain.

- For each α , $\psi(\Omega'(\alpha), \alpha) = (\Omega'_c, \alpha)$. Thus, a coordinate parametrization of Ω'_c is defined by $\kappa \mapsto \psi(\mathbf{x}_b(\alpha, \kappa), \alpha)$, for each $\alpha \in \mathcal{A}$.
- For each α , the induced mapping

$$\mathbf{x} \mapsto \mathbf{x}_c : \Omega(\alpha) \mapsto \Omega_c$$

is incompressible (isocheric).

The velocity field over the canonical domain. Invoking (58), an admissible mapping ψ induces a mapping of velocity fields over the physical domain to velocity fields over the canonical computational domain, via:

$$\begin{aligned} \Psi(\mathbf{u}, v, \mathbf{x}, \alpha) &= \left(\frac{d}{dt} \psi(\mathbf{x}, \alpha), \psi(\mathbf{x}, \alpha) \right) \\ &= ((J_{\mathbf{x}_c, \mathbf{x}} \mathbf{u} + J_{\mathbf{x}_c, \alpha} v, v), \psi(\mathbf{x}, \alpha)), \end{aligned} \quad (60a)$$

where

$$J := \begin{bmatrix} J_{\mathbf{x}_c, \mathbf{x}} & J_{\mathbf{x}_c, \alpha} \\ 0 & I \end{bmatrix} := \begin{bmatrix} \partial_{\mathbf{x}} \mathbf{x}_c & \partial_{\alpha} \mathbf{x}_c \\ 0 & I \end{bmatrix} \quad (60b)$$

is the Jacobian of ψ . The requirement that ψ be diffeomorphic guarantees that $J_{\mathbf{x}_c, \mathbf{x}}$ is invertible, and that both this Jacobian and its inverse are smooth functions of (\mathbf{x}, α) . The inverse mapping has a similar form:

$$\begin{aligned} \Psi^{-1}(\mathbf{u}_c, v, \mathbf{x}_c, \alpha) &= \left(\frac{d}{dt} \psi^{-1}(\mathbf{x}_c, \alpha), \psi^{-1}(\mathbf{x}_c, \alpha) \right) \\ &= ((J_{\mathbf{x}_c, \mathbf{x}}^{-1} \mathbf{u}_c - J_{\mathbf{x}_c, \alpha}^{-1} J_{\mathbf{x}_c, \alpha} v, v), (\mathbf{x}, \alpha)). \end{aligned} \quad (60c)$$

The mapping Ψ translates boundary conditions in the physical and the velocity of the boundary motion, reflected by $\nu = \dot{\alpha}$, into boundary velocity conditions over the canonical domain.

An auxiliary flow. An admissible mapping ψ is associated with an auxiliary Lagrangian (particle) flow over the manifold \mathcal{M}_{Ω} : $\forall \alpha, \beta \in \mathcal{A}$,

$$\mathcal{S}(\beta, \alpha) := \psi^{-1}(\cdot, \beta) \circ \psi(\cdot, \alpha) : (\Omega(\alpha), \alpha) \rightleftarrows (\Omega(\beta), \beta). \quad (61)$$

The smooth invertibility of ψ implies that \mathcal{S} is a diffeomorphic and incompressible (isocheric) deformation of the physical domain, depending smoothly on α .

The requirement that the boundary be invariant under ψ means that \mathcal{S} gives rise to a diffeomorphic flow over the boundary:

$$\mathcal{S}_b(\beta, \alpha) : (\Omega'(\alpha), \alpha) \rightleftarrows (\Omega'(\beta), \beta), \quad (62a)$$

such that

$$\forall \alpha, \beta \in \mathcal{A}, \quad \mathcal{S}_b(\beta, \alpha) = \mathcal{S}(\beta, \alpha) |_{(\Omega'(\alpha), \alpha)}. \quad (62b)$$

The Lagrangian particle flow \mathcal{S} induces a corresponding flow of velocity fields, in complete analogy to (60):

$$\mathcal{T}(\beta, \alpha) := \Psi^{-1}(\cdot, \cdot, \dot{\beta}, \cdot, \beta) \Psi(\cdot, \cdot, \dot{\alpha}, \cdot, \alpha) \quad (63)$$

This definition leads to consistent concepts of algebra and analysis by which snapshots of the velocity field over one boundary configuration can be compared to, and algebraically co-manipulated with snapshots over another boundary configuration. The, presence of the canonical domain is kept implicit, and the governing equation, the NSE, remains unchanged!

A focus on \mathcal{S} . The following observation allows us to consider the construction of ψ and Ψ , indirectly, in terms of \mathcal{S} and \mathcal{T} :

Observation 7.1. *An admissible mapping ψ generates an ensemble of admissible, diffeomorphically equivalent maps $\{\psi_\beta\}_{\beta \in \mathcal{A}}$:*

$$\psi_\beta(\mathbf{x}, \alpha) := \mathcal{S}(\beta, \alpha)(\mathbf{x}, \alpha) \in \Omega(\beta) \times \{\beta\}. \quad (64)$$

Consequently, ψ also generates an ensemble of mappings $\{\Psi_\beta\}_{\beta \in \mathcal{A}}$, which correspond to $\{\psi_\beta\}_{\beta \in \mathcal{A}}$ in complete analogy to the definition (60) of Ψ in terms of ψ . There is therefore no loss of generality in assuming that $\Omega_c = \Omega(\beta)$, for any fixed $\beta \in \mathcal{A}$, using ψ_β and Ψ_β in the roles of ψ and Ψ .

A “spring analogy” construction of \mathcal{S} : Basic steps. Lagrangian-Eulerian methods, mentioned on p. 61, offer a natural option for the construction of \mathcal{S} . Given the extensive literature on these methods, and ongoing efforts invested in their continued improvement, we see no need or point to expend on a favorite variant. This discussion is therefore limited to a conceptual outline of generic key steps, right below, to be followed by highlight of possible points of departure from CFD considerations and implementations of spring-analogy algorithms:

- A point β is selected as the *origin* in the parameter set \mathcal{A} . In principle this selection is arbitrary, but as we shall comment later, it may be advantageous to select the parameter reflecting the elastic boundary in a relaxed state.
- A grid $\mathbf{X} := \{\mathbf{x}_i\}_{i=1}^{N_g} \subset \Omega(\beta)$, is selected to meet the desired resolution of a LOGM at the parameter value β . For later reference, we denote the

sub-grid of boundary points as $\mathbf{X}_b := \{\mathbf{x}_{b,j}\}_{j=1}^{N_{b,g}} \subset \Omega'(\beta)$.

- Boundary deformation, as α varies, translate to variations in \mathbf{X}_b . The initial selections of $\mathbf{x}_{b,j}$, for the parameter value β , therefore immediately extend to the definition of boundary grid points as functions of α . Thus

$$\mathbf{X}_b(\alpha) := \{\mathbf{x}_{b,j}(\alpha)\}_{j=1}^{N_{b,g}} \subset \Omega'(\alpha), \quad \alpha \in \mathcal{A}. \quad (65)$$

- An algorithm for smooth, incompressible mesh adaptation defines the deformation of \mathbf{X} in response to changes in $\mathbf{X}_b(\alpha)$, as α varies. Thus

$$\mathbf{X}(\alpha) := \{\mathbf{x}_i(\alpha)\}_{i=1}^{N_g} \subset \Omega(\alpha), \quad \alpha \in \mathcal{A}. \quad (66)$$

The incompressibility of the deformation is interpreted by the requirement that the volume of the grid cell represented by $\mathbf{x}_i(\alpha)$ is independent of α .

- The flow \mathcal{S} is defined by the mappings $\mathbf{X}(\alpha_1) \mapsto \mathbf{X}(\alpha_2)$, $\alpha_i \in \mathcal{A}$.
- The flow \mathcal{T} maps velocity fields over $\Omega(\alpha_1)$ to a velocity fields over $\Omega(\alpha_2)$, as a function of α_i and $\dot{\alpha}_i$, as detailed in (63).
- To extract expansion modes for a LOGM from velocity field snapshots $\{\mathbf{u}(\cdot, t)\}_{t \in \mathcal{I}}$, these snapshots need to be evaluated (interpolated) at the Lagrangian grid points $\mathbf{x}_i(\alpha)$, and viewed as functions of the Lagrangian grid points (identified by the indices, i). This way, the mapping \mathcal{T} enables the linear algebra of velocity fields from different snapshots, that can now be used in mode extraction methods, such as POD.

Note that in the discrete setting, the index j of a boundary point $\mathbf{x}_{b,j}(\alpha)$, is a discrete analogue of the parameter κ in a continuous description. Note also that the inflow and outflow boundary sections are generically steady. Thus, the generic boundary conditions for Lagrangian motion of grid points over this sections are independent of α .

The “spring analogy” construction of \mathcal{S} : Cautionary comments. It is important to highlight differences between CFD and LOGMs needs, and the essential implications of these differences on the implementation of adaptive mesh algorithms.

- The very large grids used in CFD simulations necessitate the spatial and temporal *localization* of mesh adaptation methods. Jumps and readjustments that may occur as a consequence, are viewed as a matter of course.

Consistency of the association of the instantaneous grid as a function of boundary configuration, is not required. In contrast, in order to be able to derive a viable parametrized LOGM, the essential property of (66) is that it is defined *globally*, both in space and as a function of α , and the simplicity, smoothness and robustness of this definition, held at a premium. At the same time, the far sparser grids that suffice for LOGM computations, make this type of grid definition feasible. An import of a mesh adaptation algorithm, “as is”, from a CFD context to LOGM use, is therefore very likely not to enable the desired definitions of \mathcal{S} and \mathcal{T} .

- A recurrent issue in the discussions of elasticity-based mesh adaptation concerns the adverse effects of over-stretching of the grid, such as in response to a rotational motion. Considering the simple example of a rotating cylinder, attaching boundary points of a grid formed as material points of a fictitious elastic body, to points along the boundary of the physical domain, i.e., the rotating cylinder and the steady far field boundary, will cause the elastic material to stretch in an infinite spiraling motion. This stretching will lead to loss of grid continuity and to numerical singularity. By the same token, this scenario also illustrates a situation in which the use of an adaptive mesh is not only difficult, but, is utterly unnecessary, and is easily substituted by the simple and robust implementation of an actuation / boundary mode, as discussed earlier.

What we have shown in the discussion leading to the outline of the construction of \mathcal{S} and \mathcal{T} , amounts to the observation that, when successful, that procedure can fully address the transition to a canonical domain, where fluid velocity obeys steady boundary conditions. Yet the simple example of the rotating cylinder demonstrates that the success of the outlined constructions is not guaranteed, highlighting grid stretching due to rotational motion, as a major culprit. That example reminds us of the second ingredient of the envisioned approach: The use of actuation modes. Our next step is to suggest a simple means to define actuation modes, and a way to use them to mitigate the observed shortfall.

The construction of \mathcal{S} : Slip conditions and actuation modes. As described above, and as commonly implemented in CFD applications, the elastic body analogy requires a rigid attachment of the fictitious elastic body, represents the fluid domain, to the physical domain’s boundary. That requirement ensures that the mapping of fluid velocity to the Lagrangian grid, will remain consistent with the inflow, outflow, no-penetration and no-slip conditions.

Considering the difficulty illustrated by the rotating cylinder example,

we note that its root-cause is the wall-tangent velocity, imposed by the no-slip condition. We also note that the no-slip condition has no bearing on geometry variations. The solution path outlined here is to use grid deformation *only* in order to track the unsteady geometry, as implied by the no-penetration conditions. In this framework, the boundary grid points in $\mathbf{X}_b(\alpha) = \{\mathbf{x}_{b,j}(\alpha)\}_{j=1}^{N_{b,g}}$ are allowed to slide along the walls of immersed bodies, but are held locked to the far field boundaries. Actuation modes will be used in a subsequent step, to absorb residual wall-tangent velocity, as in (56). As an aside, we note that the need to absorb residual boundary velocity may exist not only due to boundary motion, but also due to unsteady inflow velocity, whether as a control mechanism or a disturbance.

Comments & alternative guidelines. The prevention and remediation of over-stretching grid cells are critical components of elasticity-based adaptive mesh methods. The inclusion of torsional springs (Farhat et al., 1998) is an example of a quintessential preventative measure. Since CFD methods tolerate mesh discontinuity as a matter of course, a discontinuous mesh update is the generic remediation, once the benefits of the way the elastic structure is formulated, are exhausted. Giving up on the no-slip conditions, and the use of actuation modes counterparts, is generally not a viable option in CFD contexts. That said, a closer, localized look at the remeshing step would typically reveal the conceptual partition into a sliding grid component and a correction that resolve the residual slip velocity, i.e., the approach presented here as a global strategy. That analogy is explicit even in the very title of the Shear-Slip mesh update method of Tezduyar (2001). That said, some CFD methods do allow the mesh to slide over moving boundaries (Demirdžić et al., 1997).

We also note that while the removal of the no-slip condition will resolve the adverse effect of rotational stretching, it will not address the impact of large scale translational motion. Methods to address this challenge are based on multi-domain approach: A moving body is surrounded by a local subdomain that is locked to the body's geometry, and moved together with the body. The methods described here will then apply to grid adaptation within that local subdomain. Velocity fields on the local and global subdomains are then reconciled in a subsequent step which is less challenging since it does not involve unsteady geometries. Several authors have addressed the issue of large scale translational motion in CFD contexts (Tezduyar, 2001; Murman et al., 2003).

The last comment concerns the very of solid, rather than fluid mechanics to derive the mesh adaptation scheme. The motivation is clear: Even when a fluid flow is considered reversible, this applies only to the velocity

field, and not necessarily to the induced Lagrangian particle motion. That said, generic examples such as the substantial oscillations of a flexible airfoil can be handled by use of highly viscous (Stokes) simulations to define the auxiliary mappings \mathcal{S} and \mathcal{T} . The auxiliary Stokes flow is determined by boundary motion, as is derived from the original fluid simulations. In the generic case of (quasi) periodic oscillations, boundary motion can be expanded by a short harmonic expansion. Expanding the induced particle motion within the domain by a truncated harmonic expansion of the same length is a linear operation that does not affect incompressibility and defines domain (and grid) deformation that obeys the imposed boundary unsteadiness.

Example: A continuously deforming cylinder. Yet a third variant of the cylinder wake flow provides a very simple illustration of the Lagrangian-Eulerian approach to LOGMs of flows over unsteady boundaries. In this example the cylinder undergoes forced periodic deformations, and the fluid flow domain, $\Omega(\alpha)$, is parametrized by the phase, $\alpha \in [0, 2\pi] =: \mathcal{A}$, of these deformations:

$$\Omega(\alpha) := \{\mathbf{x} \in [-5, 15] \times [-5, 5] : \|\mathbf{x}\| \geq 0.5 + \epsilon \sin(\alpha) \cos(3\theta), \theta = \angle \mathbf{x}\}.$$

(The notation $\theta = \angle \mathbf{x}$ is interpreted by $\mathbf{x} = (x, y) = \|\mathbf{x}\|(\cos(\theta), \sin(\theta))$.) The deformations are illustrated by the top-left plot in Figure 12, where $\epsilon = 0.1$.

This example does not include rotational motion, and boundary unsteadiness is fully addressed by the transition to the canonical domain, defined by $\Omega_c := \Omega(0)$, or equivalently, by a transition to a Lagrangian grid. Domain deformation, i.e., the mappings ψ and Ψ , were computed both by an elasticity based adaptation and by the filtered Stokes simulation, as described in the preceding comment. As illustrated by the top-right plot in Figure 12, the maximum stroke of grid motion subsides rapidly as a function of the distance from the deforming cylinder, and is negligible near the far field boundary. A reference simulation was initiated by the steady NSE solution. As in the previous two cases, the amplitude of periodic vortex shedding oscillations grows along a transient, reaching a periodic attractor. Interestingly, following a brief alignment period, the evolution of the shedding frequency, ω , also shown in Figure 12, is quite similar to what is observed for the wake of a steady, rigid cylinder; i.e., starting with a low frequency at the early transient, and increasing as the flow approaches the attractor. That is the case even though the actuation frequency is held constant, at roughly the natural attractor shedding frequency of the flow over the rigid cylinder, which is the dominant frequency over the very near

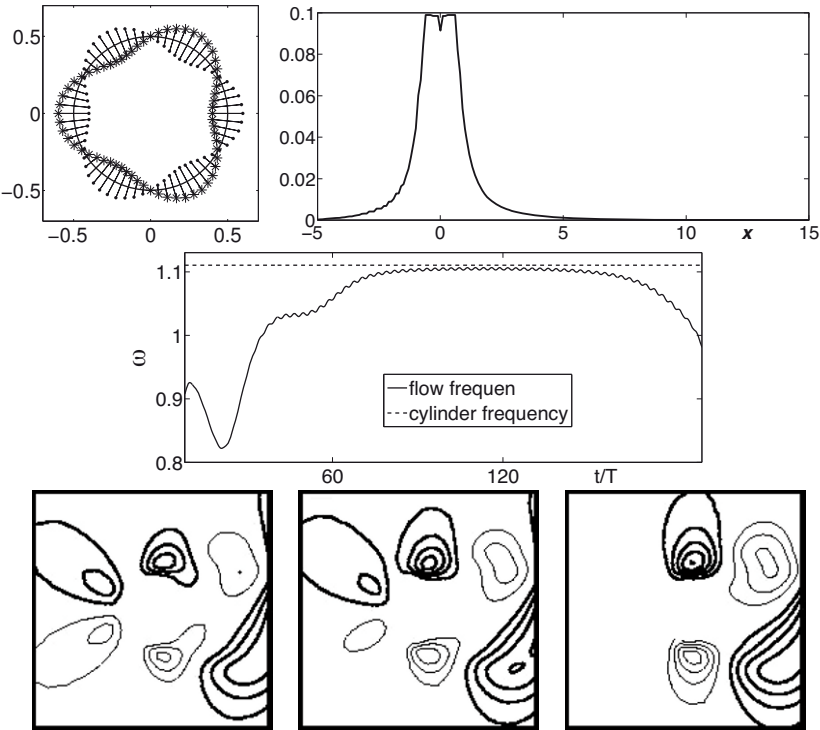


Figure 12. The periodically deforming cylinder. Top left: Grid points along the circular circumference are forced into sinusoidal fluctuations between the values indicated by bullets and asterisks. Top right: The maximal fluctuation of grid points $\{\mathbf{x}_i : |x_i(0) - x| < 0.2\}$, plotted as a function x . Center: Transient values of the instantaneous shedding frequency (solid), compared with the attractor shedding frequency of the rigid cylinder (dashed). Bottom: Near field zoom on 3 “physical domain” snapshots of the first harmonic mode $\mathbf{u}_1(\cdot \alpha)$, as it varies along an attractor period. The far field evaluation of $\mathbf{u}_1(\cdot \alpha)$ is nearly constant and similar to its counterpart over the attractor of the static cylinder wake.

field. Also noticed is the imperfect lock in of the shedding frequency onto the actuation frequency, evidenced by the dip in ω towards the end of the data stretch.

The velocity snapshots were mapped by the appropriate Ψ to equivalent snapshots over Ω_c , with a steady inflow velocity, and zero velocity over the cylinder wall. Harmonic expansion modes $\mathbf{u}_{c,i}$ were computed for the velocity field over $\Omega_c = \Omega(0)$. These modes where computed with respect to the instantaneous shedding frequency, and remain essentially constant over the attractor. The harmonic modes were pulled back to each $\Omega(\alpha)$ in the “physical domain”, using the inverse mapping, Ψ^{-1} , according to (60). This defines $(\alpha, \dot{\alpha})$ -dependent modes \mathbf{u}_i , over $\Omega(\alpha)$. (We shall revisit the revisit the general form of modes defined this way shortly; cf. (69)–(71), below.) While the harmonic modes are very similar to their rigid cylinder counterparts over the far field, the dependence on the oscillatory parameter variations is reflected by near field unsteadiness of each \mathbf{u}_i . The three plots at the bottom of Figure 12 illustrate this fact by a zoom on a streamline depiction of harmonic mode \mathbf{u}_1 over the immediate neighborhood of the cylinder, at three different points along a period.

7.4 Actuation Modes for Deforming Boundaries

The construction of actuation modes. As we have seen earlier, the need to construct actuation modes at this point arises from two types of sources: The slip velocity of grid points along walls of bodies immersed in the flow, and unsteady inflow conditions, including actuation and disturbances, global and local effects alike. The actuation modes are introduced in order to absorb these components of the boundary velocity, by an expansion of the form (56).

It will be convenient to formalize this requirement, and to discuss the construction of actuation modes, considering the embedded flow over the canonical domain Ω_c . We start, rewriting the actuation modes expansion (56) in clear reference to the embedded flow over Ω_c :

$$\mathbf{u}_{h,c} := \mathbf{u} - \mathbf{u}_{c,act} = \mathbf{u}_c - \sum_{i=1}^{N_{act}} b_i \mathbf{u}_{act,c,i}, \quad (67)$$

Here \mathbf{u}_c is the velocity field in the image of Ψ , as in (60). The notation of $\mathbf{u}_{h,c}$ indicates the velocity field obtained at the end of the transition process, satisfying traditional, steady boundary conditions: A zero velocity along solid walls and a steady inflow. The actuation modes $\mathbf{u}_{act,c,i}$ are required to be defined as incompressible velocity fields over Ω_c , they should be independent of α , but include in their span the boundary velocity that

needs to be removed from \mathbf{u}_c , which is denoted here as $\mathbf{u}_{c,act}$. The dependence on $(\alpha, \dot{\alpha})$, in (67), is delegated to the coefficients b_i , where α may parametrize both domain deformation and inflow unsteadiness.

We review two approaches for the construction of the actuation modes:

(i) Analysis of the primary data set, i.e., the simulation or experimental data intended for the computation of expansion modes:

- The first step is the identification of a restriction of the modal expansion in (67) to the boundary, Ω'_c . This task is trivial in the rotating and oscillating cylinder examples. In general, one may use the adaptation to the boundary, Ω'_c , of the empirical mode extraction methods discussed earlier, including the computation of harmonic expansions and POD analysis.
- Both the definition of harmonic modes and of POD modes are as linear combinations of data snapshots. Applying the same linear combinations that were used over the boundary to the entire snapshots, over Ω_c , defines incompressible velocity fields that agree with the boundary modes and can be used as actuation modes.

(ii) Using auxiliary simulations. Arguably, actuation modes that are intended to be used in operating conditions that are not identical to those used in model extraction, should translate boundary conditions into global modes in a manner that captures only the largest and least detailed structures possible:

- An auxiliary Stokes simulation over Ω_c is run, subject to the unsteady boundary velocity that needs to be resolved⁸.
- Expansion modes are obtained from the auxiliary flow data. These expansion modes are the sought actuation modes.

Method (i) is reminiscent of approaches that extract actuation models by comparing the actuated and un-actuated flows, e.g. in Kasnakoğlu et al. (2008). The simple actuation modes that were reviewed earlier for the oscillating and rotating cylinder fit method (ii). The simulation based derivation of actuation modes for the heaving and pitching (solid) airfoil,

⁸Note that this means that if the inflow is steady, to begin with, the inflow boundary condition for the auxiliary simulation is zero.

in the pioneering work by Lewin and Haj-Hariri (2005), is also belonging to this class.

7.5 LOGMs in flows over deforming geometries

The Galerkin approximation in deforming geometries. The fluid velocity field $\mathbf{u}_{h,c}$, in (67), is defined over the steady canonical domain Ω_c , satisfying steady boundary conditions, including zero velocity along body wall. It is therefore amenable to the computation of POD or harmonic expansion modes, with the familiar Galerkin approximation format:

$$\mathbf{u}_{h,c}(\mathbf{x}_c, t) \approx \mathbf{u}_c^B(\mathbf{x}) + \sum_{i=1}^N a_i(t) \mathbf{u}_{c,i}(\mathbf{x}_c). \quad (68a)$$

Equivalently,

$$\mathbf{u}_c(\mathbf{x}_c, t) \approx \mathbf{u}_c^B(\mathbf{x}_c) + \sum_{i=1}^N a_i(t) \mathbf{u}_{c,i}(\mathbf{x}_c) + \sum_{i=1}^{N_{act}} b_i(\alpha, \dot{\alpha}) \mathbf{u}_{act,c,i}(\mathbf{x}_c). \quad (68b)$$

Parametrized mode deformation, due to transient changes in the flow, can be included in this formulation, precisely as discussed in § 6, provided pertinent entries to the parametrization vector α .

Applying the inverse mapping, Ψ^{-1} , to the combined (68), one maps the base flow \mathbf{u}_c^B , the expansion modes $\{\mathbf{u}_{c,i}\}_{i=1}^N$, and the actuation modes $\{\mathbf{u}_{act,c,i}\}_{i=1}^N$, back to velocity fields over the deforming physical domain $\Omega(\alpha)$. The dependence of Ψ^{-1} on $(\alpha, \dot{\alpha})$ implies the same, regarding the expansion modes over the physical domain, meaning that the $\Omega(\alpha)$ -counterparts of the fields in (68b) will all be unsteady. We begin this discussion with the details of these fields.

In keeping with the convention that the base flow absorbs inhomogeneous terms, we define

$$\mathbf{u}^B(\mathbf{x}, \alpha, \dot{\alpha}) := \mathbf{u}_p^B(\mathbf{x}, \alpha) + \mathbf{u}_v^B(\mathbf{x}, \alpha)\dot{\alpha}, \quad (69)$$

where

$$\mathbf{u}_p^B := J_{\mathbf{x}_c, \mathbf{x}}^{-1} \mathbf{u}_c^B \quad \text{and} \quad \mathbf{u}_v^B := -J_{\mathbf{x}_c, \mathbf{x}}^{-1} J_{\mathbf{x}_c, \alpha}. \quad (70)$$

The term \mathbf{u}_p^B , on the right hand side of (69), is in standard change of coordinate form. It is determined by the slowly varying \mathbf{u}_c^B , and its dependence on α is static, and does not involve $\dot{\alpha}$. The term $\mathbf{u}_v^B \dot{\alpha}$ reflects the velocity field of the Lagrangian grid, and therefore includes the dependence on $\dot{\alpha}$.

With this definition of the base flow, actuation modes and expansion modes depend on α , but not on $\dot{\alpha}$. Moreover, expansion modes will satisfy

homogeneous boundary conditions:

$$\mathbf{u}_i(\mathbf{x}, \alpha) = J_{\mathbf{x}_c, \mathbf{x}}(\mathbf{x}, \alpha)^{-1} \mathbf{u}_{c,i}(\psi(\mathbf{x}, \alpha)) \quad (71)$$

$$\mathbf{u}_{act,i}(\mathbf{x}, \alpha) = J_{\mathbf{x}_c, \mathbf{x}}(\mathbf{x}, \alpha)^{-1} \mathbf{u}_{act,c,i}(\psi(\mathbf{x}, \alpha)) \quad (72)$$

The Galerkin approximation, in the original domain, is therefore of the form

$$\begin{aligned} \mathbf{u}(\mathbf{x}, t) \approx & \mathbf{u}_p^B(\mathbf{x}, \alpha) + \mathbf{u}_v^B(\mathbf{x}, \alpha) \dot{\alpha} + \sum_{i=1}^N a_i(t) \mathbf{u}_i(\mathbf{x}, \alpha) \\ & + \sum_{i=1}^{N_{act}} b_i(\alpha, \dot{\alpha}) \mathbf{u}_{act,i}(\mathbf{x}, \alpha). \end{aligned} \quad (73)$$

The Galerkin Dynamical System. The Galerkin dynamical system can be computed now in two equivalent ways, working over the steady computational domain or over the physical domain. The first approach is to rewrite the NSE in terms of the vector field \mathbf{u}_c over the spatial domain Ω_c . In that case, unsteady change of variables, dependent on $(\alpha, \dot{\alpha})$, must be included in the appropriately modified NSE, followed by the projection on the time invariant expansion set. Here we detail only the alternative computation over the physical, unsteady domain, where the NSE retains its original, time invariant form.

Following the standard Galerkin paradigm, the acceleration field is approximated as the time derivative of the Galerkin approximation of the velocity field:

$$\begin{aligned} \partial_t \mathbf{u}(\mathbf{x}, t) \approx & \sum_{i=1}^N \dot{a}_i \mathbf{u}_i \\ & + \sum_{i=1}^{N_{act}} (\partial_\alpha b_i \cdot \dot{\alpha} + \partial_{\dot{\alpha}} b_i \cdot \ddot{\alpha}) \mathbf{u}_{act,i} \\ & + \left(\partial_\alpha \mathbf{u}_p^B + \sum_{i=1}^N a_i \partial_\alpha \mathbf{u}_i + \sum_{i=1}^{N_{act}} b_i \partial_\alpha \mathbf{u}_{act,i} \right) \dot{\alpha} \\ & + \partial_\alpha \mathbf{u}_v^B \dot{\alpha}^2 + \mathbf{u}_v^B \ddot{\alpha}. \end{aligned} \quad (74)$$

The first sum on the right hand side of (74) is the mainstay of the standard Galerkin system computation, the subsequent, $\dot{\alpha}$, $\dot{\alpha}^2$ and $\ddot{\alpha}$ terms reflect the changing geometry and the velocity and acceleration that this change induces along $\Omega(\alpha)$.

The Galerkin projection of the NSE on the expansion set will therefore

be of the following general form

$$\begin{aligned}
 \dot{a}_i = & c_i(\alpha) + \sum_{j=1}^N l_{ij}(\alpha) a_j + \sum_{j,k=1}^N q_{ijk}(\alpha) a_j a_k \\
 & + \sum_{i=1}^{N_{act}} l_{act, ij}(\alpha, \dot{\alpha}) b_j \\
 & + \left(c'_i(\alpha) + \sum_{j=1}^N l'_{ij}(\alpha) a_j \right. \\
 & \quad \left. + \sum_{i=1}^{N_{act}} l'_{act, ij}(\alpha, \dot{\alpha}) b_j \right) \dot{\alpha} \\
 & + \left(\sum_{i=1}^{N_{act}} l''_{act, ij}(\alpha, \dot{\alpha}) b_j \right) \ddot{\alpha} \\
 & + c_{2,i}(\alpha) \dot{\alpha}^2 + c_{3,i}(\alpha) \ddot{\alpha}.
 \end{aligned} \tag{75}$$

7.6 Closing Comments

Let us recap the extensions of the Galerkin methodology outlined in this section. Our starting point is the observation of an inherent inconsistency between the traditional Galerkin method and the modeling needs of systems with unsteady boundaries. As noted towards the end of the section, aspects of that inconsistency are manifest also in systems with unsteady inflow conditions.

Whereas studies that employ LOGMs for systems with unsteady boundaries commonly avoid the difficulty under a simplifying, small fluctuations assumption, solution ideas that address the problem, head on, have been proposed by a number of authors, over more than a decade. These ideas invariably include the transition to a steady computational domain, and where needed, the use of actuation modes. Methods for the transition to a canonical domain varied from very simple transformations, applicable to rigid body motion, to emulation of the string analogy, which is commonly used in CFD simulations.

The presentation of this section aimed to incorporate and extend these ideas, in a systematic, broadly applicable and computationally efficient framework, that meshes seamlessly with the formulation of LOGMs on parameterized manifolds, that was developed in § 6. Guidelines for the generation of elasticity-based, parameterized Lagrangian grids, include both the delineation of the properties required from such definitions in LOGM contexts, and the equally important highlights of the significant differences between these requirements, and the needs and implementations of Lagrangian grids in CFD simulation models.

A central theme in Lagrangian grid methods, in computational aeroelasticity, concerns the detrimental effects of excessive stretching of the fictitious

network of springs that control grid dynamics. Specifically, over-stretching may hinder the representation of grid cells by positive volume polyhedra, and requires a remeshing, a step we wish to avoid in parameterized grids used in LOGMs. To avoid this obstacle, the proposed framework removes the no-slip condition from the requirements used to define the Lagrangian grid, thus necessitating the complementary use of actuation modes, to absorb the residual wall-tangent velocity. Actuation modes are also needed to absorb unsteady boundary velocity due to actuation and or disturbances. We reviewed two alternative computations of actuation modes: One utilizes the same simulation data that is also used for mode extraction, in the derivation of the LOGM. The other utilizes auxiliary high viscosity (Stokes) fluid simulations, driven by the residual boundary conditions.

The two-step method is an enabler for a systematic, analytically derived modeling framework that is equally applicable to internal and external flows over moving boundaries, subject to unsteady inflows, allowing multiple, independently moving, immersed elastic bodies.

Finally, the singularity of boundary forcing has been a persistent impediment to the analytic incorporation of important actuation mechanisms in LOGMs. It necessitated the use of ad hoc, and often fragile calibration based substitutes, to include control mechanisms in the model. A significant aspect of the proposed framework is therefore in removing this obstacle. Indeed, the representation of forces along the boundary by global volume forces, proportional to $\ddot{\alpha}$ in (75), is analytically derived as an integral part of the Galerkin projection of the NSE, in the extended framework.

8 Feedback Design

Feedback flow control design may be characterized by a comparison of targeted response time scales to the time scales of dominant flow structure:

The regulation of a turbulent flow at rates that are much longer than those dominating flow unsteadiness is generically limited to statistical properties of the flow. The role of feedback is that of a slow adaptation of an otherwise open loop actuation, such as the amplitude and frequency of a pulsating synthetic jets (King, 2010; Becker et al., 2005; Pastoor et al., 2008; Little et al., 2009; Williams et al., 2009). Actuation is often at frequencies that are different than that of the dominant flow instability and feedback gains are not synchronized with the phase of flow oscillations. The models that are used to design control mechanisms in this class are therefore required to track and predict only the slowly varying statistical quantities of interest: The turbulent energy level of the flow or its sensed surrogates,

the aerodynamic forces acting on an airfoil, etc. Transfer functions are commonly used in such contexts, as well the mere implicit monotonicity assumption used in⁹ *model-free* designs, such as in extremum-seeking control (Ariyur and Krstić, 2003; Wiederhold et al., 2010). Referring to the discussion in the chapter by Noack et al., the control of modal energy statistics, using FTT models Noack et al. (2008, 2010) belongs in this category as well.

Feedback flow control that acts at the flow's time scale is typically geared to attenuate, or to otherwise regulate, an oscillatory instability. This class of control tasks an oscillatory actuation to be tightly choreographed with the flow. The demands from design models are escalated accordingly, to providing accurate phase predictions of flow unsteadiness. In addition to analytical PDE and high dimensional numerical models (Aamo and Krstic, 2003; Bewley, 2001; Kim and Bewley, 2007; Vazquez and Krstic, 2007), reduced order models used in here cover the gamut, from simple sine-wave tracking (Pastoor et al., 2006, 2008; Joe et al., 2008), through state-space and transfer function linear time invariant and adaptive models Kegerise et al. (2007); Cattafesta et al. (2008) and vortex models Protas (2007, 2008) to LOGMs, the subject of the current discussion.

With that focus in mind, our objective here is not to review the range of design methods that have been, or that can be employed in feedback flow control. Rather, our goal is to highlight some key issues that have been identified as critical to the successful use of LOGMs in feedback flow control design, regardless of the underlying design philosophy. We shall illustrate these issues by the simple volume force actuated cylinder wake benchmark, as described in § 2.

8.1 Volume Force Actuation of the Cylinder Wake

A volume force actuator represents, e.g., a regulated magnetic field in the domain of a magnetohydrodynamic flow. Flow dynamics in the immediate vicinity of a plasma actuators is an example of this class of actuated flows (Moreau, 2007; Little et al., 2009). For convenience we repeat here the notations of a volume force actuated Galerkin model, which have been set in (7). Actuation is included in the NSE (6) as a distributed force field, $\mathbf{f}(\mathbf{x}, t)$. The Galerkin projection of the NSE on an orthonormal set of expansion modes, includes an explicit representation of the volume force by terms

$$f_i(t) = (\mathbf{f}(\cdot, t), \mathbf{u}_i)_\Omega, \quad i = 1, \dots, N. \quad (76a)$$

⁹Arguably, *any* feedback design requires a model that predicts the response of the system to actuation or disturbance. The term “model-free” is used when the model is restricted to such rudimentary properties as an assumed continuity, monotonicity and slow response.

Modifications for non-orthogonal expansions are straightforward. The i^{th} equation in the Galerkin system is thus of the form

$$\dot{a}_i = c_i + \sum_{j \geq 1} l_{ij} a_j + \sum_{j,l \geq 1} q_{ijk} a_j a_k + f_i, \quad i \geq 1. \quad (76b)$$

We focus here on periodically dominated flows, where the volume force oscillates at harmonics of the dominant flow frequency. Suppressing space and time dependencies, the harmonic expansion of the actuation is

$$\mathbf{f} = B_0 \mathbf{g}_0 + \sum_{i=1}^N B_{2i-1} \cos(\phi_i) \mathbf{g}_{2i-1} + B_{2i} \sin(\phi_i) \mathbf{g}_{2i}. \quad (77)$$

The amplitudes B_i are treated here as slowly varying control commands. Explicit expressions are derived in these terms for the forcing terms in the *amplitude Galerkin system*, (18b):

$$\begin{aligned} F_{2i-1}(t/\tau) &= \frac{2}{t_p} \int_{-\frac{t_p}{2}}^{\frac{t_p}{2}} (\mathbf{f}(\cdot, t+r), \mathbf{u}_{2i-1})_\Omega \cos(\phi_i(t+r)) dr \\ &= (\mathbf{g}_{2i-1}, \mathbf{u}_{2i-1})_\Omega B_{2i-1}(t/\tau) \\ F_{2i}(t/\tau) &= (\mathbf{g}_{2i}, \mathbf{u}_{2i})_\Omega B_{2i}(t/\tau). \end{aligned} \quad (78)$$

These expressions translate to forcing terms in the corresponding differential equations for a_{2i-1} and a_{2i} :

$$\begin{aligned} f_{2i-1}(t) &= F_{2i-1}(t/\tau) \cos(\phi_i(t)) \\ f_{2i}(t) &= F_{2i}(t/\tau) \sin(\phi_i(t)). \end{aligned} \quad (79)$$

As in the case of (15)-(18), the expressions (78) and (79) do not require mutual orthogonality of the harmonic modes.

8.2 Direct and Indirect Design Objectives

A single, vertical force field is specified in (3) as

$$\mathbf{f}(\mathbf{x}, t) = b(t) \mathbf{g}(\mathbf{x}),$$

where \mathbf{g} is a unit amplitude vertical force field, supported over the disc Ω_{vf} , and where b is the control command.

The formal design objective, as stated in § 2, is engineering driven, with the goal to avoid the deleterious effects of cylinder oscillations:

1. Attenuate vortex shedding.

From a physical perspective, our objective is to use the actuator as a distributed deceleration force, applied to the vertical component of the velocity oscillations over the domain Ω_{vf} . An ideal selection would be at an *anti-phase* to the averaged vertical velocity field:

$$b(t) = -\kappa(t) (\mathbf{u}(\cdot, t), \mathbf{g})_\Omega = -\kappa(t) \int_{\Omega_{vf}} d\mathbf{x} v(\mathbf{x}, t), \quad (80)$$

where v is the vertical component of the velocity $\mathbf{u} = (u, v)$, and where $\kappa > 0$ is a selected gain. Using the nomenclature of energy dynamics, in (21), this selection defines the *actuation power* as $G = -\kappa|(\mathbf{u}, \mathbf{g})_\Omega|^2$, ensuring a negative contribution to the TKE; i.e., (80) defines a *dissipative control*. When κ is selected large enough, the actuation power will dominate all other contributions to the power equation (21), and ensure that the TKE will be driven to zero. This option can be easily demonstrated by DNS implementation (Gerhard et al., 2003; Lehmann et al., 2005).

In fact, the fact that feedback stabilization of flow oscillations by synchronous actuation needs to be dissipative, is generic. It is implied by the very nature of this design objective, and is therefore independent of the control theoretical approach used for solving the specific design problem. Our simple example is therefore representative of a very wide class of flow control problems, as is the ideal formulation of a dissipative control, in (80). Alas, access to the the distributed flow state, as required in (80), is available only in DNS simulations. Control decisions need to be based on realtime processing of sensor readings. In line with the focus of this chapter, this means:

2. Feedback design should be based on reduced order model based state estimates and control design.

The bulk of this section was dedicated to model development, motivated by this objective. Implicit in it is the onus on the designer to maintain the controlled flow within the validity envelope of the design model. Surely, model based state estimation, and predictions of control effects, will have little value, once the flow exits that envelope:

3. Model based feedback design should maintain the flow within the validity envelope of the reduced order model.

The purpose of the ensuing discussion is to highlight the implications of this indirect, but truly critical requirement, put in the generic context of

dissipative control design. The model we intend to use here is the least order, three state model (36). the generic property of this model is its very limited dynamic range. Regardless of any other aspect, it is valid only when the flow is characterized by periodic vortex shedding, when the shedding occurs at the frequency predicted by the model, and when the dominated coherent structures in the flows are those used as expansion modes in (36). As the discussion progresses, we shall review the options of using a fixed expansion set, comprising of the leading attractor POD modes and a shift mode, and the alternative of using the parameterized variant of this model.

The discussion will be focused, in the most part, on control and modeling related issues. To the limited degree at which state estimation issues will be discussed, that discussion will concern a broadly applicable issues, and will not relate to issues of specific observer design methods. It is therefore assumes that some text-book standard methods such as a Luenberger observer, an extended Kalman filter, and extensions thereof, are ample for the estimation task (Grewal and Andrews, 1993; Meurer et al., 2002; Åström and Murray, 2008; Crassidis, 2006). Otherwise, the assumption is that a dynamic state estimation has already been designed, producing reliable estimates of the Galerkin model's state, \mathbf{a} , and that this estimate has been reliably translated to estimates of the amplitude $A := A_1 = A_2$ and of the oscillations' phase ϕ .

8.3 Modeling Periodic Actuation

The implication of Objective 3 is that the shedding frequency will continue to dominate the dynamics, and will vary slowly, as the oscillation amplitude declines. It is therefore natural to define an actuation force that oscillates at the shedding frequency:

$$b = B \cos(\phi + \Delta\phi) = B (\cos(\Delta\phi) \cos(\phi) - \sin(\Delta\phi) \sin(\phi)). \quad (81)$$

Here ϕ is the phase of oscillatory states of (36), as in the counterpart of the Fourier expansion (19). The phase shift, $\Delta\phi$, determines the relationship between the oscillations of the unknown full state \mathbf{u} and the actuation force \mathbf{f} . In particular, it determines whether the negative forcing power (dissipativity) requirement (80) is satisfied. A wrong selection of $\Delta\phi$ may not only render the actuation ineffectual, but it may actually become destabilizing. In what follows we shall analyze this condition in terms of the actuated version of the LOGM (36). Our first task is therefore to compute the forcing term in that equation.

We have two options to explore the response: One is in terms of a direct appeal to the Galerkin projection, in the time domain. The other option

is an appeal to the expressions(78) and (79). This second option is based on the stipulation of periodic dominance, in line with Objective 3. We now review both options:

The forcing terms: A Direct Galerkin Projection. This computation is facilitated by the fact that, in this particular example, the three modes used in (36) are mutually orthogonal (Noack et al., 2003). The respective forcing terms are thus defined as in (76): $f_\Delta := (\mathbf{f}, \mathbf{u}_\Delta)_\Omega$, is the actuation force in the shift mode equation, and $f_i := (\mathbf{f}, \mathbf{u}_i)_\Omega$, $i = 1, 2$, are the respective forces for the two oscillatory states. These definitions lead to the following values:

- $f_\Delta = 0$. The symmetry of the shift mode and the anti-symmetry of the force field \mathbf{g} with respect to the x -axis¹⁰ causes $(\mathbf{g}, \mathbf{u}_\Delta)_\Omega = 0$.
- To define the forcing terms acting on the oscillatory state we introduce the notations of $g_i := (\mathbf{g}, \mathbf{u}_i)_\Omega$, $i = 1, 2$, The projection of the force field \mathbf{f} is defined in these terms as:

$$\begin{aligned} f_1 &= (\mathbf{f}, \mathbf{u}_1)_\Omega = b(\mathbf{g}, \mathbf{u}_1)_\Omega = R_g B \cos(\theta) \cos(\phi + \Delta\phi) \\ &= R_g B \cos(\theta)(\cos(\Delta\phi) \cos(\phi) - \sin(\Delta\phi) \sin(\phi)), \\ f_2 &= (\mathbf{f}, \mathbf{u}_2)_\Omega = b(\mathbf{g}, \mathbf{u}_2)_\Omega = R_g B \sin(\theta) \cos(\phi + \Delta\phi) \\ &= R_g B \sin(\theta)(\cos(\Delta\phi) \cos(\phi) - \sin(\Delta\phi) \sin(\phi)). \end{aligned} \quad (82)$$

We note that the angle θ , in these expressions, is a function of g_1 and g_2 , hence of the expansion modes \mathbf{u}_1 and \mathbf{u}_2 . It remains constant if mode deformation is not accounted for, and it varies along with the expansion modes, when parameterized models are used.

Amplitude and phase equations are derived in terms of the polar coordinates representation of the oscillatory Galerkin states, $a_1 = A \cos(\phi)$ and $a_2 = A \sin(\phi)$. Explicitly, these equations are computed by substituting these expressions in the actuated variant of (36b) followed by an

¹⁰We say that a 2D vector field $\mathbf{u} = (u, v)$ is symmetric with respect to the x -axis when $u(x, y) = u(x, -y)$ and $v(x, y) = -v(x, -y)$. The vector field is anti-symmetric with respect to the x -axis when $u(x, y) = -u(x, -y)$ and $v(x, y) = v(x, -y)$.

inner-product with $\begin{bmatrix} \cos(\phi) \\ \sin(\phi) \end{bmatrix}$ and $\begin{bmatrix} -\sin(\phi) \\ \cos(\phi) \end{bmatrix}$, respectively:

$$\dot{a}_\Delta = -\sigma^B a_\Delta + \beta^B (a_1^2 + a_2^2), \quad (83a)$$

$$\dot{A} = (\sigma^C - \beta^C a_\Delta) A + B R_g \cos(\phi - \theta) \cos(\phi + \Delta\phi) \quad (83b)$$

$$\dot{\phi} = \omega - \frac{R_g B}{A} \sin(\phi - \theta) \cos(\phi + \Delta\phi). \quad (83c)$$

The forcing terms: A phasor equation derivation. Here the starting point of the computation is the assumption of harmonic dominance of the flow and the dynamic phasor equations (18b). Deriving the forcing terms for the phasor amplitude equations from the general formulae (78) leads to the following equalities:

$$\begin{aligned} F_1 &= (\mathbf{g}, \mathbf{u}_1)_\Omega B \cos(\Delta\phi) = R_g B \cos(\theta) \cos(\Delta\phi) \\ F_2 &= -(\mathbf{g}, \mathbf{u}_2)_\Omega B \sin(\Delta\phi) = -R_g B \sin(\theta) \sin(\Delta\phi). \end{aligned} \quad (84)$$

Dynamic equations for the oscillations amplitudes are obtained by adding the forcing terms (84) to the homogeneous amplitude equation, (18b). We recall that the precise form of the homogeneous equation for the linear cylinder wake model, (8), has already been computed in (20). An obvious adaptation to a model that includes the shift model, leads to the equations:

$$\begin{aligned} \frac{d}{dt} A_1 &= (\sigma^C - \beta^C a_\Delta) A_1 + F_1 \\ &= (\sigma^C - \beta^C a_\Delta) A_1 + R_g B \cos(\theta) \cos(\Delta\phi) \end{aligned} \quad (85a)$$

$$\begin{aligned} \frac{d}{dt} A_2 &= (\sigma^C - \beta^C a_\Delta) A_2 + F_2 \\ &= (\sigma^C - \beta^C a_\Delta) A_2 - R_g B \sin(\theta) \sin(\Delta\phi). \end{aligned} \quad (85b)$$

Examining these equation, one observes an apparent discrepancy: The two oscillation amplitudes are essentially identical, $A_1 = A_2$, in our phase averaged system. In contrast, eq:act:pgap suggests the possibility of two distinct dynamic rules. We shall revisit this issue shortly.

The tasks ahead includes the derivation of guidelines for the selection of the control parameters B and $\Delta\phi$, and the reconciliation of the two sets of equations, i.e., (82) and (83), which were derived by direct projection, and (84) and (85), which were derived in a dynamic phasor formulation. In addition, the observed mismatch between the two equations in (85), needs to be addressed. The analysis of these issues will reveal important modeling and design aspects of the generic scenario where the goal of flow control is

the stabilization of oscillatory flow instabilities. Indeed, our motivation for employing the dual formulation is precisely as an opportunity to unveil and illustrate these issues.

8.4 Detailed Design Guidelines

Dissipative actuation phase. We examine the requirement that actuation will have a dissipative, stabilizing effect in each of the presented formulations.

Let us start with the amplitude equation (83b). Here the requirement is that the oscillatory forcing term be (maximally) negative:

$$\cos(\phi - \theta) \cos(\phi + \Delta\phi) < 0.$$

This objective is achieved with the selection of

$$\Delta\phi = \pi - \theta \Rightarrow \cos(\phi - \theta) \cos(\phi + \Delta\phi) = -\cos(\phi - \theta)^2. \quad (86a)$$

A by product of this selection is that this selection creates an oscillatory forcing term in the phase equation (83c):

$$-\sin(\phi - \theta) \cos(\phi + \Delta\phi) = \frac{1}{2} \sin(2(\phi - \theta)). \quad (86b)$$

We shall revisit this added term shortly.

Next, let us consider the effect of the same selection on the two phasor based amplitude equations, in (85). Indeed, here too, both forcing terms become negative when $\Delta\phi = \pi - \theta$:

$$\cos(\theta) \cos(\Delta\phi) = -\cos(\theta)^2, \quad -\sin(\theta) \sin(\Delta\phi) = -\sin(\theta)^2. \quad (87)$$

While the assignment of $\Delta\phi$ has the desired dissipative effects in each of the two settings, the expressions we computed appear to include several inherent inconsistencies:

Creating an oscillatory frequency in (86b). The validity envelope characterized by a slowly varying frequency. The actual frequency now second harmonic sinusoidal fluctuation in ω , which is modulated by the growing inverted amplitude, $1/A$, in the closed loop (83c).

An imbalance in (87). Unless $\theta = \frac{2k+1}{4}\pi$ and $g_1 = \pm g_2$, the closed loop forcing terms in the two equations, in (87), are not identical. (In the extreme, either g_1 or $g_2 = 0$.) In particular there appears to be a possibility of driving the values of A_1 and A_2 apart, thus violating the characterization

$A = A_1 = A_2$ of the model's validity envelope.

An inconsistency between (86a) and either of the two expressions in (87). The directly derived forcing term in the amplitude equation is oscillatory, whereas the alternative counterparts in the phasor description are constant (or slowly varying).

It is left to the reader to observe that a joint root cause for these issues is the fact that the benchmark under consideration stipulates the use of only a single actuator. Two independent control inputs, would have enabled the independent regulation of a_1 and a_2 , and similarly, of A and of ω . That extra degree of freedom could have been used to ensure that, indeed, the forcing in (83b) be slowly varying, that it will agree with both forcing terms in (87), and that not actuation effects will be felt by ω . Under actuation, however, is the reality one faces in fluid flow systems, and at least in this sense, the difficulties observed here are generic. In fact, there generic in yet another aspect, which we discuss next.

Time scale separation as an inherent design guideline. A requirement that closed loop stabilization adhere to a time scale separation between the shedding half-period and the attenuation of the oscillations amplitude, emerges as a common solution to the apparent inconsistencies listed above: As long as changes in $1/A$ are small over a half period, the net forcing effect on ω over a shedding period, will be small. The same time scale separation ensures that the period averaged contribution of the periodic fluctuations in $-\cos(\phi - \theta)^2$ to the amplitude dynamics, under (86a), will also be negligible. The net effect of the actuation in (83b) will therefore be nearly equivalent to that of the slowly varying input $\frac{1}{2} B R_g$.

Phase averaging requirement in phasor models actuation. To understand the case of $g_1 \neq \pm g_2$ we refer to the FTT terminology (Noack et al., 2008) that was introduced in the chapter by Noack et al., and used in our discussion of energy dynamics. The dynamic role of the skew symmetric component of the original matrix coefficient in (36b), is precisely the continuous exchange of TKE between the two oscillatory states, a_1 and a_2 , leading to equal time averages of the respective K_1 and K_2 , hence of A_1 and A_2 . In fact, this implicit energy redistribution is an essential property of harmonically dominant systems and of their models, and is equivalent to a generalized weighted variant of the phase averaging property, allowing, e.g. elliptical limit cycles.

An inherently implied property of a system that maintains a constant

(or slowly varying) ratio between the TKE contents of oscillatory state-pairs, is that the energy redistribution that is mediated by the oscillations, occur at substantially higher rates than the actuated or natural transient changes in these TKE levels. In effect, harmonic dominance implies that the actuation inputs into each such pair of states will be phase averaged in the same manner as the said states. The upshot of this discussion is that the use of the “raw” g_i in the phasors of the forcing terms, in (84), and subsequently, in (85), constitutes a contradiction in terms. The correct gains in the phasor dynamics formulation are, indeed, $g_i = \pm \frac{1}{\sqrt{2}} R_g$, $\theta = \frac{2k+1}{4}\pi$ and the identical actuation terms in the two equations, in (85), are $\frac{1}{2} R_g B$. That is, these equations are precisely the period averaged variants of (83b). For convenience we rewrite this equation here:

$$\dot{A} = (\sigma^C - \beta^C a_\Delta) A - \frac{1}{2} R_g B. \quad (88)$$

In summary, time scale separation between actuation and (half) the vortex shedding period justifies the suppression of nearly zero mean terms in the closed loop (85), as well as the corrected phase averaged modeling of the actuation term, in a dynamic phasor model.

Actuation amplitude, subject to dissipation and time scale separation constraints. The observations above lead to two requirements from the actuation amplitude, B : It needs to be high enough, to overcome the instability in (88), and yet low enough, to ensure the required time scale separation between the oscillations period and the rate of decay in the actuated flow. This dual requirement is simply formulated a a two sided inequality, on B :

$$\left(\frac{\sigma^C - \beta^C a_\Delta}{R_g} + \epsilon \right) A < B < \left(\frac{\sigma^C - \beta^C a_\Delta}{R_g} + \delta \right) A. \quad (89)$$

The values of ϵ and δ , in (89), represent the minimal and the maximal acceptable decay rates, with corresponding time constants $\tau_\epsilon := 1/\epsilon$ and $\tau_\delta := 1/\delta$.

8.5 Performance Limitations

Like many nonlinear control problems, flow control is often subject to performance limitations that stem from the very structure of the system. Here we highlight two types of generic limitations, illustrated by our running example.

Stability of the operating point: An amplitude perspective. The expressions on both sides of (89) involve both a_Δ and A . Simplifying these expressions for the purpose of this discussion, let us slave a_Δ to A^2 . The two expressions bounding B are then cubic polynomials in A , defining the normalized destabilizing force in (88). The solid curve in Figure 13 is a schematic representation of the amplitude of that destabilizing force, drawn as a function of A . Considering this representation, we observe that a constant actuation amplitude, B , would balance the destabilizing force in (88), at two distinct values of A , illustrated by the examples of A_{low} and A_{high} , in Figure 13. The fixed point at A_{high} is dynamically stable: Oscillations

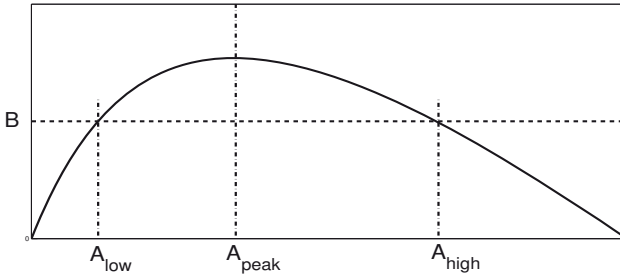


Figure 13. A schematic illustrating the existence of two oscillating amplitudes, A_{low} and A_{high} , at which an actuation level, B , balances the destabilizing force (solid curve) in (88). The fixed point at A_{low} is dynamically unstable, whereas that at A_{high} is dynamically stable.

at an amplitude $A > A_{high}$ create a destabilizing force that is lower than the actuation force, and will be attenuated. Oscillations at an amplitude $A < A_{high}$ generate a destabilizing force that is higher than the actuation force, and will grow. In contrast, the same reasoning shows that the fixed point at A_{low} is dynamically unstable and is therefore intrinsically more difficult to enforce. Furthermore, the reasoning we have just provided also applies to the slow feedback stabilization, as the system traverses a slowly decaying actuated transient $A(t)$. That threshold for dynamic instability is the value A_{peak} , at which the destabilizing force, on the right hand side of (88), reaches its maximal value.

This observation reveals an important root cause of the observed phenomenon, whereby controllers designed to stabilize an oscillatory instability, seem to “lose their grip”, once the fluctuations level has been reduced below a certain threshold. At that point, the flow begins to displays chaotic

oscillations. Careful design may nonetheless succeed in maintaining a low averaged TKE. In other cases, the emerging oscillations stimulate new instabilities which are not covered by the model, leading to a return higher oscillation levels.

Stability of the operating point: A phase perspective. The exact definition of the phase ϕ requires knowledge of the distributed velocity field, \mathbf{u} . This information is not available and a observer is needed to produce an estimate $\hat{\phi}$ of ϕ . That estimate is then used instead of ϕ , in the applied actuation force:

$$b = B \cos(\hat{\phi} + \Delta\phi) = -B \cos(\hat{\phi} - \theta). \quad (90)$$

We us consider this actuation command, using the assignment (86) for $\Delta\phi$. Later we shall comment also on the issue of the correct evaluation of $\Delta\phi$.

We shall now illustrate the growing difficulty in maintaining a good estimate in the closed loop actuated system, as the shedding instability is increasingly attenuated. To do so, we consider the closed loop actuated dynamics of ϕ . The use of $\hat{\phi}$ instead of ϕ brings (83c) to the following period averaged form:

$$\dot{\phi} = \omega - \frac{R_g B}{A} \overline{\sin(\theta - \phi) \cos(\hat{\phi} - \theta)} \approx \omega - \frac{R_g B}{2A} \sin(\hat{\phi} - \phi). \quad (91)$$

In this formulation an overline indicates period average. The approximation is justified when the phase estimated error, denoted $\tilde{\phi} := \phi - \hat{\phi}$, is sufficiently small to make $\phi + \hat{\phi} - 2\theta$ close to $2(\phi - \theta)$, allowing to neglect the period averaged contribution of $\cos(\phi + \hat{\phi} - 2\theta)$. As noted earlier, this equation coincides with the un-actuated phase dynamics, in (18a), in the ideal case of a precisely known phase.

To illustrated the estimation difficulty, let us consider a dynamic observer of ϕ , with a correction term h

$$\dot{\hat{\phi}} = \omega + h. \quad (92)$$

As a simplifying hypothesis, we implicitly assumed in this formulation that the slowly varying (effective) ω is known. The purpose of this analysis is to reveal the growing demands on a stabilizing h .

Following the standard derivation of the estimation error dynamics, we subtract (92) from (91), followed by a linearization, justified for small values of $\tilde{\phi}$.

$$\dot{\tilde{\phi}} = \frac{R_g B}{2A} \sin(\tilde{\phi}) - h \approx \frac{R_g B}{2A} \tilde{\phi} - h. \quad (93)$$

Indeed, not only is this equation anti-stable, but its growth rate is reversely proportional to the oscillations amplitude, A . The correction term h therefore needs to overcome this instability, a task that becomes ever harder, as A approaches zero.

An interesting observation concerns the stability of dynamic phase estimation in the closed loop system, under the reversed objective, of feeding energy into the instability. Backtracking on our computations, above, the ideal selection of the actuation phase shift is $\Delta\phi = -\theta$, precisely an anti-phase to the stabilizing selection. In that case, however, the sign of the right hand side of (93) will be reversed, and the homogeneous component of this equation will become stable. Indeed its small signal stability will only increase for small values of A !

This simple analysis is aligned with the observation of a generic tendency of a fluid flow system to extract energy from an active external source that is coupled with the flow, till the coupled system reaches an equilibrium.

The role of mode deformation. Both the analysis of the actuation amplitude and of the actuation phase reveals the dependence of an effective actuation on the exact *definition* and correct estimation of the flow phase ϕ and of the values of the projections g_i , hence of the amplitude R_g and phase θ . A dynamic observer used to translate sensor readings into state estimates is also dependent on the phase shifts and amplitude relations between sensor oscillations and the oscillations of the time coefficients a_i , $i = 1, 2$ in the actuated flow. The deformation of the leading oscillatory modes along natural and actuated transients lead to growing discrepancies between the correct relations between the required quantities and those predicted by a model based on a constant mode set. These facts were illustrated by the observations in Figures 2, 3 and 9. The deleterious effects of using constant modes in model based control have been clearly demonstrated, in this example, in Gerhard et al. (2003); Lehmann et al. (2005); Luchtenburg et al. (2006). These studies showed that the feasible closed loop TKE attenuation is meager, and can be improved several folds when control design employs a parameterized mode set. This observation is aligned with similar observations by numerous investigating teams. References to some pertinent literature can be found in § 6.

9 Concluding Remarks

The evolution of the field of fluid flow control has been driven by significant and still growing engineering needs, and by an accumulating body of experimental and numerical studies. The adaptation of control design

and related modeling methods to the needs of fluid flow applications, have been by a potpourri of pioneering theoretical investigations and ad-hoc experimentation with diverse methods and ideas, borrowed from a similarly diverse ensemble of fields.

Of the many types of models used in the design of feedback flow control, the Galerkin paradigm is clearly a dominant presence. It has the advantage of allowing a more direct contact between the reduced order model and the constitutive equations than black-box identified linear models, while maintaining manageable complexity, when compared with CFD models, or even with the often unruly, Lagrangian vortex models. The use of Galerkin models have been further popularized by the efficient approximation offered by POD mode sets. Within this vibrant realm, observations of fundamental discrepancies between ends and means, methods and needs, have been made early on, and are now widely recognized by the flow control community.

Building on our presentations in the previous two chapters (i.e., by Morzyński et al. and by Noack et al.), our goal here is to systematically identify the root causes of a number of persistent obstacles, and to propose an equally systematic enhancement of the Galerkin paradigm, that is geared, by design to remove these obstacles. Issues covered included the mean field and subgrid models, mode deformation and unsteady boundaries. At the model development level we have also reviewed a useful framework based on temporal harmonics, that is especially suitable for the generic task of controlling periodically dominated instabilities.

We closed the discussion with an illustration of generic feedback design issues that arise specifically, because of the use of low and least order models.

Bibliography

- O. Aamo and M. Krstic. *Flow Control by Feedback Stabilization and Mixing*. Springer Verlag, 2003.
- B. Adams, M. Ovsjanikov, M. Wand, H.-P. Seidel, and L. J. Guibas1. Meshless modeling of deformable shapes and their motion. In M. Gross and D. James, editors, *Eurographics / ACM SIGGRAPH Symposium on Computer Animation*, 2008.
- S. Ahuja, C. W. Rowley, I. G. Kevrekidis, M. Wei, T. Colonius, and G. Tadmor. Low-dimensional models for control of leading-edge vortices: Equilibria and linearized models. In *45th AIAA Aerospace Sciences Meeting and Exhibit*, 2007. AIAA Paper 2007-709.
- A. Amanatiadis and I. Andreadis. A survey on evaluation methods for image interpolation. *Meas. Sci. Technol.*, 20(104015), 2009.
- D. Amsallem and C. Farhat. Interpolation method for adapting reduced-

- order models and application to aeroelasticity. *AIAA J.*, 46:1803–1813, 2008.
- D. Amsallem, J. Cortial, K. Carlberg, and C. Farhat. A method for interpolating on manifolds structural dynamics reduced-order models. *Int. J. Numer. Meth. Engng.*, 80:1241–1257, 2009.
- P. B. Andersen, M. Gaunaa, C. Bak, and M. H. Hansen. A dynamic stall model for airfoils with deformable trailing edges. In J. N. Sørensen, M. O. L. Hansen, and K. S. Hansen, editors, *The Science of Making Torque from Wind*, volume 75 of *J. Phys.: Conference Series*, 2007.
- S. A. Ansari, R. Źbikowski, and K. Knowles. Aerodynamic modelling of insect-like flapping flight for micro air vehicles. *Prog. Aerospace Sci.*, 42: 129–172, 2006.
- A. Antoulas. *Approximation of Large-scale Dynamical Systems*. SIAM press, 2005.
- J. S. R. Anttonen, P. I. King, and Beran P. S. POD-based reduced-order models with deforming grids. *Math. Comp. Modeling*, 38:41–62, 2003.
- J. S. R. Anttonen, P. I. King, and P. S. Beran. Applications of multi-pod to a pitching and plunging airfoil. *Math. Comp. Modeling*, 42:245–259, 2005.
- H. Aref, M. Brøns, and M. A. Stremler. Bifurcation and instability problems in vortex wakes. *J. of Phys.: Conf. Series*, 64(012015), 2007. 2nd Int. Symp. on Instability and Bifurcations in Fluid Dynamics.
- E. Arian, M. Fahl, and E. W. Sachs. Trust-region proper orthogonal decomposition for flow control. Technical Report A283773, ICASE, NASA, May 2000.
- K. B. Ariyur and M. Krstić. *Real-time optimization by extremum-seeking control*. Wiley & Sons, Inc., 2003.
- K. J. Åström and R. M. Murray. *Feedback Systems: An Introduction for Scientists and Engineers*. Princeton University Press, 2008.
- P. J. Attar, E. H. Dowell, J. R. White, and J. P. Thomas. Reduced order nonlinear system identification methodology. *AIAA J.*, 44:1895–1904, 2006.
- N. Aubry, P. Holmes, J.L. Lumley, and E. Stone. The dynamics of coherent structures in the wall region of a turbulent boundary layer. *J. Fluid Mech.*, 192:115–173, 1988.
- D. Barkley. Linear analysis of the cylinder wake mean flow. *Europhys. Letters*, 75:750–756, 2006.
- T. K. Barlas and G. A. M. van Kuik. Aeroelastic modelling and comparison of advanced active flap control concepts for load reduction on the upwind 5MW wind turbine. In *Proc. European Wind Energy Conference & Exhibition (EWEC)*, 2009.

- J. T. Batina. Unsteady euler airfoil solutions using unstructured dynamic meshes. *AIAA J.*, 28:381–1388, 1990.
- R. Becker, M. Garwon, C. Gutknecht, G. Bärwolff, and R. King. Robust control of separated shear flows in simulation and experiment. *J. Process Cont.*, 15:691–700, 2005.
- D. E. Berg, D. G. Wilson, B. R. Resor, M. F. Barone, J. C. Berg, S. Kota, and G. Ervin. Active aerodynamic blade load control impacts on utility-scale wind turbines. In *Proc. of WindPower Conf. & Exhib.*, 2009.
- M. Bergmann and L. Cordier. Optimal control of the cylinder wake in the laminar regime by trust-region methods and POD reduced-order models. *J. Comp. Phys.*, 227:7813–7840, 2008.
- M. Bergmann, L. Cordier, and J.-P. Branger. Optimal rotary control of the cylinder wake using POD reduced order model. *Phys. Fluids*, 17:097101, 1–21, 2005.
- M. Bergmann, L. Cordier, and J.-P. Branger. Drag minimization of the cylinder wake by trust-region proper orthogonal decomposition. In R. King, editor, *Active Flow Control*, volume 95 of *Notes on Numerical Fluid Mechanics and Multidisciplinary Design*, pages 309–324. Springer Verlag, 2007.
- T. R. Bewley. Flow control: new challenges for a new renaissance. *Progress in Aerospace Sciences*, 37:21–58, 2001.
- I. Bijelonja, I. Demirdžić, and S. Muzaferija. A finite volume method for incompressible linear elasticity. *Comput. Methods Appl. Mech. Engrg.*, 195:6378–6390, 2006.
- F. J. Blom. Considerations on the spring analogy. *Int. J. Numer. Meth. Fluids*, 32:647–668, 2000.
- J. Borggaard, A. Hay, and D. Pelletier. Interval-based reduced order models for unsteady fluid flow. *Int. J. Num. Anal. & Modeling.*, 4:353–367, 2007.
- R. Bourguet, M. Braza, A. Sévrain, and A. Bouhadj. Capturing transition features around a wing by reduced-order modeling based on compressible navier-stokes equations. *Phys. Fluids*, 21(094104), 2009. Submitted.
- M. P. Boyce. *Gas turbine engineering handbook*. Elsevier, Jordan Hill, Oxford, UK, 2006.
- J. Braun, C. Thieulot, P. Fullsack, M. DeKool, C. Beaumont, and R. Huismans. DOUAR: A new three-dimensional creeping flow numerical model for the solution of geological problems. *Phys. Earth and Planetary Inter.*, 171:76–91, 2008.
- A. C. Carruthers, A. L. R. Thomas, and G. K. Taylor. Automatic aeroelastic devices in the wings of a steppe eagle Aquila nipalensis. *J. Exp. Biology*, 210:4136–4149, 2007.

- L. N. Cattafesta, Q. Song, D. R. Williams, C. W. Rowley, and F. S. Alvi. Active control of flow-induced cavity oscillations. *Prog. Aerospace Sci.*, 44:479–502, 2008.
- X. Chen, I. M. Navon, and F. Fang. A dual-weighted trust-region adaptive POD 4D-VAR applied to a finite-element shallow-water equations model. *Int. J. Numer. Meth. Fluids*, 60:709–732, 2009.
- M-C. Chiang, A.D. Leow, A.D. Klunder, R.A. Dutton, M. Barysheva, S.E. Rose, K.L. McMahon, G.I. de Zubicaray, A.W. Toga, and P.M. Thompson. Fluid registration of diffusion tensor images using information theory. *IEEE Trans. Medical Imaging*, 27:442–456, 2008.
- R. Clark, E. H. Dowell, D. Cox, H. C. Curtiss, J. W. Edwards, K. C. Hall, D. A. Peters, T. W. Strganac, R. H. Scalan, E. Simiu, and F. Sisto. *A Modern Course In Aeroelasticity*. Springer Verlag, 2004.
- L. Cordier, B. Abou El Majd, and J. Favier. Calibration of POD reduced-order models using Tikhonov regularization. *Int. J. Numer. Meth. Fluids*, 63:269–296, 2010.
- M. Couplet, C. Basdevant, and P. Sagaut. Calibrated reduced-order pod galerkin system for fluid flow modeling. *J. Comput. Phys.*, 207:192–220, 2005.
- J. L. Crassidis. Sigma-point Kalman filtering for integrated GPS and inertial navigation. *IEEE Transactions on Aerospace and Electronic Systems*, 42:750–756, 2006.
- J. D’Adamo, R. Sosa, A. Cammilleri, and G. Artana. Reduced order models for EHD controlled wake flow. *J. of Phys.: Conf. Series*, 166(012014), 2009. X Meeting on Recent Advances in the Physics of Fluids and their Applications.
- M. J. de C. Henshaw, K. J. Badcock, G. A. Vio, C. B. Allen, J. Chamberlain, I. Kaynes, G. Dimitriadis, J. E. Cooper, M. A. Woodgate, A. M. Rampurawala, D. Jones, C. Fenwick, A. L. Gaitonde, N. V. Taylor, D. S. Amor, T. A. Eccles, and C. J. Denley. Non-linear aeroelastic prediction for aircraft applications. *Prog. Aerospace Sci.*, 43:63–137, 2007.
- E. de Langre. Effects of wind on plants. *Ann. Rev. Fluid Mech.*, 40:141–168, 2008.
- A.E. Deane, I.G. Kevrekidis, G.E. Karniadakis, and S.A. Orszag. Low-dimensional models for complex geometry flows: Application to grooved channels and circular cylinders. *Phys. Fluids A*, 3(10):2337–2354, 1991.
- J. D. DeLaurier. An aerodynamic model for flapping-wing flight. *Aeronaut. J.*, 97:125–130, 1993.
- C.L. DeMarco and G.C. Verghese. Bringing phasor dynamics into the power system load flow. In *North American Power Symposium*, pages 463–469, 1993.

- L. Demasi and E. Livne. Dynamic aeroelasticity of structurally nonlinear configurations using linear modally reduced aerodynamic generalized forces. *AIAA J.*, 47:70–90, 2009.
- I. Demirdžić, S. Muzaferija, M. Perić, and E. Schreck. Numerical method for simulation of flow problems involving moving and sliding grids. In *Proc. 7th Int. Symp. Comp. Fluid Dyn.*, pages 359–364, 1997.
- R. Diziol and J. Bender D. Bayer. Volume conserving simulation of deformable bodies. In *Proc. Eurographics*, 2009. computer graphics, spring analogy, elastic body, numerical methods.
- H. Dong, M. Bozkurttas, R. Mittal P. Madden, and G. V. Lauder. Computational modelling and analysis of the hydrodynamics of a highly deformable fish pectoral fin. *J. Fluid Mech.*, 645:345–373., 2010.
- E. H. Dowell and K. C. Hall. Modeling of fluid-structure interaction. *Ann. Rev. Fluid Mech.*, 33:445–490, 2001.
- Q. Du and M. Gunzburger. Centroidal voronoi tessellation based proper orthogonal decompositon analysis. In *Control and Estimation of Distributed Parameter Systems*, volume 143 of *International Series of Numerical Mathematics*, pages 137 –150. Birkhauser, 2003.
- A. Edelman, T. A. Arias, and S. T. Smith. The geometry of algorithms with ortogonality constraints. *SIAM J. Matrix Anal. Appl.*, 20:303–353, 1998.
- B. I. Epureanu, E. H. Dowell, and K. C. Hall. Mach number influence on reduced-order models of inviscid potential flows in turbomachinery. *J. Fluids Engineering*, 124:977–987, 2002.
- M. Fahl. *Trust-region methods for flow control based on reduced order modelling*. PhD thesis, Universität Trier, 2000.
- C. Farhat, C. Degand, B. Koobus, and M. Lesoinne. Torsional springs for two-dimensional dynamic unstructured fluid meshes. *Comput. Meth. Appl. Mech. Engrg.*, 163:231 – 245, 1998.
- Z. Feng and A. Soulaïmani. Nonlinear aeroelasticity modeling using a reduced order model based on proper orthogonal decomposition. In *ASME Pressure Vessels and Piping Division Conference*, 2007. Paper PVP2007-26006.
- FFAST. Ffast: Future fast aeroelastic simulation technologies. Technical report, European South Africa Science and Technology Advancement Programme (ESASTAP), 2010.
- F. E. Fish and G. V. Lauder. Passive and active flow control by swimming fishes and mammals. *Ann. Rev. Fluid Mech.*, 38:193–224, 2006.
- K. Fitzpatrick, Y. Feng, R. Lind, A. J. Kurdila, and D. W. Mikolaitis. Flow control in a driven cavity incorporating excitation phase differential. *J. Guidance, Control, and Dynamics*, 28:63–70, 2005.

- C. Foiaş, O. Manley, and R. Temam and. Modelling of the interaction of small and large eddies in two dimensional turbulent flows. *RAIRO - Modél. math. et anal. numér.*, 22:93 – 118, 1988.
- C. Foias, G. R. Sell, and R. Temam. Inertial manifolds for nonlinear evolutionary equations. *J. Diff. Eqs.*, 73:309–353, 1988.
- B. D. O. Anderson G. Obinata. *Model Reduction for Control System Design*. Springer Verlag, 2000.
- B. Galletti, A. Bottaro, C.-H. Bruneau, and A. Iollo. Accurate model reduction of transient and forced wakes. *Eur. J. Mech., B/Fluids*, 26:354–366, 2007.
- J. Gerhard, M. Pastoor, R. King, B.R. Noack, A. Dillmann, M. Morzyński, and G. Tadmor. Model-based control of vortex shedding using low-dimensional Galerkin models. In *33rd AIAA Fluids Conference and Exhibit*, 2003. AIAA Paper 2003-4262.
- A. Glezer and M. Amitay. Synthetic jets. *Annu. Rev. Fluid Mech.*, 34: 503–529, 2002.
- M. Goman and A. Khrabrov. State space representation of aerodynamic characteristics of an aircraft at high angles of attack. *J. Aircraft*, 31 (1109–1115), 1994.
- A.N. Gorban, N. K. Kazantzis, I. G. Kevrekidis, H.C. Öttinger, and C. Theodoropoulos, editors. *Model Reduction and Coarse-Graining Approaches for Multiscale Phenomena*. Springer Verlag, 2006.
- W. R. Graham, J. Peraire, and K. Y. Tang. Optimal control of vortex shedding using low order models - Part I Open loop model development. *Int. J. Numer. Meth. Fluids*, 44:945–972, 1999a.
- W. R. Graham, J. Peraire, and K. Y. Tang. Optimal control of vortex shedding using low order models - Part II model based control. *Int. J. Numer. Meth. Fluids*, 44:973–990,, 1999b.
- M. S. Grewal and A. P. Andrews. *Kalman Filtering: Theory and Practice*. Prentice Hall, 1993.
- J. Guckenheimer and P. Holmes. *Nonlinear Oscillations, Dynamical Systems, and Bifurcation of Vector Fields*. Springer Verlag, 6th printing edition, 2002.
- B. Günther, F. Thiele, R. Petz, W. Nitsche, J. Sahner, T. Weinkauf, and H.C. Hege. Control of separation on the flap of a three element high-lift configuration'. In *45th AIAA Aerospace Sciences Meeting and Exhibit*, 2007. Paper AIAA-2007-0265.
- K. C. Hall, R. E. Kielb, and J. P. Thomas, editors. *Unsteady aerodynamics, aeroacoustics and aeroelasticity of turbomachines*. Springer Verlag, 2006.
- A. Hay, J. Borggaard, and D. Pelletier. Local improvements to reduced-order models using sensitivity analysis of the proper orthogonal decomposition. *J. Fluid Mech.*, 629:41–72, 2009.

- S. Ho, H. Nassef, N. Pornsinsirirak, Y.-C. Taib, and C.-M. Hoa. Unsteady aerodynamics and flow control for flapping wing flyers. *Prog. Aerospace Sci.*, 39:635–681, 2003.
- C. A. Holmes. Bounded solutions of the nonlinear parabolic amplitude equation for plane Poiseuille flow. *Proc. Roy. Soc. London A*, 402:299–322, 1985.
- P. Holmes, J.L. Lumley, and G. Berkooz. *Turbulence, Coherent Structures, Dynamical Systems and Symmetry*. Cambridge University Press, 1998.
- C. Homescu, L. R. Petzold, and R. Serban. Error estimation for reduced-order models of dynamical systems. *SIAM J. Numer. Anal.*, 43:1693–1714, 2005.
- M. Hong, S. Jung, M.-H. Choi, and S. W.J. Welch. Fast volume preservation for a mass-spring system. *IEEE Comp. Graph. Appl.*, 26:83–91, 2006.
- S.-Y. Hsu and C.-L. Chang. Mesh deformation based on fully stressed design: The method and two-dimensional examples. *Int. J. Numer. Meth. Engng.*, 72:606–629,, 2007.
- G.-H. Hu, D.-J. Sun, X.-Y. Yin, and B.-G. Tong. Hopf bifurcation in wakes behind a rotating and translating circular cylinder. *Phys. Fluids*, 8: 1972–1974, 1996.
- G. Irving, C. Schroeder, and R. Fedkiw. Volume conserving finite element simulations of deformable models. *Int. Conf. Comp. Graphics and Interactive Techniques (ACM SIGGRAPH)*, 2007.
- D. Ishihara and S. Yoshimura. A monolithic approach for interaction of incompressible viscous fluid and an elastic body based on fluid pressure Poisson equation. *Int. J. Numer. Meth. Fluids*, 64:167–203, 2005.
- W.-T. Joe and T. Colonius. Feedback control of vortex shedding from an inclined flat plate. *Theor. Comp. Fluid Dyn.*, 2010.
- W.-T. Joe, K. Taira, T. Colonius, D. G. MacMynowski, and G. Tadmor. Closed-loop control of vortex shedding on a two-dimensional flat-plate airfoil at a low Reynolds number. In *46th AIAA Aerospace Sciences Meeting and Exhibit*, 2008. AIAA P-2008-634.
- K. Kaepernick, L. Koop, and K. Ehrenfried. Investigation of the unsteady flow field inside a leading edge slat cove. In *11th AIAA/CEAS Aeroacoustics Conference*, 2005. AIAA Paper 2005-2813.
- R. Kamakoti and W. Shyy. Fluid–structure interaction for aeroelastic applications. *Prog. Aerospace Sci.*, 40:535–558, 2004.
- C. Kasnakoğlu, A. Serrani, and M. Ö. Effe. Control input separation by actuation mode expansion for flow control problems. *Int. J. Control*, 81: 1475–1492, 2008.
- C. Kasnakoğlu, R. C. Camphouse, and A. Serrani. Reduced-order model-based feedback control of flow over an obstacle using center manifold methods. *ASME J. Dyn. Sys. Meas. Contr.*, 131(011011), 2009.

- N. Kato and S. Kamimura. *Bio-mechanisms of Swimming and Flying*. Springer Verlag, 2008.
- M. A. Kegerise, R. H. Cabell, and L. N. Cattafesta. Real-time feedback control of flow-induced cavity tones—Part 1: Fixed-gain control, Part 2: Adaptive control. *J. Sound and Vibration*, 300:906–923, 924–940, 2007.
- J. Kim and T. R. Bewley. A linear systems approach to flow control. *Ann. Rev. Fluid Mech.*, 39:383–417, 2007.
- R. King (editor) *Active Flow Control II*. Number 108 in Lecture Notes on Numerical Fluid Mechanics and Interdisciplinary Design. Springer Verlag, Berlin, 2010.
- S. Kota, R. Osborn, G. Ervin, D. Maric, P. Flick, and D. Paul. Mission adaptive compliant wing—design, fabrication and flight test. In *Morphing Vehicles*, number RTO-MP-AVT-168-18 in . NATO Research and Technology Organization, 2009.
- I. Lasiecka and R. Triggiani. *Control theory for partial differential equations: continuous and approximation theories*. Cambridge University Press, 2000.
- E. Lauga and T. R. Powers. The hydrodynamics of swimming microorganisms. *Rep. Prog. Phys.*, 72(096601), 2009.
- O. Lehmann, M. Luchtenburg, B.R. Noack, R. King, M. Morzynski, and G. Tadmor. Wake stabilization using POD Galerkin models with interpolated modes. In *44th IEEE Conference on Decision and Control and European Control Conference ECC, Seville, Spain*, pages 500–505, 2005.
- J. G. Leishman. *Principles of helicopter aerodynamics*. Cambridge University Press, 2006.
- H. Lev-Ari and A. Stanković. Phasor-banks: Customizable filter banks for robust dynamic time-frequency analysis. In *40th North American Power Symposium (NAPS)*, 2008.
- G. C. Lewin and H. Haj-Hariri. Reduced-order modeling of a heaving airfoil. *AIAA J.*, 43:270–283, 2005.
- Y. Liang, Y. Yuga, and M. Taya. Design of membrane actuator based on ferromagnetic shape memory alloy composite for synthetic jet applications. *Sens. Act. A: Physical*, 125:512–518, 2006.
- E. Liberge and A. Hamdouni. Reduced order modelling method via proper orthogonal decomposition (POD) for flow around an oscillating cylinder. *J. Fluids and Structures*, 26:292–311, 2010.
- E. Liberge, M. Benaouicha, and A. Hamdouni. Proper orthogonal decomposition investigation in fluid structure interaction. *Euro. J. Comp. Mech.*, 16:401–418, 2008.
- J. Little, M. Nishihara, I. Adamovich, and M. Samimy. High-lift airfoil trailing edge separation control using a single dielectric barrier discharge plasma actuator. *Exps. Fluids*, 48:521–537, 2009.

- E. Livne. Future of airplane aeroelasticity. *J. Aircraft*, 40:1066–1091, 2003.
- D. Lo Jacono, J. N. Sørensen, M. C. Thompson, and K. Hourigan. Control of vortex breakdown in a closed cylinder with a small rotating rod. *J. Fluids and Structures*, 24:1278–1283, 2008.
- I. Lopez and N. Sarigul-Klijn. A review of uncertainty in flight vehicle structural damage monitoring, diagnosis and control: Challenges and opportunities. *Prog. Aerospace Sci.*, 46:247–273, 2010.
- M. Luchtenburg, G. Tadmor, O. Lehmann, B. R. Noack, R. King, and M. Morzynski. Tuned POD Galerkin models for transient feedback regulation of the cylinder wake. In *44th AIAA Aerospace Sciences Meeting and Exhibit*, 2006. Paper AIAA-2006-1407.
- M. Luchtenburg, B. R. Noack, B. Günther, R. King, and G. Tadmor. A generalised mean-field model of the natural and high-frequency actuated flow around a high-lift configuration. *J. Fluid Mech.*, 623:283–316, 2009.
- M. Manhart. Energy transfer between coherent structures in the wake of a hemisphere. In J.N. Sorensen, E.J. Hopfinger, and N. Aubry, editors, *Simulation and Identification of Organized Structures in Flows*, pages 499–508. Kluwer Academic Publishers, 1998.
- J. E. Marsden and M. McCracken. *The Hopf Bifurcation and Its Applications*. Springer Verlag, 1976.
- L. Mathelin and O. P. Le Maitre. Robust control of uncertain cylinder wake flows based on robust reduced order models. *Computers & Fluids*, 38: 1168–1182, 2009.
- W. J. McCroskey. Unsteady airfoils. *Ann. Rev. Fluid Mech.*, 14:285–311, 1982.
- T. Meurer, K. Graichen, and E.-D. Gilles, editors. *Control and observer design for nonlinear finite and infinite dimensional Systems*, volume 322 of *Lecture Notes in Control and Information Sciences*. Springer Verlag, 2002.
- I. Mezić. Spectral properties of dynamical systems, model reduction and decompositions. *Nonlinear Dynamics*, 41:309–325, 2005.
- A. Mishra, G. Tadmor, and Z. Rusak. The dynamics of the axisymmetric vortex breakdown in a pipe. In *38th AIAA Fluid Dynamics / 4th Flow Control Conference and Exhibit*, 2008. AIAA Paper 2008-3799.
- A. Mishra, G. Tadmor, and Z. Rusak. Bifurcation analysis of the axisymmetric vortex breakdown in a pipe. In *39th AIAA Fluid Dynamics Conference / 27th AIAA Applied Aerodynamics Conference*, 2009. AIAA Paper-2009-3709.
- S. Mittal and B. Kumar. Flow past a rotating cylinder. *J. Fluid Mech.*, 476:303–334, 2003.

- P. Mokhasi and D. Rempfer. Sequential estimation of velocity fields using episodic proper orthogonal decomposition. *Physica D*, 237:3197–3213, 2008.
- P. Mokhasi, D. Rempfer, and S. Kandala. Predictive flow-field estimation. *Phys. D*, 238:290–308, 2009.
- E. Moreau. Airflow control by non-thermal plasma actuators. *J. Phys. D: Appl. Phys.*, 40:605–636, 2007.
- M. Morzyński, W. Stankiewicz, B. R. Noack, R. King, F. Thiele, and G. Tadmor. Continuous mode interpolation for control-oriented models of fluid flow. In R. King, editor, *Active Flow Control*, volume 95 of *Notes on Numerical Fluid Mechanics and Multidisciplinary Design*, pages 260–278. Springer Verlag, Berlin, Germany, 2007.
- S. M. Murman, M. J. Aftosmis, and M. J. Berger. Implicit approaches for moving boundaries in a 3-D Cartesian method. In *41st AIAA Aerospace Sciences Meeting*, 2003. AIAA Paper 2003-1119.
- I. M. Navon. Data assimilation for numerical weather prediction : A review. In S. K. park and L. Xu, editors, *Data Assimilation for Atmospheric, Oceanic, and Hydrologic Applications*, pages 21–66. Springer Verlag, I. M. Navon.
- H. Nijmeijer and A.J. van der Schaft. *Nonlinear Dynamical Control Systems*. Springer-Verlag, New York, 1990.
- B. R. Noack, M. Schlegel, M. Morzyński, and G. Tadmor. System reduction strategy for Galerkin models of fluid flows. *Int. J. Numer. Meth. Fluids*, 63:231–248, 2010. doi: 10.1002/fld.2049.
- B.R. Noack and H. Eckelmann. A low-dimensional Galerkin method for the three-dimensional flow around a circular cylinder. *Phys. Fluids*, 6(1): 124–143, 1994.
- B.R. Noack, P. Papas, and P.A. Monkewitz. Low-dimensional Galerkin model of a laminar shear-layer. Technical Report 2002-01, Laboratoire de Mécanique des Fluides, Département de Genie Mécanique, Ecole Polytechnique Fédérale de Lausanne, Switzerland, 2002.
- B.R. Noack, K. Afanasiev, M. Morzyński, G. Tadmor, and F. Thiele. A hierarchy of low-dimensional models for the transient and post-transient cylinder wake. *J. Fluid Mech.*, 497:335–363, 2003.
- B.R. Noack, G. Tadmor, and M. Morzyński. Actuation models and dissipative control in empirical Galerkin models of fluid flows. In *The 2004 American Control Conference*, volume 6, pages 5722 –5727, Boston, MA, U.S.A., 2004a. Paper **FrP15.6**.
- B.R. Noack, G. Tadmor, and M. Morzyński. Low-dimensional models for feedback flow control. Part I: Empirical Galerkin models. In *2nd AIAA Flow Control Conference*, 2004b. AIAA Paper 2004-2408.

- B.R. Noack, P. Papas, and P.A. Monkewitz. The need for a pressure-term representation in empirical Galerkin models of incompressible shear flows. *J. Fluid Mech.*, 523:339–365, 2005.
- B.R. Noack, M. Schlegel, B. Ahlborn, G. Mutschke, M. Morzyński, P. Comte, and G. Tadmor. A finite-time thermodynamics of unsteady flows. *J. Nonequilibrium Thermodynamics*, 33:103–148, 2008.
- T. E. Noll, S. D. Ishmael, B. Henwood, M. E. Perez-Davis, G. C. Tiffany, J. Madura, M. Gair, J. H. Brown, and T. Wierzbowski. Technical findings, lessons learned, and recommendations resulting from the helios prototype vehicle mishap. In *RTO Applied Vehicle Technology Panel (AVT) Workshop*, volume RTO-MP-AVT-145 of *UAV Design Processes / Design Criteria for Structures*. NATO Research and Technology Organisation, 2007.
- M. Pastoor, R. King, B.R. Noack, and G. Tadmor. Observers & feedback control for shear layer vortices. In *44th IEEE Conference on Decision and Control and European Control Conference ECC, Seville, Spain*, 2005.
- M. Pastoor, B. R. Noack, R. King, and G. Tadmor. Spatiotemporal waveform observers and feedback in shear layer control. In *44th AIAA Aerospace Sciences Meeting and Exhibit*, 2006. Paper AIAA-2006-1402.
- M. Pastoor, L. Henning, B. R. Noack, R. King, and G. Tadmor. Feedback shear layer control for bluff body drag reduction. *J. Fluid Mech.*, 608:161–196, 2008.
- M. J. Patil. Nonlinear gust response of highly flexible aircraft. In *Proc. 48th AIAA , Structural Dynamics, and Materials Conf.*, 2007. AIAA Paper 2007-2103.
- E. Pendleton. Back to the future: How active aeroelastic wings are a return to aviation’s beginnings and a small step to future bird-like wings. In *RTO AVT Symposium on Active Control Technology for Enhanced Performance Operational Capabilities of Military Aircraft, Land Vehicles and Sea Vehicles*, 2000.
- P.-O. Persson and J. Peraire. Curved mesh generation and mesh refinement using Lagrangian solid mechanics. In *47th AIAA Aerospace Sciences Meeting and Exhibit*, 2009. AIAA Paper 2009-949.
- D. A. Peters, M.-C. Hsieh, and A. Torrero. A state-space airloads theory for flexible airfoils. *J. Amer. Helicopter Soc.*, 51:329–342, 2007.
- R. D. Prabhu, S. Scott Collis, and Y. Chang. The influence of control on proper orthogonal decomposition of wall-bounded turbulent flows. *Phys. Fluids*, 13:520—537, 2001.
- B. Protas. Center manifold analysis of a point-vortex model of vortex shedding with control. *Phys. D*, 228:179–187, 2007.
- B. Protas. Vortex dynamics models in flow control problems. *Nonlinearity*, 21:R203–R250, 2008.

- B. Raghavan and M. J. Patil. Flight control for flexible, high-aspect-ratio flying wings. *AIAA J. Guidance, Control, and Dynamics*, 33:64, 2010.
- S. S. Ravindran. Reduced-order adaptive controllers for fluid flows using POD. *J. Scientific Computing*, 15:457–478, 2000.
- D. Rempfer. *Kohärente Strukturen und Chaos beim laminar-turbulenten Grenzschichtumschlag* (transl.: *Coherent structures and chaos of the laminar-turbulent boundary-layer transition*). PhD thesis, Fakultät Verfahrenstechnik der Universität Stuttgart, 1991. (Part of this work has been published by Rempfer, D. and Fazle, F.H. (1994) in *J. Fluid Mech.* 260 & 275).
- R. Roszak, P. Posadzy, W. Stankiewicz, and M. Morzyński. Fluid structure interaction for large scale complex geometry and non-linear properties of structure. *Archives of Mechanics*, 61:1–24, 2009.
- C. W. Rowley, I. G. Kevrekidis, J. E. Marsden, and K. Lust. Reduction and reconstruction for self-similar dynamical systems. *Nonlinearity*, 16: 1257–1275, 2003.
- C.W. Rowley. Model reduction for fluids, using balanced proper orthogonal decomposition. *Int. J. on Bifurcation and Chaos*, 15:997–1013, 2005.
- A. E. Russell. Some factors affecting large transport aeroplanes with turbo-prop engines: The thirteenth Wright brothers lecture. *J. Aeronautical Sciences*, 17:67–93, 1950.
- R. Sánchez-Peña and M. Sznaier. *Robust Systems Theory and Applications*. Wiley & Sons, Inc., 1998.
- T. P. Sapsis and P. F. J. Lermusiaux. Dynamically orthogonal field equations for continuous stochastic dynamical system. *Phys. D*, 238:2347–2360, 2009.
- M. Schatz, B. Günther, and F. Thiele. Computational investigation of separation control over high-lift airfoil flows. In R. King, editor, *Active Flow Control*, volume 95 of *Notes on Numerical Fluid Mechanics and Multidisciplinary Design*. Springer Verlag, Berlin, 2007.
- W. H. A. Schilders, H. A. van der Vorst, and J. Rommes, editors. *Model Order Reduction: Theory, Research Aspects and Applications*, volume 13 of *The European Consortium for Mathematics in Industry*. Springer Verlag, 2008.
- D. M. Schuster, D. D. Liu, and L. J. Hutton. Computational aeroelasticity: Success, progress, challenge. *J. Aircraft*, 40:843–856, 2003.
- W. Shyy, H. Aono, S. K. Chimakurthi, P. Trizila, C.-K. Kang, C. E. S. Cesnik, and H. Liu. Recent progress in flapping wing aerodynamics and aeroelasticity. *Prog. Aerospace Sci.*, 2010.
- S. Siegel, K. Cohen, J. Seidel, M. Luchtenburg, and T. McLaughlin. Low dimensional modelling of a transient cylinder wake using double proper orthogonal decomposition. *J. Fluid Mech.*, 2008. accepted for publication.

- W. A. Silva, V. N. Vasta, and R. T. Biedron. Development of unsteady aerodynamic and aeroelastic reduced-order models using the FUN3D code. In *Int. Forum on Aeroelasticity and Structural Dynamics (IFASD)*, 2009.
- W. Stankiewicz, M. Morzyński, R. Roszak, B. R. Noack, and G. Tadmor. Reduced order modelling of flow around an airfoil with a changing angle of attack. *Archives of Mechanics*, 60:509–526, 2008.
- T. Stathopoulos and C. C. Baniotopoulos, editors. *Wind Effects on Buildings and Design of Wind-Sensitive Structures*. Springer Verlag, 2007.
- E. Strømmen. *Theory of Bridge Aerodynamics*. Springer Verlag, 2006.
- G. Tadmor. On approximate phasor models in dissipative, bilinear systems. *IEEE Transaction on Circuits & Systems I: Fundamental Theory*, 49: 1167–1179, 2002.
- G. Tadmor and B.R. Noack. Dynamic estimation for reduced Galerkin models of fluid flows. In *The 2004 American Control Conference*, volume 1, pages 746 –751, Boston, MA, U.S.A., 2004. Paper **WeM18.1**.
- G. Tadmor, B.R. Noack, M. Morzyński, and S. Siegel. Low-dimensional models for feedback flow control. Part II: Controller design and dynamic estimation. In *2nd AIAA Flow Control Conference*, 2004. AIAA Paper 2004-2409.
- G. Tadmor, M. D. Centuori, B. R. Noack, M. Luchtenburg, O. Lehmann, and M. Morzyński. Low Order Galerkin Models for the Actuated Flow Around 2-D Airfoils. In *45th AIAA Aerospace Sciences Meeting and Exhibit*, 2007a. AIAA Paper 2007-1313.
- G. Tadmor, J. Gonzalez, O. Lehmann, B. R. Noack, M. Morzyński, and W. Stankiewicz. Shift Modes and Transient Dynamics in Low Order, Design Oriented Galerkin Models. In *45th AIAA Aerospace Sciences Meeting and Exhibit*, 2007b. Paper AIAA 2007-111.
- G. Tadmor, D. Bissex, B. R. Noack, M. Morzyński, T. Colonius, and K. Taira. Temporal-harmonic specific POD mode extraction. In *4th Flow Control Conference / 38th AIAA Fluid Dynamics Conference and Exhibit*, 2008. AIAA Paper 2008-4190.
- G. Tadmor, O. Lehmann, B. R. Noack, and M. Morzyński. Mean field representation of the natural and actuated cylinder wake. *Phys. Fluids*, 22(034102), 2010.
- T. E. Tezduyar. Finite element methods for flow problems with moving boundaries and interfaces. *Arch. of Comp. Methods in Eng.*, 2001.
- T. Theodorsen. General theory of aerodynamic instability and the mechanism of flutter. Technical Report 496, National Advisory Committee for Aeronautics (NACA), 1935.
- R. Vazquez and M. Krstic. A closed-form feedback controller for stabilization of the linearized 2-D Navier–Stokes Poiseuille system. *IEEE Trans. Autom. Contr.*, 52:2298–2312, 2007.

-
- T. von Kármán and H. Rubach. über den mechanismusdes fl”ussigkeits-und luftwiderstandes. *Phys. Z.*, 13:49–59, 1912.
- O. Wiederhold, R. King, and B. R. Noack. Robust control in turbomachinery configurations. In R. King, editor, *Active Flow Control II*, volume 108 of *Lecture Notes on Numerical Fluid Mechanics and Interdisciplinary Design*, pages 187–201. Springer Verlag, 2010.
- D. R. Williams, G. Tadmor, T. Colonius, W. Kerstens, V. Quach, and S. Buntain. The lift response of a stalled wing to pulsatile disturbances. *AIAA J.*, 47:3031–3037, 2009.
- C.H.K. Williamson. Vortex dynamics in the cylinder wake. *Annu. Rev. Fluid Mech.*, 28:477–539, 1996.
- D. G. Wilson, D. E. Berg, M. F. Barone, J. C. Berg, B. R. Resor, and D. W. Lobitz. Active aerodynamic blade control design for load reduction on large wind turbines. In *Proc. Euro. Wind Energy Conf. and Exhibit (EWEC)*, 2009.
- X. Xie, L. C. Musson, and M. Pasquali. An isochoric domain deformation method for computing steady free surface flows with conserved volumes. *J. Comp. Phys.*, 226:398–413, 2007.
- H. Yu, M. Leeser, G. Tadmor, and S. Siegel. Real-time particle image velocimetry for feedback loops using FPGA implementation. *AIAA J. Aerospace Computing, Information, and Communication*, 3:52–56, 2006.

Feedback Flow Control in Experiment and Simulation Using Global Neural Network Based Models

Stefan Siegel

Department for Aeronautics, 2354 Fairchild Dr. Ste 6H27, United States Air Force Academy, CO 80840, USA

Abstract For feedback control of complex spatio-temporally evolving flow fields, it imperative to use a global flow model for both flow state estimation, as well as controller development. It is important that this model correctly presents not just the natural, unforced flow state, but also the interaction of actuators with the flow for both open and closed loop situations. In order to achieve this, a novel extension of POD is introduced in this chapter, which we refer to as Double POD (DPOD). This decomposition allows the construction of a POD basis that is valid for a variety of flow conditions, which may be distinguished by changes in actuation, Reynolds number or other parameters. While traditionally the velocity field has been used as input for POD, other variables, for example the pressure or density field, may be used as well. The mode amplitudes of the DPOD spatial modes are then used as input for a system identification process, the nonlinear ANN-ARX method is employed here. The result is a dynamic model that represents both the unforced, open loop forced and closed loop flow fields with good accuracy.

1 Introduction

One of the main purposes of flow control is the improvement of aerodynamic characteristics of air vehicles and munitions enabling augmented mission performance. An important area of flow control research involves the phenomenon of vortex shedding in the wake behind bluff bodies where the flow separates from the bluff body's surface. Shedding of counter-rotating vortices is observed in the wake of a two-dimensional cylinder above a critical Reynolds number of $Re_{crit} \approx 47$, non-dimensionalized with respect to freestream velocity and cylinder diameter. This phenomenon is often referred to as the von Kármán vortex street, shown schematically in Figure 1. The vortex shedding leads to a sharp rise in drag, noise and fluid-induced

vibration. The ability to control the wake of a bluff body could be used to reduce drag, increase mixing and heat transfer, and enhance combustion. The benchmark problem of a circular cylinder wake is studied at a Reynolds number of $Re_D \approx 100$, which corresponds to the range in which the wake is laminar and two-dimensional. When active open-loop forcing of the wake is employed, the vortices in the wake can be "locked" to the forcing signal. This also strengthens the vortices and consequently increases the drag. As opposed to the open-loop approach, the goal is to control the unsteady wake using a feedback controller in order to reduce or suppress the vortex shedding. The feedback control law is designed using a reduced order model of the unsteady flow. A common method used to substantially reduce the order of the model is Proper Orthogonal Decomposition (POD). This method is an optimal approach in that it will capture the largest amount of the flow energy for fixed amount of modes of any decomposition of the flow. However, a number of extensions to the POD decomposition are necessary in order to derive a numerical model suitable for feedback controller development.

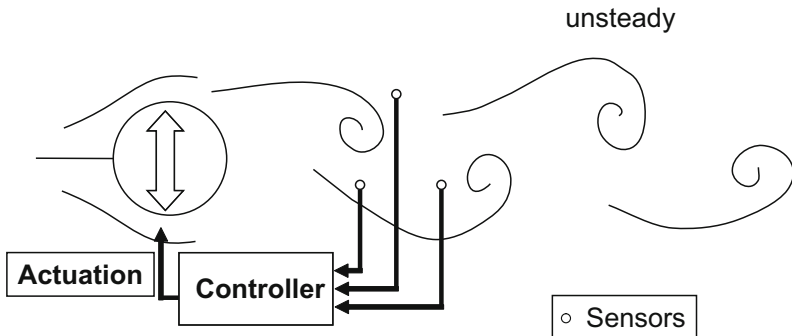


Figure 1. Feedback Control Setup

Low dimensional model development based on POD decomposition is a three step process, as shown in Figure 2. In the first step, data on the flow field to be modelled is gathered using either numerical or experimental methods. Selection of suitable data sets is a crucial step in model building and will be discussed in detail below. In the second step, spatial modes and their mode amplitudes are derived from the flow field data. The most often used approach is the method of snapshots developed by Sirovich (1987). Various methods of deciding how to precondition or cluster the data have been suggested in literature and are discussed below.

In conjunction with the spatial POD modes, the associated mode amplitudes may be calculated using an inner product or least square fit approach.

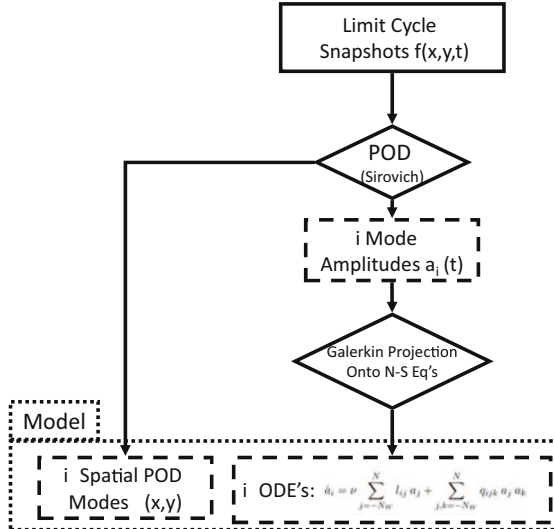


Figure 2. Flow Chart of traditional POD modeling process (see Chapter by Noack et al.)

To arrive at a low dimensional model, the mode set is truncated, usually based on an energy criterion (the eigenvalues in the Karhunen-Loève system represent twice the modal kinetic energy if POD is applied to the velocity field). The third and final step is the development of a model for the remaining mode amplitudes. This is commonly achieved by a Galerkin projection on the Navier-Stokes equations, which yields a system of equations that describes the evolution of the mode amplitudes over time. This set of equations can then be used to develop feedback control algorithms in a systematic fashion, or to test the performance of control algorithms against this model. All three steps of model development described above involve assumptions and potential problems, with many different solution proposed in literature, which will be discussed in the following.

Figure 3 gives an overview over the newly developed DPOD-ANN-ARX modeling approach discussed in this Chapter. The overview flow diagram illustrates the modifications made to the traditional approach shown in

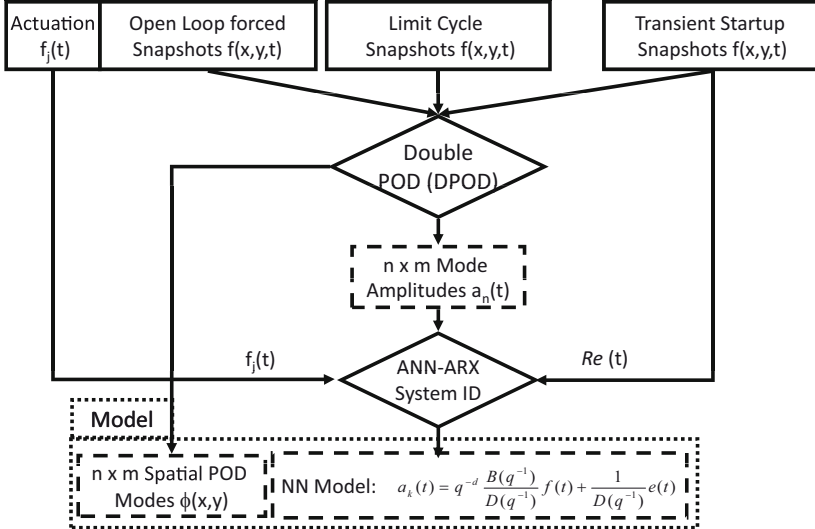


Figure 3. Flow Chart of DPOD-ANN-ARX modeling process

Figure 2. At the input data level, transient data from both a change in Reynolds number as well as open loop forced flow states is included. Then, a modified POD procedure which we refer to as Double Proper Orthogonal Decomposition (DPOD) is employed. The main benefit of this method lies in the ability to derive spatial POD modes that cover a large range of flow conditions with small estimation errors, for details refer to the DPOD section in the following. Instead of the traditional Galerkin projection, a nonlinear ARX (Auto Regressive eXternal input) system identification method based on Artificial Neural Networks (ANN) is used in order to develop a dynamic model of the flow. For the benchmark problem of the circular cylinder wake, it is shown that this approach yields a numerically stable model that is not just valid for the data used in its derivation, but also for a range of different Reynolds numbers, different open loop forcing conditions and, most importantly, feedback controlled flow states (Siegel et al., 2008). Further details on the DPOD-ANN-ARX modeling approach are included in the following subsections of this chapter, while the modeling results as well as feedback controlled flow simulations are discussed in the

later sections of this chapter.

2 Wake stabilization benchmark

The approach to model development discussed in this chapter can be used with either experimental or numerical data, since it is not dependent on e.g. solving the Navier Stokes equations inverse in time or similar processes that cannot be performed in an experiment. However, due to the abundance of data available from simulations, all results presented here have been obtained from DNS simulations. It is worth while noting that most CFD solvers, in particular commercially available codes, are not well suited to time resolved simulations. This is manifest either in excessively slow calculation times, or the inability to properly resolve the dynamic flow behavior due to artificial viscosity inherent in code, grid or both leading to nonphysical simulation results. Thus, it is paramount to check the performance of the candidate CFD solver not just for time averaged quantities like lift or drag, but more importantly for dynamic quantities like shedding frequencies (as done below) or even better, transient flow time scales. All numerical simulations reported here were conducted with Cobalt Solutions COBALT solver for direct numerical solution of the Navier-Stokes equations with second order accuracy in time and space. A structured two-dimensional grid with 63,700 nodes and 31,752 elements was used Figure 4. The grid extended from $\frac{x}{D} = -16.9$ to $\frac{x}{D} = 21.1$ in the x (streamwise) direction, and $\frac{|y|}{D} \leq 19.4$ cylinder diameters in the y (flow normal) direction. While this size of a domain is necessary to obtain accurate CFD results, the region of interest for feedback flow control is much smaller as indicated in Figure 4. While truncation in the spatial domain would pose major problems for many other model development approaches due to boundary condition issues, our approach does not involve boundary conditions as will be described later, and thus the truncation to a much smaller spatial domain is possible.

For validation of the computations of the unforced cylinder wake at $Re = 100$, the resulting value of the mean drag coefficient, c_d , was compared to experimental and computational investigations reported in the literature. Experimental data reported by Oertel (1990) point to c_d values between 1.26 and 1.4. Furthermore, Min and Choi (1999) report on several numerical studies that obtained drag coefficients between 1.34 and 1.35. The current simulations yield $c_d = 1.35$, which compares well with the reported literature. Another important benchmark parameter is the non-dimensional shedding frequency (Strouhal number, $St = \frac{fD}{U}$ for the unforced cylinder wake. Experimental results presented by Williamson (1996) point to values of $St \in [0.167, 0.168]$. The computations used in this effort result in

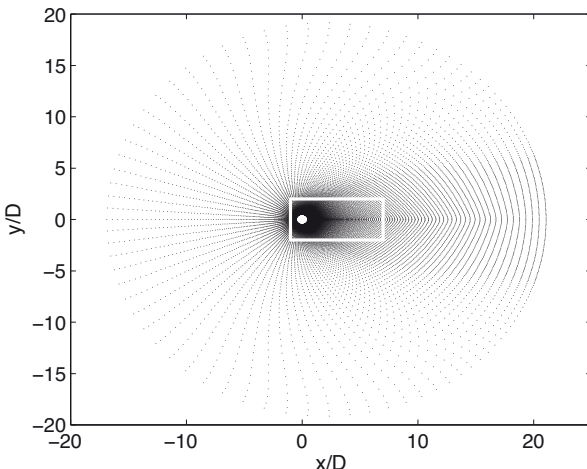


Figure 4. Circular Cylinder Grid and POD domain

$St = 0.163$, which also compares well with the reported literature. Beyond the unforced flow condition, cylinder displacement normal to the flow direction was used to investigate the interaction between this type of actuation and the flow field. A typical transient forcing signal is shown in Figure 5, where the cylinder displacement is sinusoidal in time with a frequency f and peak amplitude A . The flow response in Figure 5 shows a lock-in behavior which leads to a fixed phase relationship between forcing and the oscillating lift force after a few shedding cycles. At the beginning and end of the forcing, the flow exhibits transient behaviour. These dynamic adjustment periods are a manifestation of the underlying dynamics of the flow field, and as such contain important information for the development of a dynamic model of the flow behavior.

As the aim is to develop an effective numerical model of the fluid dynamic behavior of the flow when subject to various forcing inputs where lock-in can be achieved, a number of simulations to cover different frequency and forcing amplitudes were conducted. Figure 6 shows the selected parameter combinations, along with the boundaries beyond which lock in cannot be achieved any more. Nine different data sets for the open loop forced cases, were obtained using forcing amplitudes of 10, 15, 20, 25 and 30% cylinder displacement. Some of the cases use a 5-10 % lower or higher frequency at 30% displacement, which is still within the lock-in region. Lock-in is defined

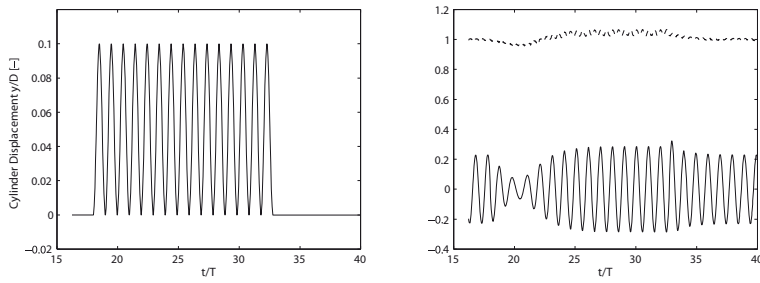


Figure 5. Left, Cylinder displacement. $f/f_0 = 1$; $A/D = 0.05$. Forcing activated at $t/T = 18$ and stopped at $t/T = 33$, after 15 full forcing cycles. Right, transient forced normalized lift coefficient c_l/c_{d0} (solid line) and drag coefficients c_d/c_{d0} (dashed line).

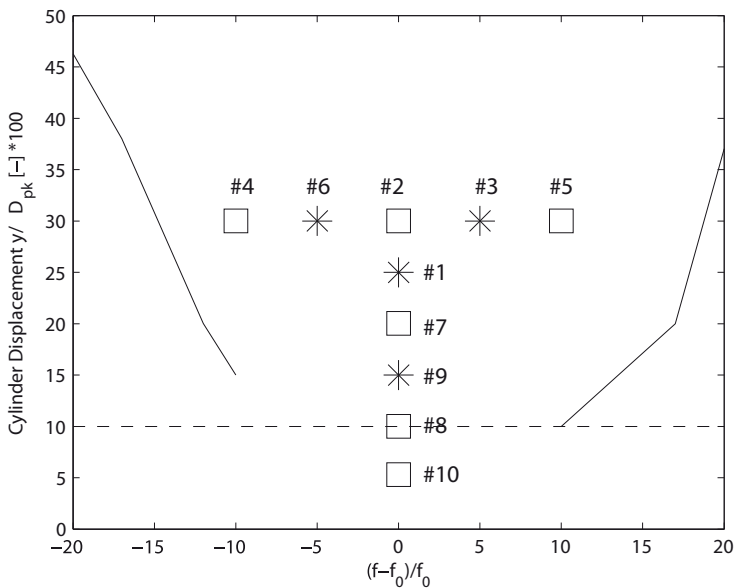


Figure 6. "Lock-In" Envelope with Design and Off-Design Cases

as the flow developing a fixed phase relationship between the actuation and the vortex shedding. The simulations indicated as squares were used as design cases for model development, while the cases indicated as stars, are utilized for model validation. The goal is to develop a model based on the design cases, that still yields accurate results for the validation cases.

3 Description of transient coherent structure via DPOD

The POD decomposition has been introduced in earlier chapters in this book, and is used it here employing the method of snapshots introduced by Sirovich (1987).

$$u(x, y, t) = \sum_{i=1}^I a_i(t) \phi_i(x, y). \quad (1)$$

However, in all data presented in this chapter, the mean flow is never subtracted from the snapshot set beforehand. Thus, Equation 1 will yield the mean flow as the first mode of index $i=1$. This is an important requirement for the development of a mode bases that tracks changes in the mean flow, as will be shown in the following sections.

3.1 Short Time POD - SPOD

In order to gather some intuitive understanding of the effect of the number of snapshots used in order to derive spatial POD modes, data sets of a 2D CFD simulation of the circular cylinder wake at a Reynolds number of 100 were used. The sampling interval was 1/25th or 4% of a shedding cycle, and a maximum of four shedding cycles was available to calculate the spatial POD modes. These four shedding cycles were obtained from the steady state vortex shedding and identical to each other. Proper Orthogonal Decomposition was performed on snapshot ensembles with varying length consisting of 2 to 100 snapshots of the flow field. This corresponds to 0.05 to 4 shedding cycles. Figure 7 shows the mean difference between the POD modes obtained from these snapshot ensembles compared to the POD modes from all 100 snapshots or four shedding cycles. The first mode, representing the mean flow, is reaching close to zero error for every integer number of cycles. It can also be seen that the mean flow error reaches a maximum for snapshot ensembles containing 1.5, 2.5 and further multiples plus half shedding cycles. These maxima decrease in amplitude with increasing number of shedding cycles. While the Kármán shedding modes show the same trend of decreasing error maxima with increasing number of

shedding cycles, they feature a periodicity of twice that of the mean flow mode. For all modes, using a snapshot ensemble of less than one shedding cycle leads to a large increase in mode error. From the error plots in Figure 7, we conclude that exactly one shedding cycle is the smallest possible snapshot ensemble that will yield spatial POD modes comparable to those obtained from a large number of identical shedding cycles. This can be compared to Nyquist's theorem that states that at least two samples per shedding cycle are needed to avoid aliasing problems. It can also be observed that the error minima at integer shedding cycles are very small, demonstrating the importance of selecting the snapshot ensemble to be exactly one shedding cycle in length. Inspecting the spatial distribution of the mean flow mode, shown in Figure 8, for a very short snapshot ensemble compared to a snapshot ensemble comprising exactly one shedding cycle, it can be seen that the short snapshot ensemble results in a mean flow mode that is not symmetric around the x axis, which is what would be expected from a large snapshot ensemble (which looks like the one shown in Figure 8 top right). The snapshot ensemble consisting of exactly one shedding cycle, however, results in a perfectly symmetric mean flow. Inspecting the 1st von Kármán shedding mode shown in Figure 8, one can observe the same effect of a small ensemble of a non-integer number of shedding cycles leading to an asymmetric mode distribution. This investigation into the effect of snapshot ensemble length demonstrates the possibility of selecting snapshot ensembles of integer number of shedding cycles in length in order to obtain the same spatial POD modes that would be obtained from snapshot ensembles that are many shedding cycles in length. For time periodic data sets this finding can be used to minimize the computational effort by minimizing the snapshot ensemble size. More importantly, however, for transient data sets which slowly change on a time scale much larger than a shedding cycle, one can obtain spatial POD modes for each individual shedding cycle and thus track the change in spatial modes over time. However, the steep increase in POD modal error for non-integer numbers of shedding cycle snapshot ensembles poses a problem for real life application of this short term POD decomposition. In order to use a snapshot ensemble of exactly one shedding cycle, a data set relatively finely resolved in time is needed. Additionally, an effective method of isolating exactly one shedding cycle is required. If either of these requirements is not met, a steep increase in error of the POD mode is encountered.

In summary, by applying POD decomposition to snapshot ensembles of varying length, an integer numbers of shedding cycles is needed in order to obtain spatial POD modes that are identical to those obtained from snapshot ensembles that are many cycles in length. Snapshot ensembles

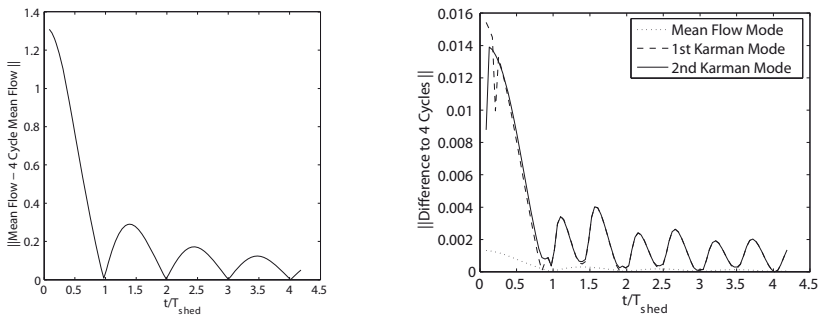


Figure 7. Average difference between Mean Flow Mode and the first two von Kármán Modes calculated from different fractions of a shedding cycle to mean flow calculated using all four shedding cycles

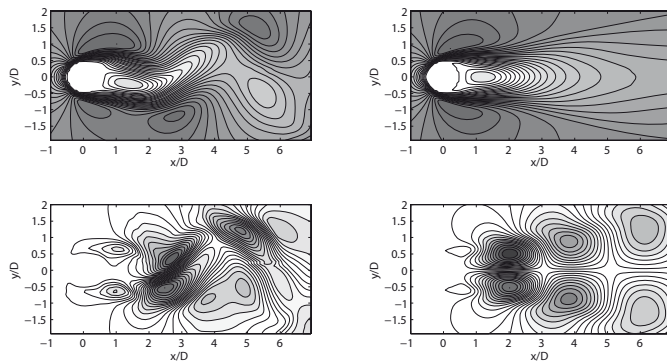


Figure 8. Mean Flow Modes (Top) and 1st Kármán Modes (Bottom) calculated from 4% of a shedding cycle (left) and 100% of a shedding cycle (right). Flow from left to right

that are non-integer multiples of shedding cycles lead to distorted POD modes. No useful POD modes could be obtained for snapshot ensembles that are less than one shedding cycle in length.

Gillies (1995) and Siegel et al. (2005) have shown that for time periodic flows, modes identical to those obtained from snapshot ensembles containing a large number of shedding cycles can be obtained using snapshot ensembles of small integer number of cycles, down to a minimum of one shedding cycle. Siegel et al. (2005) demonstrate that the difference between a spatial mode obtained from integer numbers of shedding cycles is minimal compared to a POD decomposition obtained from a large number (in the limit infinite) number of shedding cycles. Similar behaviour is observed in a fast Fourier transformation (FFT). While in an FFT the error due to non-integer numbers of cycles can be alleviated using windowing functions, this approach does not appear to work for POD decompositions (Siegel et al., 2005). Siegel et al. (2005) refer to POD of only a single oscillation cycle as short time POD or SPOD, due to its similarity to procedures like Short Time Fourier decomposition. SPOD allows for a decomposition of time evolving flow fields with some approximate periodicity into (k) individual events of exactly one cycle of the dominant frequency,

$$u^{(k)}(x, y, t) = \sum_{i=1}^I a_i^{(k)} \phi_i^{(k)}(x, y). \quad (2)$$

The result is a collection of K cycles in individual bins. Note that these bins may contain a different number of samples in time, or span slightly varying time intervals as the period of a cycle changes. However, since SPOD yields K bins of spatial POD modes that are valid for one individual cycle of a transient flow change, it is not as low dimensional as one would wish: The result of SPOD is one entire mode set for each period of the flow. It should also be noted that modes obtained from an individual cycle are a priori not orthogonal to modes from other cycles. In fact, if the data is completely periodic, the modes obtained from different bins are identical if the number of snapshots is constant per cycle.

3.2 Double POD - DPOD

Building on the resulting spatial modes of a SPOD decomposition, one could conceive the following mode construction procedure: if the modes in two consecutive cycles vary only slightly, it should be possible to obtain a representation of the modes of the second cycle as the corresponding mode of the first cycle plus a small shift. This procedure, borne from the aforementioned mean flow mode or shift mode idea, can be formalized by

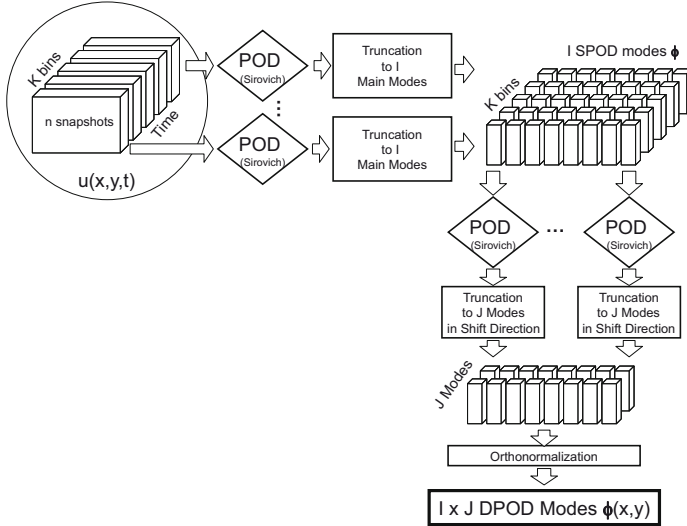


Figure 9. Flowchart of DPOD decomposition process.

realizing that mode i of all bins (k) from the SPOD procedure can be viewed as the input to a second POD (the bins now act similar to time above) as shown in

$$u^{(k)}(x, y) = \sum_{j=1}^J w_{ij}^{(k)} \Phi_{ij}(x, y) \quad (3)$$

This leads again to an optimal representation of all SPOD main modes i . Equation 4 summarizes the Double POD (DPOD) decomposition of the velocity vector field u :

$$u(x, y, t) = \sum_{i=1}^I \sum_{j=1}^J a_{ij}(t) \Phi_{ij}(x, y) \quad (4)$$

This DPOD formulation takes the concept of the shift mode one step further: we can now develop a shift mode, even a series of higher order shift modes, for all main modes i by applying the POD procedure to the

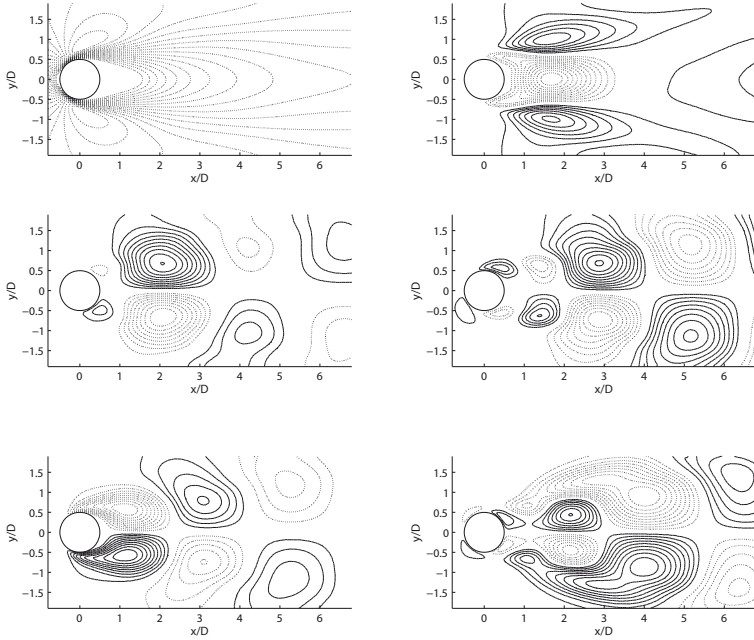


Figure 10. Transient forced DPOD spatial mode set using one shift mode for each main mode, the first 3×2 DPOD modes are shown. Iso-contours of streamwise velocity are shown, solid lines are positive, dashed lines negative.

POD mode sets. The resulting mode ensemble in its untruncated form has as many main modes I as there were snapshots in the smallest SPOD bin, and as many shift modes J as there were bins. It can then be truncated in both i and j , leading to a mode ensemble that is $I_M \times J_M$ in size. We will thus refer to the size of the truncated DPOD mode sets by indicating the truncation indices $I_M \times J_M$ in the following. A pictorial representation of the DPOD procedure is given in Figure 9.

Starting in the top left corner, the data is split into K bins and each bin is used as an input data set for its individual POD procedure. The resulting SPOD modes are then collected across the bins and POD is applied again to obtain the shift modes. The resulting Eigenfunctions can be truncated in both I and J in the same way as a regular POD decomposition. After orthonormalization, the decomposition is again optimal in the sense of POD. In the limit of $J = 1$, the original POD decomposition is recovered. While

the different modes distinguished by the index i remain the main modes described above, the index j identifies the transient changes of these main modes: For $J > 1$, the energy optimality of the POD decomposition in that direction leads to modes that are the optimum decomposition of a given main mode as it evolves throughout a transient data set. If $J = 2$, then modes $\phi_{1,1}$ and $\phi_{1,2}$ are similar to the mean flow and its shift mode or mean flow mode as described by Noack et al. (2003) and Siegel et al. (2003), respectively. Thus the modes with indices $j > 1$ can be referred to as first, second and higher order shift modes that allow the POD mode ensemble to adjust for changes in the spatial modes. We will refer to all of these additional modes obtained by the DPOD decomposition as shift modes, since they modify a given main mode to match a new flow state due to either a recirculation zone length or formation length change. This may be due to effects of forcing, a different Reynolds number, feedback or open loop control or similar events. Thus, in the truncated DPOD mode ensemble for each main mode, one or more shift modes may be retained based on inspection of energy content or spatial structure of the mode.

In Figure 10, a set of DPOD modes is shown that covers both the unforced time periodic vortex shedding state of the circular cylinder wake, as well as the low amplitude forced flow within the lock-in region. This mode ensemble will thus cover not just the limit cycle, but also the influence of forcing onto the vortex shedding process. The corresponding mode amplitudes contain the entire dynamics of the flow, and can thus be used to derive a set of equations describing the global flow dynamics for these flow states. In the following chapter, this is achieved using a system identification technique.

4 Artificial neural network system identification to develop a numerical plant model

With the DPOD spatial mode basis, developed in the previous section, covering a range of both Reynolds numbers and forcing conditions, the entire time dependent global dynamic behaviour of the flow is captured in the corresponding mode amplitudes. Thus, the next goal is to develop a set of equations describing the dynamic behaviour of these mode amplitudes. These equations are needed both for development of control algorithms, as well as for testing of these controllers. Traditionally, Galerkin projections of various types have been used to project the mode amplitudes onto the Navier Stokes equations. However, this approach has led to a variety of problems which are discussed both in the introduction and the following section, leading to the use of a different modelling approach as described in

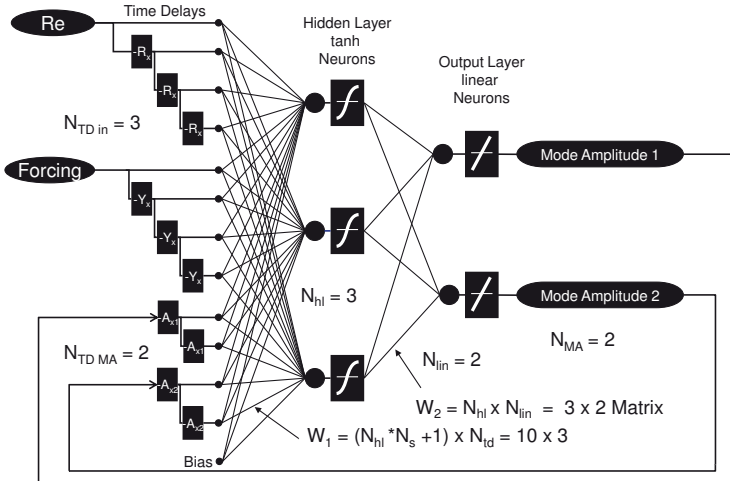


Figure 11. Example ANN-ARX system identification network topology. The model displays a two-layer (tanh and linear), 3 neuron, 2 mode output, 12 input neural network. The periodic sampling rates R_x , Y_x , A_x , account for the number of time delays between sampled data points. Refer to table 1 for actual time delays and number of inputs for the 2×3 DPOD-ANN-ARX model.

the following sections.

In an alternative approach to assuring model stability, the ARX (Auto Regressive eXternal input) dynamic model structure, which is very widely used in the system identification community, is incorporated. A salient feature of the ARX predictor is that it is inherently stable even if the dynamic system to be modelled is unstable. This characteristic of ARX models often lends itself to successful modelling of unstable processes (Nelles, 2001). While system identification for a circular cylinder wake is demonstrate here, the nonlinearity of this flow is typical for a wide range of flow fields of technical interest, and thus this approach is applicable to other fluid dynamic modeling problems as well. The mathematical decription of the linear ARX system indentification is as follows:

$$a(t) = q^{-d} \frac{B(q^{-1})}{D(q^{-1})} f(t) + \frac{1}{D(q^{-1})} e(t) \quad (5)$$

where $a(t)$ is the state vector representing the POD mode amplitudes $a_i(t)$ shown Equation 4. $f(t)$ describes the external input, which in the current effort is the vertical displacement of the cylinder and $e(t)$ is the white noise vector. For the above case, B and D are matrix polynomials in q^{-1} . The time delay operator is defined as

$$q^{-d}a(t) = a(t - d) \quad (6)$$

where d is a multiple of the sampling period. The parameter matrix, θ , and the regression vector, $\phi(t)$, are respectively defined as

$$\theta = [d_{ij} b_{ij}]^T \quad (7)$$

$$\phi = [a(t - 1), \dots, a(t - n), f(t - d), \dots, f(t - d - m)]^T \quad (8)$$

As can be seen in Equation 8, the vector $\phi(t)$ is comprised of past states and past inputs. The ARX predictor (Ljung, 1999) may then be written as

$$\hat{a}(t|\theta) = q^{-d}B(q^{-1})f(t) + [1 - D(q^{-1})]a(t) = \phi^T(t)\theta \quad (9)$$

Equation 9 represents an algebraic relationship between the prediction, given on the left hand side, and past inputs and states, summarized by $\phi(t)$. The parameter matrix, θ , is determined during the estimation process. The main advantage of the ARX predictor is that it is always stable, even when the dynamic plant (the flow field in this case) being estimated is unstable. This feature is of utmost importance when modelling an unstable system such as the absolutely unstable cylinder wake flow.

The main drawback of this approach is that it is limited to modelling of linear systems which, as described above, is insufficient for modelling of unstable limit cycles. A general representation of nonlinear system identification, based on a hybrid ANN-ARX approach (Norgaard et al., 2003), may be written as:

$$a(t|\theta) = g[\phi(t), \theta] + e(t), \quad (10)$$

where θ is the matrix containing the weights of the ANN that are estimated by a back propagation algorithm using a training data set (Norgaard et al., 2003), and g is the nonlinear mapping realized by the feed-forward structure of the ANN.

The ANN-ARX predictor can then be expressed as

$$\hat{a}(t|\theta) = g[\phi(t), \theta], \quad (11)$$

The ANN-ARX algorithms used in this effort are a modification of the toolbox developed by Norgaard et al. (2003). We performed three main modifications to the toolbox. The first extends the toolbox for use in simulations, as opposed to one step prediction, of MIMO (multi-input, multi-output) systems. Secondly, the implementation of the time tapped delay system allows for the periodic sampling rate of inputs to the network. This helps to decrease network training times and also extends the time history of the inputs while keeping the number of inputs low. Thirdly, the network was decoupled, meaning the modes could be trained separately for individual mode amplitudes, and compiled to one large network at the end. This allowed for greater flexibility in training each individual mode. Although this resulted in much larger, more complex final network, simulation times are negligible when compared to training times. A schematic representation of the feed-forward ANN-ARX network topology is presented in Figure 11. After the DPOD mode amplitudes were obtained from the CFD data as described in the previous section, a single hidden layer ANN-ARX architecture is selected. The training set comprised input-output data obtained from CFD simulations. The model is validated for off-design cases and if the estimation error is unacceptable, then the ANN architecture is modified. This cycle was repeated until estimation errors were acceptable for all off-design cases.

The ANN-ARX predictor is inherently stable because, although the modelling approach is nonlinear, the algebraic relationship between the prediction and past states and inputs is preserved. This is extremely important when dealing with nonlinear systems represented by PDEs like the Navier Stokes equations, since the stability problems are more severe than in linear systems. The ANN-ARX approach is an ideal choice when the system to be modelled is deterministic and the signal to noise ratio (SNR) of the data is good (Norgaard et al., 2003).

The choice of the specific artificial neural network (ANN) architecture was based on three main design criteria. The first concerns the number of hidden layers. This was selected as one, i.e. a single hidden layer, since it is the simplest form that allows for a universal approximator (Cybenko, 1989) and its effectiveness for system identification problems has been shown by Norgaard et al. (2003). The second decision concerns the number of nodes. If the number of nodes in the hidden layer is small, the resulting error is unacceptable. As the number of nodes is increased, the error is reduced at the cost of computational complexity until a number of nodes is reached beyond which no further improvement in error is observed. The third design criterion is the choice of the network inputs time histories and delays. Larger sampling periods (more data inputs) allow for a more dynamical based

network. Networks with larger time histories are more accurate because of their ability to predict future outputs based on a better knowledge of the past. The trade off is that training time is greatly increased with larger input vectors. The time tapped delay technique allows for a much broader sampling period while keeping the number of inputs low, thus improving the training speed. For example, instead of using every single past delay input for a certain period of time, the time tapped delay can be set to 2 and the network will skip every other data point, thus reducing the number of inputs by 50% while maintaining the same total length of the sampling history. The time tapped delays for the Reynolds number input (Re), actuator input (Y) and previous mode amplitudes ($A \times n$) are presented in Table 1. Figure 11 represents a simple example of an ANN-ARX model.

Input	Number of past inputs or outputs to neural net	Delay between inputs	Total time history
Reynolds number	1	R_x	10
Actuator position	4	Y_x	2
Mode 1,1	1	$A_{x1,1}$	1
Mode 2,1	3	$A_{x2,1}$	8
Mode 3,1	3	$A_{x3,1}$	8
Mode 1,2	1	$A_{x1,2}$	1
Mode 2,2	1	$A_{x2,2}$	12
Mode 3,2	1	$A_{x3,2}$	12

Table 1. Network topology representing inputs and their time delays of the 3×2 DPOD-ANN-ARX model. The number of past inputs per signal and the delay which is the number of time steps in between sampling periods (R_x, Y_x, A_{xn}) are shown. The product of these two is the total time history.

Initially, neural networks were designed and trained for the 6 mode (3×2 DPOD) model. However, training times were very excessive, leading to the realization that new techniques needed to be established. The network was split into smaller sub-networks which could be trained much more efficiently. These smaller networks can be superimposed and compiled into a larger, overall network. Thus, many parameters exist in the design of ANN-ARX models. The resulting ANN has the following features:

4.1 Input Layer

Two network input parameters, the normalized cylinder displacement and the Reynolds number. In addition to these readings, in order to obtain a

strong representation of the dynamics of the system, the input layer includes past outputs of the 6 modes and past inputs for each of the two inputs (Reynolds number and cylinder displacement) as described in the toolbox developed by Norgaard et al. (2003), Table 1 presents the actual input / output time delays. The number of time delays for the past outputs was about one shedding cycle. On the other hand, the number of time delays for the past inputs was about half of a shedding cycle. The selection of time delays for past inputs/outputs was based on a sensitivity study which investigated the trade-off between estimation accuracy and network complexity. Therefore, the final configuration of the input layer chosen includes six mode outputs, namely, the first three main DPOD modes $i = 1, j = 1; i = 2, j = 1; i = 3, j = 1$ and their shift modes with a maximum of twenty-four time delays; two inputs, the Reynolds number and the actuator position for a maximum of 10 time delays; and one bias input. The total number of inputs to the net is therefore 15 (see Table 1).

4.2 Hidden Layer

One hidden layer consisting of 130 neurons. The activation function in the hidden layer neurons is the tanh function. A single bias input has been added to the output from the hidden layer.

4.3 Output Layer

6 outputs, namely, the 6 states representing the DPOD mode amplitudes of the 3×2 DPOD spatial mode basis. The output neurons have linear activation functions.

4.4 Weighing Matrices

The weighing matrix between the input layer and the hidden layer is of size (130×16) , whereas the weighing matrix between the hidden layer and the output layer is of size (6×131) . These weighing matrices are initialized randomly before training.

4.5 Training the ANN

Back propagation, based on the Levenberg-Marquardt algorithm, was used to train the ANN using the toolbox of Norgaard et al. (2003). The training data (21,790 time steps) is comprised of output from multiple CFD simulations. The first portion of the training consists of open loop forced transient simulations comprising design cases 1, 4, 5, 8, 10. The forcing of case 10 is repeated four times, with different starting phase angles of

0, 90, 180 and 270 degrees between the shedding of the vortices in the wake and the actuation signal at the start of the actuation. This leads to very different transient adjustment in the wake, which was found to be an essential feature for network training. During these open loop actuation simulations, the Reynolds number is fixed at $Re = 100$. The second portion of the training data set is comprised of transients in Reynolds number, while the actuation is kept at zero level. The Reynolds number transient training data include ramping from $Re = 100$ to $Re = 40$, from $Re = 100$ to $Re = 60$ and from $Re = 100$ to $Re = 160$.

Along with the 3×2 DPOD mode amplitudes, the Reynolds number as well as the cylinder displacement were provided as inputs to the network. The training procedure converged after 50 to 150 iterations depending on which mode was being trained.

As a measure of the model quality, Figure 12 shows both the mode amplitudes derived from the CFD simulation data, as well as the output of the ANN-ARX model. This is one of the open loop forced cases that were not used for model development, and the fact that there is good agreement between model and simulation data is an indication that this model is usable for controller development. In Siegel et al. (2008) more detailed comparison and error estimates for this model can be found.

5 Feedback control wake stabilization results

The amplitudes of the DPOD modes were used both for feedback, as described in the following section, as well as for evaluation of the effectiveness of the controller. In order to be used for feedback control, the amplitudes of the modes that were used for feedback were estimated using a least square fit of the sensor data onto the spatial POD modes. The sensor locations, developed by Siegel et al. (2005), were chosen to evenly cover the entire portion of the flow of interest for control, using 35 flow sensors.

The controller development is based on a Proportional and Differential (PD) controller. As mentioned earlier, active forcing is introduced into the wake by displacement of the cylinder in the flow normal direction as shown schematically in Figure 1. The full state estimator provides estimates for all 15 DPOD amplitudes which may then be used as input to a full state controller. Since a neural network model of the flow has been developed, several indirect control designs can be employed. The indirect design is very flexible and applicable in real-time for the problem at hand. Relevant concepts include approximate pole placement, minimum variance and predictive control. The approximation is based on instantaneous linearization, which is a popular method for control of ANN models. Following the effort

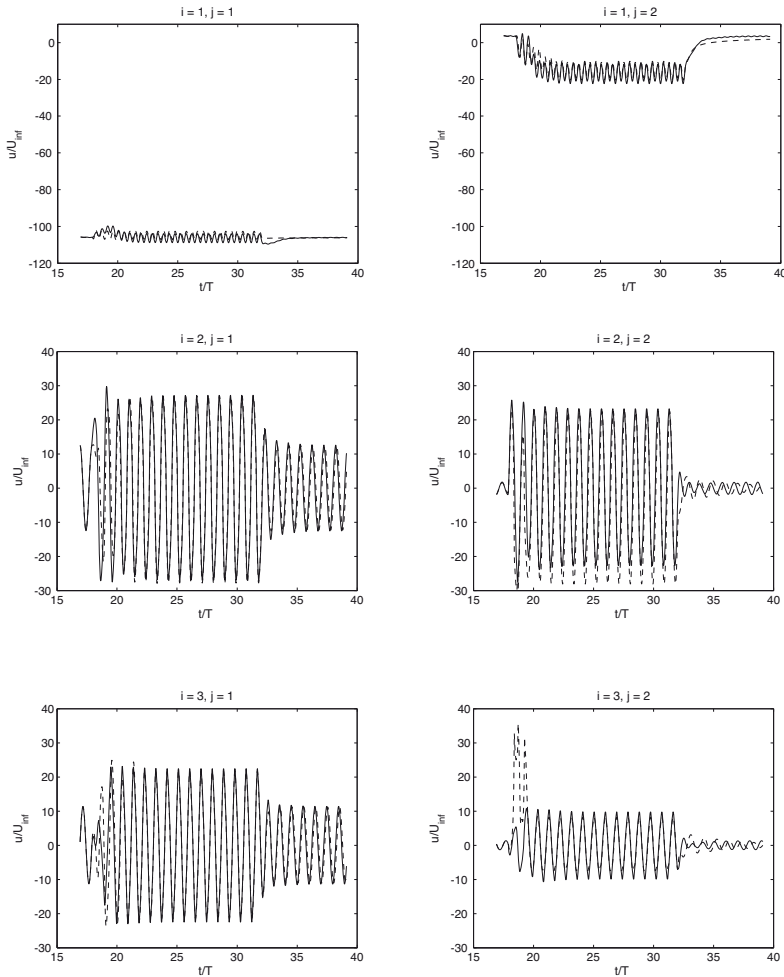


Figure 12. Mode amplitudes a_{ij} of the first 6 DPOD modes for the off-design case 3, forcing with $f/f_0 = 1.05$ and A/D = 0.30. This data was not used for training of the ANN-ARX network. Lines, mode amplitudes from the CFD simulation; dot-dash lines, mode amplitude estimation from the ANN-ARX model.

by Siegel et al. (2005), a similar PD feedback control strategy is employed for the single mode feedback control law:

$$y_{cyl} = K_{p21}a_{21} + K_{d21}\frac{da_{21}}{dt}, \quad (12)$$

Instead of directly specifying the K_p and K_d gains, these can be expressed in terms of an overall gain K and a phase advance ϕ for mode i :

$$K_{pi} = K_i \cos(\phi_i), \quad (13)$$

$$K_{di} = \frac{K_i \sin(\phi_i)}{2\pi f}. \quad (14)$$

with f being the natural vortex shedding frequency. Equation 12 refers to the single-input closed-loop control based on feedback using an estimate of a_{21} . We will refer to this control law as a Single Input Single Output (SISO) controller in the following, since only one mode is used for determining the feedback response. The control law may be modified to enable dual-input from two modes, and a simple example is adding proportional control of the shift mode of the von Kármán shedding mode, a_{22} . This control law which essentially constitutes a multi input single output (MISO) PD controller is:

$$y_{cyl} = K_{p21}a_{21} + K_{d21}\frac{da_{21}}{dt} + K_{p22}a_{22} + K_{d22}\frac{da_{22}}{dt} \quad (15)$$

where it is possible to substitute the proportional and differential gains in the same fashion as for the SISO controller, with an overall amplitude gain K and a phase shift ϕ for each of the two modes independently.

5.1 Single Mode Feedback - SISO

This section presents the results both of single mode feedback, as well as multi mode feedback based on the DPOD model. The effectiveness of the single mode feedback was evaluated by keeping the overall gain K constant at $K = 5 \cdot 10^{-4}$, while varying the phase ϕ of the feedback from 0 to 360 degrees. The controller amplitude was chosen such that the overall cylinder displacement would remain within the range of validity of model, i.e. limiting the maximum displacement $y/D < 0.3$. The resulting closed loop lift and drag force are shown in Figure 13. It can be seen that for the range of feedback phases between about 30 and 250 degrees the drag is increased compared to the unforced flow field, while between 250 and 30 degrees a decrease in drag is observed. The normalized lift and drag forces for both $\phi = 90^\circ$ (drag increase) and $\phi = 330^\circ$ (drag decrease) is shown in Figure 14. In both cases the wake is stabilized at its new state, with about

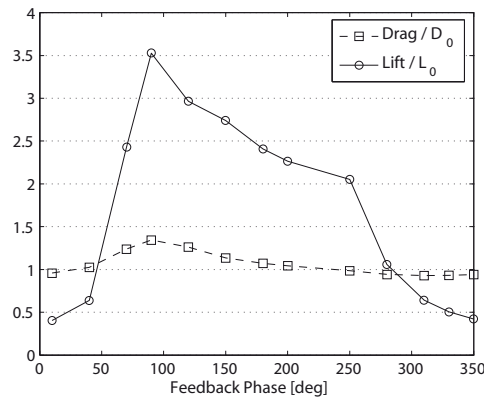


Figure 13. Non-dimensional RMS amplitudes of the stabilized lift and drag forces using single mode feedback (L_0 and D_0 are the RMS amplitudes of the unforced flow's lift and drag force, respectively).

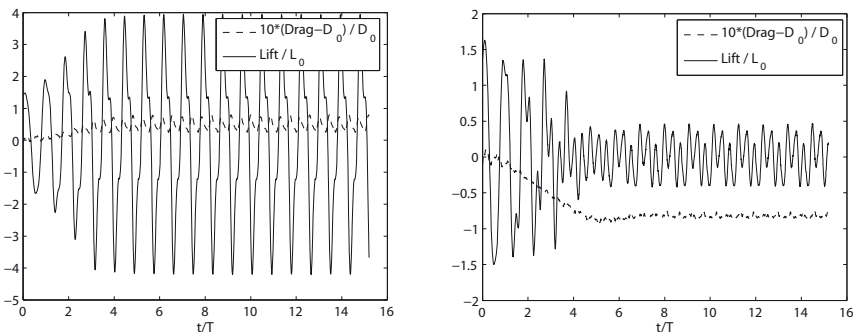


Figure 14. Lift and drag for feedback using $\phi_{21} = 90^\circ$ (left) and $\phi_{21} = 330^\circ$ (right), SISO feedback

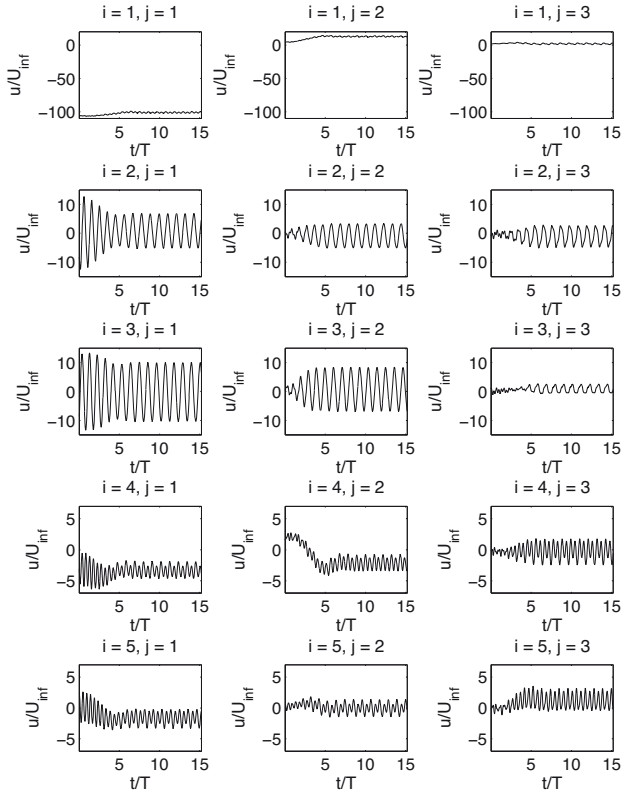


Figure 15. DPOD Mode Amplitudes for SISO feedback of a_{21} . $K_{21} = 5 \cdot 10^{-4}$, $\phi_{21} = 330^\circ$. The controller is activated at $t/T = 0$.

10% drag decrease for the feedback phase of 330 degrees. The DPOD mode amplitudes for this case are shown in Figure 15. The amplitude of the mode used for feedback, a_{21} , is greatly reduced by the effect of feedback control. However, the amplitude of its first shift mode, a_{22} , is actually increased as a result of feedback. This observation led to the implementation of multi mode feedback, where both a_{21} and a_{22} are fed back with individual gains K and phases ϕ .

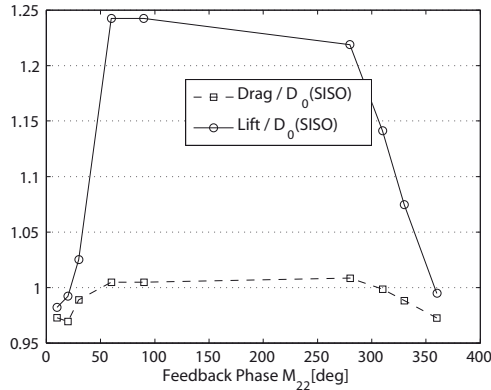


Figure 16. MISO feedback of a_{21} and a_{22} , with $K_{21} = K_{22} = 5 \cdot 10^{-4}$ and a fixed phase $\phi_{21} = 330^\circ$. The feedback phase of a_{22} is varied, and the resulting lift and drag forces are normalized by those of the SISO feedback of a_{21} with $K_{21} = K_{22} = 5 \cdot 10^{-4}$ and $\phi_{21} = 330^\circ$

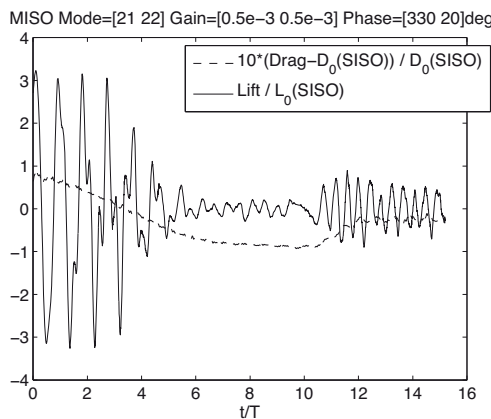


Figure 17. MISO feedback of a_{21} and a_{22} , with $K_{21}=K_{22} = 5 \cdot 10^{-4}$ and phases $\phi_{21} = 330^\circ$ and $\phi_{22} = 20^\circ$.

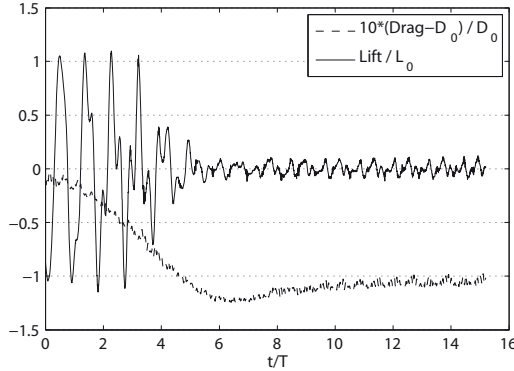


Figure 18. MISO feedback of a_{21} and a_{22} , with $K_{21} = 5 \cdot 10^{-4}$, $K_{22} = 3.75 \cdot 10^{-4}$ and phases $\phi_{21} = 330^\circ$ and $\phi_{22} = 20^\circ$.

5.2 Two Mode Feedback - MISO

Figure 16 shows a parameter scan varying the feedback phase of a_{22} , while keeping all other gains as well as the phase of a_{21} constant. Again a range of detrimental phases exists, where the drag is compared to the new baseline of SISO feedback with 330 degrees phase. However, for a small range of feedback phases between $\phi = 310^\circ$ and $\phi = 50^\circ$, a further reduction in drag beyond SISO control can be observed. This demonstrates the benefit of using MISO control over SISO control. However, the detailed analysis of the MISO control run that led to the largest reduction in drag. Figure 17 shows that there is a lack of stabilization in this type of feedback control. While the drag initially is decreased by more than 6% compared to the SISO level, it is followed by an increase in drag to a stable level about 3% below the baseline. Analyzing the DPOD mode amplitudes for this case (not shown), it turns out that feedback of a_{22} actually destabilizes a_{21} later in the simulation.

With some fine tuning of the gains applied to a_{21} and a_{22} , the flow field can be stabilized using multi mode feedback. Figure 18 and Figures 19 demonstrate this, where the flow is stabilized at a lift fluctuation level more than one order of magnitude smaller than the unforced flow, and at a reduction of drag of more than 10%. However, in this situation the fluctuating amplitude of the shift modes is increased as well not just for the von Kármán modes, but also for the higher harmonic modes. From a flow physics perspective, this indicates a shift of the vortex formation further downstream as the controller becomes effective in stabilizing the near wake.

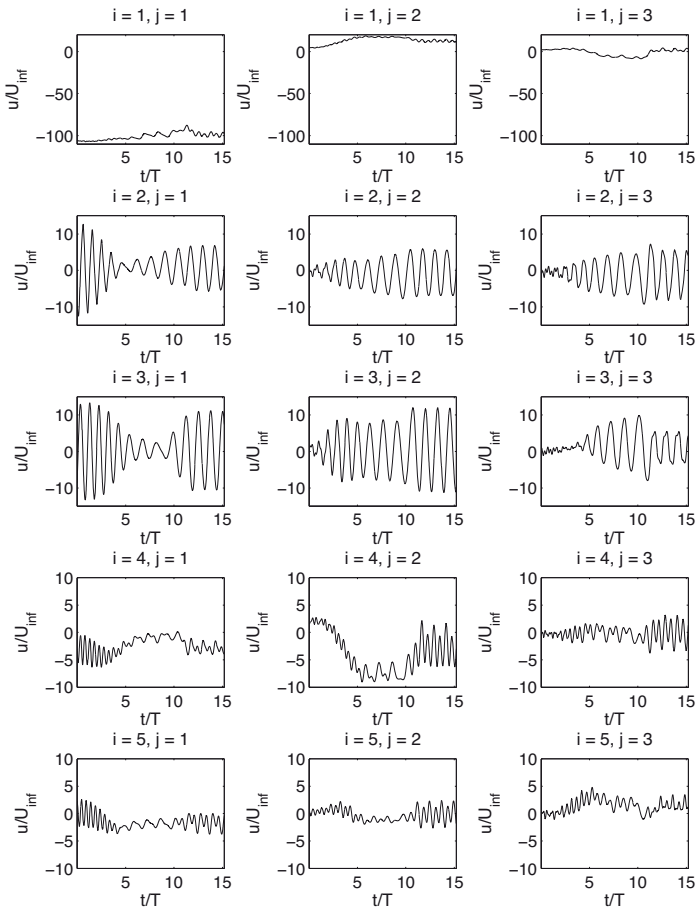


Figure 19. DPOD Mode Amplitudes for MISO feedback. $K_{21} = K_{22} = 5 \cdot 10^{-4}$, $\phi_{21} = 330^\circ$, $\phi_{22} = 20^\circ$. The controller is activated at $t/T = 0$.

At the same time, the actuation which remains at the cylinder location becomes less and less efficient in controlling this remaining vortex shedding far away from the cylinder. We demonstrate CFD results of feedback control of the two-dimensional circular cylinder at $Re = 100$ based on one or two modes of a DPOD model developed using transient data truncated to 15 Modes. The objective of the control is stabilization of the von Kármán vortex street. Two different controllers are investigated, a Single Input Single Output (SISO) feeding back the von Kármán mode amplitude, and a Multi Input Single Output controller (MISO), feeding back the von Kármán mode and its shift mode. The SISO control leads to a reduction of the overall drag force of about 10% for the best combination of proportional and differential gains. It is worth mentioning that all investigated SISO feedback gains lead to a stabilized wake, which is not the case for simpler POD models that do not include transient data. However, while the amplitude of the von Kármán mode used for feedback is reduced, as a result of feedback, the amplitude of its shift mode is increased. This observation leads to the use of the MISO controller, where in addition to PD feedback with the best combination of gains found in SISO control the shift mode, a_{21} , is used for feedback as well. The MIMO control is able to further reduce the drag compared to the best SISO case temporarily by more than 6 percent, in its stabilized state by more than 3 percent. The investigated MISO gains so far did lead to some partial destabilization of the flow. The overall conclusion of this investigation when compared to the results achieved by Siegel et al. (2005) is that a DPOD model is able to greatly increase the stability and performance of the feedback controller. This demonstrates the importance of obtaining a model that covers the entire parameter range that the feedback controller covers, rather than a point design type of a model that is only valid for the time periodic uncontrolled flow. While demonstrated for the benchmark case of a laminar circular cylinder wake, we expect similar trend for more complex flows which we will investigate in the future.

6 Key enablers / strategy

The focus of this chapter - as well as of this book in general - is on low dimensional modeling, as opposed to control theory. This already demonstrates that the main enabling strategy lies in understanding and properly representing the flow field to be controlled, rather than conceiving elaborate control strategies. In the previous chapter, simple linear controllers were sufficient to stabilize the flow, while at the same time a nonlinear model was necessary to properly and accurately represent the flow physics. Thus,

the first and foremost enabling strategy lies in accurate, global and non-linear modeling of the flow physics, without which the results shown here cannot be achieved.

The main idea behind the modeling approach introduced in this chapter is a shift away from the Galerkin projection of data onto the Navier Stokes equations. While this might seem counter intuitive, it resolves many physical and mathematical problems. As any data obtained from either numerical simulations or experiments does not constitute an exact solution of these equations, the projection process will always be fraught with peril. For this reason, a more generic approach will have less numerical problems in that aspect. However, as has been shown above, one can still obtain a global model of complex flow fields, and in addition, establish fairly accurate input-output type relationships between actuation, Reynolds number or other parameters governing the flow. These input-output relationships are very difficult to include in a Galerkin projection due to the limits on boundary conditions that can be implemented. The quality of these relationships is what ultimately determines the useability of a model for feedback flow control controller development and testing.

6.1 Integration of Experiments, Modelling and Simulation

Beyond the use of simulation data for the purpose of deriving a numerical model, simulations offer many advantages at the start of a feedback flow control investigation. Typically, it is faster to develop a numerical grid for a given flow geometry than for example, to design and build a wind or water tunnel model with actuation capabilities. This makes simulations a great tool for development of the actual experiment, for example, to investigate the performance of an actuation system without having to actually build it (Siegel et al., 2009). On the other hand, once a physical model for the flow field of interest is available, performing parameter studies covering different actuation conditions and Reynolds numbers is done much faster in an experiment than in a simulation. Especially for high Reynolds number turbulent flow fields, the computation cost is often in the order of thousands of CPU hours for investigating a single forcing condition, whereas a parameter study of actuation parameters can be achieved in a wind tunnel in a matter of seconds to minutes. This makes experiments a preferred option to determine for example the lock-in range for a flow under investigation. However, experiments will always only yield very limited amounts of flow data, as even with state of the art PIV measurement techniques at most a two dimensional slice of the flow can be measured simultaneously. This circumstance makes experimental data of limited use when a global model of

the flow field is to be developed. Therefore, a typical work flow would use the experiment to determine particular flow conditions of interest, which then can be investigated in greater detail using CFD simulations.

6.2 Applicability to Other Flow Fields

In this chapter, the applicability of the DPOD-ANN-ARX modeling approach to the benchmark problem of a two dimensional circular cylinder wake at a Reynolds number of 100 has been shown. In this section, the applicability of the method to more complex flows is discussed. While the aim is to avoid unsupported speculation as much as possible, it is beneficial to share some insight that has been gained into this issue from preliminary investigations.

The circular cylinder wake at $Re = 100$ is not an entirely two dimensional flow, as has been shown in literature for example by Williamson (1996) for the unforced wake, or by Seidel et al. (2006) for the feedback controlled wake. The latter investigation demonstrates how feedback control can cause a spanwise phase shift of the vortex shedding until the two dimensional control approach is only effective in a narrow vicinity of the two-dimensional sensing plane that was used in this investigation. This poses the question if the DPOD-ANN-ARX approach can be extended to three dimensional flows. The answer is an unequivocal yes, since there is no limitation of the DPOD decomposition to two dimensions as was pointed out in a previous section.

As the Reynolds number of the circular cylinder flow is increased beyond $Re \approx 180$, secondary instabilities lead to the formation of streamwise vortices (Williamson, 1996). While modeling these flow features will lead to additional DPOD modes, there is no apparent obstacle in applying POD based modeling to flow fields that contain both two and three-dimensional features, as has been shown in the hybrid approach proposed by Ma and Karniadakis (2002). Extending their work to use the DPOD procedure introduced here, one could derive dynamic models capturing the effect of actuation and/or changes in Reynolds number for these types of flows. This could then be used to develop feedback controllers to suppress the von Kármán type vortex shedding. Based on results of Cohen et al. (2003), where feedback of the von Kármán mode only suppressed higher order harmonic modes, there is hope that suppressing the Kármán vortex street might eliminate the streamwise vortices as well, since they are the result of a secondary instability that only exists in the presence of the von Kármán vortex shedding. If this conjecture is in fact true remains to be shown.

At yet higher Reynolds numbers ($Re > 3900$), the von Kármán vortices break down into smaller and smaller turbulent structures that ultimately dissipate their energy into heat. These smaller structures can be quite energetic and thus more and more POD modes will need to be retained in order to model a given fraction of the overall flow energy content. This behaviour of POD is due to the energy optimality of the procedure, and DPOD inherits this property from POD. As a result, both POD and DPOD models will become inherently large for flows that break down into turbulence. If the purpose of model development is feedback control, however, there may not be a need to model the small turbulent eddies in order to capture the dynamic behaviour of the large vortical structures. In the case of the circular cylinder wake, one may only be interested in modeling the von Kármán type shedding for the reasons outlined in the previous paragraph. Thus, an approach where the flow data is subjected to either spatial or temporal filtering may be applied, as has been pursued by the authors with good preliminary results (Siegel et al., 2007). The approach proposed in this work removes small scale turbulent structures from the data used for POD mode derivation while retaining the large structures (i.e. von Kármán vortices) that are of interest for feedback controller development. This approach is much like the use of spatial filtering in large eddy simulations employed in state of the art CFD solvers. With this approach, one introduces a choice of how much or how little of the smaller structures are included in the model. Thus, one can derive models with relatively few modes that nonetheless capture the dynamics of the flow that is relevant for feedback control. The DPOD-ANN-ARX approach is particularly suited to this type of modeling, since no turbulence model is required: As the entire model development is data driven and does not include projection onto the Navier Stokes equations, no closure equations are needed. The approach can thus be used as introduced here, with the only added step being a filtering process before the derivation of the DPOD modes. However, more detailed investigations into filter kernel type, size and cutoff wave length are needed.

Another approach to modeling of turbulent flows, in this case a turbulent shear layer, has been demonstrated by Seidel et al. (2009). Instead of removing small vortex structures by spatial or temporal filtering, the enabling approach to modeling of the large vortex structures shown there is based on using a different flow quantity altogether. By deriving POD spatial modes from the density field, all small vortical structures are removed from the flow field while preserving the large shear layer vortices of interest. While the DPOD-ANN-ARX approach allows for the development of a global dynamic model based on density, a traditional Galerkin projection is not suitable for deriving such a model that does not even attempt to describe the velocity

field.

An important question pertaining to the application of DPOD to flow fields with multiple equally dominant frequencies is the selection of appropriate bin boundaries. In the present investigation, higher frequency content was small in amplitude compared to the fundamental frequency of the vortex shedding, and thus the lift force with a simple peak detection algorithm was suitable for bin segmentation. If several dominant frequencies coexist, there are different possible approaches to segmentation. Using a phase accurate temporal notch filter as a preprocessing step, one may recover the fundamental frequency and determine bin boundaries in the same fashion as introduced in this work. Alternatively, it is conceivable to use open loop forcing to elevate the amplitude of one of the dominant frequencies at a time, thus allowing for discovery of the spatial flow features related to each frequency using multiple SPOD procedures, one for each of the frequencies of interest. Having outlined possible pathways of how the DPOD-ANN-ARX approach may be applied and extended to flow fields at Reynolds number of technical interest, the question remains how applicable this approach may be to other flow geometries. We consider the circular cylinder wake a prototype flow featuring separated free shear layers that develop instabilities leading to vortex shedding. As such, there are similarities to many other flows of technical interest that contain free shear layers, featuring both simpler and more complex flow behavior. Examples that have been investigated by the authors are the separated flow over a stalled airfoil, free shear layers formed behind a D shaped cylinder, and the wake of an axisymmetric bluff body. While we yet have to apply the DPOD-ANN-ARX approach to these flows, we consider them promising candidates since they all feature large coherent structures resulting from instabilities. The interaction of these instabilities and their resulting structures with flow actuators of various kinds is of great technical interest, both for open and closed loop flow control. DPOD-ANN-ARX models may be used to investigate this interaction in a structured and quantitative fashion.

In summary, this approach was developed with the intent to use the resulting models for controller development in order to achieve control of the formation of large structures caused by flow instabilities. From a technical perspective, these types of flows are the most promising candidates for feedback flow control since instabilities can be influenced with relatively small amounts of actuation energy. This is important in the context of the power limitations inherent in state of the art of dynamic flow actuators. Our approach supports flow fields with many different modes present, and can also accommodate multiple actuator interaction allowing for MIMO control. We did not intend it to be used for random turbulent flows, but find that there

are many technical applications where this limitation is of no importance.

Bibliography

- K. Cohen, S.G. Siegel, T. McLaughlin, and E. Gillies. Feedback control of a cylinder wake low-dimensional model. *AIAA Journal*, 41(7):1389–1391, 2003.
- G. V. Cybenko. Approximation by superpositions of a sigmoidal function. *Maths Control Signals Syst*, Vol. 2:303–314, 1989.
- E. A. Gillies. *Low-dimensional characterization and control of non-linear wake flows*. PhD thesis, Faculty of Engineering, University of Glasgow, UK, 1995.
- H. Oertel. Wakes behind blunt bodies. *Ann. Rev. Fluid Mech.*, 22:539–564, 1990.
- L. Ljung. *System Identification Theory for the User*. Prentice-Hall, 2nd edition, 1999.
- X. Ma and G. Karniadakis. A low-dimensional model for simulating three-dimensional cylinder flow. *J. Fluid Mech.*, 458:181–190, 2002.
- C. Min and H. Choi. Suboptimal feedback control of vortex shedding at low Reynolds numbers. *J. Fluid Mech.*, 401:123–156, 1999.
- O. Nelles. *Nonlinear System Identification*. Springer, 2001.
- B. R. Noack, K. Afanasiev, M. Morzynski, G. Tadmor, and F. Thiele. A hierarchy of low-dimensional models for the transient and post-transient cylinder wake. *J. Fluid Mech.*, 497:335–363, 2003.
- M. Norgaard, O. Ravn, N. K Poulsen, and L. K Hansen. *Neural Networks for Modelling and Control of Dynamic Systems*. Springer Series Advanced Textbooks in Control and Signal Processing, Springer, London, 2003.
- J. Seidel, S.G. Siegel, K. Cohen, V. Becker, and T. McLaughlin. Simulations of three dimensional feedback control of a circular cylinder wake. *AIAA Paper 2006-1404*, 2006.
- J. Seidel, S.G. Siegel, and T. McLaughlin. Computational investigation of aero-optical distortions in a free shear layer. *AIAA Paper 2009-0362*, 2009.
- S. Siegel, K. Cohen, and T. McLaughlin. Feedback control of a circular cylinder wake in experiment and simulation (invited). *AIAA Paper 2003-3569*, 2003.
- S. G. Siegel, K. Cohen, J. Seidel, and T. McLaughlin. Short time proper orthogonal decomposition for state estimation of transient flow fields. *AIAA Paper 2005-0296*, 2005.
- S.G. Siegel, S. Aradag, J. Seidel, K. Cohen, and T. McLaughlin. Low dimensional POD based estimation of a 3D turbulent separated flow. *AIAA Paper 2007-0112*, 2007.

- S.G. Siegel, J. Seidel, C. Fagley, D.M. Luchtenburg, K. Cohen, and T. McLaughlin. Low-dimensional modelling of a transient cylinder wake using double proper orthogonal decomposition. *J. Fluid Mech.*, 610:1–42, 2008.
- S.G. Siegel, J. Seidel, and T. McLaughlin. Experimental study of aero-optical distortions in a free shear layer. *AIAA Paper* 2009-0361, 2009.
- L. Sirovich. Turbulence and the dynamics of coherent structures. Part I: Coherent structures. *Quarterly of Applied Mathematics*, 45(3):561 – 571, 1987.
- C. H. K. Williamson. Vortex dynamics in the cylinder wake. *Ann. Rev. Fluid Mech.*, 28:477–539, 1996.

Optimal Closed-Loop Approaches in Flow Control

Rudibert King

Berlin Institute of Technology ER2-1, Department of Process and Plant Technology, Hardenbergstr. 36a, D-10623 Berlin, Germany

Abstract Different experimentally validated procedures to synthesize closed-loop flow controllers are presented which use the solution of an optimization problem in various ways. The controller synthesis or the control laws itself are based on the knowledge of low dimensional models. These range from Galerkin systems as introduced in other chapters of this volume and identified black-box models to the most simplest process model which only assumes that some kind of extremum exists. Numerous experimental results show the power of extremum seeking control, robust control or model predictive control in closed-loop flow control applications.

1 Introduction

In addition to the methods shown in the chapter by L. Cordier optimal approaches are presented here which do not need the solution of a system of adjoint equations. They focus on the synthesis of closed-loop control systems in contrast to the open-loop nature of the aforementioned Hamiltonian approach. By this, the robustness concerning unavoidable disturbances acting on the fluid flow and model uncertainties entering the control law and existing in every low dimensional model is greatly enhanced. A selection of control concepts is introduced which uses optimization-based steps in different aspects and different levels. In model predictive control a value function considering the future behavior of a process will be minimized either analytically in an unconstrained or numerically in a constrained case. In extremum seeking control and its generalization slope seeking a gradient-based minimization or maximization is exploited which is purely based on online available experimental data. Robust control minimizes an H_∞ -norm to guarantee robust stability, robust performance and to limit the control energy spend.

Some of the methods introduced rely on low dimensional models which are set up to describe the input-output behavior of a process in a black-box

manner. Here, the central task in model identification is the solution of an optimization problem to determine model parameters. Galerkin systems, which are considered as well, may need a calibration of model parameters which again goes back to an optimization problem. Hence, optimization methods are abounded in closed-loop control engineering science in general and in particular in closed-loop flow control.

Although fluid flow systems as described by the Navier-Stokes equation are inherently nonlinear much can be achieved in closed-loop control exploiting linear concepts. This partly stems from the fact that in some applications a controller tries to keep the process near an operating point around which a linearization gives a good approximation. Moreover, the basic reason for applying closed-loop control is tackling uncertainty. If no disturbances would act on a process and the process could be completely described by a model (which can be solved online) open-loop concept would suffice. As these assumptions will never be valid outside a simulation study closed-loop control is a must and uncertainties coming from only roughly approximating linear model can be tolerated. For this, § 2 recapitulates some basic facts about linear systems and system identification. Different controllers are introduced next starting with the most simple extremum seeking-type of approach in § 3.1. Linear models are then used in the synthesis of robust and state space controllers in § 3.2. For model-based estimation techniques necessary to implement such controllers the reader is referred to the chapter of G. Tadmor in this volume. Finally, different nonlinear controllers, especially model predictive controllers (MPC) are considered in § 3.3. Here the Galerkin system of the flow around a circular cylinder which is used in other chapters as well will be used inside a MPC scheme. Various real-life applications are given in § 4 before a comparison is presented in § 5.

A special word is necessary concerning nomenclature in flow control as two formerly distinct disciplines, namely fluid mechanics and control engineering, meet. As a consequence different important variables in the respective disciplines are given the same symbols. Most notably \mathbf{u} , i.e. $\mathbf{u} = \mathbf{u}(t)$, relates to the (scalar) control input / plant input / manipulated variable in control whereas it represents the time- and space-dependent velocity fluctuation $u = u(t, x, y, z)$ in fluid mechanics. As this chapter would be almost the only one in this book using its own nomenclature and to help the reader who is new both to low dimensional modeling **and** control an adaptation of the control engineering nomenclature to the fluid mechanics notation would make sense. However, many good arguments exist as well for using the control engineering notation in this chapter. To name just a few: 1) Somebody working in an interdisciplinary field must know and understand the

meaning of double used symbols from the actual context. 2) This chapter cannot give a comprehensive introduction in control. Therefore, the reader has to be referred to control engineering textbooks and articles quite often which use the standard control engineering notation anyway. 3) This chapter summarizes some of the ideas which had been followed by the authors' group in the last 10 years. Not all details will be repeated here. Instead, references are made to different articles where details can be found given again in control notation. 4) Only very few symbols will be redefined here in comparison to the rest of the book and will be typeset in a teletype style which should help reading. A comparison of some important variables is given in Table 1 to help cross-references.

symbol	control	symbol	fluid mechanics
s	Laplace variable	s	sensor signal
u	plant input, $u \in \mathbb{R}^1$	u	streamwise
\mathbf{u}	plant input, $\mathbf{u} \in \mathbb{R}^p$	\mathbf{u}	velocity fluctuation
\mathbf{x}	state, $\mathbf{x} \in \mathbb{R}^n$	\mathbf{x}	$= (u, v, w)$ velocity field
y	plant output, $y \in \mathbb{R}^1$	y	unit vector
\mathbf{y}	plant output, $\mathbf{y} \in \mathbb{R}^q$		wall-normal coordinate

Table 1. Important symbols in control and fluid mechanics. Control related symbols will be used in this chapter.

2 Linear systems

Irrespective whether the flow around a bluff body, an aircraft wing, see Fig. 1, in a turbomachine or the flow and combustion in a burner is considered, an input-output point of view can be adopted for several approaches in control. In all cases the system involved reacts to some flow control inputs, such as periodic blowing or suction, acoustic actuation, magneto-hydrodynamic forces, by an application-defined output signal. For the bluff body and the wing it could be drag and/or lift. In turbomachines the noise emitted might be the interesting output signal in one application and the pressure increase over a compression stage in another. The focus in a burner study might be on pressure fluctuations from a thermo-acoustic instability or on the NO_x -production. Hence, the output has to be newly defined for every new application.

In the single-input-single-output (SISO) case with a scalar input $u(t)$ and a scalar output $y(t)$, a linear system can be described by an n -th order

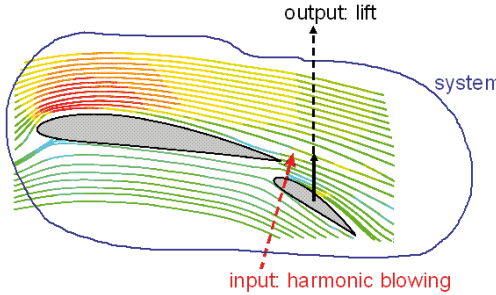


Figure 1. Wing with flap viewed as a system. The size of a harmonic blowing at the leading edge of the flap is chosen as the input and the lift force as output signal.

ordinary linear differential equation with constant coefficients

$$\begin{aligned} a_n^{(n)} y(t) &+ a_{n-1}^{(n-1)} y(t) + \cdots + a_1 \dot{y}(t) + a_0 y(t) \\ &= b_0 u(t) + b_1 \dot{u}(t) + \cdots + b_m^{(m)} u(t) \end{aligned} \quad (1)$$

and appropriate initial conditions. For implementation of algorithms in real-time and for system identification a discrete-time version of this equation is more appropriate. The most simplest although not best version starting from Eq. (1) would be an approximation of the differential operators by difference operators, such as

$$\dot{y}(t)|_{t=kT} \approx \frac{y(kT) - y((k-1)T)}{T} = \frac{y_k - y_{k-1}}{T} \quad (2)$$

with sampling period T yielding

$$y_k + \alpha_1 y_{k-1} + \cdots + \alpha_n y_{k-n} = \beta_1 u_k + \beta_2 u_{k-1} + \cdots + \beta_m u_{k-m+1} \quad . \quad (3)$$

As a result, the output at the (actual) time k can be expressed as a function of old outputs and old and actuals controls u_{k-j} , $j = 0, 1, \dots, m-1$.

$$y_k = -\alpha_1 y_{k-1} - \cdots - \alpha_n y_{k-n} + \beta_1 u_k + \beta_2 u_{k-1} + \cdots + \beta_m u_{k-m+1} \quad . \quad (4)$$

For systems from fluid mechanics an additionally pure time-delay d , i.e. $T_0 = dT$, is very often observed between input and output leading to

$$y_k = -\alpha_1 y_{k-1} - \cdots - \alpha_n y_{k-n} + \beta_1 u_{k-d} + \beta_2 u_{k-d-1} + \cdots + \beta_m u_{k-d-m+1} \quad . \quad (5)$$

Hence, the actual input does not directly influence the actual output. This time-delay is affected by the convection time between the location of the actuator and the position of the sensor.

Introducing the shift operator q with $y_{k-1} = q^{-1}y_k$ and $y_{k-\nu} = q^{-\nu}y_k$ gives

$$(1 + \alpha_1 q^{-1} + \cdots + \alpha_n q^{-n})y_k = (1 + \beta_1 q^{-1} + \cdots + \beta_m q^{-m+1})q^{-d}u_k$$

which can be formally solved for the actual output

$$y_k = \frac{1 + \alpha_1 q^{-1} + \cdots + \alpha_n q^{-n}}{1 + \beta_1 q^{-1} + \cdots + \beta_m q^{-m+1}} q^{-d} u_k = G(q^{-1}) u_k . \quad (6)$$

Hence, the output can be written as the input signal u_k times a discrete time transfer function $G(q^{-1})$.

The same input-output behavior is described by a state-space model which is given first in the continuous time domain

$$\begin{aligned} \dot{x}(t) &= A'x(t) + b'u(t) , \quad x(t_0) = x_0 \\ y(t) &= c^T x(t) + du(t) \end{aligned} \quad (7)$$

with¹ $x \in \mathbb{R}^n$. For the simple example

$$\overset{(3)}{\dot{y}}(t) + 3\overset{(2)}{\dot{y}}(t) + 2\ddot{y}(t) + 5y(t) = 2u(t)$$

chose for example $x_1 \equiv y$, $x_2 \equiv \dot{y}$ and $x_3 \equiv \ddot{y}$ to obtain

$$\begin{aligned} \dot{x}(t) &= \begin{pmatrix} 0 & 1 & 0 \\ 0 & 0 & 1 \\ -5 & -2 & -3 \end{pmatrix} x(t) + \begin{pmatrix} 0 \\ 0 \\ 1 \end{pmatrix} u(t) \\ y(t) &= (1 \ 0 \ 0)x(t) \end{aligned} \quad (9)$$

with appropriate initial conditions. If derivatives of the input appear on the right hand side of Eq. (1), more involved transformations are necessary, see standard control engineering textbooks or refer to standard control engineering software such as MATLAB®.

In the multiple-input-multiple-output (MIMO) case the state-space model reads without a time-delay between input and output

$$\dot{x}(t) = A'x(t) + B'u \quad (10)$$

$$y = Cx(t) + Du . \quad (11)$$

¹ A' , B' , b' refer to a continuous-time model while A , B , b are used in a discrete-time version below. The transpose of a matrix is denoted by T .

In this case an exact discrete-time description is obtained for systems with piecewise constant inputs, i.e. $\mathbf{u} = \mathbf{u}(k) = \text{const.}$ for $kT \leq t < (k+1)T$, using the general solution of Eq. (10)

$$\mathbf{x}(t) = e^{\mathbf{A}'(t-t_0)}\mathbf{x}_0 + \int_{t_0}^t e^{\mathbf{A}'(t-\tau)}\mathbf{B}'\mathbf{u}(\tau)d\tau \quad . \quad (12)$$

Then, the discrete version reads

$$\mathbf{x}(k+1) = \mathbf{Ax}(k) + \mathbf{Bu}(k) \quad (13)$$

$$\mathbf{y}(k) = \mathbf{Cx}(k) + \mathbf{Du}(k) \quad (14)$$

with

$$\mathbf{A} = e^{\mathbf{A}'T} , \quad \mathbf{B} = \int_0^T e^{\mathbf{A}'(T-\tau)}\mathbf{B}'d\tau = (\mathbf{A}')^{-1}(\mathbf{A} - \mathbf{I})\mathbf{B}'$$

and an identity matrix \mathbf{I} of appropriate dimension.

Stability of the open-loop system is given when all eigenvalues of \mathbf{A}' or \mathbf{A} stay in the open left half complex plane in the time continuous case or in the unit circle in the discrete-time case, respectively.

Classical control is often done in the Laplace or frequency domain. Applying the Laplace transformation with complex variable $\mathbf{s} = \sigma + j\omega$

$$L\{\mathbf{f}(t)\} = \mathbf{f}((\mathbf{s})) = \int_0^\infty \mathbf{f}(t)e^{-(\mathbf{s})t}dt \quad (15)$$

to Eq. (1) for vanishing initial conditions yields

$$\mathbf{y}(\mathbf{s}) = G(\mathbf{s})\mathbf{u}(\mathbf{s}) \quad (16)$$

with the transfer function $G(\mathbf{s})$ which is now given in the Laplace domain

$$G(\mathbf{s}) = \frac{b_0 + b_1\mathbf{s} + \dots + b_ms^m}{a_0 + a_1\mathbf{s} + \dots + a_n\mathbf{s}^n} \quad .$$

Hence, the input-output behavior of a dynamic system can be described by a simple multiplication of the transformed input $\mathbf{u}(\mathbf{s})$ by the transfer function $G(\mathbf{s})$. This will ease the treatment of the closed loop, see below.

Applying the Laplace transformation to Eq. (7) and Eq. (8) shows the relation between the two sorts of system descriptions

$$G(\mathbf{s}) = \mathbf{c}^T(\mathbf{s}\mathbf{I} - \mathbf{A}')^{-1}\mathbf{b}' + d \quad . \quad (17)$$

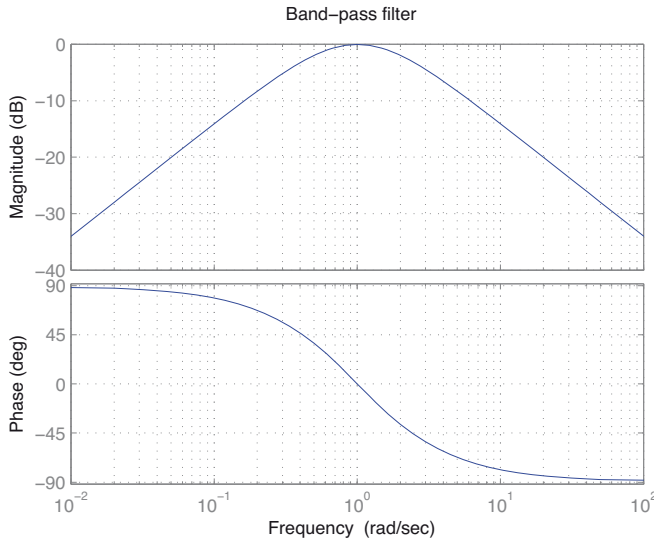


Figure 2. Bode plot of a band-pass filter of second order $G(j\omega) = Kj\omega\omega_2/[(j\omega + \omega_1)(j\omega + \omega_2)]$ with $\omega_1 = \omega_2 = 10\text{rad/sec}$ and $K = 2$. Observe that for $\omega = \omega_1 = \omega_2$ no damping and no phase shift occurs. However, slower and faster components are damped.

If $s = j\omega$, the frequency response $G(j\omega)$ is obtained which gives a frequency-dependent gain, $|G(j\omega)|$, and phase-shift, $\arg\{G(j\omega)\}$, between input and output for sinusoidal inputs. A graphical representation is given in the Bode plot in which $20\log_{10}|G(j\omega)|$, the so-called magnitude, and the phase $\arg\{G(j\omega)\}$ are plotted as a function of $\omega = 2\pi f$, cf. Fig. 2.

If the linear model is not obtained through linearization of a given nonlinear model of the flow, for example a Galerkin system, it has to be identified from experiments in a black-box approach. In this case the real flow around a setup is replaced, conceptually, by a black-box for which only an input-output relation has to be determined. Such a black-box will present in the high-lift device introduced above only the relation between the actuation amplitude $u(t)$ and the mean lift. As the mean lift cannot be measured on a real wing a surrogate output variable can be defined in this example. It is well known, cf. Becker et al. (2007), that a relation exists between the lift and a pressure difference along the suction side of the wing or flap. This signal will be defined as the surrogate output. No information about

flow velocity, vorticity, etc. will be contained in such model. Nor will it be able to predict for example the drag imposed on the wing. However, this model will suffice completely if only the lift has to be controlled.

To identify a black-box model, the system is excited by appropriate input signals $u(t)$. Most often step-wise changes in the control input are used, see Fig. 4. These are easy to analyze. However, a theoretical study shows that the information content in the answer to a step input is limited in the frequency range. A better input signal is a pseudo random binary signal (PRBS) which consists of many step-ups and step-downs in an almost random fashion, see Ljung (1999) for more details and Fig. 3.

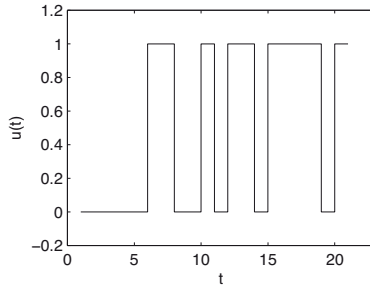


Figure 3. PRBS-signal with unity amplitude. Fourier analysis shows that this signal contains many discrete frequencies. It is used instead of a white noise process as an excitation signal in identification. A white noise would possess a continuum of all frequencies with the same intensity which would be good for identification of an unknown system. However, as its energy content would be infinity, a white noise process does not exist and is replaced by this deterministic sequence.

The coefficients α_i , β_j and the dimensions and time-delay n , m and d , respectively, of the time-discrete model Eq. (5) are then estimated in general by the solution of the following optimization problem

$$\min_{\alpha_i, \beta_j, n, m, d} \sum_{l_e} \sum_k w_{l_e k} (y_k^{(l_e)} - \tilde{y}_k^{(l_e)})^2$$

where l_e runs over all experiments used, k indicates individual instants and $w_{l_e k}$ are weights to improve identification. The real measurements are denoted by y . Measurements calculated by the model, \tilde{y} , depend on the design variables of the optimization problem, i.e. $\tilde{y}_k = \tilde{y}_k(\alpha_i, \beta_j, n, m, d)$. Care has to be taken concerning unavoidable noise present in every experiment. Only

if the influence of this noise is included in a correct fashion in identification as it is done for example in so-called prediction-error-methods, good parameter estimates are obtained. More information about system identification can be found in Ljung (1999).

After a time-discrete model is identified it can be transformed to a continuous-time form, either to a transfer function $G(s)$ or to the state-space matrices A' , B' , C and D . The latter can be identified directly as well by subspace methods, see Ljung (1999). Fig. 4 shows a comparison between measured data and a simulation of an identified model for a step-wise excitation. In this case a rather simple flow, namely the flow over a backward-facing step, is considered. Despite its simplicity, a rich dynamic can be observed in the right panel of Fig. 4 on the one hand. On the other hand an input-output view with a restriction to the reattachment length as the output signal shows a very simple input-output behavior which suffice for controller synthesis.

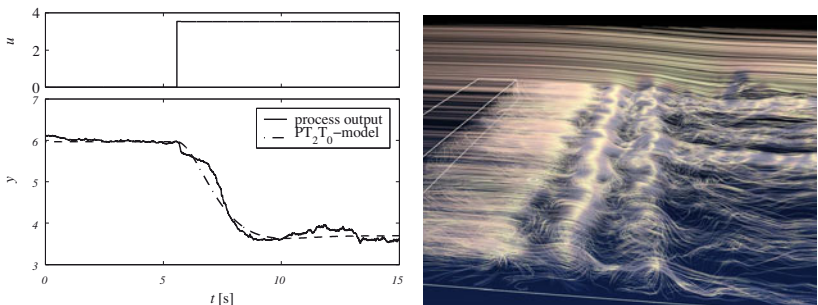


Figure 4. Left: Comparison of the measured reattachment length behind a backward-facing step (solid line) and a fit with a second order model with time delay, $G(s) = b_0/(1 + a_1 s + a_2 s^2)e^{-dT s}$, see King et al. (2004). Right: Illuminated streamlines of a LES of the flow around a backward-facing step from Weinkauf et al. (2003)

3 Methods in closed-loop control

Various methods of control are introduced starting with model-free approaches in § 3.1. A recapitulation of classical linear control and robust control is summarized in § 3.2. Finally, § 3.3 gives details about nonlinear approaches including model predictive control.

3.1 Extremum and slope seeking control

The following section is adopted from Henning et al. (2008) where more information can be found. Extremum- and slope-seeking feedback controllers are adaptive gradient-based, model-independent feedback schemes that search for optimal actuation parameters (Garwon et al., 2003; Beaudoin et al., 2006; Henning et al., 2007). The only (extremely low dimensional) modeling concept used, though not explicitly stated in the sense of an equation, is the knowledge that some kind of extremum in an input-output map exists. An extremum-seeking control can be used to find areas around distinct minima or maxima in the steady-state map of a plant. As many flow applications are rather characterized by a plateau-type map, slope-seeking is better suited. Here, the system is driven to a preset reference slope which is representative for a value just below the plateau. Two different configurations are used in this study, a single SISO and a multiple SISO slope-seeking controller. Extensions to the truly multiple input case can be found in King et al. (2006). As the extremum-seeking controller forms the basis for the slope-seeking variant, the former is reviewed first.

Classical extremum seeking control Extremum-seeking control is an effectively model-free method for the control of nonlinear plants characterised by an output extremum in the steady-state (Morosanov, 1957; Krstic and Wang, 2000; Ariyur and Krstic, 2003) and for linear or nonlinear plants for which the output is defined as the norm of the difference between a reference value $r(t)$ and the plant output y , e.g. $(r(t) - y(t))^2$ in a SISO-setting. Typical examples in flow control are the maximizations of the lift of a wing or the mixing in a burner, the minimizations of the drag of a car or the noise emitted in a turbomachine. As every minimisation problem can easily be transformed into a maximisation problem, all explanations are given for the latter case. The Fig. 5 shows the structure of the basic SISO extremum-seeking control loop. Here, the process is described by both, it's steady-state map $y_s = f(u_s)$ and it's dynamical model for ease of further discussion.

The idea of this gradient based method is an on-line optimisation of the average value, u_s , of the control input $u(t)$ such that the average of the output equals the maximum steady-state value, $y_s = y_s^*$. With extremum-seeking control this can be accomplished without knowing the steady-state input-output map $y_s = f(u_s)$. The controller works as follows: Assume that the initial control input u'_0 , see Fig. 5, which is calculated by some higher level control hierarchy, see below, and a slowly changing part $\Delta u(t)$, i.e. $u'_0 = u_0 + \Delta u(t)$, are superimposed with a sinusoidal signal $a \sin(\omega_{\sin} t)$

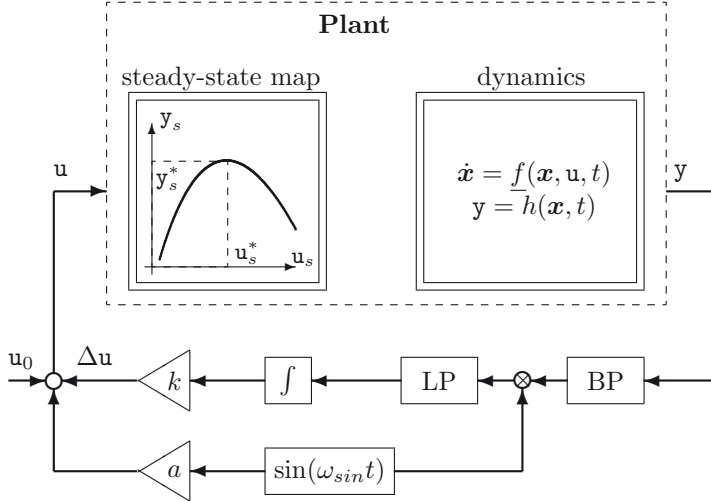


Figure 5. Block diagram of closed-loop extremum-seeking. The BP and LP represent band- and low-pass filters, respectively. Both the steady state map and the nonlinear dynamic system representation are given for the same plant.

which has a small amplitude a .

$$u(t) = u_0 + \Delta u(t) + a \sin(\omega_{\sin} t) \quad (18)$$

If the period of this harmonic perturbation is larger than the largest time constant of the process, the output of the process will also be approximately sinusoidal, centred initially around $y_{s,0} = f(u'_0)$. Likewise, the amplitude will be approximately af' . Hence,

$$y(t) \approx y_s + af' \sin(\omega_{\sin} t) \quad . \quad (19)$$

This output perturbation is analysed in order to detect the slope (gradient) of the input-output map which is used for gradient based optimisation. To do this, the mean value y_s is removed by a band-pass filter (BP), for example of second order²

$$G_{BP}(j\omega) = \frac{j\omega\omega_2}{(j\omega + \omega_1)(j\omega + \omega_2)} \quad , \quad (20)$$

²A high-pass filter was proposed originally. However, for flow control with rather noisy measurements a BP is recommended.

with the lower cut-off frequency ω_1 and the upper cut-off frequency ω_2 , see as well Fig. 2. By application of a BP the output of the filter reads

$$y_{BP}(t) \approx |G_{BP}(j\omega_{sin})| af' \sin(\omega_{sin}t + \varphi_{BP}) . \quad (21)$$

The product $y_P(t)$ of this filtered output and the zero-mean sine signal $\sin(\omega_{sin}t)$ indicates the slope of the unknown map $y_s = f(u_s)$:

$$\begin{aligned} y_P(t) &= \sin(\omega_{sin}t) \left(|G_{BP}(j\omega_{sin})| af' \sin(\omega_{sin}t + \varphi_{BP}) \right) \\ &= |G_{BP}(j\omega_{sin})| af' \times \\ &\times \left(\sin^2(\omega_{sin}t) \cos(\varphi_{BP}) + \sin(\omega_{sin}t) \cos(\omega_{sin}t) \sin(\varphi_{BP}) \right) . \end{aligned} \quad (22)$$

This product leads to a non-zero mean signal obtained with a low-pass filter (LP), see Fig. 5, as long as the maximum is not obtained. If the plant is initially to the left of the maximum, the input and output perturbations are in phase, that is the product will be positive, see as well Fig. 6. An

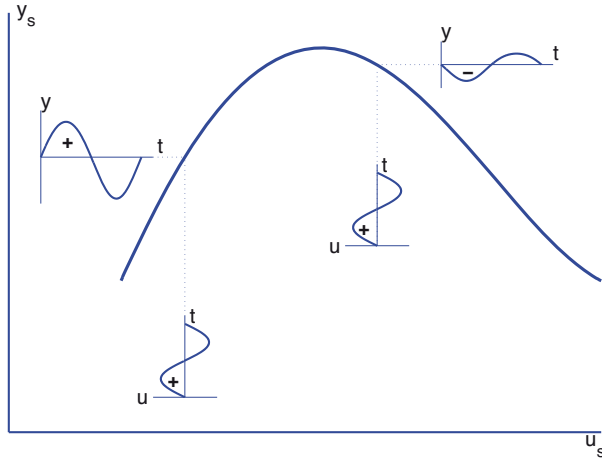


Figure 6. Sketch of a nonlinear static map and quasi-steady state responses when the sinusoidal input u is either on the left or right hand side of the maximum. Only the offset-free part of the output y obtained after the BP is depicted.

anti-phase relation which gives a negative product is an indication that the plant is on the right of the maximum. To see this, approximate the output $y_{LP}(t)$ of the LP by an average calculated for one period $T = 2\pi/\omega_{sin}$, that is

$$\begin{aligned} y_{LP}(t) &\approx \frac{1}{T} \int_0^T y_P(t) dt \\ &= \frac{1}{T} |G_{BP}(j\omega_{sin})| \mathbf{a} f' \frac{T}{2} \cos(\varphi_{BP}) \\ &= \frac{\mathbf{a} f'}{2} \Re\{G_{BP}(j\omega_{sin})\} . \end{aligned} \quad (23)$$

With this information an additional term $\Delta u(t)$, added to $u_0 + \mathbf{a} \sin \omega_{sin} t$, see Eq. (18) and Fig. 5, is calculated by time integration and multiplication by k . As long as the output of the LP is positive, that is the system is on the left side of the maximum, a steadily increasing control input u is obtained. For a negative output of the LP, the opposite is true. The adaptation of u converges to $u = u^*$.

The constant u_0 is set by the user to a value for which a non-zero gradient is expected. If this value is chosen too low, for example, the flow system will not react to the variation of the input signal. Hence, no reliable operation is guaranteed.

The extremum-seeking scheme is an adaptive closed-loop type of control. It guarantees closed-loop stability if designed properly, see Krstic and Wang (2000) and Ariyur and Krstic (2003) for details. The choice of certain design parameters determines the speed of convergence. For the results given below we chose $\omega_{BP} = \omega_1 = \omega_2 = \omega_{sin}$. The LP is not necessary, but it is helpful in filtering out the perturbation after the multiplier. Therefore, the cut-off frequency of the LP should be chosen to $\omega_{LP} \leq \omega_{sin}$. In addition, the adaption gain k needs to be small. If the plant behaviour varies due to uncertainties, the time scale of the perturbation signal has to be slower than the slowest possible plant dynamic. The main advantage of this extremum-seeking control is that no plant model is needed for controller synthesis. However, the control suffers from both, the permanent harmonic input and output perturbations, and the relative slow dynamic behaviour. Therefore, some extensions will be proposed later.

Slope seeking control In flow control, situations are encountered in which the static input-output map does not show a distinct maximum. Instead it is characterised by a plateau-type behaviour as illustrated in Fig. 7. A detached flow over an aircraft wing, to give an example, can be influenced by active flow control such that it reattaches again. At some point,

however, the flow is completely attached. A further increase of the control input will not result in a further increase nor in a decrease of the lift. The extremum-seeking control described above will work correctly in this situation if it starts left of the plateau. However, when the control input is larger than the smallest value necessary to be on top of the plateau, it will not be minimised. Such a waste of control energy can be observed likewise when the system's behaviour - due to a change in operating conditions - will change. In such a case, the plateau-type map might be shifted to the left. The smallest value necessary to be on top of the plateau found for the last operating condition now lays somewhere on the plateau without any gradient information for the controller. To tackle such systems, slope-seeking is considered next.

The slope-seeking is an extension of the extremum-seeking scheme, for details see Ariyur and Krstic (2003). It drives the plant output to a value that corresponds to a reference slope of the steady-state input-output-map:

$$f'_{ref} = \left. \frac{\partial y_s}{\partial u_s} \right|_{ref}. \quad (24)$$

Therefore, according to Eq. (23), a negative reference value

$$r(f'_{ref}) = -\frac{a f'_{ref}}{2} \Re \{G_{BP}(j\omega_{sin})\}, \quad (25)$$

as a function of f'_{ref} is added to the actually detected slope, see Fig. 7. Thus, the apparent extremum is shifted. Since extremum-seeking is a special case of slope-seeking, when the reference slope is zero, designing the filters, the integrator gain, and the sinusoidal perturbation are the same.

Increase of bandwidth Different methods to improve extremum- and slope-seeking control are given in Henning et al. (2008). A very powerful modification to speed-up the closed-loop behavior will be shown in the sequel. In the meantime this approach has been used in turbomachines, in an industrial high-lift design, bluff bodies and burner studies to accelerate settling time by a factor of 3-9.

As in the classical extremum-seeking control we still assume that the harmonic perturbation of the process is slower than the slowest time constant of the process. Hence, the static input-output map is reflected by the behaviour of the output $y(t)$. If the input perturbation a is small enough, the output perturbation should be af' , as already mentioned in Sec. 3.1. The output itself consists of an approximately constant value plus this perturbation, that is

$$y(t) \approx y_s + af' \sin(\omega_{sin}t) .$$

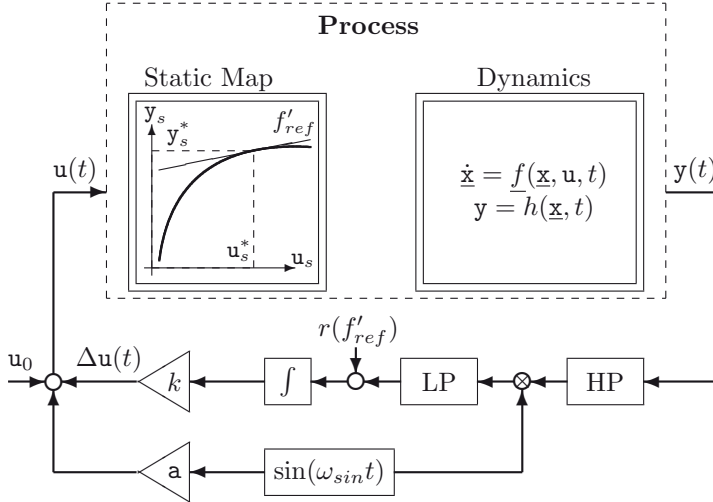


Figure 7. Block diagram of closed-loop slope-seeking.

With Eq. (18)

$$\begin{aligned} y(t) &\approx \underbrace{y_s - f'u_0 - f'\Delta u(t)}_{x_1} + \underbrace{\overbrace{f'}^{x_2} u(t)} \\ &= x_1 + u(t)x_2 . \end{aligned} \quad (26)$$

The idea is to observe these two parameters x_1 and x_2 . A dynamical model for the two parameters reads in discrete time

$$\mathbf{x}(t_{k+1}) = \begin{bmatrix} 1 & 0 \\ 0 & 1 \end{bmatrix} \mathbf{x}(t_k) + \mathbf{w}_k . \quad (27)$$

If Eq. (26) is used as a measurement equation, an observability analysis shows that x_1 and x_2 are not observable. However, when time-shifted input-output pairs $(u(t), y(t))$ and $(u(t-n\Delta t), y(t-n\Delta t))$ are considered, observability is given. With $y_1(t_k) = y(t_k)$ and $y_2(t_k) = y(t_{k-n})$ the measurement equation now reads

$$\mathbf{y}(t_k) = \begin{bmatrix} 1 & u_1 \\ 1 & u_2 \end{bmatrix} \mathbf{x}(t_k) + \mathbf{v}_k \quad (28)$$

with $u_1 = u(t_k)$ and $u_2 = u(t_{k-n})$. The vectors \mathbf{w}_k and \mathbf{v}_k denote Gaussian white noises. An extended Kalman filter (Gelb, 1986) can be used for

real-time estimation of the states. The modification of the slope-seeking control by inclusion of this model-based sensor is shown in Fig. 8. Since the extended Kalman filter estimates the slope $\hat{f}' = \dot{\hat{x}}_2$, the reference slope f'_{ref} is subtracted directly from \hat{f}' .

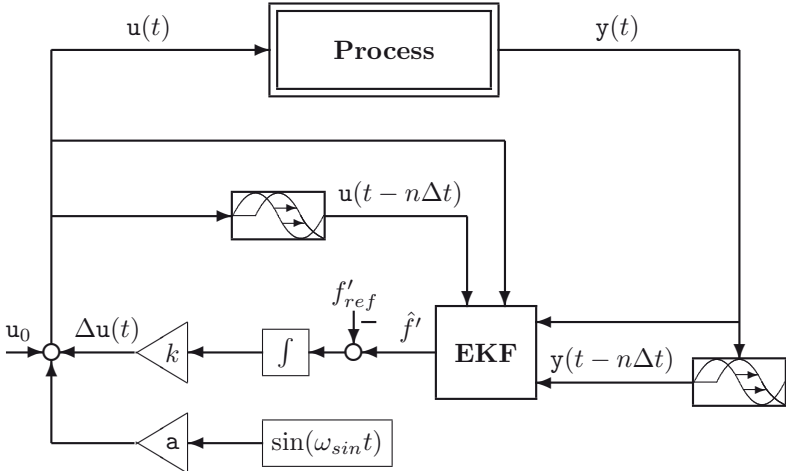


Figure 8. Block diagram of the closed-loop slope-seeking with an extended Kalman filter (EKF) algorithm for fast real-time estimation of the local gradient of the steady-state map.

3.2 Linear and robust control

For linear systems using the Laplace domain it is very easy to describe the output of a closed loop as a function of its inputs, see Fig. 9. For the scalar case the system output $y(s)$ is given by

$$\begin{aligned} y(s) &= \frac{C(s)P(s)}{1 + C(s)P(s)}r(s) - \frac{C(s)P(s)}{1 + C(s)P(s)}m(s) + \frac{G_d(s)}{1 + C(s)P(s)}d(s) \\ &= T(s)r(s) - T(s)m(s) + S(s)d(s) \end{aligned} \quad (29)$$

depending on the transfer functions $C(s)$, $P(s)$ and $G_d(s)$ of the controller, the plant and the disturbance coupling, respectively. Measurement noise is given by m and the other disturbances by d .

In flow control applications the identification of local linear models around an operating point applying different step heights give rise to a family of different models reflecting the nonlinearity of the process. Quite often, a main

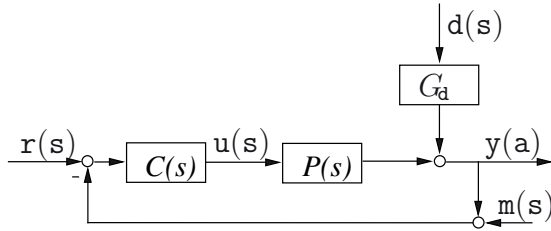


Figure 9. General closed loop with controller $C(s)$, plant $P(s)$, disturbance transfer function $G_d(s)$, reference $r(s)$, disturbances $d(s)$ and $m(s)$ and system output $y(s)$.

difference in these linear models can be seen in the gain of the identified models $P(s)$

$$K = P(s=0) = \frac{b_0}{a_0} .$$

which can be approximated as a function of the step height \hat{u} used, i.e. $K = f(\hat{u})$. Physically, this reflects the situation that for example in the case of the high-lift device the lift force will not continuously increase when the actuation amplitude is increased. At some point the separated flow which is responsible for a reduced lift will completely reattach and any further increase in actuation will not result in any improvement. Hence, the ratio between increase in lift to actuation amplitude will decrease with increasing \hat{u} .

Exploiting this knowledge, the degree of nonlinearity can be reduced by post-multiplying the calculated control signal $u^*(t)$ by the inverse of f . By this, the plant 'seen' by the controller, i.e. the sequence f^{-1} and the real physical plant P , does not behave as nonlinear as the real plant alone, see as well Fig. 10.

The design of the controller $C(s)$ is further simplified when a dynamic feed-forward $C_{ff}(s)$ is added, see Fig. 11. If in the completely linear case with $f(u^*) = u^*$ the product $C_{ff}(s)r(s)$ with reference r and $C_{ff}(s) = P^{-1}(s)$ is realizable, the system output y exactly equals the reference for vanishing disturbances d and m and exactly known plant model. Hence, the closed-loop controller $C(s)$ is only responsible for disturbance rejection in this ideal situation.

From different classical control synthesis methods loop-shaping approaches will be applied here. In a loop-shaping approach a controller $C(s)$ is determined such that in the case without feed-forward filter, see Eq. (29), the

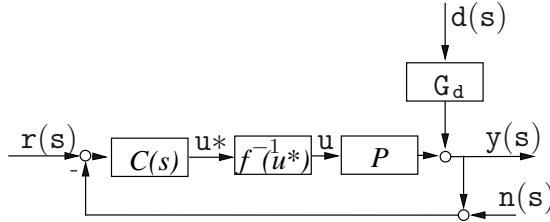


Figure 10. Closed loop with the physical control input u . The control input u^* calculated by the linear controller is nonlinearly transformed through f^{-1} inside the control system to determine u which is sent to the process. With this compensation of a Hammerstein-like nonlinear model the plant output y seen from the controller output u^* looks more linear.

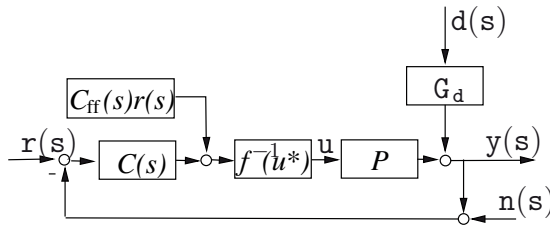


Figure 11. Closed loop with dynamic feed-forward filter.

frequency-dependent gain is $|T(j\omega)| \approx 1$ in the frequency range related to the reference signal r and low in the frequency range of the measurement noise n . Additionally, the gain of the sensitivity $|S(j\omega)|$ should be low to have a sufficient disturbance rejection. Most importantly, the controller must be such that the closed-loop system is asymptotically stable. In such a case the roots of all denominators of the closed-loop transfer functions, cf. Eq. (29), lie in the open left half complex plane. When transforming the transfer functions to the state space, these roots equal the eigenvalues of an appropriate A' matrix. For more information consult standard textbooks. With a feed-forward filter a faster response to set-point changes can be achieved and loop-shaping can concentrate on disturbance rejection.

Although the compensation of a nonlinear gain reduces the degree of nonlinearity, fluid flow systems remain inherently nonlinear. This will be reflected as well in other model parameters a_i , b_j and a variable system order

when different experiments are analyzed. A linear controller synthesized as indicated above will only work well if the system is not driven too far away from a constant setpoint around which the linearization is valid and if the control inputs are not high. Especially stability will only be guaranteed if this assumption holds. To account for nonlinear effects nonlinear methods, cf. Khalil (2002), can be used. They will be addressed later in this chapter in conjunction with Galerkin systems. Another approach is linear robust control. In robust control the uncertainty of a linear model is explicitly accounted for. Very good introductions to robust control are given in Skogestad and Postlethwaite (1996); Maciejowski (1994); Morari and Zafriou (1989). A simple way to build a robust controller is to identify a family of linear models from different experiments related to different input signals or setpoints first as mentioned above, see Fig. 12.

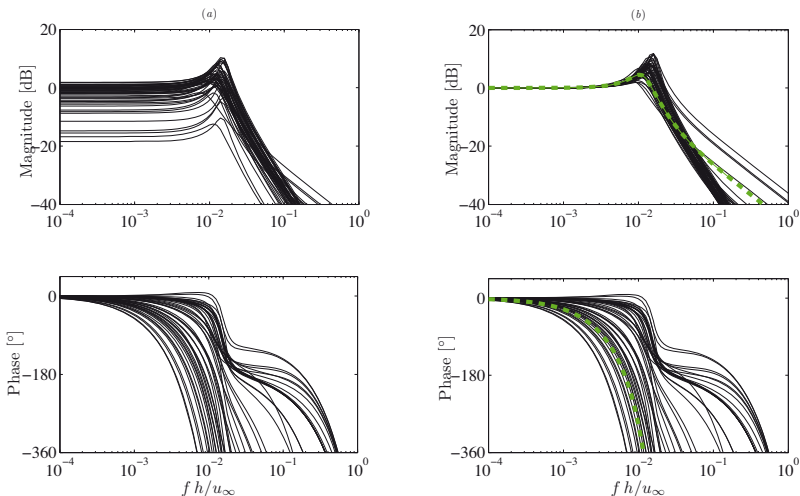


Figure 12. Left: Identified family of black-box models for the flow past a 2D bluff body for $\text{Re}=46000$ from Henning (2008). Right: The same model family with a compensated static gain and a nominal model depicted by a broken line. All plots are given as a function of a normalized frequency, i.e. as a function of the Strouhal number.

Now a controller is synthesized, loosely speaking, which is able to stabilize all models of the model family in the closed loop. Moreover, the

controller is chosen such that some requirements concerning performance are fulfilled. An automated way to do this is given by the theory of H_∞ -control. In H_∞ -control an optimization problem is solved to determine the controller thereby improving the overall goal for the 'poorest' situation.

All methods mentioned so far readily extend to the MIMO case. A MIMO flow control application based on robust control in the frequency domain can be found in Henning et al. (2008).

When working in the time instead of the frequency domain, controller synthesis is simplified for MIMO systems. For a plant

$$\dot{\mathbf{x}}(t) = \mathbf{A}'\mathbf{x}(t) + \mathbf{B}'\mathbf{u}(t) \quad (30)$$

minimization of

$$I = \frac{1}{2} \int_0^\infty (\mathbf{x}^T \mathbf{Q} \mathbf{x} + \mathbf{u}^T \mathbf{R} \mathbf{u}) dt \quad (31)$$

leads to a well known state space controller

$$\mathbf{u}(t) = -\mathbf{K}\mathbf{x}(t) \quad (32)$$

where \mathbf{K} is determined by the solution of a steady state quadratic Riccati equation. Beside providing an optimal solution by a closed-loop control law this Riccati controller guarantees robustness with respect to model uncertainties.

Another popular way to determine \mathbf{K} is through pole placement. Substituting \mathbf{u} by $-\mathbf{K}\mathbf{x}$ gives the equation of the closed loop

$$\dot{\mathbf{x}}(t) = (\mathbf{A}' - \mathbf{B}'\mathbf{K})\mathbf{x}(t) = \mathbf{A}'_c\mathbf{x}(t) \quad . \quad (33)$$

Stability of the steady state solution $\mathbf{x}_s = \mathbf{0}$ is given when all eigenvalues of \mathbf{A}'_c stay in the open left half plane. For a scalar input u and an n -dimensional state vector n eigenvalues can be chosen. This fully determines \mathbf{K} if the system is controllable. In the multi-input case free parameters in \mathbf{K} can be chosen to fulfil further requirements concerning decoupling, eigenstructure assignment, minimization of control energy, etc.

State space controller assume the knowledge of the complete state \mathbf{x} . However, with

$$\mathbf{y}(t) = \mathbf{C}\mathbf{x}(t) + \mathbf{D}\mathbf{u}(t)$$

only a linear combination of the components of \mathbf{x} (and of the control inputs) is available. To get a full state estimate a Luenberger observer or Kalman filter has to be applied, see the contribution by G. Tadmor in this book and Gelb (1986). For an extension to nonlinear systems, extended Kalman filters are recommended. Kalman filters perform better as well in the linear case as they explicitly take into account the noise which is prevalent in every real-live experiment.

3.3 Model predictive control

In the last two decades model predictive control (MPC) has been shown to be one of the most powerful and versatile control methods in process engineering. With the availability of constantly increasing computing power and the advent of highly efficient optimization methods MPC is within reach for the use in very fast flow control applications as well. This contribution gives an introduction into MPC and shows an example.

MPC is best explained by means of Fig. 13. The basic idea of MPC is to calculate future control inputs such that some performance criterion is optimized. In doing so, system constraints referring to states x , outputs y and manipulated variables u are respected. For this purpose, the future control input $u_f(t)$ is parameterized by, for example, piece-wise constant trajectories over a discrete-time horizon H_c . Usually, the sampling period

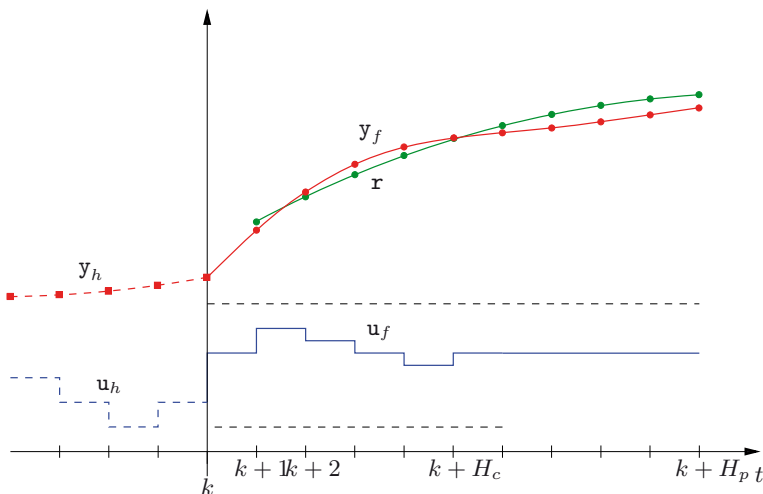


Figure 13. Basic scheme of MPC for a SISO system. Indices f and h refer to the future and the past, i.e. history, respectively. The reference signal r is specified starting from $k + 1$, because the actual system output $y(k)$ cannot be changed by the actual or future inputs.

h for the piece-wise constant control input is fixed. It coincides with the sampling period T of the model if a discrete-time model of the process is used. In the study of the von Kármán vortex street below it coincides with half the period of the flow. A variable sampling period, however, is possible as well, see e.g. Waldruff et al. (1997).

Let us assume that the actual discretized time instant is given by $t = k$. Hence, $t < k$ represents the past and $t > k$ the future. The actual control input for $t = k$, i.e. $\mathbf{u}(k) = \mathbf{u}_f(k)$, and future control inputs $\mathbf{u}_f(k+1), \mathbf{u}_f(k+2), \dots$ are now determined such that the system output $\mathbf{y}_f(k+i)$ is driven back to a reference trajectory $\mathbf{r}(k+i)$ for $H_1 \leq i \leq H_p$ in an optimal fashion. If a system with a pure time-delay d is considered, the output \mathbf{y} will not be influenced by the actual input $\mathbf{u}(k)$ before $t = k + d$. In such cases, H_1 should be equal or larger than d . Even without time-delays, a $H_1 > 1$ might be beneficial for the overall performance.

Due to the piece-wise constant control input a finite parametric optimization problem results with optimization or design variables $\mathbf{u}_f(k), \mathbf{u}_f(k+1), \dots$. The prediction horizon H_p is usually chosen (much) larger than the control horizon H_c in which control moves are allowed. A larger prediction horizon in comparison to the control horizon is beneficial for closed-loop stability. A thorough study shows that stability can be guaranteed if a terminal penalty or a terminal penalty and a terminal constraint are included, see Mayne et al. (2000) for a survey. A possible criterion or quality function may read without a terminal cost

$$J = \sum_{i=H_1}^{H_p} \|\mathbf{r}(k+i) - \mathbf{y}_f(k+i)\|_{\mathbf{Q}} + \sum_{i=0}^{H_c} \|\mathbf{u}_f(k+i)\|_{\mathbf{R}} \stackrel{!}{=} \min \quad , \quad (34)$$

in which \mathbf{Q} and \mathbf{R} are symmetric weighting matrices used in the norms $\|\cdot\|$, i.e. $\|\mathbf{z}\|_{\mathbf{S}} = \mathbf{z}^T \mathbf{S} \mathbf{z}$. Both weights may depend on the time index $k+i$ as well. With the weights a different importance of manipulated values $\mathbf{u}_f(k+i)$ and future errors between reference $\mathbf{r}(k+i)$ and system output $\mathbf{y}_f(k+i)$ is accounted for. If changes in the control input $\Delta \mathbf{u}_f(k+i) = \mathbf{u}_f(k+i) - \mathbf{u}_f(k+i-1)$ are critical to avoid too large changes of the actuator amplitudes from one sampling instant to the next, these changes can be included in eq. (34) readily. Likewise, if the future control input for $t > k + H_c$ is not zero, its cost can be included as well. When constraints have to be considered, these can be dealt with via Lagrange operators or via penalty functions to name just two possibilities.

So far it was assumed that the optimal control input calculated after processing the measurement obtained at $t = k$ could be immediately applied at the same time instant. If the numerical burden is high, however, the measurements taken at $t = k$ are used to calculate the next control moves starting from $t = k + 1$. In such a case, the second summation in eq. (34) would start at $i = 1$.

In MPC, just the first control move $\mathbf{u}_f(k)$ of the calculated optimal input trajectory is applied to the plant. To react almost immediately when the

next measurement \mathbf{y} for $t = k + 1$ is obtained, preparatory calculations can be done in the period from k to $k+1$. Then, the optimization starts from the beginning at the next sampling instant. By this, the influence of unknown disturbances and model errors is accounted for as these uncertainties show up in the next value of the measured output variable $\mathbf{y}(k+1)$. This repeated solution of an optimization problem has led to an alternative name of MPC, namely receding horizon optimal control.

In the general case, when the process model is nonlinear, a numerical solution of the optimization problem has to be done. This leads to a nonlinear model predictive controller (NMPC). A similar approach has to be taken for linear models in case of equality or inequality constraints which have to be met. This numerical solution, however, is responsible for the large numerical burden involved in solving (N)MPC problems. The beauty of the (N)MPC-method rests in its unifying framework. Irrespective of the kind of model, linear or nonlinear, continuous or discrete-time, SISO or MIMO, and irrespective of the optimization problem to be solved, unconstrained or constrained, the same principle can be used to derive a control signal.

To show the most simplest version of a MPC-scheme which leads to an explicit control law, a couple of assumptions will be made in the following. It is assumed that 1) the process model is given as a linear, discrete-time state-space model, 2) the plant output $\mathbf{y}(k)$ at time k will not directly depend on the control input $\mathbf{u}(k)$, i. e. there is no direct feed through, 3) the time for evaluating the control law obtained can be neglected, 4) no terminal cost or terminal constraint is included, and 5) no constraints are considered.

MPC formulation for linear unconstrained problems As stated above every linear system can be described by a state-space model of the form

$$\mathbf{x}(k+1) = \mathbf{A}\mathbf{x}(k) + \mathbf{B}\mathbf{u}(k) \quad (35)$$

$$\mathbf{y}(k) = \mathbf{C}\mathbf{x}(k) \quad (36)$$

in which \mathbf{x} , \mathbf{u} and \mathbf{y} represent the internal state of the process, the control input and the process output, respectively. For ease of illustration, \mathbf{D} is set to zero which is usually true in most applications.

Starting from time k , the future development of the process can be predicted exploiting Eq. (35). If a state prediction made at $t = k$ for $t = k+j$

is denoted by $\mathbf{x}(k+j|k)$, it follows

$$\begin{aligned}\mathbf{x}(k+1|k) &= \mathbf{A}\mathbf{x}(k) + \mathbf{B}\mathbf{u}(k) \\ \mathbf{x}(k+2|k) &= \mathbf{A}\mathbf{x}(k+1|k) + \mathbf{B}\mathbf{u}(k+1) \\ &= \mathbf{A}^2\mathbf{x}(k) + \mathbf{AB}\mathbf{u}(k) + \mathbf{B}\mathbf{u}(k+1) \\ &\vdots \\ \mathbf{x}(k+H_p|k) &= \mathbf{A}^{H_p}\mathbf{x}(k) + \sum_{i=0}^{H_p-1} \mathbf{A}^i \mathbf{B}\mathbf{u}(k+H_p-1-i)\end{aligned}\quad (37)$$

Hence, the future or predicted output for $k+j$ reads

$$\mathbf{y}_f(k+j) = \mathbf{y}(k+j|k) = \mathbf{C}\mathbf{A}^j\mathbf{x}(k) + \sum_{i=0}^{j-1} \mathbf{C}\mathbf{A}^i \mathbf{B}\mathbf{u}_f(k+j-1-i) \quad (38)$$

in which \mathbf{u} was replaced by \mathbf{u}_f as future values of the control input are addressed. All future outputs will now be concatenated in $\mathbf{y}_p = (\mathbf{y}^T(k+1|k) \ \mathbf{y}^T(k+2|k) \dots \mathbf{y}^T(k+H_p|k))^T$. Accordingly, $\mathbf{u}_p = (\mathbf{u}_f^T(k) \ \mathbf{u}_f^T(k+1) \ \dots \ \mathbf{u}_f^T(k+H_c) \ \dots \ \mathbf{u}_f^T(k+H_p))^T$ with $\mathbf{u}_f(k+j) = \mathbf{u}_f(k+H_c)$ for $j = H_c + 1, H_c + 2, \dots, H_p$ to account for a constant manipulated variable for the last section of the prediction horizon H_p .

All future outputs inside the prediction horizon can now be written as

$$\mathbf{y}_p = \mathbf{A}_p\mathbf{x}(k) + \mathbf{B}_p\tilde{\mathbf{u}}_p \quad (39)$$

with

$$\mathbf{A}_p = \begin{pmatrix} \mathbf{CA} & & & \\ & \mathbf{CA}^2 & & \\ & \vdots & & \\ & \mathbf{CA}^{H_c} & & \\ & \vdots & & \\ & \mathbf{CA}^{H_p} & & \end{pmatrix}$$

$$\mathbf{B}_p = \begin{pmatrix} \mathbf{CB} & \mathcal{O} & \dots & \mathcal{O} \\ \mathbf{CAB} & \mathbf{CB} & \dots & \mathcal{O} \\ \vdots & \vdots & \ddots & \vdots \\ \mathbf{CA}^{H_c}\mathbf{B} & \mathbf{CA}^{H_c-1}\mathbf{B} & \dots & \mathbf{CB} \\ \mathbf{CA}^{H_c+1}\mathbf{B} & \mathbf{CA}^{H_c}\mathbf{B} & \dots & \mathbf{CB} + \mathbf{CAB} \\ \vdots & \vdots & \ddots & \vdots \\ \mathbf{CA}^{H_p-1}\mathbf{B} & \mathbf{CA}^{H_p-2}\mathbf{B} & \dots & \sum_{i=0}^{H_p-H_c-1} \mathbf{CA}^i \mathbf{B} \end{pmatrix}$$

$$\tilde{\mathbf{u}}_p = \begin{pmatrix} \mathbf{u}_f(k) \\ \mathbf{u}_f(k+1) \\ \vdots \\ \mathbf{u}_f(k+H_c) \end{pmatrix}$$

In the new variables \mathbf{y}_p , $\tilde{\mathbf{u}}_p$, the cost functional, Eq. (34), reads with $\mathbf{r}_p = (\mathbf{r}^T(k+1) \ \mathbf{r}^T(k+2) \ \dots \ \mathbf{r}^T(k+H_p))^T$

$$\begin{aligned} J &= (\mathbf{r}_p - \mathbf{y}_p)^T \mathbf{Q}_p (\mathbf{r}_p - \mathbf{y}_p) + \tilde{\mathbf{u}}_p^T \mathbf{R}_p \tilde{\mathbf{u}}_p \\ &= (\mathbf{r}_p - \mathbf{A}_p \mathbf{x}(k) - \mathbf{B}_p \tilde{\mathbf{u}}_p)^T \mathbf{Q}_p (\mathbf{r}_p - \mathbf{A}_p \mathbf{x}(k) - \mathbf{B}_p \tilde{\mathbf{u}}_p) + \tilde{\mathbf{u}}_p^T \mathbf{R}_p \tilde{\mathbf{u}}_p \quad (40) \end{aligned}$$

The block diagonal matrices \mathbf{Q}_p and \mathbf{R}_p consist of \mathbf{Q} and \mathbf{R} matrices from Eq. (34) on the main diagonal if $H_1 = 1$. For $H_1 > 1$, the first entries in the main diagonal are zero. Equating $dJ/d\tilde{\mathbf{u}}_p = 0^T$ as a necessary and sufficient condition for an extremum yields for the future control input

$$\tilde{\mathbf{u}}_p = (\mathbf{B}_p^T \mathbf{Q}_p \mathbf{B}_p + \mathbf{R}_p)^{-1} \mathbf{B}_p^T \mathbf{Q}_p (\mathbf{r}_p - \mathbf{A}_p \mathbf{x}(k)) \quad . \quad (41)$$

As no constraints are considered, a closed form of the control law is obtained. From $\tilde{\mathbf{u}}_p = (\mathbf{u}_f(k) \ \mathbf{u}_f(k+1) \ \dots)$ only the first entry, i.e. $\mathbf{u}(k) = \mathbf{u}_f(k)$, is applied to the process. Then, the optimization starts from the beginning using the measurement $\mathbf{y}(k+1)$ to determine a new state $\mathbf{x}(k+1)$, and so forth. To obtain a state estimate, a model-based measuring technique such as a Kalman filter (Gelb, 1986) has to be applied if the full state vector $\mathbf{x}(k+1)$ cannot be measured.

As the following application of model predictive control will be limited to a nonlinear example exploiting a Galerkin system, the reader is referred to King et al. (2008); Muminovic et al. (2008); Gelbert et al. (2008) where a linear MPC is applied in experiments to a burner and a bluff body.

MPC formulation for constrained and /or nonlinear problems If constraints relating to the state \mathbf{x} , output \mathbf{y} , control input \mathbf{u} or changes in the control input $\Delta\mathbf{u}$ have to be respected, a closed solution of the optimization problem will be impossible. Numerical optimization methods have to be used then. With simple models, for example for the 3D bluff body considered in Muminovic et al. (2008), and appropriate numerical methods, for example active set methods, see Ferreau et al. (2007), we have already realized linear, constrained MPC with 8000Hz sampling frequency.

For nonlinear process models the prediction of the future behavior has to be done by a numerical integration. Moreover, the estimation of the gradient of the cost function with respect to future control moves is performed numerically too by repeating the prediction many times, each time slightly

changing one entry in the vector of future control inputs. Hence, even without constraints a huge numerical burden will be involved in nonlinear MPC. Today, this is still a limiting factor for flow control applications. Nevertheless, a nonlinear constrained simulation problem will be considered in the following to show the prospects of NMPC.

3.4 General nonlinear control

Much progress has been made in nonlinear control in the last decades. Any attempt to summarize this effort in this chapter is bound to fail. Therefore, the reader is referred to textbooks on nonlinear systems and control, see Khalil (2002); Isidori (2002), and to a contribution in which different nonlinear controllers were applied in a direct numerical simulation of a flow around a cylindrical cylinder based on a Galerkin system (King et al., 2005). Only one very simple nonlinear control method will be given here as it readily extends from the linear concepts introduced above.

If the state vector of a system \mathbf{x}_1 can be split up into a slowly changing part \mathbf{x}_s and fast components \mathbf{x} , i.e. $\mathbf{x}_1 = [\mathbf{x}_s^T \ \mathbf{x}^T]^T$ and if the evolution equations can be given in the form

$$\dot{\mathbf{x}} = \mathbf{A}(\mathbf{x}_s)\mathbf{x} + \mathbf{B}\mathbf{u} \quad (42)$$

a linear parametrically varying (LPV-) system is given. Now, for fixed \mathbf{x}_s pole placement can be used to find a state space controller, see Eq. (33).

4 Applications

In the collaborative research center 'Control of complex turbulent shear flows' at TU Berlin which was funded by the German Research Foundation the author and his group had the chance to test the above mentioned methods in numerous experimental tests. These involved the flow (and acoustics) for/with

- a backward-facing step in a SISO and MIMO setting
- a single 2-dimensional bluff body and a tandem configuration of two 2-dimensional bluff bodies
- a 3-dimensional Ahmed body
- various 2- and 3-dimensional wings with a flap as a high-lift device
- Tollmien-Schlichting instabilities over a profile
- noise-producing and/or stalling turbomachines
- mixers, a burner chamber, diffusors, and in a pipe.

From these examples only a small selection is considered here. A 2-dimensional bluff body is chosen to compare slope-seeking control, its extension with a

Kalman filter, robust control and phase control (see contribution of G. Tadmor in this book). Although not tested experimentally, the flow past a cylindrical cylinder, which is covered in several other chapters in this book, is included as well using nonlinear MPC and LPV-control.

Information about the other experimental closed-loop flow control studies can be found in the literature.

4.1 Two-dimensional bluff body - slope seeking

The flow separation behind bluff bodies, such as vehicles, shows complex space- and time-dependent topology which results in an increase in aerodynamic drag. A principle sketch of the investigated two-dimensional D-shaped body is shown in Fig. 14. The flow around the D-shaped body is governed by an absolute wake instability (Huerre and Monkewitz, 1990). This mechanism generates a von Kármán vortex street with an alternating sequence of vortices at characteristic frequencies. The natural flow is characterised by a short dead water region and alternating vortices in the vicinity of the base. Both are responsible for a low base pressure and thus for a high pressure-induced drag. The proposed active control strategy enforces a decoupling of the vortex formation in the shear layers and the wake by synchronising the roll-up of upper and lower shear layers. This delays the appearance of asymmetries in the wake flow and thus mitigates the wake instability. The dead water region is enlarged and the base pressure increases (Henning et al., 2007). Details, dimensions, etc. of the test section can be found in Pastoor et al. (2008).

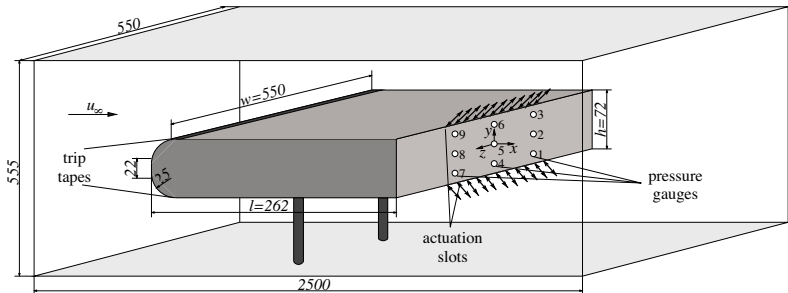


Figure 14. Sketch of the D-shaped body and the test section. All dimensions are in mm. Trip tapes are placed 30 mm downstream of the nose in order to trigger boundary layer transition.

A sinusoidal zero-mass actuation is applied by loudspeakers through

spanwise slots located at the upper and lower trailing edges. With this harmonic actuation the unstable processes of shear layer roll-up are triggered. By this means a maximum response of the flow can be generated with a minimum amount of input of energy. The actuation frequency f_a is related to natural instability frequencies of the flow. It should not be mistaken with the perturbation frequency $f_{sin} = 2\pi\omega_{sin}$ of the extremum controller used first.

The intensity of the actuation which will be modified in the following is characterised by the non-dimensional excitation momentum coefficient (Greenblatt and Wygnanski, 2000)

$$c_\mu = \frac{2 s q_a^2}{h u_\infty^2} , \quad (43)$$

in which q_a is the effective velocity of the actuation.

The base pressure is monitored by 3×3 difference pressure gauges mounted in three parallel rows on the rear end. The reference pressure is taken in front of the body. Four strain gauges are applied to the aluminium rods supporting the model for measurement of drag. The base pressure and drag are described by the non-dimensional coefficients

$$c_p(y, z, t) = \frac{\Delta p}{\rho u_\infty^2 / 2} \quad (44)$$

$$c_d(t) = \frac{f_x}{\rho u_\infty^2 h w / 2} , \quad (45)$$

respectively. In the present work, Δp is the instantaneous pressure difference between a rear end-mounted pressure gauge and the reference pressure, ρ denotes the density, and f_x is the drag force. Spatially and spatially and temporally averaged base pressure across the stern are marked by $c_{pb}(t)$ and \bar{c}_{pb} , respectively.

The data acquisition and the implementation of the controllers are realized on a rapid prototyping hardware (*dSPACE-PPC1005* controller board). The sampling frequency is 1 000 Hz.

Fig. 15 (a) shows the steady-state map with the time-averaged base pressure coefficient as a function of the momentum coefficient at a constant Reynolds number $Re_h = 40\,000$ obtained from open-loop experiments in Henning et al. (2007). The Reynolds number is calculated with the body's height h and free stream velocity u_∞ . Both actuators operate in-phase with an optimal frequency $St_a = f_a h / u_\infty = 0.17$, which was indicated as the most effective actuation parameter for synchronisation of the shear layer development and for drag reduction in Henning et al. (2007). This steady-state

map is characterised by a plateau for $c_\mu \geq 7 \times 10^{-3}$. In order to achieve maximum base pressure with the minimum control input a slope-seeking controller with reference slope $f'_{ref} = 5$ is applied.

In the present study, the momentum coefficient is chosen as the input variable $u(t) = c_\mu(t)$, and the output is given by the spatially averaged base pressure coefficient $y(t) = c_{pb}(t)$. Information about the controller parameters are found in Henning et al. (2008).

The experimental data for a single operating point is shown in Fig. 15 (*b–d*). The controller starts at $c_\mu = 2 \times 10^{-3}$. The sinusoidal modifications

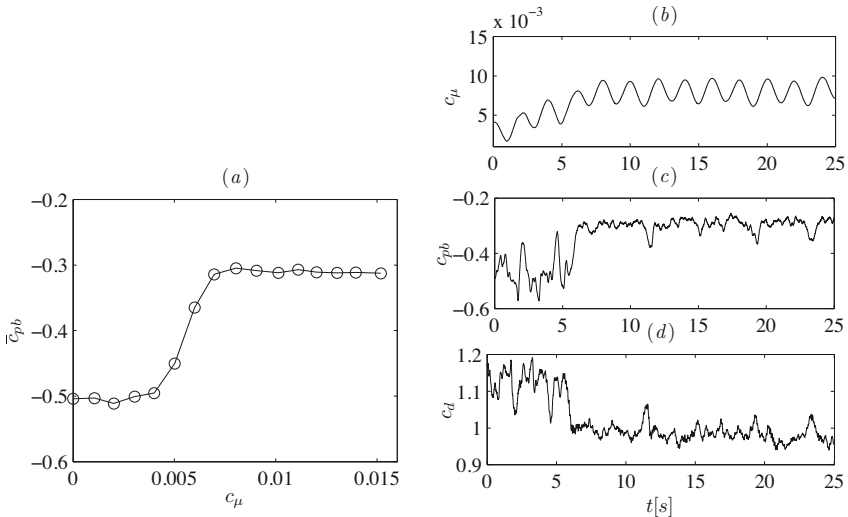


Figure 15. Steady-state map $\bar{c}_{pb} = f(c_\mu)$ obtained from open-loop experiments (*a*) and experimental implementation of slope-seeking feedback for optimal drag reduction of the D-shaped body (*b–d*). The controller adapts the actuation amplitude (*b*) until the maximum base pressure (*c*) has been reached and a maximum drag reduction of approximately 15% can be achieved. All experiments are performed at Reynolds number 40 000, in-phase forcing with a Strouhal number $t_a = 0.17$.

of c_μ are applied to obtain information about the local slope. According to the gradient, the actuation amplitude is raised until a state in front of the plateau is reached. This leads to a significant increase in the base pressure coefficient as shown in Fig. 15 (*c*), corresponding to the steady-state map. A reduction of the drag coefficient by 15% can be observed.

To show disturbance rejection of this controller, the Reynolds number is

increased continuously from 35 000 up to 60 000 in Fig. 16 *d*. Corresponding to the steady-state maps for various Reynolds numbers shown in Fig. 16 (*a*) the optimal actuation amplitude is automatically decreased with increasing Reynolds number. The experimental results in Fig. 16 (*b*, *c*) indicate that the desired averaged base pressure $c_{pb} = -0.3$ is maintained with the minimum control input.

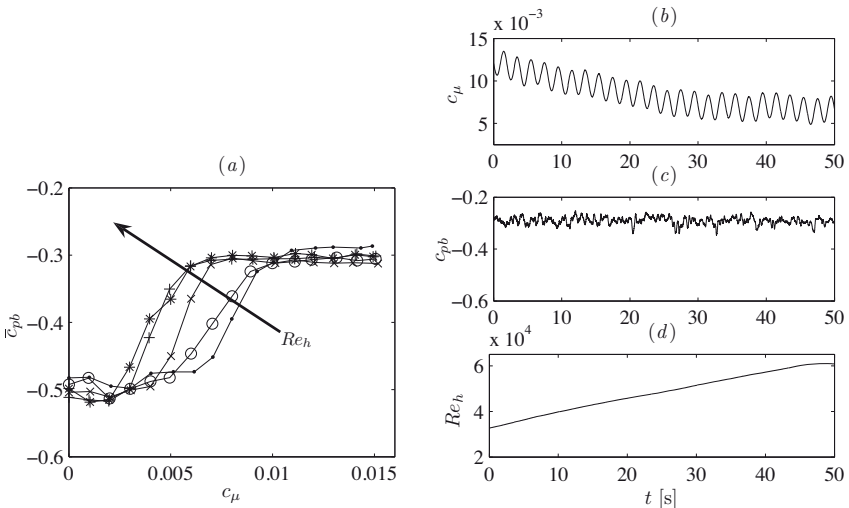


Figure 16. Slope-seeking feedback in an experiment with an increasing Reynolds numbers (*b-d*). Steady-state maps $\bar{c}_{pb} = f(c_\mu)$ are displayed (*a*) for various Reynolds numbers $Re_h = 20\,000$ (\bullet), $30\,000$ (\circ), $40\,000$ (\times), $50\,000$ ($+$), $60\,000$ ($*$). These maps are used only to indicate the success of control. They are not required for the controller. Strouhal number of the in-phase forcing is $St_a = 0.17$.

The experimental results with the slope-seeking controller extended by the Kalman filter are shown in Fig. 17. The time delay is set to $n\Delta t = 2\pi/(3\omega_{sin})s = 660\Delta t$ with sampling time $\Delta t = 0.001s$. An almost three times faster response is observed compared to the classical approach due to the fast estimation of the local gradient \hat{f}' , see Fig. 17 (*d*).

4.2 Two-dimensional bluff body - robust control

To identify a low dimensional dynamical model different experiments with different actuation signals are run. In this case, the actuation am-

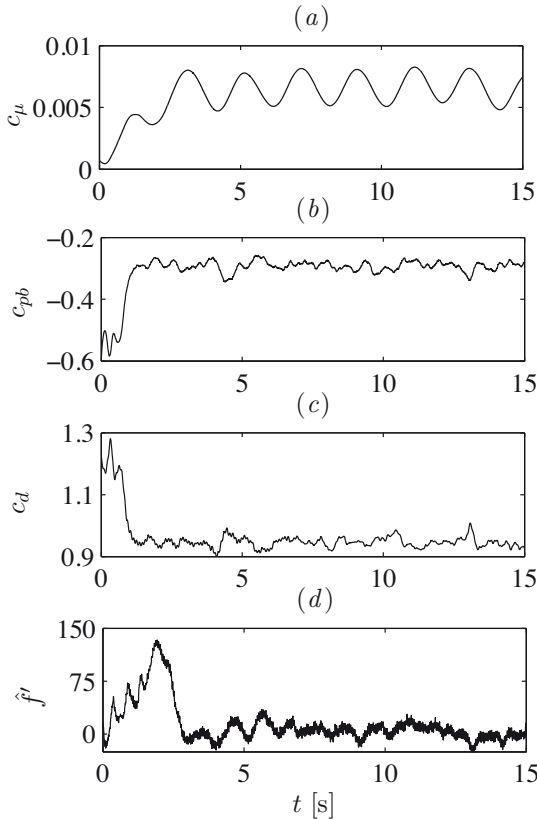


Figure 17. A fast extended Kalman filter algorithm is used to estimate the current slope (d) of the steady-state map. Thus the slope-seeking controller can achieve the optimal momentum coefficient faster (a) which leads to an increase in base pressure (b) and a reduction of the drag coefficient (c) of the D-shaped body. Harmonic in-phase actuation with $St_a = 0.17$ at $Re_h = 40\,000$ is applied.

plitude $u(t) = \hat{u}$ is switched on/off to/from different levels of \hat{u} . Each experiment is identified with a linear black-box model. A Bode plot of all models found for a certain Reynolds number is given in Fig. 12. For a truly linear system all identified models should be equal. The spread in the Bode plots seen, however, is an indication of the nonlinearity of the plant.

For the gain of all identified models in the left panel of Fig. 12 a nonlinear

static relationship $f(\cdot)$ with respect to the input amplitude \hat{u} is found. This knowledge can be used to reduce the uncertainty in the model description as outlined above. The result is given in right panel of Fig. 12. From the latter a so-called nominal model of second order with time-delay T_0

$$T_2^2 \ddot{y}(t) + T_1 \dot{y}(t) + y(t) = K(u(t - T_0) + T_d \dot{u}(t - T_0)) \quad (46)$$

is obtained, see as well Fig. 12. Instead of using parameters a_i and b_j , time constants and a power of a time constant are introduced here. With respect to the model parameters K , T_0 , T_1 , T_2 and T_d this nominal model shows the smallest distance to all other models identified. The non-dimensionalized parameterized uncertainties are given by

$$\begin{aligned} K &= 1 \\ T_0 u_\infty / h &= 68.65(1 + 0.98\delta) \\ T_1 u_\infty / h &= 9.19(1 + 0.73\delta) \\ T_2 u_\infty / h &= 13.76(1 + 0.32\delta) \\ T_d u_\infty / h &= 5.49(1 + 1.0\delta) \end{aligned} \quad (47)$$

with $-1 \leq \delta \leq 1$.

Although the flow in the recirculation region behind the body is highly complex, a very simple nominal model is obtained relating actuation amplitude $u(t)$ with mean base pressure $y(t) = c_{Pb}(t)$.

To increase the bandwidth of the closed loop with respect to reference signals a dynamic pre-filter $G_{ff}(s)$ is included as well, see King et al. (2005); Henning (2008) for more details.

Based on the nominal model and the uncertainty description a robust controller is synthesized using the MATLAB® robust control toolbox. With this robust controller the behavior of the controlled system is tested in wind tunnel experiments with respect to tracking response and disturbance rejection. Fig. 18 shows the tracking response of the closed-loop after stepwise changes of the reference command. A good tracking performance can be observed. High-frequency disturbances are not rejected because of both the system's inherent limited tracking dynamics and the requirement of robustness giving a limitation of the closed-loop performance. A main advantage of closed-loop control in comparison to open-loop control is disturbance rejection. To demonstrate the robustness of the closed-loop control the Reynolds number is varied in the same experiment from 7×10^4 to 4×10^4 . The setpoint-tracking capability is not effected by this disturbance which is unknown to the controller. More information can be found in Henning and King (2005); Henning (2008).

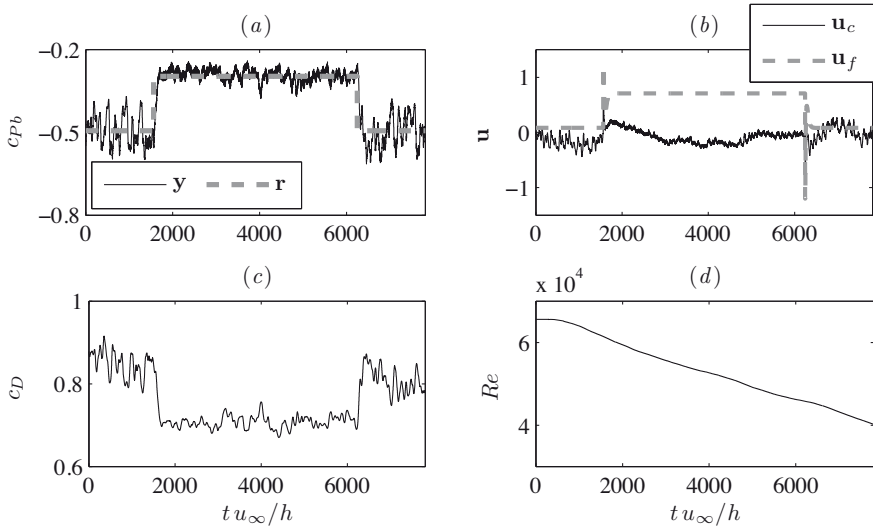


Figure 18. Robust control of the base pressure $y = c_{Pb}$ while changing the setpoint r and the Reynolds number Re from Henning (2008). The obtained drag c_D is given for reference. The control input $u(t)$ is given by the sum of the fast feed-forward term u_f and the controller output u_c .

This robust controller is significantly faster than an extremum- or slope-seeking controller. This has to be payed for, however, by an increased effort in identifying the model family and running the appropriate identification experiments.

The application of the robust controller suffers from rather large values of the manipulated variable. Hence, another idea to save energy is to reject the detrimental alternate vortex shedding and to generate a synchronized vortex shedding in the near wake, instead. This can be accomplished by one actuation slot only which is synchronized with naturally occurring vortices of the opposite side. By this, see contribution of G. Tadmor in this volume or Pastoor et al. (2008), the same control success as with the robust controller can be achieved with a reduction of the spend control energy of 40%.

4.3 MPC, energy-based and LPV-control of the cylinder wake

We consider the 3-dimensional Galerkin system including a shift mode introduced by B.R. Noack, see chapter by Noack et al. and Noack et al.

(2003), with $a_1 = A \cos \Phi$, $a_2 = A \sin \Phi$

$$\begin{bmatrix} \dot{A} \\ \dot{\Phi} \\ \dot{a}_3 \end{bmatrix} = \begin{bmatrix} (\sigma_r - \beta a_3)A \\ \omega + \gamma a_3 \\ \alpha A^2 - \sigma_3 a_3 \end{bmatrix} + \begin{bmatrix} g_c \cos(\Phi - \theta) \\ -(g_c/A) \sin(\Phi - \theta) \\ 0 \end{bmatrix} u . \quad (48)$$

Several nonlinear control synthesis methods have been applied in King et al. (2005) to dampen the von Kármán vortex street. Although these formally derived methods successfully controlled the wake, none was better than a formerly proposed controller which is build upon physical insight of the system, cf. Gerhard et al. (2003). One of the controller tested in King et al. (2005) is based on an LPV-point of view. It will be given below. However, the physically motivated controller will be reviewed first.

The original work (Gerhard et al., 2003) was a proof-of-concept study showing that an empirical Galerkin model derived from natural flow data can also be employed for an actuated flow. One conclusion was that the system should stay in the region of validity of the low dimensional model. Following this argument, more classical nonlinear methods of controller synthesis were ruled out in Gerhard et al. (2003), as it was expected that these methods do not preserve the range of model validity. A simple energy-based controller was proposed, instead, with $u = -u_0$ if $g_c \cos(\Phi - \theta) > 0$, and $u = +u_0$ otherwise. With a rather complicated formula, see as well (Tadmor et al., 2003), the amplitude u_0 was determined once every period in agreement with a desired decay rate of the amplitude A . The mean impact of the force on the phase Φ was small because of the sign-change of the angle force-term $g_c \sin(\Phi - \theta)$, see Eq. (48), during the time of constant force direction.

With this control law, the turbulent kinetic energy, expressed as $\sum_{i=1}^N \langle a_i^2 \rangle / 2$, could not only be reduced for the model used in the controller synthesis itself, with 3 POD-modes. The very same control law synthesized with a third order system reduces also the energy in higher-order Galerkin modes in the real system, since the higher harmonics get their energy from the suppressed first harmonics. This was shown by applying the controller to Galerkin approximations with $N = 7$ and $N = 9$ states. Finally, the complete system was controlled in a DNS study. A nonlinear observer (Zeitz, 1987) was build up using the measurement device shown in Fig. 19 to implement the control in the DNS. The gain of the nonlinear observer was determined so that the linearized dynamics of the state-space estimation error was stable.

In the following, a new and simpler version of this energy-based control is proposed. If $g_c \cos(\Phi - \theta) \geq 0$, the mean influence of the control on \dot{A} during half a period $T/2$ can be approximated, using $\phi \approx \omega t$ and $\omega T \approx 2\pi$,

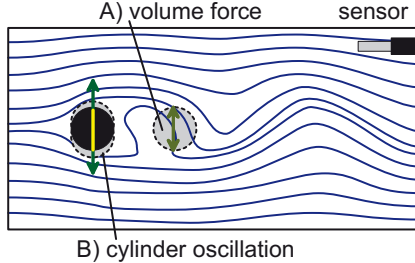


Figure 19. Principal sketch of the actuated cylinder wake. The figure displays the streamlines of the natural flow around a circular cylinder with diameter $D = 1$ (solid circle). Actuation is provided by transverse cylinder oscillation or by a transverse volume force in the grey circle. The flow state is sensed with a hot-wire anemometer, located at a typical position. Success of control is monitored in the observation region $-5 < x < 15$, $-5 < y < 5$, with $x = y = 0$ in the center of the cylinder, see Fig. 21 as well.

by

$$\frac{2g_c}{2\pi} \int_{-\pi/2}^{\pi/2} \cos(\Phi - \theta) d(\Phi - \theta) = \frac{2g_c}{\pi} . \quad (49)$$

Replacing $g_c \cos(\Phi - \theta)$ in the first equation of (48) by the mean influence $2g_c/\pi$, and demanding that

$$(\sigma_r - \beta a_3)A + u_0 \frac{2g_c}{\pi} = -kA ,$$

with a decay rate $-k$, yields the control

$$u_0 = \frac{\pi}{2g_c} (-k - \sigma_r + \beta a_3)A . \quad (50)$$

For $\cos(\Phi - \theta) < 0$ an opposite sign is needed. This finally leads to the new energy-based (*eb*) control

$$u_{eb} = -\frac{\pi A(k + \sigma_r - \beta a_3)}{2g_c} \operatorname{sign}\{\cos(\Phi - \theta)\} . \quad (51)$$

The LPV-character of the system is better seen when it is further transformed using $b_1 = r \sin(\Phi - \theta)$ and $b_2 = r \cos(\Phi - \theta)$

$$\begin{bmatrix} \dot{b}_1 \\ \dot{b}_2 \\ \dot{a}_3 \end{bmatrix} = \begin{bmatrix} (\sigma_r - \beta a_3)b_1 + (\omega + \gamma a_3)b_2 \\ -(\omega + \gamma a_3)b_1 + (\sigma_r - \beta a_3)b_2 \\ -\sigma_3 a_3 + \alpha(b_1^2 + b_2^2) \end{bmatrix} + \begin{bmatrix} 0 \\ g_c \\ 0 \end{bmatrix} u . \quad (52)$$

As the shift mode $a_3(t)$ is only slowly varying the first two equations make up an LPV-system. In a pole placement approach the poles of the closed-loop are placed at each sampling instant such that in an energy optimal sense the unstable poles of the open-loop system are mirrored at the imaginary axis and shifted 0.001 to the left. The control law can be written as

$$u_{LPV} = -\frac{A(t)}{g_c} \left(K_{LPV1}(a_3(t)) \cos(\Phi - \theta) - K_{LPV2}(a_3(t)) \sin(\Phi - \theta) \right) \quad (53)$$

where K_{LPV1} and K_{LPV2} are more intricate functions of $a_3(t)$.

Applying this controller in a direct numerical simulation (DNS) with a code provided by M. Morzyński resulted in an 24% post-transient reduction of the turbulent kinetic energy compared to the physically proposed controller which achieved 32%. However, better results are obtained with a nonlinear model predictive controller.

To test the NMPC the direct numerical simulations are performed on a grid with 8712 nodes. For state estimation based on the velocity measurement depicted in Fig. 19, an extended Kalman filter is applied. As the Galerkin system is nonlinear, integration of the system equations for prediction and the solution of the extended Kalman filter equations has to be done numerically. Likewise, a numerical optimization routine is used to minimize the cost functional. In this example not a constant reference trajectory for the velocity measured is used. Instead a reference trajectory for the first mode amplitude is given. A very simple cost functional is used here instead of Eq. (34)

$$J = \int_t^{t+H_p} e^2(l) dl \quad \text{with} \quad e(t) = r(t) - \hat{a}_1 \quad , \quad (54)$$

i.e. the control effort is neglected. The scalar reference $r(t)$ is chosen as a sinusoidal signal with exponentially decreasing amplitude. This choice is motivated by the limited validity of the low dimensional Galerkin system. The variable $\hat{a}_1(t)$ denotes the estimated value of the state variable $a_1(t)$. To make the optimization problem easier, we use even more physical knowledge about the process. From the physically motivated controller it is known that good results are obtained when a piece-wise constant u is synchronized with $\cos(\Phi - \theta)$. This knowledge is exploited here as well. No arbitrary sampling period h , see Fig. 13, is chosen, but one that exactly matches the physics of the process. Inside a sampling period, u_f is chosen to be constant.

To respect the validity of the model, the calculated future control inputs are constraint to $|u_f(t+l)| < 0.1$. For more details see Aleksic et al. (2008). A comparison in Fig. 20 shows the superiority of NMPC which is significantly faster than energy-based control and leads to a recirculation zone of

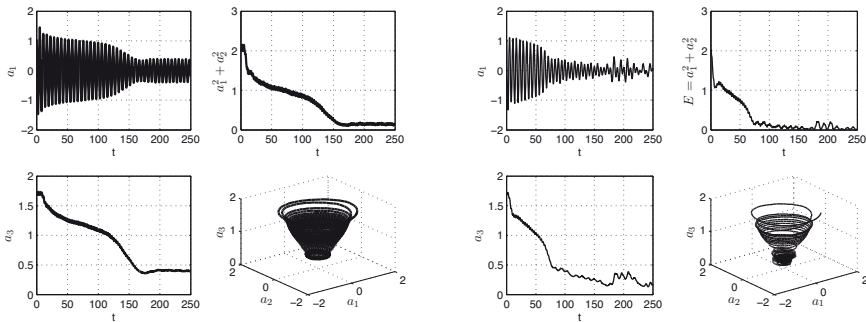


Figure 20. Fourier coefficients a_i obtained in a closed-loop controlled DNS by applying the controller based on physical intuition from Gerhard et al. (2003) (left) and NMPC (right). State estimation is done with an extended Kalman filter. The success of the control is observed by $a_1^2 + a_2^2$ which describes the major part of the turbulent kinetic energy.

length 5.2 in contrast to 4.1 for the energy-based control, see Fig 15. With no other controller using the very same measurement information and the same actuation concept such good results were found in King et al. (2005). Even with the improved versions of the backstepping and Lyapunov-based controllers in Aleksic et al. (2007), a poorer performance was obtained. Fig. 21 shows a plot of the streamlines of the unactuated and the actuated case with the NMPC controller at $t=120$. The damping effect of the actuation and the significant mitigation of the instability is clearly visible in the observation region.

5 Conclusions

Comparing the different controllers proposed a hierarchy concerning robustness, velocity and modeling effort can be given, see Fig. 22.

Physically motivated controllers can be very fast and, certainly depending on the application, rather robust when strong and reproducible coherent events take place. A rational exploitation of these phenomena necessitates a good physical understanding of the process as in the case of the phase control shown in the part of G. Tadmor or needs a good model as the Navier-Stokes equation derived Galerkin model of the 2D flow around a circular cylinder treated above.

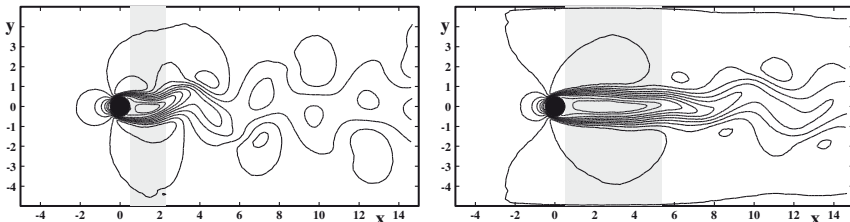


Figure 21. Left: Unactuated flow. Right: Actuated flow with an NMPC controller shown for $t = 120$. The figures display isocontours of the streamwise velocity component U . Negative values are indicated by thinner curves and show the extent of the recirculation region. The shaded area depicts the length of the recirculation zone.

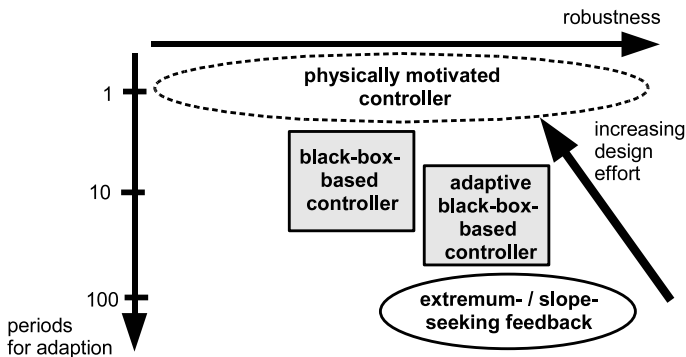


Figure 22. Time scales, robustness and required modeling effort of different controllers.

In many classical controllers, models of a process are only used during synthesis of the controller. In contrast, the phase control and MPC exploit a process model inside the algorithm. As an optimization problem over a future horizon is considered in MPC, there are no restrictions concerning the variables which are used to describe the success of control as long as they can be calculated by that model. Very different criteria can be formulated, combining different aspects at the same time. Moreover, when enough computing power is available, equality and inequality constraints can be included in the optimization in a straightforward manner. With no

other control technique this practically very important issue can be dealt with so easily. However, as the name tells, MPC is based on a model. If this model is not derived theoretically, it has to be identified based on experimental data in a black-box manner. The time needed for this step should not be underestimated. In the MPC approaches shown here, robustness is not dealt with explicitly. If this has to be done, the computational burden increases significantly.

Robustness issues can be addressed with more classical techniques, such as a H_∞ -control. Numerous experimental tests with different flow configurations have shown their good performance.

For all approaches mentioned so far as well as for the slow but easy to apply extremum-seeking control methods the limitations or difficulties often do not arise from control engineering (when you know this subject) but from the search of appropriate actuators and sensors to influence the flow and get informative information, respectively.

Bibliography

- K. Aleksic, R. King, B.R. Noack, O. Lehmann, M. Morzynski, and G. Tadmor. Nonlinear flow control using a low dimensional galerkin model. In *X Triennial International SAUM Conference on Systems, Automatic Control and Measurements*, Nis, Serbia, 2007.
- K. Aleksic, R. King, B.R. Noack, O. Lehmann, M. Morzynski, and G. Tadmor. Nonlinear model predictive control based on a low dimensional model of fluid flow. In *Int. Conf. on Jets, Wakes and Separated Flows 2008*, Berlin, Germany, 2008.
- K.B. Ariyur and M. Krstic. *Real-Time Optimization by Extremum-Seeking Control*. John Wiley & Sons, Hoboken, 2003.
- J.-F. Beaudoin, O. Cadot, J.-L. Aider, and J.-E. Wesfried. Drag reduction of a bluff body using adaptive control methods. *Physics of Fluids*, 18: 085107, 1–10, 2006.
- R. Becker, R. King, R. Petz, and W. Nitsche. Adaptive closed-loop separation control on a high-lift configuration using extremum seeking. *AIAA Journal*, 45:1382–1392, 2007.
- H.J. Ferreau, P. Ortner, P. Langthaler, L. del Re, and M. Diehl. Predictive control of a real-world diesel engine using an extended online active set strategy. *Annual Reviews in Control*, 31(2):293–301, 2007.
- M. Garwon, F. Urzynicok, L. H. Darmadi, G. Bärwolff, and R. King. Adaptive control of separated flows. In *Proc. of the ECC 2003*, Cambridge, 2003.
- A. Gelb. *Applied Optimal Estimation*. The M.I.T. Press, Cambridge, 1986.

- G. Gelbert, J.P. Moeck, M.R. Bothien, R. King, and C.O. Paschereit. Model predictive control of thermoacoustic instabilities in a swirl-stabilized combustor. *AIAA Paper 2008-1055*, 46th AIAA Aerospace Sciences Meeting and Exhibit, 2008.
- J. Gerhard, M. Pastoor, R. King, B. R. Noack, A. Dillmann, M. Morzynski, and G. Tadmor. Model-based control of vortex shedding using low-dimensional Galerkin models. *AIAA Paper 2003-4262*, 2003.
- D. Greenblatt and I. Wygnanski. The control of flow separation by periodic excitation. *Prog. Aerospace Sci.*, 36:487–545, 2000.
- L. Henning. *Closed-loop control of separated shear flows by active means (in german)*. PhD thesis, TU Berlin, opus.kobv.de/tuberlin/volltexte/2008/1861/, Berlin, 2008.
- L. Henning and R. King. Drag reduction by closed-loop control of a separated flow over a bluff body with a blunt trailing edge. In *Proc. of the 44th IEEE Conference on Decision and Control and European Control Conference, CDC-ECC'05*, Seville, Spain, 2005.
- L. Henning, M. Pastoor, R. King, B.R. Noack, and G. Tadmor. Feedback control applied to bluff body wake. In R. King, editor, *Active Flow Control*, pages 325–228, Springer-Verlag, Berlin, 2007.
- L. Henning, G. Feuerbach, R. Muminovic, A. Brunn, W. Nitsche, and R. King. Extensions of adaptive slope-seeking for active flow control. *Proc. IMech, Part I: J. Systems and Control Engineering*, pages 309–322, 2008.
- P. Huerre and P. A. Monkewitz. Local and global instabilities in spatially developing flows. *Annual Review Fluid Mechanics*, 22:473–537, 1990.
- A. Isidori. *Nonlinear Control Systems*. Springer, 2002.
- H.K. Khalil. *Nonlinear Systems*. Prentice Hall, 2002.
- R. King, R. Becker, M. Garwon, and L. Henning. Robust and adaptive closed-loop control of separated shear flows. *AIAA-Paper 2004-2519*, 2004.
- R. King, M. Seibold, O. Lehmann, B.R. Noack, M. Morzynski, and G. Tadmor. Nonlinear flow control based on a low dimensional model of fluid flow. In Meurer et al., editor, *Lecture Notes in Control and Information Science*, volume 322, pages 365–386. Springer, 2005.
- R. King, R. Becker, G. Feuerbach, L. Henning, R. Petz, W. Nitsche, O. Lemke, and W. Neise. Adaptive flow control using slope seeking. In *14th IEEE Mediterranean Conference on Control Automation*, Ancona, 2006.
- R. King, K. Aleksic, G. Gelbert, N. Losse, R. Muminovic, A. Brunn, W. Nitsche, M. R. Bothien, J. P. Moeck, C. O. Paschereit, B. R. Noack, U. Rist, and M. Zengl. Model predictive flow control. *AIAA Paper 2008-3975*, *Proc. of the 4th AIAA Flow Control Conference*, Seattle, 2008.

- M. Krstic and H.-H. Wang. Stability of extremum seeking feedback for general nonlinear dynamic systems. *Automatica*, 36:595–601, 2000.
- L. Ljung. *System Identification: Theory for the User*. Prentice Hall, Englewood Cliffs, New Jersey, 1999.
- J. M. Maciejowski. *Robust Process Control*. Addison-Wesley, Wokingham, England, 1994.
- D. Q. Mayne, J. B. Rawlings, C. V. Rao, and P. O. M. Scokaert. Constrained model predictive control: Stability and optimality. *Automatica*, 36:789–814, 2000.
- M. Morari and E. Zafiriou. *Robust Process Control*. Prentice-Hall, Englewood Cliffs, New Jersey, 1989.
- I. S. Morosanov. Method of extremum control. *Automation Remote Control*, 18:1077–1092, 1957.
- R. Muminovic, L. Henning, R. King, A. Brunn, and W. Nitschev. Robust and model predictive control for a generic car model. *AIAA Paper 2008-3859*, 4th AIAA Flow Control Conference, 2008.
- B.R. Noack, K. Afanasiev, M. Morzynski, G. Tadmor, and F. Thiele. A hierarchy of low-dimensional models of the transient and post-transient cylinder wake. *J. Fluid Mechanics*, 497:335–363, 2003.
- M. Pastoor, L. Henning, B.R. Noack, R. King, and G. Tadmor. Feedback shear layer control for bluff body drag reduction. *J. Fluid. Mech.*, 608: 161–196, 2008.
- S. Skogestad and I. Postlethwaite. *Multivariable Feedback Control - Analysis and Design*. John Wiley & Sons, Chichester, England, 1996.
- G. Tadmor, B.R. Noack, A. Dillmann, J. Gerhard, M. Pastoor, R. King, and M. Morzynski. Control, observation and energy regulation of wake flow instabilities (paper 909). In *Proc. of the 42nd IEEE Conference on Decision and Control*, pages 2334–2339, Maui, USA, 2003.
- W. Waldraff, R. King, and E.D. Gilles. Optimal feeding strategies by adaptive mesh selection for fed-batch bioprocesses. *Bioprocess Engineering*, 17:221–227, 1997.
- T. Weinkauf, H.-C. Hege, M. Schlegel, and A. Dillmann. Coherent structures in a transitional flow around a backward facing step. *Phys. Fluids*, 15: S3, 2003.
- M. Zeitz. The extended Luenberger observer for nonlinear systems. *Systems and Control Letters*, 9:149–156, 1987.